

Travail de Fin d'Etudes : Photonic and thermal properties of periodic arrays of nanometer-wide metal lines

Auteur : Elias, Quentin

Promoteur(s) : Vanderheyden, Benoit

Faculté : Faculté des Sciences appliquées

Diplôme : Master en ingénieur civil physicien, à finalité approfondie

Année académique : 2019-2020

URI/URL : <http://hdl.handle.net/2268.2/10788>

Avertissement à l'attention des usagers :

Tous les documents placés en accès ouvert sur le site le site MatheO sont protégés par le droit d'auteur. Conformément aux principes énoncés par la "Budapest Open Access Initiative"(BOAI, 2002), l'utilisateur du site peut lire, télécharger, copier, transmettre, imprimer, chercher ou faire un lien vers le texte intégral de ces documents, les disséquer pour les indexer, s'en servir de données pour un logiciel, ou s'en servir à toute autre fin légale (ou prévue par la réglementation relative au droit d'auteur). Toute utilisation du document à des fins commerciales est strictement interdite.

Par ailleurs, l'utilisateur s'engage à respecter les droits moraux de l'auteur, principalement le droit à l'intégrité de l'oeuvre et le droit de paternité et ce dans toute utilisation que l'utilisateur entreprend. Ainsi, à titre d'exemple, lorsqu'il reproduira un document par extrait ou dans son intégralité, l'utilisateur citera de manière complète les sources telles que mentionnées ci-dessus. Toute utilisation non explicitement autorisée ci-avant (telle que par exemple, la modification du document ou son résumé) nécessite l'autorisation préalable et expresse des auteurs ou de leurs ayants droit.

UNIVERSITY OF LIÈGE - FACULTY OF APPLIED SCIENCES

GRADUATION STUDIES CONDUCTED FOR OBTAINING THE MASTER'S
DEGREE IN ENGINEERING PHYSICS, 2019-2020

Photonic properties of periodic arrays of nanometer-wide metal lines

Author:
Quentin ELIAS

Supervisors:
Benoît VANDERHEYDEN
Janusz BOGDANOWICZ
Andrzej GAWLIK



August 21, 2020

Contents

1	Introduction	13
1.1	Context	13
1.2	Metrology	13
1.2.1	Scatterometry	14
1.2.2	Raman spectroscopy	14
1.3	State of the art	15
1.4	Outline	16
2	Important theoretical concepts	17
2.1	Maxwell's equations	17
2.1.1	Interface conditions	17
2.2	Electromagnetic waves	18
2.2.1	Electromagnetic waves in vacuum	18
2.2.2	Electromagnetic waves in non-dissipative media	20
2.2.3	Electromagnetic waves in dissipative media	21
2.2.3.1	Drude model	21
2.2.3.2	Complex formulation	22
2.3	Polarization	24
2.3.1	Linear polarization	25
2.3.2	TE and TM polarizations	26
2.4	Light interaction at the interface between two semi-infinite media	26
2.4.1	Snell's law	26
2.4.2	TE polarization	27
2.4.3	TM polarization	28
2.4.4	Reflectance, Transmittance and Absorptance	28
2.5	Light interaction with multiple interfaces	30
2.5.1	Multiple reflections	30
2.5.2	Absorptance as a function of thickness	33
2.6	Light interaction with patterned structures	35
2.6.1	Perfect electrical conductor parallel plate waveguide	36
2.6.1.1	TE polarization	36
2.6.1.2	TM polarization	39
2.6.2	Diffraction grating	42
2.6.3	Surface plasmons polaritons	45
3	Light interaction with periodic arrays of nanometer-wide PEC lines	48
3.1	Methodology and modeling	48
3.1.1	COMSOL Multiphysics®	50
3.2	Effect of the geometry	53
3.2.1	Effect of pitch	54
3.2.1.1	Region 1: $\Lambda \in [0, 127]$ nm	61
3.2.1.2	Region 2: $\Lambda \in [127, 217]$ nm	64

3.2.1.3	Region 3: $\Lambda \in [217, 256]$ nm	67
3.2.1.4	Region 4: $\Lambda \in [256, 384]$ nm	69
3.2.1.5	Region 5: $\Lambda \in [384, 398]$ nm	72
3.2.1.6	Region 6: $\Lambda \in [398, 512]$ nm	74
3.2.1.7	Region 7: $\Lambda \in [512, 532]$ nm	77
3.2.1.8	Region 8: $\Lambda \in [532, 581]$ nm	79
3.2.1.9	Region 9: $\Lambda \in [581, 763]$ nm	82
3.2.1.10	Region 10 and 11: $\Lambda \in [763, 1000]$ nm	85
3.2.2	Effect of width	91
3.2.3	Effect of height	95
3.2.3.1	Region 1': $\Lambda \in [0, 215]$ nm	100
3.2.3.2	Region 2': $\Lambda \in [215, 400]$ nm	103
3.2.3.3	Region 3': $\Lambda \in [400, 580]$ nm	108
3.2.3.4	Region 4': $\Lambda \in [580, 763]$ nm	111
3.2.3.5	Region 5': $\Lambda \in [763, 945]$ nm	116
3.2.3.6	Region 6': $\Lambda \in [945, 1000]$ nm	119
3.3	Summary	125
4	Light interaction with periodic arrays of nanometer-wide metal lines	125
4.1	Methodology and modeling	125
4.2	Effect of the geometry	127
4.2.1	Effect of pitch	128
4.2.2	Effect of width	136
4.2.3	Effect of height	143
4.3	Summary	155
5	Conclusion and outlooks	156
6	Acknowledgments	158
7	Appendix	159

List of Figures

2	Orientation of the fields for a plane wave traveling along the z axis.	19
3	Spatial periodicity of the uniform fields of a plane wave, traveling along \mathbf{k}	20
4	Refractive index n and extinction coefficient κ of copper as a function of the wavelength.	25
5	Linear polarization along a single axis (left). Linear polarization along both axis (right).	26
6	Refraction of light at an interface between two semi-infinite media.	27
7	Reflection and transmission of TE polarized light at an interface between two media.	28
8	Reflection and transmission of TM polarized light at an interface between two media.	29

9	Reflection and transmission of a light beam at an interface.	30
10	Multiple reflections inside a thin film of thickness d	31
11	Reflectance $R = r ^2$ and transmittance $T = (n_2/n_1) t ^2$ for a thin film of thickness h and real refractive index $n = 1.46$ with $n_1 = 1$ and $n_2 = 4.15$, as a function of the film thickness normalized to multiples of a quarter wavelength, under normal illumination with $\lambda_0 = 532$ nm.	32
12	Reflectance $R = r ^2$ for a thin film of thickness h and several real refractive indices n with $n_1 = 1$ and $n_2 = 4.15$, as a function of the film thickness normalized to multiples of a quarter wavelength, under normal illumination with $\lambda_0 = 532$ nm. The consequence of a negative reflection coefficient (i.e. when $n < n_1$, in this case when $n = 0.9$, is to induce a π phase shift which swaps the condition for constructive and destructive interferences).	33
13	Reflectance, transmittance and absorptance of a sample of increasing thickness h with refractive index $n = 1.46$ and extinction coefficient $\kappa = 0.25$, with $n_1 = 1$ and $n_2 = 4.15$. The light normally incident and has a free-space wavelength $\lambda_0 = 532$ nm.	34
14	Reflectance, transmittance and absorptance of a sample of thickness $h = 100$ nm and real refractive index $n = 1.46$, as a function of the extinction coefficient κ , with $n_1 = 1$ and $n_2 = 4.15$. The incident light is TE polarized and has a free-space wavelength $\lambda_0 = 532$ nm.	35
15	Incoming TE plane wave on a PEC parallel plate waveguide.	37
16	Spatial distribution along x of the $E_{y,m}$ component, for the four first modes of the TE polarization.	37
17	Band structure for the five first modes of the TE polarization for PEC parallel plate waveguide, for a free-space wavelength $\lambda_0 = 532$ nm and $\tilde{n} = 1.45$. The solid lines represent the real part of the wave number, while the dashed lines represent the opposite of its imaginary part.	39
18	Incoming TM plane wave on a PEC parallel plate waveguide.	39
19	Spatial distribution along x of the $H_{y,m}$ component, for the four first modes of the TM polarization.	40
20	Band structure for the six first modes of the TM polarization for PEC parallel plate waveguide, for a free-space wavelength $\lambda_0 = 532$ nm and $\tilde{n} = 1.45$. The solid lines represent the real part of the wave number, while the dashed lines represent the opposite of its imaginary part.	41
21	Phase matching condition on the tangential component of the incoming wave vector incident on a periodic grating with wave vector \mathbf{K}	42
22	Example of diffraction orders for an incoming plane wave with incidence angle θ_i . In this case, $n_t > n_i$ and more modes are available in transmission than in reflection.	43
23	Band structure for 0^{th} order and three first modes in reflection of a diffraction grating, for a free-space wavelength $\lambda_0 = 532$ nm, $\tilde{n}_i = \tilde{n}_r = 1$ and $\theta_i = 15^\circ$. The solid lines represent the real part of the wave number, while the dashed lines represent the opposite of its imaginary part.	44

24	Band structure for 0^{th} order and three first modes in transmission of a diffraction grating, for a free-space wavelength $\lambda_0 = 532\text{ nm}$, $\tilde{n}_i = \tilde{n}_r = 1$ and $\theta_i = 15^\circ$. The solid lines represent the real part of the wave number, while the dashed lines represent the opposite of its imaginary part.	45
25	Color map of the $ E_y ^2$ field resulting from the interaction of a plane wave at normal incidence with a silver thin film grating on top of a substrate layer and below an air layer. The field is decomposed into the diffraction (25a and 25b) and SPPs (25c and 25d) contributions. The period is $1.62\text{ }\mu\text{m}$, the thickness of the thin film is 50 nm and its width is $1.48\text{ }\mu\text{m}$	47
26	Model of the idealized periodic array of PEC lines upon which a plane wave is incident.	49
27	Band structure for the array of PEC lines under TE illumination, which features only the modes that are excited below a pitch $\Lambda = 1000\text{ nm}$, for a free-space wavelength $\lambda_0 = 532\text{ nm}$, width $w = 34\text{ nm}$, refractive indices $n_{air} = 1$, $n_{Si} = 4.15$, $n_{SiO_2} = 1.45$ and $\theta_i = 0^\circ$. The solid lines represent the real part of the wave number, while the dashed lines represent the opposite of its imaginary part. Blue curves correspond to waveguide modes, green curves correspond to diffraction in reflection modes and red curves correspond to diffraction in transmission modes. To make the plot more readable, only the first few diffraction modes are plotted since the higher order ones are barely excited. Similarly, only the symmetric TE waveguide modes are plotted, as the asymmetric modes are not excited by a symmetrical plane wave.	51
28	Band structure for the array of PEC lines under TM illumination, which features only the modes that are excited below a pitch $\Lambda = 1000\text{ nm}$, for a free-space wavelength $\lambda_0 = 532\text{ nm}$, width $w = 34\text{ nm}$, refractive indices $n_{air} = 1$, $n_{Si} = 4.15$, $n_{SiO_2} = 1.45$ and $\theta_i = 0^\circ$. The solid lines represent the real part of the wave number, while the dashed lines represent the opposite of its imaginary part. Blue curves correspond to waveguide modes, green curves correspond to diffraction in reflection modes and red curves correspond to diffraction in transmission modes. To make the plot more readable, only the first few diffraction modes are plotted since the higher order ones are barely excited. Similarly, only the symmetric TM waveguide modes are plotted, as the asymmetric modes are not excited by a symmetrical plane wave.	52
29	Geometry defined in the COMSOL software.	53
30	Reflectance spectrum of a normally incident TE polarized plane wave interacting with an array of PEC lines with width $w = 34\text{ nm}$ and height $h = 100\text{ nm}$, as a function of the pitch Λ . The plot features the different diffraction orders. The spectrum is calculated using FEM.	55
31	Transmittance spectrum of a normally incident TE polarized plane wave interacting with an array of PEC lines with width $w = 34\text{ nm}$ and height $h = 100\text{ nm}$, as a function of the pitch Λ . The plot features the different diffraction orders. The spectrum is calculated using FEM.	55

32	Reflectance spectrum of a normally incident TM polarized plane wave interacting with an array of PEC lines with width $w = 34$ nm and height $h = 100$ nm, as a function of the pitch Λ . The plot features the different diffraction orders. The spectrum is calculated using FEM.	56
33	Transmittance spectrum of a normally incident TM polarized plane wave interacting with an array of PEC lines with width $w = 34$ nm and height $h = 100$ nm, as a function of the pitch Λ . The plot features the different diffraction orders. The spectrum is calculated using FEM.	56
34	Band structure for the array of PEC lines under TM illumination, which features only the modes that are excited below a pitch $\Lambda = 1000$ nm, for a free-space wavelength $\lambda_0 = 532$ nm, width $w = 34$ nm, refractive indices $n_{air} = 1$, $n_{Si} = 4.15$, $n_{SiO_2} = 1.45$ and $\theta_i = 0^\circ$. The solid lines represent the real part of the wave number, while the dashed lines represent the opposite of its imaginary part. Blue curves correspond to waveguide modes, green curves correspond to diffraction in reflection modes and red curves correspond to diffraction in transmission modes. To make the plot more readable, only the first few diffraction modes are plotted since the higher order ones are barely excited. Similarly, only the symmetric TM waveguide modes are plotted, as the asymmetric modes are not excited by a symmetrical plane wave. The TEM mode is replaced by the EMA mode obtained by effective medium approximation.	59
35	Label of the different spectral regions extracted from the band structure and defined by the cutoff pitch of each mode, for a PEC grating with width $w = 34$ nm and height $h = 100$ nm.	60
36	Distribution of the phasor norm of the TE electric field in the unit cell, for an array of PEC lines with width $w = 34$ nm, height $h = 100$ nm in pitch region 1 (Λ between 0 nm and 127 nm).	62
37	Distribution of the phasor norm of the TM electric field in the unit cell, for an array of PEC lines with width $w = 34$ nm, height $h = 100$ nm in pitch region 1 (Λ between 0 nm and 127 nm).	63
38	Distribution of the phasor norm of the TE electric field in the unit cell, for an array of PEC lines with width $w = 34$ nm, height $h = 100$ nm in pitch region 2 (Λ between 127 nm and 217 nm).	65
39	Distribution of the phasor norm of the TM electric field in the unit cell, for an array of PEC lines with width $w = 34$ nm, height $h = 100$ nm in pitch region 2 (Λ between 127 nm and 217 nm).	66
40	Distribution of the phasor norm of the TE electric field in the unit cell, for an array of PEC lines with width $w = 34$ nm, height $h = 100$ nm in pitch region 3 (Λ between 217 nm and 256 nm).	68
41	Distribution of the phasor norm of the TM electric field in the unit cell, for an array of PEC lines with width $w = 34$ nm, height $h = 100$ nm in pitch region 3 (Λ between 217 nm and 256 nm).	68
42	Distribution of the phasor norm of the TE electric field in the unit cell, for an array of PEC lines with width $w = 34$ nm, height $h = 100$ nm in pitch region 4 (Λ between 256 nm and 384 nm).	70

43	Distribution of the phasor norm of the TM electric field in the unit cell, for an array of PEC lines with width $w = 34$ nm, height $h = 100$ nm in pitch region 4 (Λ between 256 nm and 384 nm).	71
44	Distribution of the phasor norm of the TE electric field in the unit cell, for an array of PEC lines with width $w = 34$ nm, height $h = 100$ nm in pitch region 5 (Λ between 384 nm and 398 nm).	73
45	Distribution of the phasor norm of the TM electric field in the unit cell, for an array of PEC lines with width $w = 34$ nm, height $h = 100$ nm in pitch region 5 (Λ between 384 nm and 398 nm).	73
46	Distribution of the phasor norm of the TE electric field in the unit cell, for an array of PEC lines with width $w = 34$ nm, height $h = 100$ nm in pitch region 6 (Λ between 398 nm and 512 nm).	75
47	Distribution of the phasor norm of the TM electric field in the unit cell, for an array of PEC lines with width $w = 34$ nm, height $h = 100$ nm in pitch region 6 (Λ between 398 nm and 512 nm).	76
48	Distribution of the phasor norm of the TE electric field in the unit cell, for an array of PEC lines with width $w = 34$ nm, height $h = 100$ nm in pitch region 7 (Λ between 512 nm and 532 nm).	78
49	Distribution of the phasor norm of the TM electric field in the unit cell, for an array of PEC lines with width $w = 34$ nm, height $h = 100$ nm in pitch region 7 (Λ between 512 nm and 532 nm).	78
50	Distribution of the phasor norm of the TE electric field in the unit cell, for an array of PEC lines with width $w = 34$ nm, height $h = 100$ nm in pitch region 8 (Λ between 532 nm and 581 nm).	80
51	Distribution of the phasor norm of the TM electric field in the unit cell, for an array of PEC lines with width $w = 34$ nm, height $h = 100$ nm in pitch region 8 (Λ between 532 nm and 581 nm).	81
52	Distribution of the phasor norm of the TE electric field in the unit cell, for an array of PEC lines with width $w = 34$ nm, height $h = 100$ nm in pitch region 9 (Λ between 581 nm and 763 nm).	83
53	Distribution of the phasor norm of the TM electric field in the unit cell, for an array of PEC lines with width $w = 34$ nm, height $h = 100$ nm in pitch region 9 (Λ between 581 nm and 763 nm).	84
54	Distribution of the phasor norm of the TE electric field in the unit cell, for an array of PEC lines with width $w = 34$ nm, height $h = 100$ nm in pitch region 10 (Λ between 763 nm and 946 nm).	86
55	Distribution of the phasor norm of the TM electric field in the unit cell, for an array of PEC lines with width $w = 34$ nm, height $h = 100$ nm in pitch region 10 (Λ between 763 nm and 946 nm).	87
56	Distribution of the phasor norm of the TE electric field in the unit cell, for an array of PEC lines with width $w = 34$ nm, height $h = 100$ nm in pitch region 11 (Λ between 946 nm and 1000 nm).	88
57	Distribution of the phasor norm of the TM electric field in the unit cell, for an array of PEC lines with width $w = 34$ nm, height $h = 100$ nm in pitch region 11 (Λ between 946 nm and 1000 nm).	89

58	Reflectance spectrum of a normally incident TE polarized plane wave interacting with an array of PEC lines for several pitches for a height $h = 100$ nm, as a function of the fill factor w/Λ . The spectrum is calculated using FEM.	91
59	Reflectance spectrum of a normally incident TM polarized plane wave interacting with an array of PEC lines for several pitches for a height $h = 100$ nm, as a function of the fill factor w/Λ	92
60	Reflectance spectrum of a normally incident TE polarized plane wave interacting with an array of PEC lines for a pitch $\Lambda = 1000$ nm, for a height $h = 100$ nm, as a function of the width w . The plot features the different diffraction orders. The spectrum is calculated using FEM.	93
61	Reflectance spectrum of a normally incident TM polarized plane wave interacting with an array of PEC lines for a pitch $\Lambda = 1000$ nm, for a height $h = 100$ nm, as a function of the width w . The plot features the different diffraction orders. The spectrum is calculated using FEM.	93
62	Reflectance spectrum of a normally incident TE polarized plane wave interacting with an array of PEC lines with pitch $\Lambda = 400$ nm and height $h = 100$ nm, as a function of the width w . The plot features the different diffraction orders. The spectrum is calculated using FEM.	94
63	Reflectance spectrum of a normally incident TM polarized plane wave interacting with an array of PEC lines with pitch $\Lambda = 400$ nm and height $h = 100$ nm, as a function of the width w . The plot features the different diffraction orders. The spectrum is calculated using FEM.	95
64	Reflectance spectrum of a normally incident TE polarized plane wave interacting with an array of PEC lines with width $w = 34$ nm and height $h = 500$ nm, as a function of the pitch Λ . The plot features the different diffraction orders. The spectrum is calculated using FEM.	96
65	Transmittance spectrum of a normally incident TE polarized plane wave interacting with an array of PEC lines with width $w = 34$ nm and height $h = 500$ nm, as a function of the pitch Λ . The plot features the different diffraction orders. The spectrum is calculated using FEM.	96
66	Reflectance spectrum of a normally incident TM polarized plane wave interacting with an array of PEC lines with width $w = 34$ nm and height $h = 500$ nm, as a function of the pitch Λ . The plot features the different diffraction orders. The spectrum is calculated using FEM.	98
67	Transmittance spectrum of a normally incident TM polarized plane wave interacting with an array of PEC lines with width $w = 34$ nm and height $h = 500$ nm, as a function of the pitch Λ . The plot features the different diffraction orders. The spectrum is calculated using FEM.	98
68	Label of the different spectral regions extracted from the band structure and defined by the cutoff pitch of each grating mode, for a PEC grating with width $w = 34$ nm and height $h = 500$ nm.	99
69	Distribution of the phasor norm of the TE electric field in the unit cell, for an array of PEC lines with width $w = 34$ nm, height $h = 500$ nm in pitch region 1' (Λ between 0 nm and 215 nm).	101

70	Distribution of the phasor norm of the TM electric field in the unit cell, for an array of PEC lines with width $w = 34$ nm, height $h = 500$ nm in pitch region 1' (Λ between 0 nm and 215 nm).	102
71	Distribution of the phasor norm of the TE electric field in the unit cell, for an array of PEC lines with width $w = 34$ nm, height $h = 500$ nm in pitch region 2' (Λ between 215 nm and 400 nm).	105
72	Distribution of the phasor norm of the TM electric field in the unit cell, for an array of PEC lines with width $w = 34$ nm, height $h = 500$ nm in pitch region 2' (Λ between 215 nm and 400 nm).	107
73	Distribution of the phasor norm of the TE electric field in the unit cell, for an array of PEC lines with width $w = 34$ nm, height $h = 500$ nm in pitch region 3' (Λ between 400 nm and 580 nm).	109
74	Distribution of the phasor norm of the TM electric field in the unit cell, for an array of PEC lines with width $w = 34$ nm, height $h = 500$ nm in pitch region 3' (Λ between 400 nm and 580 nm).	110
75	Distribution of the phasor norm of the TE electric field in the unit cell, for an array of PEC lines with width $w = 34$ nm, height $h = 500$ nm in pitch region 4' (Λ between 580 nm and 763 nm).	113
76	Distribution of the phasor norm of the TM electric field in the unit cell, for an array of PEC lines with width $w = 34$ nm, height $h = 500$ nm in pitch region 4' (Λ between 580 nm and 763 nm).	115
77	Distribution of the phasor norm of the TE electric field in the unit cell, for an array of PEC lines with width $w = 34$ nm, height $h = 500$ nm in pitch region 5' (Λ between 763 nm and 945 nm).	117
78	Distribution of the phasor norm of the TM electric field in the unit cell, for an array of PEC lines with width $w = 34$ nm, height $h = 500$ nm in pitch region 5' (Λ between 763 nm and 945 nm).	118
79	Distribution of the phasor norm of the TE electric field in the unit cell, for an array of PEC lines with width $w = 34$ nm, height $h = 500$ nm in pitch region 6' (Λ between 945 nm and 1000 nm).	120
80	Distribution of the phasor norm of the TM electric field in the unit cell, for an array of PEC lines with width $w = 34$ nm, height $h = 500$ nm in pitch region 6' (Λ between 945 nm and 1000 nm).	121
81	Reflectance spectrum of a normally incident TE polarized plane wave interacting with an array of PEC lines with width $w = 34$ nm as a function of the height h . The plot features several values for the pitch of the grating. The spectrum is calculated using FEM.	123
82	Reflectance spectrum of a normally incident TM polarized plane wave interacting with an array of PEC lines with width $w = 34$ nm as a function of the height h . The plot features several values for the pitch of the grating. The spectrum is calculated using FEM.	124

83	Band structure for the symmetric grating modes of the array of copper lines under TE illumination below $\Lambda = 1000$ nm, for a free-space wavelength $\lambda_0 = 532$ nm, width $w = 34$ nm, refractive indices $n_{air} = 1$, $n_{Si} = 4.15$, $n_{SiO_2} = 1.45$ and $\theta_i = 0^\circ$. The solid lines represent the real part of the wave number, while the dashed lines represent the opposite of its imaginary part.	126
84	Band structure for the symmetric grating modes of the array of copper lines under TM illumination below $\Lambda = 1000$ nm, for a free-space wavelength $\lambda_0 = 532$ nm, width $w = 34$ nm, refractive indices $n_{air} = 1$, $n_{Si} = 4.15$, $n_{SiO_2} = 1.45$ and $\theta_i = 0^\circ$. The solid lines represent the real part of the wave number, while the dashed lines represent the opposite of its imaginary part.	127
85	Reflectance spectrum of a normally incident TE polarized plane wave interacting with an array of copper lines with width $w = 34$ nm and height $h = 100$ nm, as a function of the pitch Λ . The plot features the different diffraction orders. The spectrum is calculated using FEM.	129
86	Transmittance spectrum of a normally incident TE polarized plane wave interacting with an array of copper lines with width $w = 34$ nm and height $h = 100$ nm, as a function of the pitch Λ . The plot features the different diffraction orders. The spectrum is calculated using FEM.	129
87	Absorptance spectrum of a normally incident TE polarized plane wave interacting with an array of copper lines with width $w = 34$ nm and height $h = 100$ nm, as a function of the pitch Λ . The spectrum is calculated using FEM.	130
88	Reflectance spectrum of a normally incident TM polarized plane wave interacting with an array of copper lines with width $w = 34$ nm and height $h = 100$ nm, as a function of the pitch Λ . The plot features the different diffraction orders. The spectrum is calculated using FEM.	131
89	Transmittance spectrum of a normally incident TM polarized plane wave interacting with an array of copper lines with width $w = 34$ nm and height $h = 100$ nm, as a function of the pitch Λ . The plot features the different diffraction orders. The spectrum is calculated using FEM.	131
90	Absorptance spectrum of a normally incident TM polarized plane wave interacting with an array of copper lines with width $w = 34$ nm and height $h = 100$ nm, as a function of the pitch Λ . The spectrum is calculated using FEM.	132
91	Distribution of the phasor norm of the TE electric field in the unit cell, for an array of copper lines with width $w = 34$ nm, height $h = 100$ nm, and for several pitches between 0 nm and 1000 nm.	134
92	Distribution of the phasor norm of the TM electric field in the unit cell, for an array of copper lines with width $w = 34$ nm, height $h = 100$ nm, and for several pitches between 0 nm and 1000 nm.	136
93	Reflectance spectrum of a normally incident TE polarized plane wave interacting with an array of copper lines for several pitches for a height $h = 100$ nm, as a function of the fill factor w/Λ . The spectrum is calculated using FEM. .	137

94	Transmittance spectrum of a normally incident TE polarized plane wave interacting with an array of copper lines for several pitches for a height $h = 100$ nm, as a function of the fill factor w/Λ . The spectrum is calculated using FEM. .	138
95	Reflectance spectrum of a normally incident TM polarized plane wave interacting with an array of copper lines for several pitches for a height $h = 100$ nm, as a function of the fill factor w/Λ . The spectrum is calculated using FEM. .	139
96	Transmittance spectrum of a normally incident TM polarized plane wave interacting with an array of copper lines for several pitches for a height $h = 100$ nm, as a function of the fill factor w/Λ . The spectrum is calculated using FEM. .	139
97	Reflectance spectrum of a normally incident TE polarized plane wave interacting with an array of copper lines with pitch $\Lambda = 1000$ nm and height $h = 100$ nm, as a function of the width w . The plot features the different diffraction orders. The spectrum is calculated using FEM.	140
98	Reflectance spectrum of a normally incident TM polarized plane wave interacting with an array of copper lines with pitch $\Lambda = 1000$ nm and height $h = 100$ nm, as a function of the width w . The plot features the different diffraction orders. The spectrum is calculated using FEM.	141
99	Reflectance spectrum of a normally incident TE polarized plane wave interacting with an array of copper lines with pitch $\Lambda = 400$ nm and height $h = 100$ nm, as a function of the width w . The plot features the different diffraction orders. The spectrum is calculated using FEM.	141
100	Reflectance spectrum of a normally incident TM polarized plane wave interacting with an array of copper lines with pitch $\Lambda = 400$ nm and height $h = 100$ nm, as a function of the width w . The plot features the different diffraction orders. The spectrum is calculated using FEM.	142
101	Distribution of the squared norm of the y electric field component $ E_y ^2$ at a pitch $\Lambda = 533$ nm, i.e. at the passing of the first diffraction order in reflection, for a 100 nm thin film with width $w = 420$ nm under TM illumination at $\lambda_0 = 532$ nm.	143
102	Reflectance spectrum of a normally incident TE polarized plane wave interacting with an array of copper lines with width $w = 34$ nm and height $h = 500$ nm, as a function of the pitch Λ . The plot features the different diffraction orders. The spectrum is calculated using FEM.	144
103	Transmittance spectrum of a normally incident TE polarized plane wave interacting with an array of copper lines with width $w = 34$ nm and height $h = 500$ nm, as a function of the pitch Λ . The plot features the different diffraction orders. The spectrum is calculated using FEM.	144
104	Absorptance spectrum of a normally incident TE polarized plane wave interacting with an array of copper lines with width $w = 34$ nm and height $h = 500$ nm, as a function of the pitch Λ . The spectrum is calculated using FEM.	145
105	Reflectance spectrum of a normally incident TM polarized plane wave interacting with an array of copper lines with width $w = 34$ nm and height $h = 500$ nm, as a function of the pitch Λ . The plot features the different diffraction orders. The spectrum is calculated using FEM.	146

106	Transmittance spectrum of a normally incident TM polarized plane wave interacting with an array of copper lines with width $w = 34\text{ nm}$ and height $h = 500\text{ nm}$, as a function of the pitch Λ . The plot features the different diffraction orders. The spectrum is calculated using FEM.	146
107	Absorptance spectrum of a normally incident TM polarized plane wave interacting with an array of copper lines with width $w = 34\text{ nm}$ and height $h = 500\text{ nm}$, as a function of the pitch Λ . The spectrum is calculated using FEM.	147
108	Distribution of the phasor norm of the TE electric field in the unit cell, for an array of copper lines with width $w = 34\text{ nm}$, height $h = 500\text{ nm}$, and for several pitches between 0 nm and 1000 nm	149
109	Distribution of the phasor norm of the TM electric field in the unit cell, for an array of copper lines with width $w = 34\text{ nm}$, height $h = 500\text{ nm}$, and for several pitches between 0 nm and 1000 nm	152
110	Reflectance spectrum of a normally incident TE polarized plane wave interacting with an array of copper lines with width $w = 34\text{ nm}$ as a function of the height h . The plot features several values for the pitch of the grating. The spectrum is calculated using FEM.	154
111	Reflectance spectrum of a normally incident TM polarized plane wave interacting with an array of copper lines with width $w = 34\text{ nm}$ as a function of the height h . The plot features several values for the pitch of the grating. The spectrum is calculated using FEM.	154
112	Band structure for the array of PEC lines under TM illumination, which features all the modes contained below a pitch $\Lambda = 1000\text{ nm}$, for a free-space wavelength $\lambda_0 = 532\text{ nm}$, width $w = 34\text{ nm}$, refractive indices $\tilde{n}_{air} = 1$, $\tilde{n}_{Si} = 4.15$, $\tilde{n}_{SiO_2} = 1.45$ and $\theta_i = 45^\circ$. The solid lines represent the real part of the wave number, while the dashed lines represent the opposite of its imaginary part. Blue curves correspond to waveguide modes, green curves correspond to diffraction in reflection modes and red curves correspond to diffraction in transmission modes.	159
113	Band structure for the array of PEC lines under TE illumination, which features all the modes contained below a pitch $\Lambda = 1000\text{ nm}$, for a free-space wavelength $\lambda_0 = 532\text{ nm}$, width $w = 34\text{ nm}$, refractive indices $\tilde{n}_{air} = 1$, $\tilde{n}_{Si} = 4.15$, $\tilde{n}_{SiO_2} = 1.45$ and $\theta_i = 45^\circ$. The solid lines represent the real part of the wave number, while the dashed lines represent the opposite of its imaginary part. Blue curves correspond to waveguide modes, green curves correspond to diffraction in reflection modes and red curves correspond to diffraction in transmission modes.	160
114	Periodic Periodicity boundary conditions.	161
115	Input and output ports.	161
116	Automatic triangular mesh.	162

List of Tables

1	Cutoff pitches (nm) for each mode featured on the band structure associated to a normally incident plane wave on an array of PEC lines of width $w = 34\text{ nm}$. The polarization label for the grating modes indicate for which polarization the associated mode is symmetric. The dashes correspond to modes which have a cutoff pitch larger than 1000 nm and are therefore not featured here or which are barely excited and not relevant to the study.	54
2	Key features presented in each spectral region for Figs. 36 to 57.	90
3	Key features presented in each spectral region for Figs. 69 to 80.	122

1 Introduction

1.1 Context

Thanks to an advantageously low electrical resistivity, copper has been the metal of choice for interconnects in modern nanoelectronics, covering virtually all layers of the back end of line. However, the resistivity of nanostructured copper rises dramatically as the dimensions are reduced below 30 nm, as a result of extra carrier scattering at the sidewalls and on grain boundaries. At a system level, this unacceptably leads to more latency and a higher power consumption as we move forward into the CMOS roadmap. Subsequently, alternative metals, and most promisingly ruthenium and metals of the platinum group, are being considered for replacement of copper. Despite a lower bulk electrical conductivity than copper, these metals have indeed shown a reduced sensitivity to dimensions such that they might outperform copper at the smallest dimensions. In this context, characterizing these metals and understanding how their properties are impacted by dimensions become of the utmost importance.

At those scales however, the mechanical electrical characterization of materials becomes difficult. As a result, the traditional four-points probe technique becomes inadequate and one has to move to other type of characterization, such as optical characterization of materials. The nanoscopic world is full of promising features that are able to overcome the limitations of the bulk materials, and there is therefore a need for studies on nanomaterials to explore those properties. Nowadays, they may be characterized electrically and mechanically by direct contact with the nanomaterials. However, due to their non-contact and non-invasive nature, the optical methods are able to characterize nanomaterials without significantly modifying or damaging them. Common optical characterization methods include reflectance/absorbance/transmittance spectra, photoluminescence, and Raman scattering measurement [1] [2] [3] [4].

These properties related to nanometric scales are of particular interest in the semiconductor industry, where the dimensions of the features kept decreasing over time. In that field, there are two main manufacturing processes that call for a particular monitoring and characterization. The front-end-of-line (FEOL) is the first step of fabrication in integrated circuits (IC) where the individual devices (transistors, capacitors, resistors, etc.) are patterned in the semiconductor. FEOL generally covers everything necessary to form isolated devices, which then require metallic interconnection. The back end of line (BEOL) is the second portion of IC fabrication where the devices get interconnected with wiring on the wafer. Metals such as copper or aluminum are typically used. This work deal with the photonic properties of periodical arrays of nanometer-wide metal lines, which belong to the back end of the line [5] [6] [7].

1.2 Metrology

Metrology is the science of measuring and characterizing structures and materials. It is a concept that refers not only to an act of measurement itself but to a measurement performed by taking errors and accuracy into account. If measurements are not within a given specified

range, a manufactured device might operate as designed, in which case the manufacturing details of the device must be reworked. Metrology and inspection are important for the management of the semiconductor manufacturing process. There are 400 to 600 steps in the overall manufacturing process of semiconductor wafers. If any defect is detected early, all the subsequent work will be wasted. Metrology and inspection processes are therefore established at critical points of semiconductor manufacturing process to ensure that a certain yield can be confirmed and maintained. There are different tools and technologies available, whether mechanical or optical, as for example: atomic force microscopy (AFM), critical-dimension scanning electron microscope (CD-SEM), X-ray scattering metrology, model-based infrared reflectometry (MBIR), optical critical dimension (OCD) scatterometry, spectroscopic ellipsometry, transmission electron microscope (TEM), Raman spectroscopy, [8] [9] [10] [11] [12]... This work focuses on the photonic properties of arrays of metal lines, and in particular, on the effect of the geometry on those properties. Two techniques are of particular interest: OCD scatterometry and Raman spectroscopy.

1.2.1 Scatterometry

Scatterometry is a novel metrology approach for process control that in addition to being precise and accurate, is fast, cheap and versatile. The method can simultaneously measure critical dimension (CD), side wall angle (SWA), and thickness of more than one layer. It analyzes the scattered light from a periodic array of lines or holes that represent the surface structure of the measured sample. As the structure dimension shrinks considerably, producing high precision results becomes more critical. As technology advances, the FEOL did not only shrink in size but also moved on to new geometries such as 3D transistors like the finFETs or GAAFETs, while the BEOL mostly kept decreasing in size. Conventional metrology tools are unable to precisely monitor some interconnect attributes such as trench sidewall angle due to limited capability or excessive cycle time. But scatterometry can be used to address these shortcomings while also potentially providing additional measurement capabilities that enable more comprehensive characterization of interconnect attributes. To date, reports on the deployment of scatterometry in real production environment have focused on FEOL applications, however, BEOL process control has not been widely reported [13] [14] [15].

1.2.2 Raman spectroscopy

Raman spectroscopy is a non-contact and non-destructive characterization method for the molecular composition and external structure of a material, which exhibits a non-linear electric field sensitivity.

In the semiconductor field, Raman spectroscopy is particularly efficient in establishing the characteristics of microelectronic devices. The ability to measure alloy composition and strain in semiconductor structures is essential for the calibration of growth processes and control of the electrical and optical behavior of these materials.

Raman spectroscopy has recently been extended to probe nanometer-scaled volumes such as finFETs. Because of its high sensitivity to the electric field transmitted in the substrate, it is also extremely sensitive to the geometry of the nanostructure. This feature can be

used to understand how light couples into complex heterostructures and to study photonic properties of nanostructures such as periodic arrays of semiconducting lines as a function of their geometry [16] [17].

1.3 State of the art

Recently, Raman measurements on periodic arrays of deep subwavelength semiconducting trenches (which geometry is typical to that of finFETs) have put forward the existence of a resonant coupling phenomenon when light is TM polarized and the trench width becomes small compared to the incident wavelength. This discovery has relaunched the hope for the possible non-contact characterization of mechanical stress in state-of-the-art semiconductor devices with Raman spectroscopy. It is key to understand this enhancement to extend non-destructive optical measurements of semiconductor devices to dimensions smaller than the diffraction limit and to reach the sensitivity required to probe very small devices [18].

Later, it was shown how the light coupling into periodic arrays of nanoscale silicon lines strongly depends on the geometry of the grating, namely on the periodicity, and that the coupling is enhanced when it is increased. The insight developed there is crucial to understand the effect of 3D geometry on the light interactions with such structures and will facilitate the design of optical process and metrology tools required for the fabrication and the characterization of 3D device [19].

Then, it was shown how it is possible to geometrically tailor the refractive properties of periodic structures to values different than those of the material constituting the arrays depending on the spectral region considered. Some fundamental insight was established which could facilitate the development and manufacturing of nanoelectronic devices, such as finFETs, as well as the design of light harvesting applications like photovoltaics [20].

The strong dependence on CD of the Raman signal when light is TM polarized was shown in [17]. This effect was used to analyze the geometric dependence of the signal for a tungsten nanograting.

In [21], the unexpected optical properties of a metallic film with subwavelength holes were highlighted. It was also described how they can be controlled by tailoring the geometry of the structure.

In [22] it is shown how nanometric gaps in noble metals can lead to enhanced light-matter interactions, such as enhanced emission, absorption or Raman scattering, which are function of the size of the gap. It is also shown that these are induced by surface plasmon polaritons.

In [23], the optical properties of a 1D metal nanograting made of gold on quartz substrate are studied and surface plasmon polaritons (SPPs) are observed.

It appears that the FEOL is of greater importance to the applied physics community than the BEOL, as FEOL metrology was more extensively studied than BEOL metrology.

Some studies deal with the interaction of light with 1D metallic nanograting. However, they are mostly concerned with the plasmonic effects like SPPs rather than the effect of geometry and they usually base their observations on experimental data. The purpose of this work is to understand how the geometry of such a metallic nanograting impacts the propagation of light, using theory and computer simulations.

1.4 Outline

To begin with, some theory necessary to the thorough understanding of this master thesis is covered in section 2.

In section 3, the theory derived in the previous section is applied to a periodic array of perfect electrical conductor (PEC) lines and a qualitative analytical model is derived to study the reflectance and transmittance spectra as a function of the pitch (periodicity of the array), width and height of the PEC lines. The model is compared with quantitative numerical FEM simulations.

In section 4, the same procedure is applied to an array of copper lines and the observations are compared to the ones obtained for the PEC lines.

Finally, 5 provides a conclusion and an outlook.

2 Important theoretical concepts

In this section, some key theoretical concepts are reviewed. Namely, both the microscopic and macroscopic formulations of the Maxwell's equations are presented along with the interface conditions that they must satisfy. These equations are used to derive the plane wave equation in non-dissipative media. The wave formalism is then extended to the dissipative media. To do so, the complex formulation is presented. Then, some key features of light propagation such as TE and TM polarizations are described. The interaction of light with homogeneous media is presented, introducing the reflection and transmission coefficient, and the reflectance, transmittance and absorptance are defined. The description is then extended to several interfaces and finally to patterned structures such as diffraction gratings and waveguides. A discussion on the surface plasmon polaritons concludes this section.

2.1 Maxwell's equations

Since this work deals with the interaction of light with different materials, Maxwell's equations are used to build an understanding of the different phenomena that are encountered. Let us therefore remind the differential form of the four Maxwell's equations [24] [25]:

$$\nabla \cdot \mathbf{D} = \rho_f \quad (\text{Gauss's law}), \quad (1)$$

$$\nabla \cdot \mathbf{B} = 0 \quad (\text{Magnetic Gauss's law}), \quad (2)$$

$$\nabla \times \mathbf{E} = -\frac{\partial \mathbf{B}}{\partial t} \quad (\text{Faraday's law}), \quad (3)$$

$$\nabla \times \mathbf{H} = \mathbf{J}_f + \frac{\partial \mathbf{D}}{\partial t} \quad (\text{Ampère's law}), \quad (4)$$

where \mathbf{E} is the electric field in V/m, \mathbf{B} is the magnetic flux density in Teslas, ρ_f is the free volume charge density in C/m³, \mathbf{J}_f is the free current density in A/m², \mathbf{D} is the electric displacement field in C/m² and \mathbf{H} is the magnetic field in A/m. The position and time dependence (\mathbf{r}, t) of the vector and scalar fields are omitted for clarity.

The electric displacement field \mathbf{D} and the magnetic field \mathbf{H} are respectively related to \mathbf{E} and \mathbf{B} by material-dependent constitutive equations. For linear, isotropic, homogeneous (LHI) media, the constitutive equations write [24]:

$$\mathbf{D} = \varepsilon \mathbf{E}, \quad (5)$$

$$\mathbf{H} = \frac{1}{\mu} \mathbf{B}, \quad (6)$$

where ε is the electric permittivity in F/m and μ is the magnetic permeability in H/m.

2.1.1 Interface conditions

Equations (1) to (4) describe the electromagnetic fields in a medium of permittivity ε and permeability μ . At an interface between two media characterized by different permittivity and permeability, they also describe what happens to those fields in terms of normal and tangential components. Each of Maxwell's equations yields a boundary condition for the

corresponding fields. From the integral form of those equations applied on the boundary between two media 1 and 2, with a normal \mathbf{n} , the following conditions are obtained [26]:

$$(\mathbf{D}_2 - \mathbf{D}_1) \cdot \mathbf{n} = \sigma_s, \quad (7)$$

$$(\mathbf{B}_2 - \mathbf{B}_1) \cdot \mathbf{n} = 0, \quad (8)$$

$$\mathbf{n} \times (\mathbf{E}_2 - \mathbf{E}_1) = 0, \quad (9)$$

$$\mathbf{n} \times (\mathbf{H}_2 - \mathbf{H}_1) = \mathbf{J}_s, \quad (10)$$

where σ_s is the surface charge density and \mathbf{J}_s is the surface current density. The consequences of those relations are the following:

- The normal component of \mathbf{D} can be discontinuous if there is a surface charge σ_s ,
- The normal component of \mathbf{B} is continuous,
- The tangential component of \mathbf{E} is continuous,
- The tangential component of \mathbf{H} can be discontinuous, if there is a surface current density \mathbf{J}_s .

However, the concept of surface charge and current densities only apply to ideal conductors which, according to Gauss's law, have no charge in their interior. Instead, the entirety of the charge of the conductor resides on the surface. In the case of finite conductivity, there exist volume charge and current densities and the fields \mathbf{D} and \mathbf{H} are also continuous across the interface [27].

2.2 Electromagnetic waves

Maxwell's equations are able to describe most of the electromagnetic physical phenomena, including the propagation of light. Let us assume that the amplitudes of the electric field and magnetic field are time-harmonic quantities with a single frequency, such that the complex exponential or phasor notation can be used. For the amplitude of a time-harmonic vector field $\mathcal{A}(t) = a \cos(\omega t + \phi)$, the phasor notation writes $A(t) = a \exp(j\phi) \exp(j\omega t)$. The time-dependence of such a field therefore only lies in the $\exp(j\omega t)$ factor. As a consequence, the time derivative of those fields is simply: $\frac{\partial}{\partial t} A(t) = j\omega A(t)$. This notation is a mathematical convenience to make calculations easier, and the physical field can be retrieved by taking the real part of the phasor: $\mathcal{A}(t) = \text{Re}(A(t))$.

2.2.1 Electromagnetic waves in vacuum

Let us consider Maxwell's equations in vacuum, with no free charge density nor current source (i.e. $\rho_f = 0$ and $\mathbf{J}_f = 0$), with free-space permittivity ε_0 and free-space permeability μ_0 . Equations (1) and (4) become

$$\nabla \cdot \mathbf{E} = 0, \quad (11)$$

$$\nabla \times \mathbf{H} = \frac{\partial \mathbf{D}}{\partial t}. \quad (12)$$

Now by using the following vector identity ($\Delta = \nabla^2$ being the Laplacian operator) :

$$\nabla \times (\nabla \times \mathbf{A}) = \nabla (\nabla \cdot \mathbf{A}) - \Delta \mathbf{A} \quad (13)$$

where on \mathbf{E} and \mathbf{H} , one obtains [26]:

$$\Delta \mathbf{E} + \omega^2 \mu_0 \varepsilon_0 \mathbf{E} = 0, \quad (14)$$

$$\Delta \mathbf{H} + \omega^2 \mu_0 \varepsilon_0 \mathbf{H} = 0, \quad (15)$$

the electromagnetic wave equations in vacuum. In accordance to the axis drawn on Fig. 2, let us seek a solution for an electric field pointing along the y direction and traveling along the z direction: $\mathbf{E} = E(z)\mathbf{e}_y$. A solution of Eq. (14) for such a field writes [24]:

$$\mathbf{E} = E_0 \exp(-jkz)\mathbf{e}_y. \quad (16)$$

Plugging this result back into (14) yields the dispersion relation, which relates the frequency and the wave number through:

$$k^2 = \omega^2 \mu_0 \varepsilon_0, \quad (17)$$

where k is the wave number in m^{-1} , which represents the spatial periodicity of the wave and is linked to the wavelength λ through $k = 2\pi/\lambda$. Moreover, the wave number k is the magnitude of the wave vector \mathbf{k} . This vector also gives the direction of propagation of the wave. The magnetic field is obtained by plugging (16) into (3) and using (6) and (17), one obtains:

$$\nabla \times \mathbf{E} = -\frac{\partial \mathbf{B}}{\partial t}, \quad (18)$$

$$\iff -jkE_0 \exp(-jkz)\mathbf{e}_x = -j\omega\mu_0 \mathbf{H}, \quad (19)$$

$$\iff \mathbf{H} = E_0 \sqrt{\frac{\varepsilon_0}{\mu_0}} \exp(-jkz)\mathbf{e}_x = H_0 \exp(-jkz)\mathbf{e}_x, \quad (20)$$

where $E_0/H_0 = \sqrt{\mu_0/\varepsilon_0} = Z_0$, the wave impedance of free space.

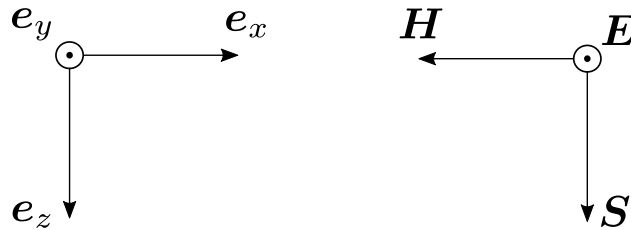


Figure 2: Orientation of the fields for a plane wave traveling along the z axis.

Furthermore, by definition of the Poynting vector $\mathbf{S} = \mathbf{E} \times \mathbf{H}$, which represents the directional energy flux of an electromagnetic wave, and therefore its direction, it appears that the wave propagates in a direction orthogonal to both \mathbf{E} and \mathbf{H} , as can be seen on Fig. 2.

In summary, the electric field solution (16) to equation (14) is independent of both x and y :

the value of \mathbf{E} is constant over any plane perpendicular to z . This solution is therefore called a plane wave solution. Moreover, the amplitudes of both \mathbf{E} and \mathbf{H} are uniform along those planes and the solutions are called uniform plane waves and can be visualized on Fig. 3. It is also noted that, at all times, the electric field and magnetic field are orthogonal to each other, and both orthogonal to the direction of propagation.

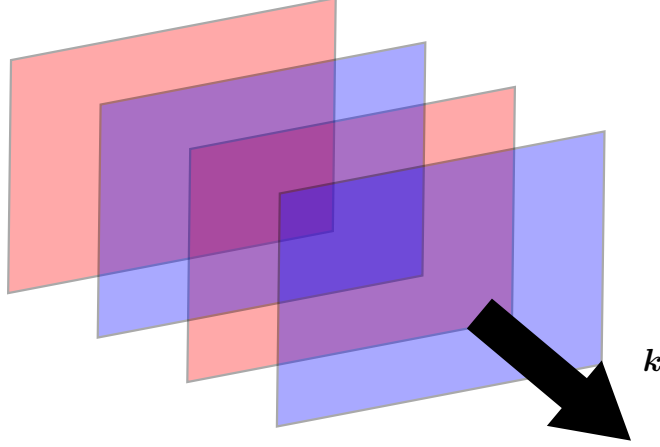


Figure 3: Spatial periodicity of the uniform fields of a plane wave, traveling along \mathbf{k} .

In vacuum, electromagnetic waves propagate at the speed of light $c = 1/\sqrt{\mu_0\epsilon_0}$.

2.2.2 Electromagnetic waves in non-dissipative media

In a linear, homogeneous and isotropic (LHI) medium with permittivity ϵ and permeability μ , the wave equation can be obtained in the same way as it was done for a vacuum: the vacuum constants (ϵ_0, μ_0) must simply be replaced by the values in the medium of interest (ϵ, μ) , such that Eq. (14) and (20) become:

$$\Delta \mathbf{E} + \omega^2 \mu \epsilon \mathbf{E} = 0, \quad (21)$$

$$\Delta \mathbf{H} + \omega^2 \mu \epsilon \mathbf{H} = 0. \quad (22)$$

When propagating through a medium characterized by a permittivity $\epsilon = \epsilon_r \epsilon_0$ and permeability $\mu = \mu_r \mu_0$, light is slowed down and travels at the *phase* velocity $v_p = c/n$, where n is the refractive index of the medium. This velocity can also be written $v_p = 1/\sqrt{\mu\epsilon}$, which results in a relation between the refractive index, the permittivity and the permeability of the medium:

$$v_p = \frac{c}{n}, \quad (23)$$

$$\iff n = \sqrt{\mu_r \epsilon_r}. \quad (24)$$

In most materials, and as will be assumed throughout this master thesis, $\mu_r = 1$ and the relation becomes:

$$n = \sqrt{\epsilon_r}. \quad (25)$$

Upon entering a medium, the frequency of a wave is unchanged, while its wavelength is scaled down by the refractive index n . Indeed, by denoting λ_0 the free-space wavelength, one has:

$$v_p = \frac{c}{n} = \frac{\lambda_0 f}{n} = \lambda f = \frac{\omega}{k}, \quad (26)$$

where λ is the compressed wavelength inside the medium and is related to the wave number through: $k = 2\pi/\lambda = 2\pi n/\lambda_0 = k_0 n$. In general, the refractive index n of a material depends on the wavelength λ_0 . Note that in some cases, the refractive index can be smaller than 1, which means that the phase velocity is greater than the speed of light. This is not a problem however, as information not necessarily travels at the phase velocity but rather at the group velocity, which is given by:

$$v_g = \frac{\partial \omega}{\partial k}, \quad (27)$$

and is typically smaller than the speed of light.

2.2.3 Electromagnetic waves in dissipative media

2.2.3.1 Drude model

Until now, only the propagation of electromagnetic waves in vacuum or in non-dissipative media has been considered. This was done under the assumption that there were no particular interaction between the light propagating in a medium and the medium itself. With that in mind, a medium where there was no free current density \mathbf{J}_f , or equivalently, a perfectly insulating material where the conductivity $\sigma = 0$, was considered.

Let us now consider the Drude model to describe an electrically conducting medium., where the material is viewed as a collection of positively charged ions from which free electrons were detached. Under the influence of an electric field, the electrons are set into motion and experience collisions with the relatively massive and immobile ions. For a direct current (DC) electric field, the Drude model results in the formulation of Ohm's law [28]:

$$\mathbf{J}_f = \left(\frac{ne^2\tau}{m} \right) \mathbf{E} = \sigma_0 \mathbf{E}, \quad (28)$$

where n is the density of free electrons, e is the elementary charge, m is the electron mass, τ is the mean free time between ionic collisions and σ_0 is the DC conductivity of the material. Joule's first law states that the passage of an electric current through a conductor produces heat, and therefore generates losses. It is therefore the ability of a material to conduct an electric current, i.e. having a finite conductivity, that is responsible for losses. In addition, the separation of charges resulting from an external electric field on a conductive material in turn generates its own electric field, which opposes the external one. As a consequence, after a characteristic time ε/σ_0 which represent the time needed for the free charges to redistribute at the surface of the conductor, the external field is screened and the field inside the conductor is zero.

Let us now consider a time-varying electromagnetic field impinging on a conductive material and examine how it responds to this excitation. The Drude model can also predict the

alternative current (AC) as a response to a time-dependent electric field with an angular frequency ω . The complex conductivity is [26] [28]:

$$\sigma(\omega) = \frac{\sigma_0}{1 - j\omega\tau} = \frac{\sigma_0}{1 + \omega^2\tau^2} - j\omega\tau \frac{\sigma_0}{1 + \omega^2\tau^2}, \quad (29)$$

The real part of the complex conductivity describes the conductive current and the imaginary part corresponds to a displacement current. The complex conductivity relates both the magnitude and the phase of the current density to the magnitude and phase of the applied electric field such that

$$\mathbf{J}_f(t) = \text{Re}(\sigma(\omega)\mathbf{E}_0 \exp(j\omega t)), \quad (30)$$

with

$$\mathbf{E}(t) = \text{Re}(\mathbf{E}_0 \exp(j\omega t)). \quad (31)$$

The higher the conductivity, the better the charges can follow the applied electric field. In other words, for sufficiently low frequency, or for a high conductivity, the charges can perfectly move and adapt to the AC field, so that the external field is effectively screened. However, if the frequency is too high or the conductivity too low, the charges cannot redistribute themselves sufficiently quickly and the external field is able to penetrate the material. The characteristic frequency at which this transition occurs is called the plasma frequency and is written as follows [29]:

$$\omega_p = \sqrt{\frac{ne^2}{\varepsilon_0 m}}. \quad (32)$$

2.2.3.2 Complex formulation

To model how a dissipative medium leads to losses and to the inhibition of wave propagation, the permittivity, refractive index and wave number are treated as complex quantities such that [26]:

$$\tilde{\varepsilon} = \varepsilon' - j\varepsilon'', \quad (33)$$

$$\tilde{n} = n - j\kappa, \quad (34)$$

$$\tilde{k} = k_0\tilde{n}, \quad (35)$$

where κ is called the extinction coefficient. In this text, the real part of the refractive index is referred to by writing n (without tilde). It is possible to relate the complex refractive index to the complex permittivity through a relation analogous to Eq. (25), by extending it to the complex formulation, which yields:

$$\tilde{n} = \sqrt{\tilde{\varepsilon}_r} = \sqrt{\varepsilon'_r - j\varepsilon''_r}. \quad (36)$$

By separating the real and imaginary parts of \tilde{n}^2 , the following relations are obtained [30]:

$$\varepsilon'_r = n^2 - \kappa^2, \quad (37)$$

$$\varepsilon''_r = 2n\kappa. \quad (38)$$

All the mathematical formulations of the previous sections on non-dissipative materials can be extended to lossy media by simply replacing the real quantities by the complex ones. To illustrate the dissipative effect of a material on a wave propagation, the complex wave number can be plugged into the plane wave solution (16) to the wave equation:

$$\mathbf{E} = E_0 \exp\left(-j\frac{2\pi}{\lambda_0}nz\right) \exp\left(-\frac{2\pi}{\lambda_0}\kappa z\right) \mathbf{e}_y, \quad (39)$$

where the imaginary exponential represents the propagation of the wave and the real decaying exponential accounts for the attenuation of the electric field in the medium due to losses through the extinction coefficient κ . The intensity of an electromagnetic wave is related to the square of the electric field, which means that it decays with a factor $\exp(-4\pi\kappa z/\lambda_0) = \exp(-\alpha z)$, where $\alpha = 4\pi\kappa/\lambda_0$ is called the absorption coefficient, and the formulation of Beer-Lambert's law is retrieved [31]:

$$I(z) = I_0 \exp(-\alpha z). \quad (40)$$

This coefficient can be linked to the penetration depth d_p , the distance after which the intensity is reduced by a factor $1/e$ through $d_p = 1/\alpha = \lambda_0/4\pi\kappa$.

Let us consider again a material with finite conductivity $\sigma(\omega)$, such that, in phasor notation, $\mathbf{J}_f = \sigma(\omega)\mathbf{E}$. The displacement field then writes $\mathbf{D} = \varepsilon_L\mathbf{E}$, where ε_L is the permittivity associated to the lattice, without the effect of the conduction electrons. Let us also consider a time-harmonic electric field with a single frequency. With those considerations in mind, and under the assumption that the total current density \mathbf{J}_{tot} is the sum of a conduction and a displacement current, respectively $\mathbf{J}_f = \sigma(\omega)\mathbf{E}$ and $\mathbf{J}_d = \partial\mathbf{D}/\partial t$, a relation for the permittivity of a conductive medium is derived:

$$\mathbf{J}_{tot} = \mathbf{J}_f + \frac{\partial\mathbf{D}}{\partial t}, \quad (41)$$

$$= \sigma(\omega)\mathbf{E} + j\omega\varepsilon_L\mathbf{E}, \quad (42)$$

$$= j\omega\left(\varepsilon_L - j\frac{\sigma(\omega)}{\omega}\right)\mathbf{E}, \quad (43)$$

$$= j\omega\tilde{\varepsilon}\mathbf{E}, \quad (44)$$

with $\tilde{\varepsilon} = \varepsilon_L - j\sigma(\omega)/\omega$. Here, the conductivity is equivalent to a dielectric conductivity which sums over all the dissipative mechanisms of the material and which includes both dielectric losses and ohmic losses, although it is understood that in metals, it is the conduction mechanism that is responsible for losses while in good dielectrics, they are associated to the polarization mechanisms. Since this text deals with the interaction of light with metals, it will be assumed from now on that the dielectric conductivity is dominated by the conduction mechanism. It is therefore possible to rewrite the complex permittivity in terms of the real permittivity and properties of the material by inserting the complex conductivity into the expression for the complex permittivity obtained above:

$$\tilde{\varepsilon} = \varepsilon_L - j\frac{\sigma(\omega)}{\omega} = \left(\varepsilon_L - \tau\frac{\sigma_0}{1 + \omega^2\tau^2}\right) - j\left(\frac{1}{\omega}\frac{\sigma_0}{1 + \omega^2\tau^2}\right), \quad (45)$$

or in terms of real and imaginary parts of the permittivity :

$$\varepsilon' = \left(\varepsilon_L - \frac{\tau \sigma_0}{1 + \omega^2 \tau^2} \right), \quad (46)$$

$$\varepsilon'' = \frac{1}{\omega} \left(\frac{\sigma_0}{1 + \omega^2 \tau^2} \right). \quad (47)$$

It is possible to derive some insight from these results. By considering the high frequency regime with which this work deals, i.e. $\omega \tau \gg 1$, the permittivity simplifies to:

$$\tilde{\varepsilon} \approx \varepsilon' \approx \varepsilon_L - \frac{\sigma_0}{\omega^2 \tau} = \varepsilon_L \left(1 - \frac{\sigma_0}{\omega^2 \tau \varepsilon_L} \right) = \varepsilon_L \left(1 - \frac{\omega_p^2}{\omega^2} \right), \quad (48)$$

where ω_p is the plasma frequency. From Eq. (48), it can be seen that the high frequency region can now be subdivided into two sub-regions: $\omega < \omega_p$ and $\omega > \omega_p$. In the first one, the permittivity ε' is negative. From Eq. (37), this means that $\kappa > n$. As it will be shown later, a high κ corresponds to a highly absorbing and highly reflecting material which inhibits the propagation of waves. In the second region, above the plasma frequency, the permittivity is positive such that $n > \kappa$ and the material is now more transparent to the incoming waves. This is also consistent with the short description of the plasma frequency of the end of section 2.2.3.1. Typically, a material with high conductivity, i.e. a metal, features a high extinction coefficient κ and has a negative real permittivity.

As an example, let us consider the case of copper. Its plasma frequency ω_p is around $\omega_p = 2.13 \cdot 10^{15}$ rad/s, or in terms of wavelength, $\lambda_p = 137$ nm. For a wavelength longer than $\lambda_{0,p}$, the extinction coefficient κ should be larger than the refractive index n . Fig. 4 depicts the optical constants of copper in the range 200 – 2000 nm, obtained from [32].

This wavelength range is above the plasma wavelength and therefore one can indeed see that $\kappa > n$. In addition, the optical constants of a metal in the visible range are not subject to extreme variations as a function of the wavelength as it is often the case for semiconductors. As a consequence, only a single wavelength for the incoming light will be considered in this work, as the result for another wavelength are not expected to differ much as it could be the case for non-metallic materials.

2.3 Polarization

Polarization is a property of waves that specifies the geometrical orientation of the oscillations. By convention, the polarization of electromagnetic waves refers to the direction of oscillation of the electric field. In the previous section, an electric field pointing along the y direction was considered. In that case, according to the phasor notations of section 2.2, the physical field writes:

$$\text{Re}(\mathbf{E}) = E_0 \cos(\omega t - kz + \phi) \mathbf{e}_y. \quad (49)$$

However, for plane wave propagating along z , the field can also have a component along the x direction in addition to the y direction, while the direction of propagation remains unchanged,

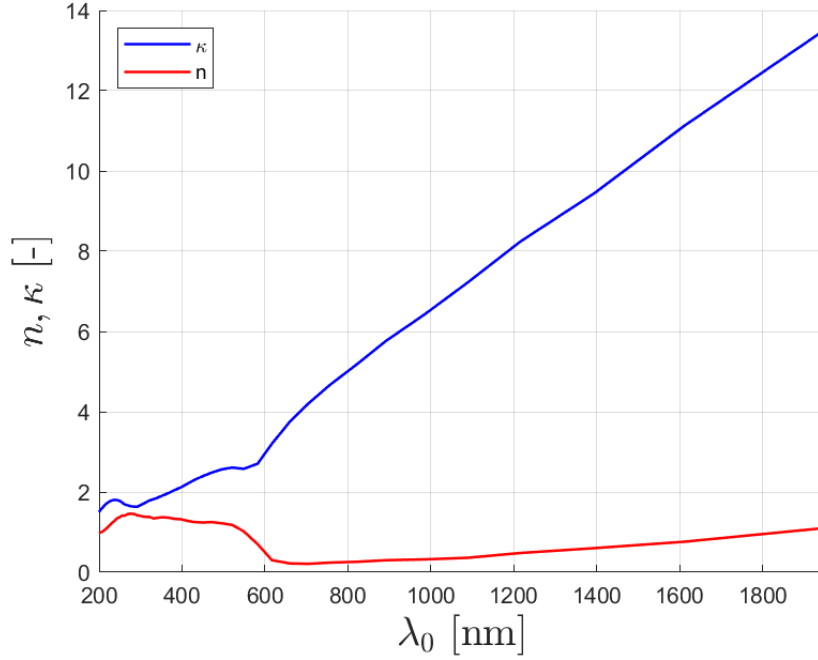


Figure 4: Refractive index n and extinction coefficient κ of copper as a function of the wavelength.

since it is only required that the electric field is perpendicular to both the magnetic field and direction of propagation. If the y component is non-zero, one has:

$$\mathbf{E} = A(z)\mathbf{e}_x + B(z)\mathbf{e}_y, \quad (50)$$

a solution to equation (14) is given by:

$$\mathbf{E} = A \exp(-jkz)\mathbf{e}_x + B \exp(-jkz)\mathbf{e}_y, \quad (51)$$

and the physical field writes:

$$\text{Re}(\mathbf{E}) = A \cos(\omega t - kz + \phi_a)\mathbf{e}_x + B \cos(\omega t - kz + \phi_b)\mathbf{e}_y. \quad (52)$$

The solution (51) can be inserted back into equation (14) to show that the dispersion remains unchanged. There exist different types of polarizations: linear, circular and elliptical. In this work however, only the linear polarization will be considered.

2.3.1 Linear polarization

An electromagnetic wave is said to be linearly polarized when its electric field oscillates in a straight line, as pictured in Fig. 5. This was the case for the field of solution (16), which oscillates only along \mathbf{e}_y . For solution (51), which has a component along two directions, x and y , the field can be decomposed into two linear polarizations, respectively along x and y , if the phase difference between those components is either 0 or π :

$$\phi_a - \phi_b = 0 \quad \text{or} \quad \phi_a - \phi_b = \pi. \quad (53)$$

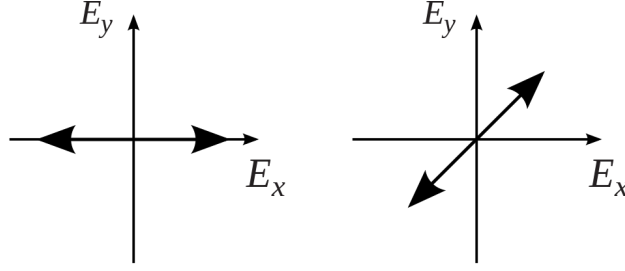


Figure 5: Linear polarization along a single axis (left). Linear polarization along both axis (right).

2.3.2 TE and TM polarizations

When light is impinging upon an interface or a device, the orientation of the fields with respect to it is relevant. Indeed, the boundary conditions for the electric and magnetic fields will differ if their direction are tangential or normal to the interface or device. Therefore, the behavior of the light when interacting might be different. By defining the plane of incidence as the plane which contains the incoming wave vector and the normal to the interface or device, two cases are distinguished: when the incident electric field only has a component perpendicular to the plane of incidence (Transverse **E**lectric) or when it is the incident magnetic field that only has a perpendicular component. (Transverse **M**agnetic).

2.4 Light interaction at the interface between two semi-infinite media

2.4.1 Snell's law

Fig. 6 depicts an electromagnetic wave impinging on an interface between a medium 1 characterized by n_1 and medium 2 characterized by n_2 . The interface is infinite along \mathbf{e}_x , the incident wave propagates along \mathbf{e}_z and \mathbf{e}_x . Upon arriving at the interface, a part of the wave will be reflected back into medium 1, while a part of it will be transmitted into medium 2.

Without loss of generality, let us consider a non-conductive medium, i.e. $\tilde{n} = n$ and $\tilde{k} = k$. Since the interface is infinite along \mathbf{e}_x , the x component of the wave vector is conserved, therefore:

$$k_{x,i} = k_{x,r} = k_{x,t}. \quad (54)$$

From this relation, we can derive Snell's law:

$$n_1 \sin \theta_i = n_2 \sin \theta_t. \quad (55)$$

Since the refractive index is the same for the incident and reflected wave, it can also be inferred that the angle of incidence must be equal to the angle of reflection: $\theta_i = \theta_r$.

In the case of an interface with a conductive medium, in accordance to the complex formulation described above, the angles can take complex values. It is possible to derive an

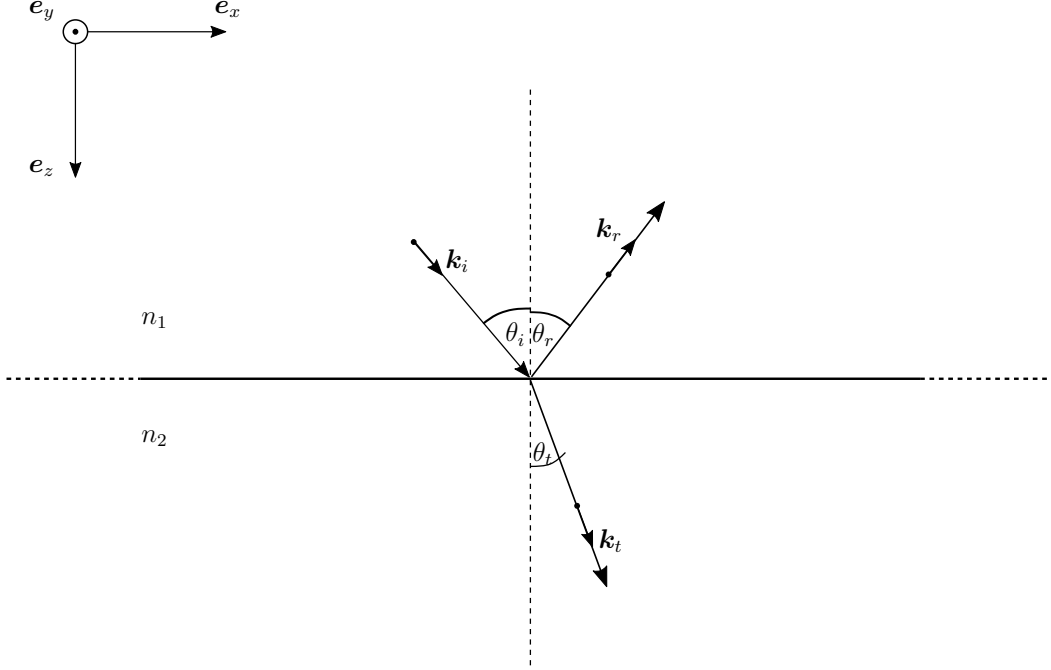


Figure 6: Refraction of light at an interface between two semi-infinite media.

expression which takes into account the absorbing nature of the material and which can be written in a form similar to Eq. (55), with a coefficient which also depends on the angle of incidence. The main result is that due to the absorption, the surfaces of constant amplitudes and the surfaces of constant phase of the wave no longer coincide with each other, yielding a wave in the metal that is inhomogeneous [33].

2.4.2 TE polarization

Fig. 7 depicts a situation similar to Fig. 6: an electromagnetic wave is impinging on an interface between a medium 1 characterized by \tilde{n}_1 and medium 2 characterized by \tilde{n}_2 . The interface is infinite along \mathbf{e}_x , the incident wave propagates along \mathbf{e}_z and \mathbf{e}_x and the electric field is linearly polarized along \mathbf{e}_y (TE mode). The magnetic field is oriented such that $\mathbf{E} \times \mathbf{H}$ gives the direction of propagation of the wave. Upon arriving at the interface, a part of the wave will be reflected back into medium 1, while a part of it will be transmitted into medium 2.

For the TE polarization, and for a finite conductivity for the two media, the tangential components of both the electric field and magnetic fields are continuous across the interface. Satisfying those conditions, we obtain the following relations [26]:

$$r_{TE} = \frac{\tilde{n}_1 \cos \theta_i - \tilde{n}_2 \cos \theta_t}{\tilde{n}_1 \cos \theta_i + \tilde{n}_2 \cos \theta_t}, \quad (56)$$

$$t_{TE} = \frac{2\tilde{n}_1 \cos \theta_i}{\tilde{n}_1 \cos \theta_i + \tilde{n}_2 \cos \theta_t}, \quad (57)$$

where r_{TE} and t_{TE} are respectively the reflection and transmission coefficient, which represent the ratio of the reflected (resp. transmitted) complex electric field amplitude to the incident

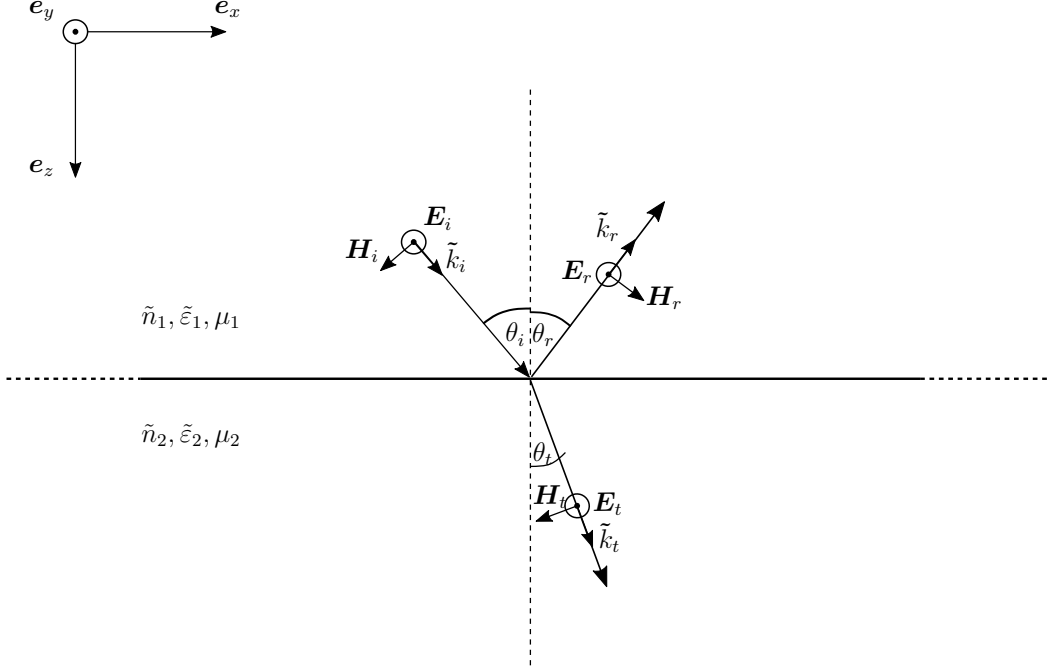


Figure 7: Reflection and transmission of TE polarized light at an interface between two media.

one, for the TE polarization. As a consequence, the following identity must hold:

$$1 + r_{TE} = t_{TE}. \quad (58)$$

2.4.3 TM polarization

Let us now consider a TM polarized wave incident on the same interface. In this case, it is the magnetic field which has a component only along \mathbf{e}_y . The electric field is oriented such that $\mathbf{E} \times \mathbf{H}$ gives the direction of propagation of the wave, as illustrated in Fig. 8. Following the same development as for TE polarization, we get, for TM polarization [26]:

$$r_{TM} = \frac{\tilde{n}_2 \cos \theta_i - \tilde{n}_1 \cos \theta_t}{\tilde{n}_2 \cos \theta_i + \tilde{n}_1 \cos \theta_t}, \quad (59)$$

$$t_{TM} = \frac{2\tilde{n}_1 \cos \theta_i}{\tilde{n}_2 \cos \theta_i + \tilde{n}_1 \cos \theta_t}. \quad (60)$$

The same identity as for TE polarization must hold:

$$1 + r_{TM} = t_{TM}. \quad (61)$$

2.4.4 Reflectance, Transmittance and Absorptance

Fig. 9 depicts an light beam impinging on an interface between two semi infinite media. The reflectance is defined as the ratio of reflected power to incident power [34]:

$$R = \frac{\Phi_r}{\Phi_i} = \frac{I_r A_r}{I_i A_i}, \quad (62)$$

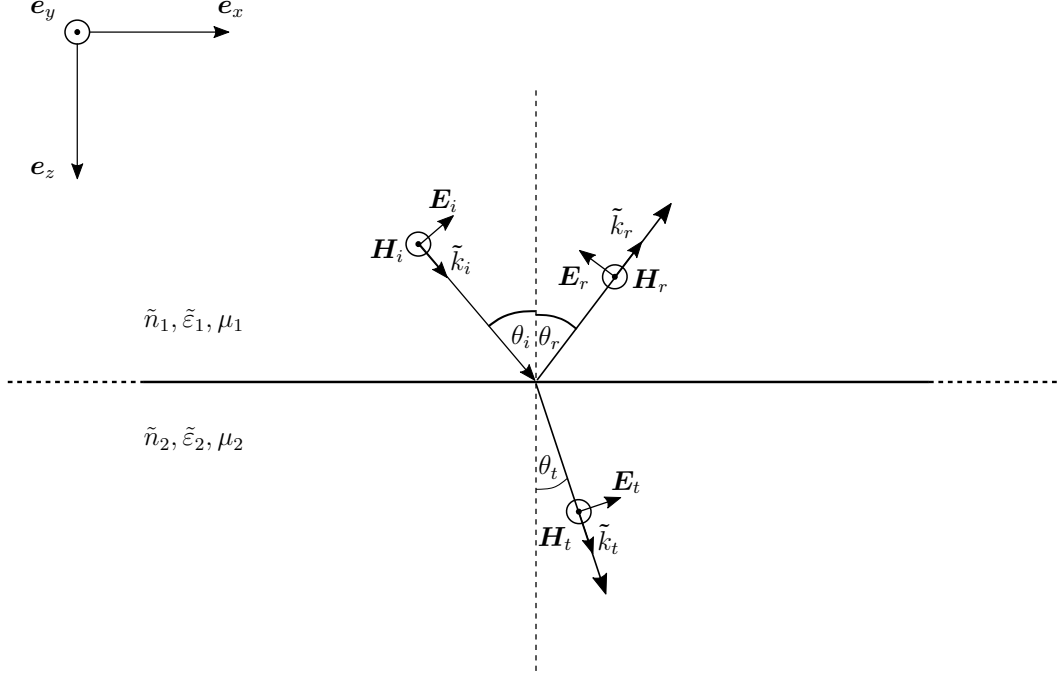


Figure 8: Reflection and transmission of TM polarized light at an interface between two media.

where I_m denotes the intensity of the light beam in medium m , given by

$$I_m = \frac{n_m \varepsilon_0 c |E_0|^2}{2}, \quad (63)$$

A_m is the area of the light beam and n_m is the real part of the refractive index of medium m . The situation is depicted in Fig. 9. Recalling that $r = E_r/E_i$, and since the medium is the same for the incident and reflected wave, we have $I_r/I_i = |r|^2$, and since the angle of incidence is equal to the angle of reflection, the area of the beam is the same and $A_r/A_i = 1$. Therefore, the reflectance is given by:

$$R = |r|^2. \quad (64)$$

Similarly to the reflectance, the transmittance is defined as the ratio of transmitted power over the incident power [34]:

$$T = \frac{\Phi_t}{\Phi_i} = \frac{I_t A_t}{I_i A_i}. \quad (65)$$

This time, the media are different and the width of the light beam changes upon crossing the interface: $A_t/A_i = w_t/w_i = \cos \theta_t / \cos \theta_i$, where w is the width of the beam. The transmittance is therefore given by:

$$T = \frac{n_t \cos \theta_t}{n_i \cos \theta_i} |t|^2 = \frac{k_t}{k_i} |t|^2, \quad (66)$$

where k_t and k_i are the real part of the wave numbers.

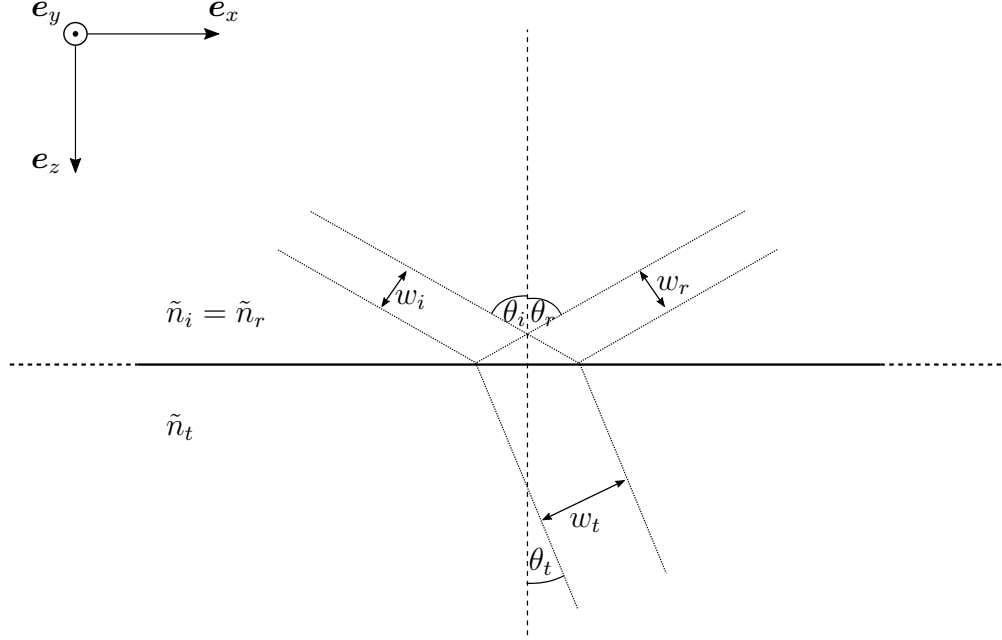


Figure 9: Reflection and transmission of a light beam at an interface.

Finally, in a dissipative material of finite thickness, light is also absorbed. Absorptance is defined as the ratio of power absorbed by the material to the incident power [34]:

$$A = \frac{\Phi_A}{\Phi_I}. \quad (67)$$

By conservation of energy and since the reflectance, transmittance and absorptance are defined with respect to the incoming power, they must add up to 1:

$$1 = T + R + A. \quad (68)$$

2.5 Light interaction with multiple interfaces

2.5.1 Multiple reflections

When there are several interfaces to cross, light is also reflected from the additional surfaces and therefore interferes with the incoming light, leading to either constructive or destructive interferences, depending on the phase change acquired by the reflected light. Now instead of a simple interface, let us consider a thin film with thickness h and refractive index \tilde{n} sandwiched between two infinite media with refractive indices \tilde{n}_1 and \tilde{n}_2 . Fig. 10 depicts how an incoming plane wave interacts with multiple interfaces: light impinging on the thin film will first be transmitted and reflected by the first interface, with coefficient r_1 and t_1 , then propagate through the thin film, then be transmitted and reflected by the second interface with coefficients r_2 and $t_2 = 1 + r_2$. Light reflected by the second interface will travel back through the film, then be transmitted and reflected through the first interface in opposite direction, with coefficients $r'_1 = -r_1$ and $t'_1 = 1 + r'_1$. Light reflected there will travel back into the thin film, get reflected again and so on until infinity. The total

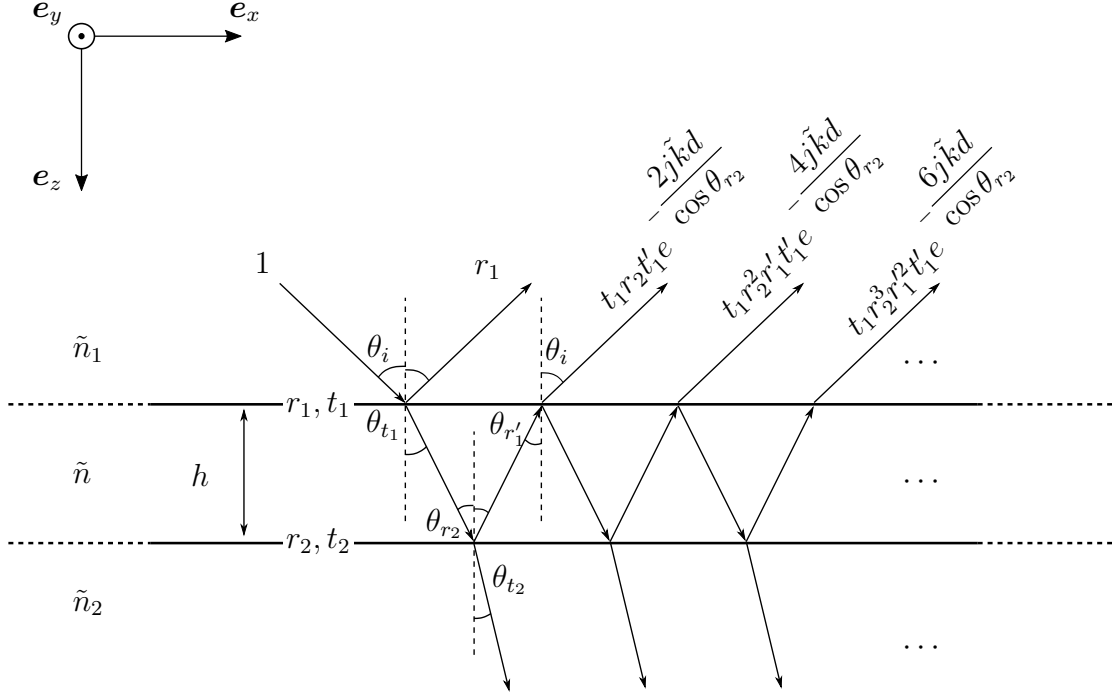


Figure 10: Multiple reflections inside a thin film of thickness d .

reflection coefficient for the thin film can be obtained thanks to the relations between Fresnel coefficients and by accounting for the multiple reflections happening inside the film through a geometrical series. At normal incidence, we obtain [35]:

$$r = \frac{r_1 + r_2 \exp(-2j\tilde{k}h)}{1 + r_1 r_2 \exp(-2j\tilde{k}h)}, \quad (69)$$

$$t = \frac{(1 + r_1)(1 + r_2) \exp(-j\tilde{k}h)}{1 + r_1 r_2 \exp(-2j\tilde{k}h)}, \quad (70)$$

where $2\tilde{k}h = 2k_0\tilde{n}h$ contains the phase change acquired by the wave during a round trip of distance $2h$ across the thin-film.

Let us first consider the case with no absorption, i.e. $\kappa = 0$ and $\tilde{n} = n$. Fig. 11 illustrates the reflectance $R = |r|^2$ and transmittance $T = (n_2/n_1)|t|^2$ for a silicon oxide thin film of thickness h below an air layer with $n_1 = 1$ and above a silicon substrate with $n_2 = 4.15$. The real refractive index n of the oxide is $n = 1.46$, such that the wave propagates into media of increasing reactive index, i.e. $n_1 < n < n_2$. The reflectance and transmittance are plotted as a function of the film thickness normalized to multiples of a quarter wavelength. As can be seen, the reflectance oscillates as a function of the height and features maxima and minima. The condition on the height for each peak can be obtained by imposing $\partial R / \partial h = 0$. This condition is satisfied and interferences (either destructive or constructive) will occur when the phase difference between the incident wave and reflected wave is an integer multiple of

π . The following relation must therefore be satisfied:

$$m\pi = 2kh, \quad m \in \mathbb{Z}. \quad (71)$$

Since $k = 2\pi n/\lambda_0$, the condition for the film thickness becomes:

$$h = \frac{m\lambda_0}{4n}, \quad m \in \mathbb{Z}, \quad (72)$$

that is, there will be interferences when the optical thickness nh is an integer multiple of a quarter wavelength.

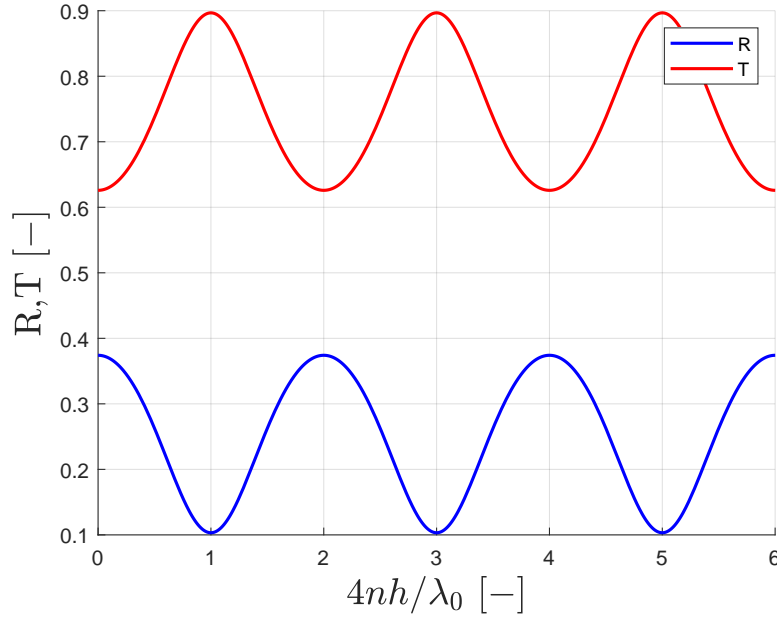


Figure 11: Reflectance $R = |r|^2$ and transmittance $T = (n_2/n_1)|t|^2$ for a thin film of thickness h and real refractive index $n = 1.46$ with $n_1 = 1$ and $n_2 = 4.15$, as a function of the film thickness normalized to multiples of a quarter wavelength, under normal illumination with $\lambda_0 = 532$ nm.

The nature of the interference (either constructive or destructive) will depend on the difference between the refractive indices of the different media. Indeed, the sign of the reflection coefficients (56) and (59) can be negative if $n_2 < n_1$ (TE polarization) or $n_1 < n_2$ (TM polarization). A negative reflection coefficient corresponds to a phase shift of π , which will swap the positions of constructive and destructive interference.

This can be visualized in Fig. 12. In this case, $n_1 = 1$ and $n_2 = 4.15$. Therefore, there is a π phase shift at the first interface if for example $n = 0.9 < 1$, which leads to a shift in the condition for constructive/destructive interferences. Since we are dealing with two interfaces, two phase shifts of π can possibly occur which can each interchange the nature of the peaks.

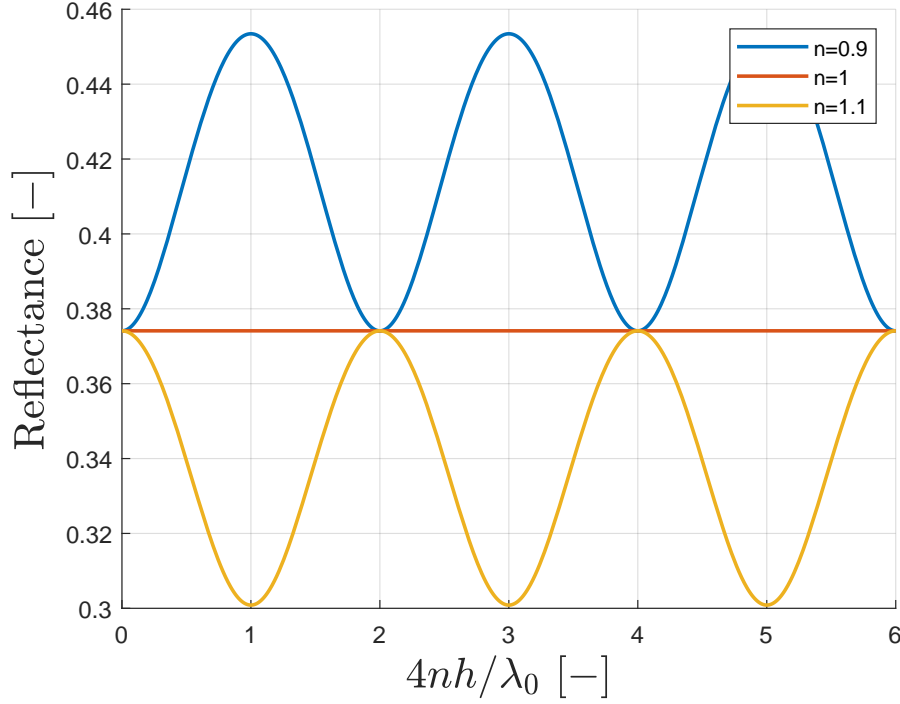


Figure 12: Reflectance $R = |r|^2$ for a thin film of thickness h and several real refractive indices n with $n_1 = 1$ and $n_2 = 4.15$, as a function of the film thickness normalized to multiples of a quarter wavelength, under normal illumination with $\lambda_0 = 532$ nm. The consequence of a negative reflection coefficient (i.e. when $n < n_1$, in this case when $n = 0.9$, is to induce a π phase shift which swaps the condition for constructive and destructive interferences).

The coefficients (69) and (70) are general and are valid in the case of absorbing materials with $\kappa \neq 0$. However in that case, the condition on the height for interferences obtained in Eq. (72) only constitutes a first approximation, as the peaks will slightly get shifted from those height values as the extinction coefficient κ increases. The analytical condition for peaks when taking absorption into account is a lot harder to derive and is out of the scope of this master thesis.

In this work, only a single thin film will be considered, but it is possible to extend this concept to a multi-layered structure with multiple films on top of each other, and deal with the mathematical expressions for an arbitrary number of films using the transfer-matrix method [35] [2].

2.5.2 Absorptance as a function of thickness

When a light beam propagates inside a dissipative material across a single interface, its intensity decreases exponentially according to Beer-Lambert's law (Eq. (40)), which takes the form:

$$\Phi_T = \Phi_E \exp(-\alpha z), \quad (73)$$

where Φ_E is the fraction of power entering the sample: $\Phi_E = \Phi_0 - \Phi_R$, α is the attenuation coefficient described in the previous section and z is the distance traveled inside the dissipative material. In the case of a film of finite thickness however, the intensity of the light inside the film is not just a decreasing exponential which follows Beer-Lambert's law. Indeed, the thin-film interferences induced by the second interface must be taken into account. However, thanks to the conservation of energy, it is easy to obtain the absorptance of a film of thickness h through $A = 1 - R - T$, where $R = |r|^2$ and $T = (n_2/n_1)|t|^2$ and the coefficients r and t are those of Eq. (69) and Eq. (70).

The finite thickness of the sample must now be taken into account: an infinitely thick absorbing sample will totally absorb the light inside the material and will not transmit anything, as illustrated in Fig. 13. The intensity of the thin-film interferences is attenuated as the thickness increases and as more light is absorbed, preventing it to go back and interfere with the incoming light.

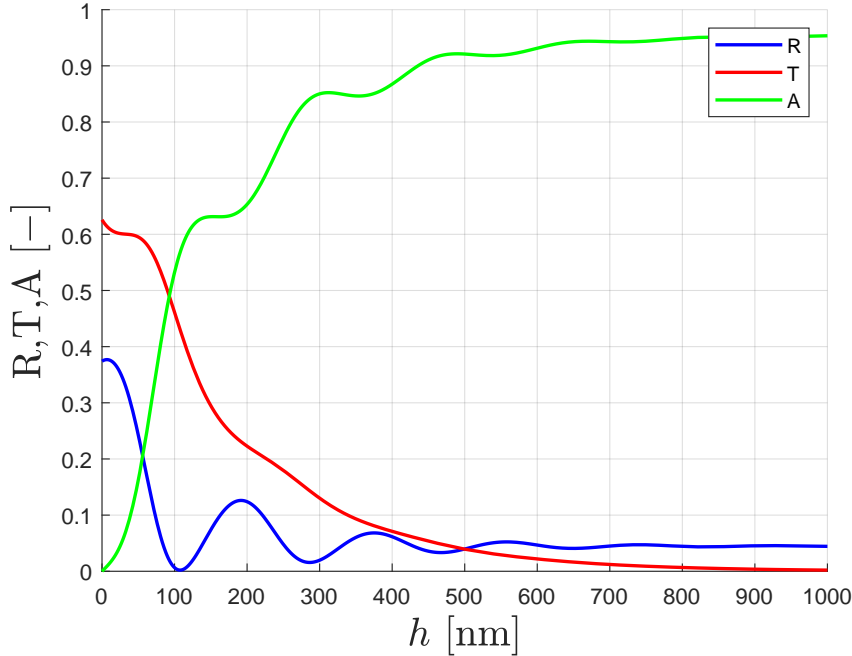


Figure 13: Reflectance, transmittance and absorptance of a sample of increasing thickness h with refractive index $n = 1.46$ and extinction coefficient $\kappa = 0.25$, with $n_1 = 1$ and $n_2 = 4.15$. The light normally incident and has a free-space wavelength $\lambda_0 = 532$ nm.

Fig. 14 illustrates the relations between reflectance, transmittance and absorptance of a sample of thickness h as a function for the extinction coefficient and for a fixed n .

Now, an important remark has to be made about a counter-intuitive result. Let us remember that the attenuation coefficient is related to the extinction coefficient through $\alpha = 4\pi\kappa/\lambda_0$. Intuitively, one would therefore expect that a piece of material with a high κ would have a very large absorptance. This is however not the case, as can be seen that the absorptance evolves non-monotonically with κ and actually decreases for large values. Indeed, the ex-

tion coefficient also intervenes in the expression of the reflection coefficients (56) and (59) when extended to dissipative materials. The reflectance increases along with κ , which reduces the amount of light penetrating inside the sample. In other words, a high extinction coefficient increases how strongly light is absorbed inside a material as a function of the depth, but also decreases the maximum amount of light that can be absorbed, since a more significant part of it will be reflected and will not penetrate the material at all. This is consistent with what can be observed in reality: metals, which have a high extinction coefficient, actually reflect a lot of light and appear shiny to the eye.

It is indeed the reflectance which dominates for large values of κ , while the absorptance and the transmittance both go to zero. When $\kappa = 0$, there is no absorptance and the reflectance and transmittance take the value for the the initial non-absorbing thin film. An interesting observation is that there exist a value of κ that maximizes the absorptance.

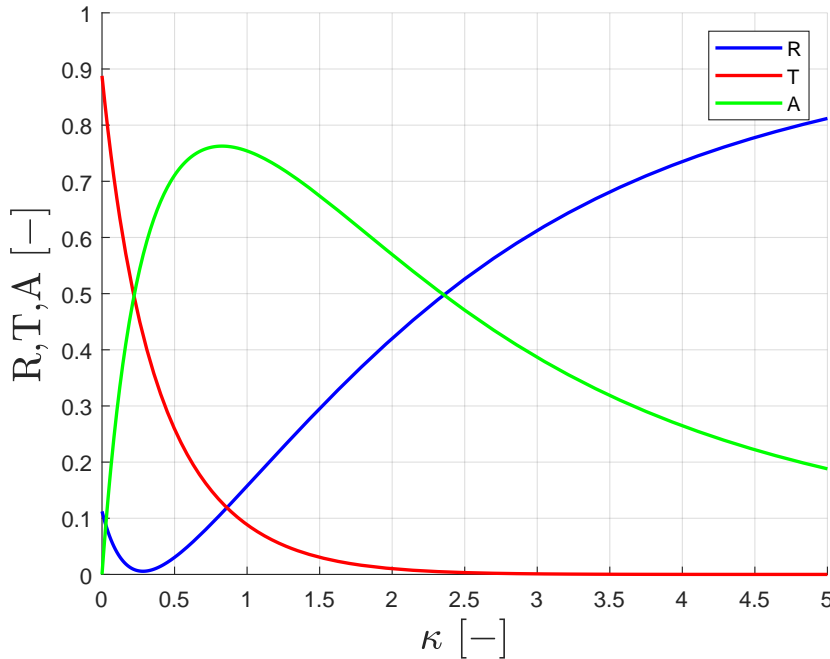


Figure 14: Reflectance, transmittance and absorptance of a sample of thickness $h = 100$ nm and real refractive index $n = 1.46$, as a function of the extinction coefficient κ , with $n_1 = 1$ and $n_2 = 4.15$. The incident light is TE polarized and has a free-space wavelength $\lambda_0 = 532$ nm.

2.6 Light interaction with patterned structures

Until now, only waves propagating in uniform media have been considered. In such media, light propagates as a uniform plane waves as described in section 2.2. However, when the wave comes across a structure with finite dimensions, the plane wave is disturbed. As a result, the propagation of the wave might be hindered, and it may propagate in forms different than that of a plane wave to accommodate to the presence of the structure. In

this work, two structures are of particular interest: the perfect electrical conductor parallel plate waveguide and the diffraction grating. Indeed, a periodic array of parallel metal lines can be considered as an array of metallic waveguides from which light can diffract due to their periodic nature. It is therefore crucial to understand how light interacts with those structures in the framework of this work.

2.6.1 Perfect electrical conductor parallel plate waveguide

A waveguide is a structure that restricts the propagation of waves into a specific direction, allowing the power to be guided into that direction instead of decreasing with the distance (for a spherical wave for example), therefore allowing the transfer of information to a specific location. Waveguides concern both electromagnetic waves or physical waves such as sound waves. These can come in various forms: a hollow metallic tube or rectangular cavity, a fiber made of dielectric material with higher refractive index than the surrounding medium, or with a varying refractive index, a periodic arrangement of reflecting material, an air duct, a horn, ... In most cases, the driving principle is the internal reflection of the wave inside the structure (reflection from metallic plates, total internal reflection for dielectric waveguides, ...).

A perfect electrical conductor (PEC) is an ideal material with infinite conductivity σ . According to the results of section 2.2.3.2, this means that the material also has an infinite extinction coefficient κ . In other words, the electric field cannot penetrate at all inside a PEC and is always 0, and any light impinging on its surface is entirely reflected.

Let us now consider a medium with permittivity $\tilde{\epsilon}$ and permeability μ_0 , sandwiched between two infinite plates of such perfect electrical conductor separated by a distance d , upon which a plane wave impinges. Since we consider a specific structure which can be characterized by a particular direction (infinite plates along y and z), the two different polarizations, TE and TM, must be treated separately.

2.6.1.1 TE polarization

In this case, the only non-zero electric field component is along y and is tangential to the PEC plates, as can be seen in Fig.15. Between the plates, the electric field must satisfy Eq.(14). Since the tangential components of the electric field are continuous, the electric field must be 0 at the PEC plates. Given the infinite nature of the plate along y and z , their presence can only influence the electric field distribution along x . The electric field, propagating along z , therefore writes:

$$\mathbf{E} = E_0 F(x) \exp(-j\tilde{k}_z z) \mathbf{e}_y, \quad (74)$$

where $F(x)$ is a function to be determined which satisfies the boundary conditions $F(0) = F(d) = 0$. Plugging this field into Eq.(14) yields [26]:

$$F(x) = \sin(k_{x,m} x), \quad (75)$$

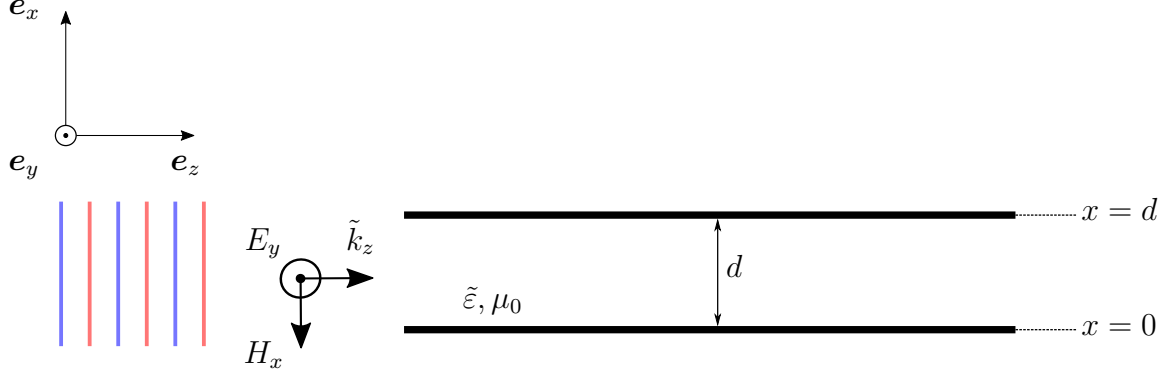


Figure 15: Incoming TE plane wave on a PEC parallel plate waveguide.

where k_x is the wave number along x and can only take discrete values according to the so-called guidance condition [26]:

$$k_{x,m} = \frac{m\pi}{d}, \quad m \in \mathbb{N}_0. \quad (76)$$

Here, the integer m is the index of the mode propagating through the waveguide. It describes the distribution of the fields along x , which are labeled with the index m and are referred to by the TE_m denomination. The corresponding magnetic fields along x and y can be obtained from Eq. (3), and the fields for each mode m are given by:

$$E_{y,m} = E_0 \sin\left(\frac{m\pi x}{d}\right) \exp(-j\tilde{k}_{z,m}z), \quad (77)$$

$$H_{x,m} = -\frac{\tilde{k}_{z,m}}{\omega\mu_0} E_0 \sin\left(\frac{m\pi x}{d}\right) \exp(-j\tilde{k}_{z,m}z), \quad (78)$$

$$H_{z,m} = \frac{jk_{x,m}}{\omega\mu_0} E_0 \cos\left(\frac{m\pi x}{d}\right) \exp(-j\tilde{k}_{z,m}z). \quad (79)$$

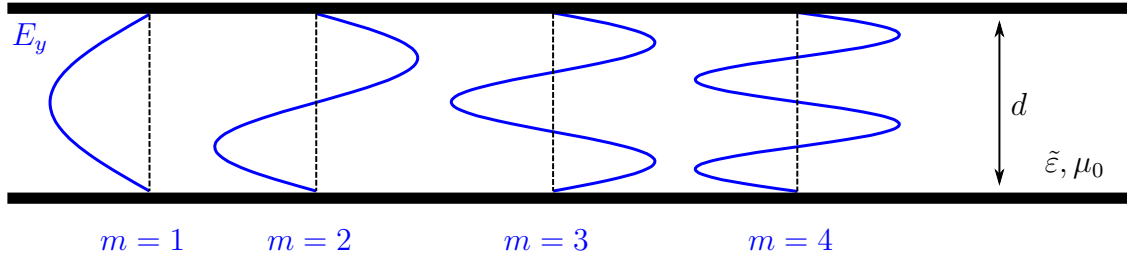


Figure 16: Spatial distribution along x of the $E_{y,m}$ component, for the four first modes of the TE polarization.

For the TE polarization considered here, $m = 0$ yields a trivial solution with $E_y = 0$ everywhere, and is therefore not acceptable. The four first modes for the electric field are plotted in Fig. 16. Each odd-labeled mode is symmetrical around the center of the waveguide, at $x = d/2$, while the even-labeled modes are anti-symmetrical.

Plugging the electric field inside the waveguide for a mode m in Eq.(14) yields the dispersion relation for the TE polarization PEC parallel plate waveguide:

$$\tilde{k}_{z,m} = \sqrt{\omega^2 \tilde{\epsilon} \mu_0 - k_{x,m}^2} = \sqrt{\omega^2 \tilde{\epsilon} \mu_0 - \left(\frac{m\pi}{d}\right)^2}, \quad m \in \mathbb{N}_0. \quad (80)$$

By normalizing the wave number along z to the free-space wave number k_0 , an expression for $\tilde{k}_{z,m}$ as a function of the refractive index and geometrical parameters is obtained:

$$\frac{\tilde{k}_{z,m}}{k_0} = \sqrt{\tilde{n}^2 - \left(\frac{m\lambda_0}{2d}\right)^2} = \tilde{n}_{eff,m}, \quad (81)$$

where \tilde{n} is the refractive index of the medium between the parallel plates. The ratio $\tilde{k}_{z,m}/k_0$ can be assimilated to an effective refractive index associated to the mode m and in this text, it will be referred to as such. In the case where the medium between the plate is non-dissipative, i.e. for air, \tilde{n} is purely real, and one can see that $\tilde{k}_{z,m}$ is either purely real or purely imaginary. In accordance to section 2.2.3.2, an imaginary wave number corresponds to an evanescent wave, while a real one corresponds to a propagating wave. When a given wave number $\tilde{k}_{z,m}$ is imaginary, the corresponding mode with index m is said to be *cutoff*. For each mode m , a cutoff frequency is defined, below which the mode does not propagate but is instead evanescent:

$$\omega_{c,m} = \frac{1}{\sqrt{\tilde{\epsilon} \mu_0}} \frac{m\pi}{d}. \quad (82)$$

Equivalently, for a fixed free-space wavelength or frequency, a cutoff distance $d_{c,m}$ below which the mode m is evanescent can be defined:

$$d_{c,m} = \frac{m\lambda_0}{2\tilde{n}}. \quad (83)$$

Since m cannot be 0 for TE, light cannot propagate inside such a waveguide until its frequency is higher than the cutoff frequency for the TE₁ mode. These results can be summarized and visualized easily with a band structure, plotted for $\tilde{n} = 1.45$ in Fig. 17. There, for a fixed wavelength, the normalized wave number of the five first modes are plotted as a function of the separation distance between the plates d . Below its cutoff distance $d_{c,m}$, a mode m has a purely imaginary wave number and the associated wave is evanescent. The imaginary part goes to infinity as d decreases, but when d increases, it goes to 0 as the wave number becomes purely real. This means that as the separation distance d gets closer to the cutoff distance, the wave is less and less evanescent and has a greater penetration depth, until it finally propagates. Above the cutoff distance, the wave number is purely real and the associated wave is propagating. As the distance between the two plates increases, the wave number of each mode converges towards $k_0 \tilde{n}$, the wave number in the medium between the plates, or equivalently, the effective refractive index of a mode converges towards that of the said medium. A band structure yields an easy way to visualize, at a fixed parameter of interest, which modes are available for propagation, along with their effective refractive index. In summary, light in a waveguide cannot propagate just as a plane wave like in an infinite medium. Instead, it must adapt to the presence of the parallel plates by having its field distribution along x modified, and it can only propagate as some particular modes, for which there exists a cutoff frequency

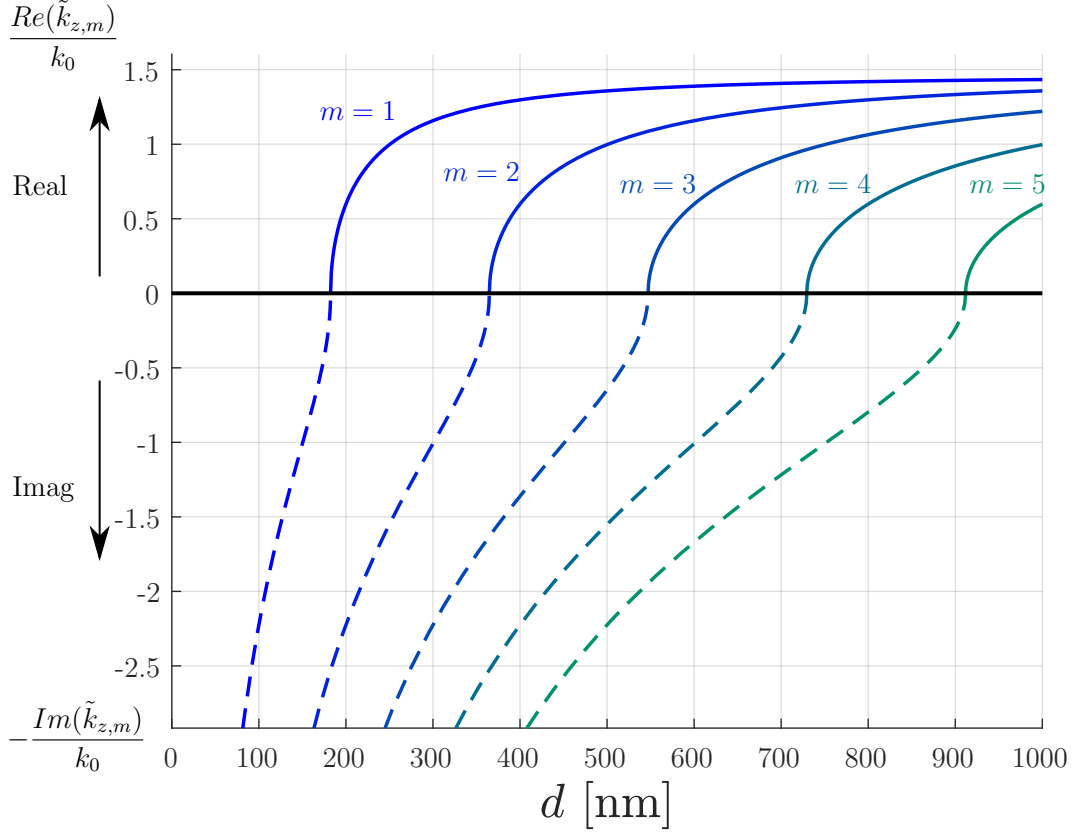


Figure 17: Band structure for the five first modes of the TE polarization for PEC parallel plate waveguide, for a free-space wavelength $\lambda_0 = 532 \text{ nm}$ and $\tilde{n} = 1.45$. The solid lines represent the real part of the wave number, while the dashed lines represent the opposite of its imaginary part.

2.6.1.2 TM polarization

In this case, it is the magnetic field which only has a non-zero component along y , and the incident electric field's only non-zero component is along x , as pictured in Fig. 18. Inside

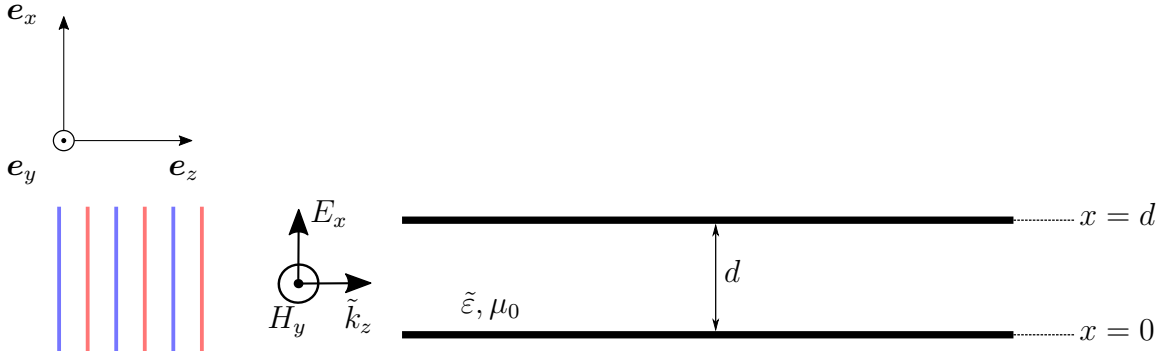


Figure 18: Incoming TM plane wave on a PEC parallel plate waveguide.

the waveguide, the magnetic field must satisfy Eq. (15), which has the same form as the wave equation for the electric field. Under the same assumptions as for the TE polarization, we write:

$$\mathbf{H} = H_0 G(x) \exp(-j\tilde{k}_z z) \mathbf{e}_y, \quad (84)$$

where $G(x)$ is a function to be determined. To do so, the boundary conditions of the PEC plates must be applied to the tangential components along z of the electric field, which are obtained from Eq. (4), and we obtain [26]:

$$G(x) = \cos(k_{x,m}), \quad (85)$$

where k_x is the wave number along x and can only take discrete values according to the same guidance condition as for the TE polarization:

$$k_{x,m} = \frac{m\pi}{d}, \quad m \in \mathbb{N}. \quad (86)$$

except that this time, $m = 0$ is a valid mode of propagation. Now the fields are referred to by the TM_m denomination, and are given by:

$$H_{y,m} = H_0 \cos\left(\frac{m\pi x}{d}\right) \exp(-j\tilde{k}_{z,m} z), \quad (87)$$

$$E_{x,m} = -\frac{\tilde{k}_{z,m}}{\omega\tilde{\epsilon}} H_0 \cos\left(\frac{m\pi x}{d}\right) \exp(-j\tilde{k}_{z,m} z), \quad (88)$$

$$E_{z,m} = \frac{j k_{x,m}}{\omega\tilde{\epsilon}} H_0 \sin\left(\frac{m\pi x}{d}\right) \exp(-j\tilde{k}_{z,m} z). \quad (89)$$

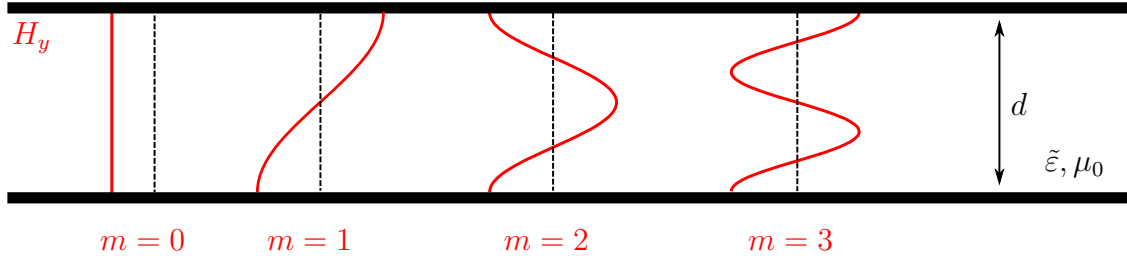


Figure 19: Spatial distribution along x of the $H_{y,m}$ component, for the four first modes of the TM polarization.

It appears that the $m = 0$ mode is similar to a plane wave, since in that case both $H_{y,0}$ and $E_{x,0}$ are uniform, although they are confined between the plates, and $E_{z,0} = 0$. As a result, this TM_0 mode is commonly referred to as TEM mode, for transverse electromagnetic mode. The magnetic field for the first four modes of the TM polarization are plotted in Fig. 19. In opposition to the TE polarization, each even-labeled mode is symmetrical around the center of the waveguide, at $x = d/2$, while the odd-labeled modes are anti-symmetrical. Plugging the solution for $H_{y,m}$ back into Eq. (15) yields the same dispersion relation as for the TE mode, although in that case $m = 0$ is valid too:

$$\tilde{k}_{z,m} = \sqrt{\omega^2 \tilde{\epsilon} \mu_0 - k_{x,m}^2} = \sqrt{\omega^2 \tilde{\epsilon} \mu_0 - \left(\frac{m\pi}{d}\right)^2}, \quad m \in \mathbb{N}. \quad (90)$$

The effective refractive index Eq. (81) is also the same for these modes although m can be zero. The cutoff frequencies and distances are the same as well:

$$\omega_{c,m} = \frac{1}{\sqrt{\tilde{\epsilon}\mu_0}} \frac{m\pi}{d}, \quad \text{and} \quad d_{c,m} = \frac{m\lambda_0}{2\tilde{n}}, \quad (91)$$

although the fact that the TEM mode exists and that it has no imaginary part means that there always is a mode available for light propagation, even at low frequency or for very close plates. Fig. 20 illustrates this with the help of the band structure calculated for $\tilde{n} = 1.45$ for the TM case. As can be seen the $m = 0$ mode is always available regardless of the separation distance d . This mode corresponds to the TEM wave propagating inside the waveguide, with a wave number equal to that of a plane wave with in the cladding medium. In summary, a TM polarized wave must adapt to the presence of the parallel plates just as

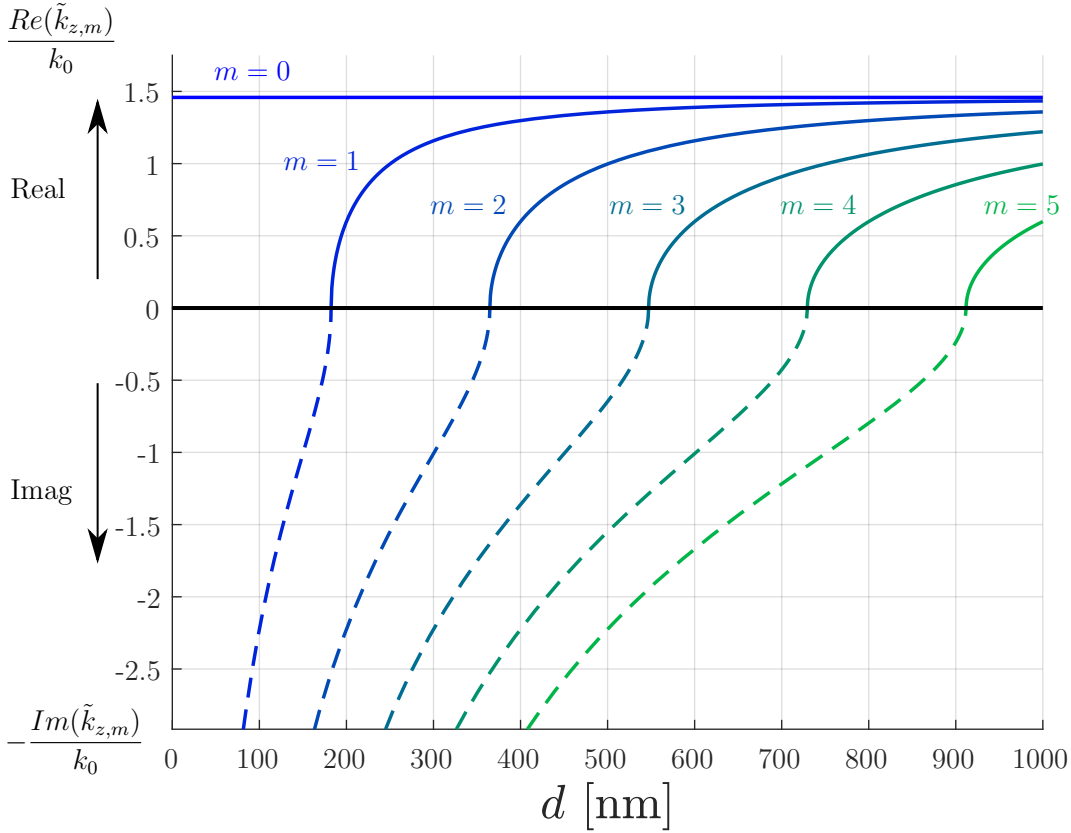


Figure 20: Band structure for the six first modes of the TM polarization for PEC parallel plate waveguide, for a free-space wavelength $\lambda_0 = 532$ nm and $\tilde{n} = 1.45$. The solid lines represent the real part of the wave number, while the dashed lines represent the opposite of its imaginary part.

a TE polarized wave does: by modifying the fields distribution along x and by allowing only certain discrete modes of propagation. The main difference lies in the fact that the $m = 0$ mode exists for TM but not for TE. The other main difference lies in the distribution of the fields themselves.

2.6.2 Diffraction grating

When light is incident on a surface with irregular profile at a length scale comparable to the wavelength, it is reflected and refracted in many different directions. If the irregularities are periodic, the interferences will produce replicas of the incident (resp. transmitted) beams in reflection (resp. transmission) and in different directions. When incident light impinges upon a grating, such as illustrated in Fig. 21 the boundary conditions require the tangential component of the wave vector to be continuous. Upon entering a periodic grating, the phase matching conditions is [36]:

$$\tilde{k}_{x,m} = \tilde{k}_{x,i} + mK, \quad m \in \mathbb{Z}, \quad (92)$$

where the subscript i stands for incident, m is an integer and K is the wave number of the grating, assuming that $\mathbf{K} = K\mathbf{e}_x$. Using Snell's identity, the so-called grating equation is

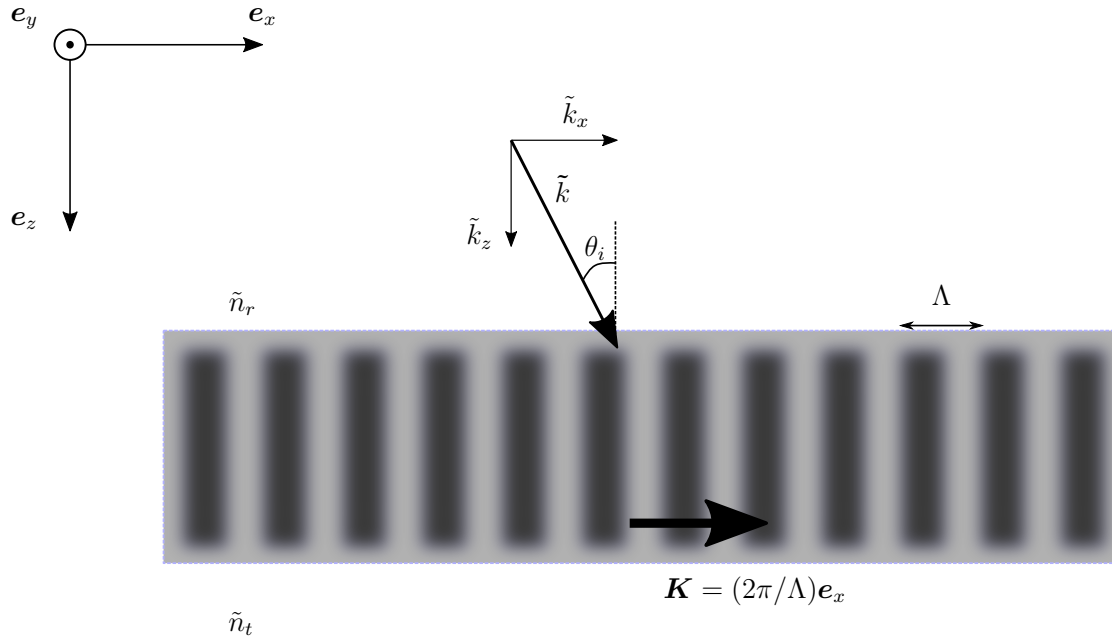


Figure 21: Phase matching condition on the tangential component of the incoming wave vector incident on a periodic grating with wave vector \mathbf{K} .

obtained:

$$\tilde{n}_{r,t} \sin(\theta_m) = \tilde{n}_i \sin(\theta_i) + m \frac{\lambda_0}{\Lambda}, \quad m \in \mathbb{Z}, \quad (93)$$

where the subscripts r, t, i stands respectively for reflection, transmission and incident, and $\Lambda = 2\pi/K$ is the periodicity of the grating. Replicas of the incident beam are created at an angle θ_m when the grating equation is satisfied for the corresponding integer m . An incident beam being diffracted by the grating is illustrated in Fig. 22. If the incident wave is a plane wave, the reflected and transmitted replicas will also be plane waves, propagating at an angle. However, those replicas will interact together and with the initially reflected/transmitted

plane wave in their respective media, leading to interference patterns in the electric field distribution.

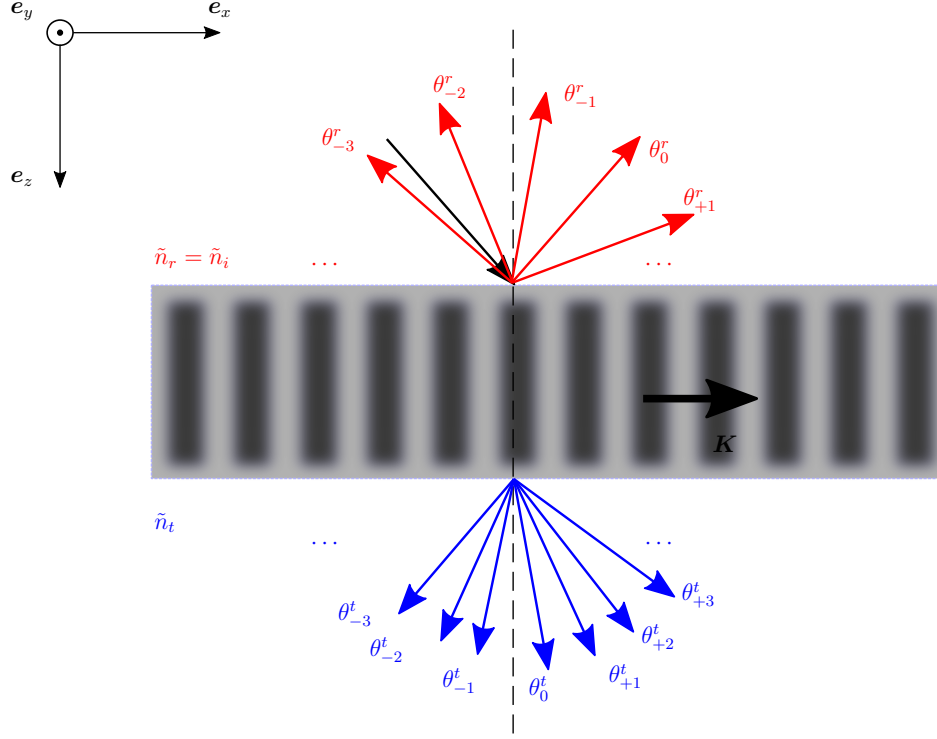


Figure 22: Example of diffraction orders for an incoming plane wave with incidence angle θ_i . In this case, $n_t > n_i$ and more modes are available in transmission than in reflection.

It is possible to derive a dispersion relation similar to those for the parallel plate waveguide from the phase matching condition (92):

$$\tilde{k}_{z,m} = \sqrt{k_0^2 \tilde{n}_{r,t}^2 - (k_0 \tilde{n}_i \sin(\theta_i) + mK)^2}, \quad m \in \mathbb{Z} \quad (94)$$

or, when normalized to the incident wave number:

$$\frac{\tilde{k}_{z,(r,t),m}}{k_0} = \sqrt{\tilde{n}_{r,t}^2 - \left(\tilde{n}_i \sin(\theta_i) + \frac{m\lambda_0}{\Lambda} \right)^2}, \quad m \in \mathbb{Z}. \quad (95)$$

Similarly to the waveguide, for each mode m , there exists a cutoff pitch below which the wave number is imaginary and for which the corresponding diffracted mode is evanescent:

$$\Lambda_{c,(r,t),m} = \begin{cases} \frac{\lambda_0 m}{(\tilde{n}_{r,t} - \tilde{n}_i \sin(\theta_i))} & \text{if } m > 0, \\ \frac{\lambda_0 |m|}{(\tilde{n}_{r,t} + \tilde{n}_i \sin(\theta_i))} & \text{if } m < 0, \end{cases} \quad (96)$$

This relation depends on the refractive index of the medium of interest, which means that modes where the refractive index is higher will become available more quickly as the pitch is

increased, since the corresponding cutoff pitches are smaller. Besides, the $m = 0$ mode always exists and corresponds to the plane wave mode propagating in the medium of refractive index $\tilde{n}_{r,t}$, or in other words, to the initially reflected and transmitted part of the incident plane wave. It is also possible to plot a band structure for the diffraction modes using Eq (95), as shown in Fig. 23 and Fig. 24, for reflection and transmission, respectively. For a given set of parameters $\tilde{n}_i, \tilde{n}_t, \theta_i$ and λ_0 , it is easy to visualize which modes are available for propagation as a function of the pitch Λ . Given a mode index m , the angle θ_m at which the corresponding mode propagates can be inferred. Fig. 24 shows how for a greater refractive index in transmission, more modes are available at a given pitch, compared to a lower refractive index (see Fig. 23 compared to 24). In reflection, $\tilde{n}_r = \tilde{n}_i$ which is equal to 1 in this example. As a result, there are fewer modes in reflection than in transmission for which $\tilde{n}_t = 4.15$.

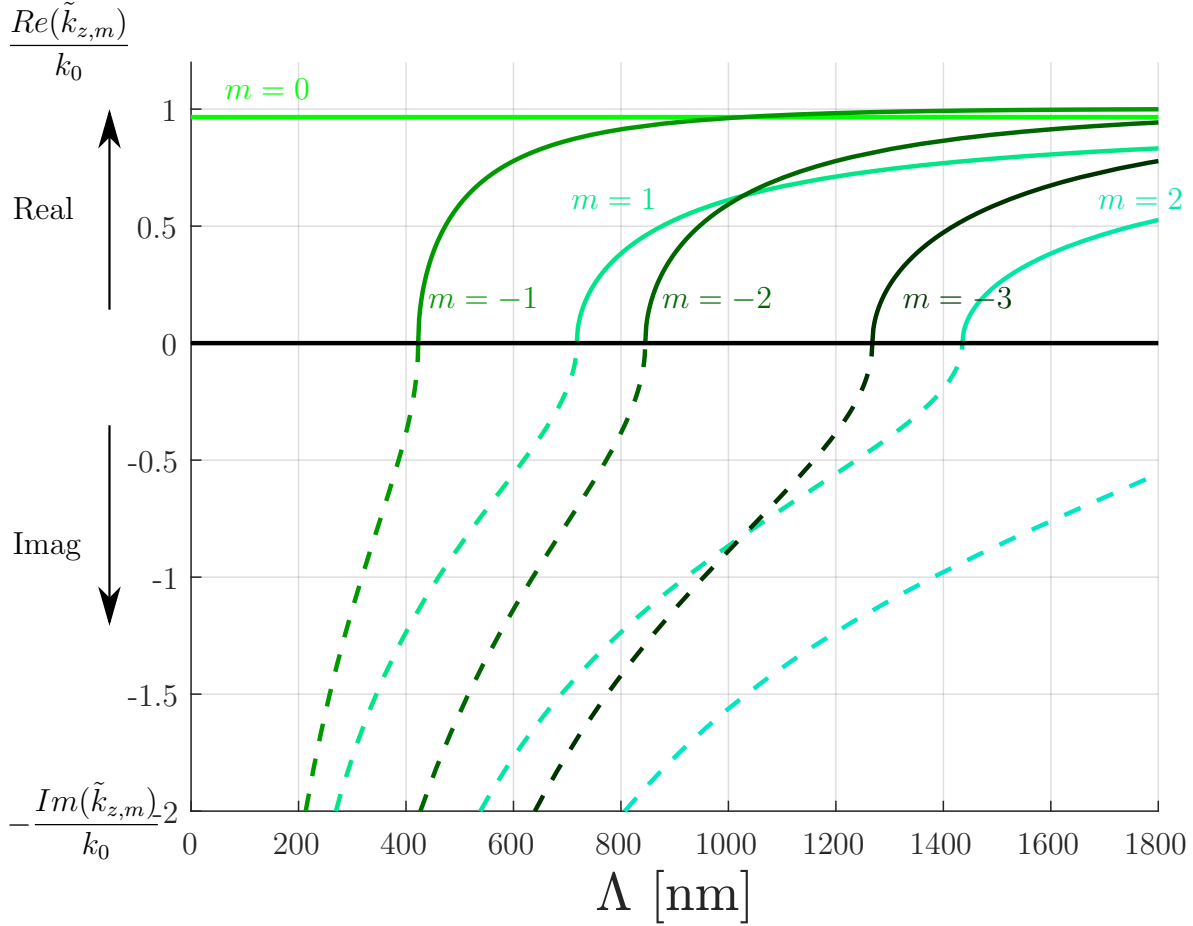


Figure 23: Band structure for 0th order and three first modes in reflection of a diffraction grating, for a free-space wavelength $\lambda_0 = 532$ nm, $\tilde{n}_i = \tilde{n}_r = 1$ and $\theta_i = 15^\circ$. The solid lines represent the real part of the wave number, while the dashed lines represent the opposite of its imaginary part.

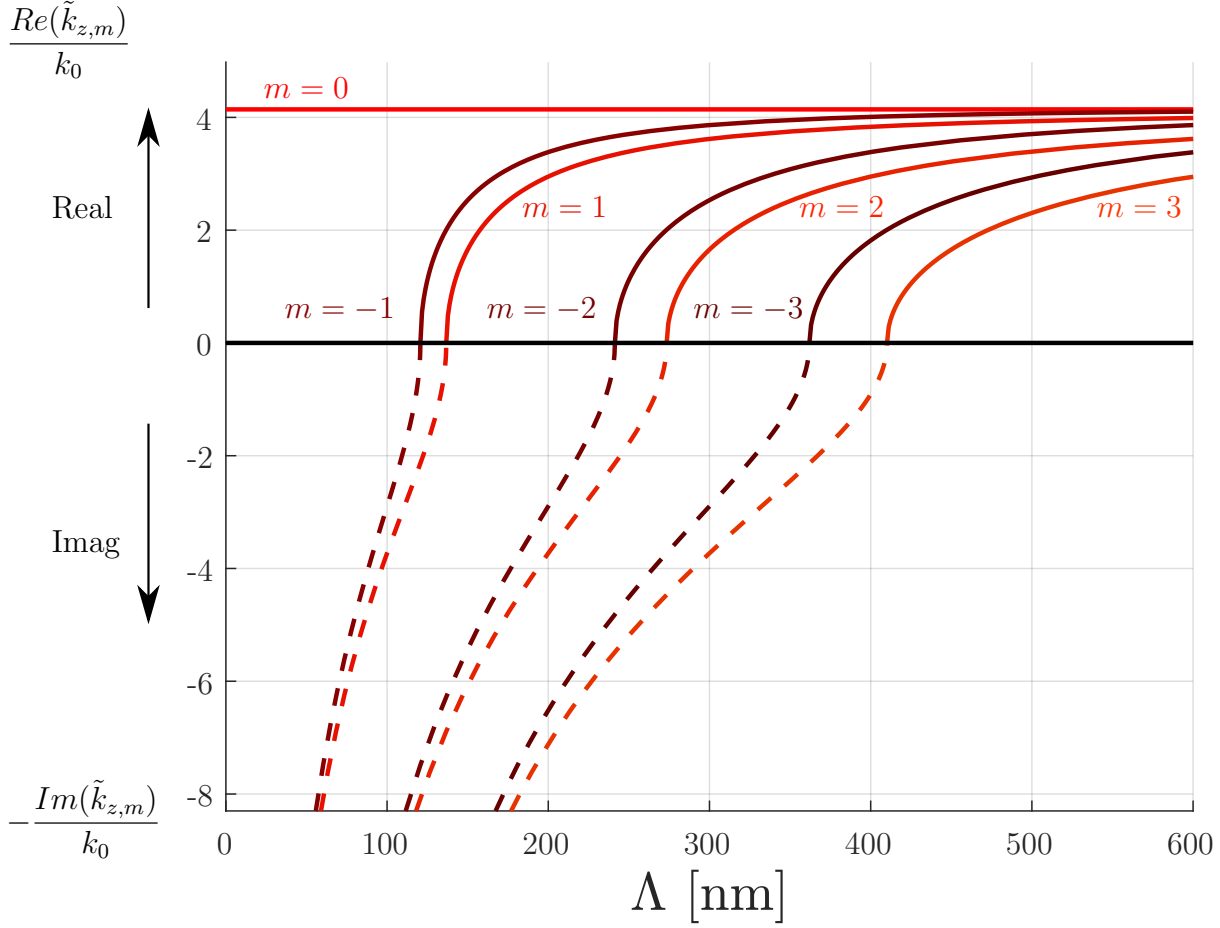


Figure 24: Band structure for 0^{th} order and three first modes in transmission of a diffraction grating, for a free-space wavelength $\lambda_0 = 532$ nm, $\tilde{n}_i = \tilde{n}_r = 1$ and $\theta_i = 15^\circ$. The solid lines represent the real part of the wave number, while the dashed lines represent the opposite of its imaginary part.

2.6.3 Surface plasmons polaritons

Surface plasmons (SPs) are coherent electron oscillations that exist at the interface between any two materials where the real part of the dielectric function changes sign across the interface (e.g. a metal-dielectric interface, such as a metal sheet in air). Surface plasmon polaritons (SPPs) are electromagnetic waves that travel along a metal-dielectric or metal-air interface. The term polariton refers to the coupling of the light with the charge density in the metal [37].

The surface charge density oscillations associated with surface plasmons at the interface between a metal and a dielectric can give rise to strongly enhanced optical near-fields which are spatially confined near the metal surface. At normal incidence, coupling of photons into SPPs can be achieved using a coupling medium such as a diffraction grating to match the

photon and SPP wave vectors. As a result, a plasmon becomes excitable at [38]:

$$k_{sp} = mK, \quad (97)$$

where k_{sp} is the wave number of the SP, m is the diffraction order and K is the wave number of the grating. In the case of a metallic grating, SPPs may be excited at the passing off of a diffraction order (termed a Rayleigh anomaly), when the associated diffracted plane wave is grazing and propagates along the metallo-dielectric interface. It is then possible to obtain a finite longitudinal component of the wave vector thanks to diffraction, even at normal incidence. The wavelength is then calculated from the dielectric functions of the assumed lossless dielectric (air in this case) and metal by [3]:

$$\lambda_{spp} \approx \sqrt{\frac{\varepsilon'_{metal} + \varepsilon_{air}}{\varepsilon'_{metal}\varepsilon_{air}}} \lambda_0, \quad (98)$$

where ε' is the real part of the dielectric function, in accordance to the notations of section 2.2.3.2, and where it was assumed that $|\varepsilon''_{metal}| \ll |\varepsilon'_{metal}|$. As SPPs propagate along the surface, they lose energy to the metal due to absorption, and they may affect the reflectance and transmittance spectra of a structure accordingly. Finally, since a SPP is propagating along the metal interface and confined in the normal direction, it requires a non-zero electric field inside the metal. Therefore, SPPs are expected only for real metals and not for a theoretical perfect electrical conductor, inside which an electric field cannot penetrate.

As an example taken from [39], Fig. 25 depicts some SPPs by plotting the squared norm of the component of the electric normal to the interface $|E_y|^2$, which is confined to it and which is responsible for the SPP propagation along \mathbf{e}_x . In this illustration, a plane wave is normally incident and interacts with a periodic silver thin film grating. The period is $1.62 \mu\text{m}$, the thickness of the thin film is 50 nm and its width is $1.48 \mu\text{m}$. The top layer is air while the bottom layer is silica.

Figs. 25a and 25b respectively show the Rayleigh anomalies, or the passing of a diffraction order, for the first diffraction order in reflection and second order in transmission. In other words, the wavelength is such that a diffraction mode becomes propagating. When this occurs, the corresponding angle is 90° and is grazing. In that case, a SPP along \mathbf{e}_x can be excited. Those are depicted in Figs. 25c and 25d for the reflection and transmission respectively. The SPPs are characterized by jets decreasing exponentially away from the grating.

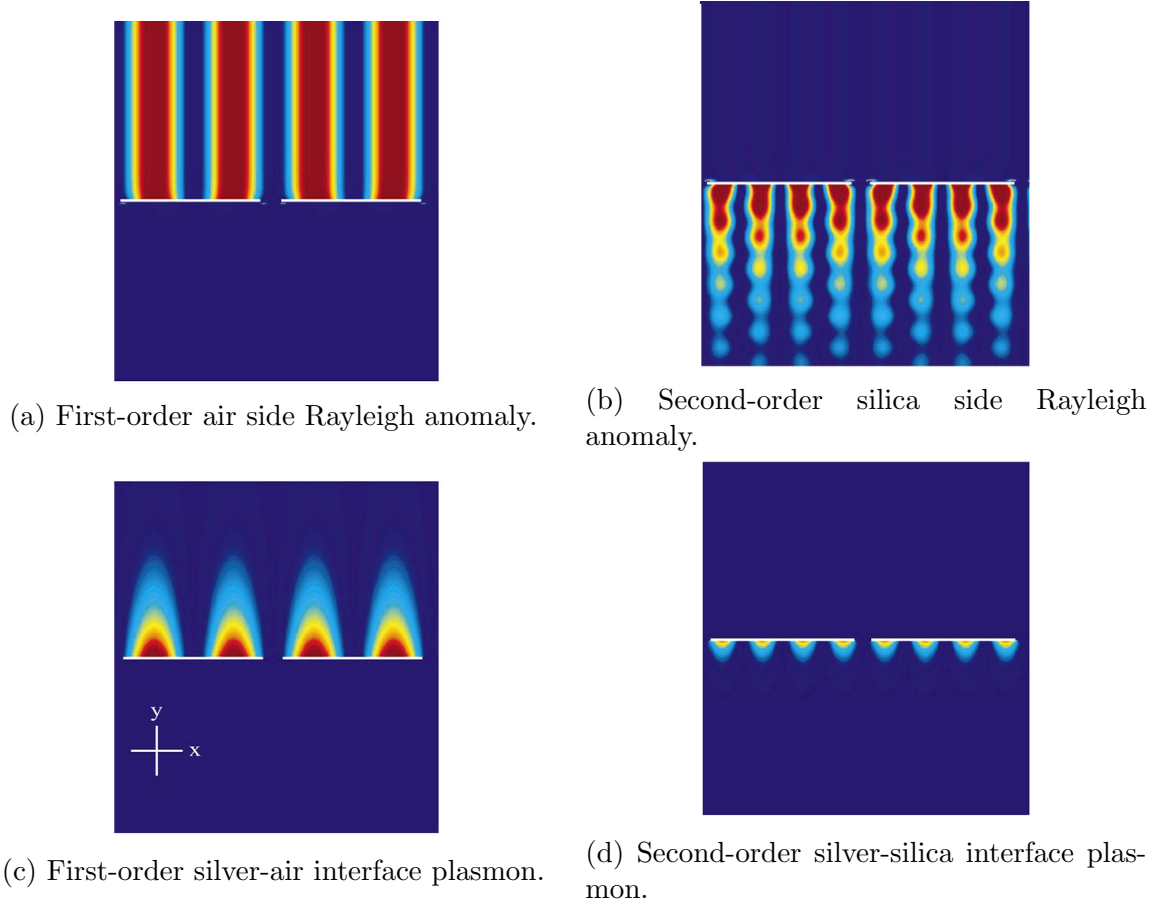


Figure 25: Color map of the $|E_y|^2$ field resulting from the interaction of a plane wave at normal incidence with a silver thin film grating on top of a substrate layer and below an air layer. The field is decomposed into the diffraction (25a and 25b) and SPPs (25c and 25d) contributions. The period is $1.62 \mu\text{m}$, the thickness of the thin film is 50 nm and its width is $1.48 \mu\text{m}$.

3 Light interaction with periodic arrays of nanometer-wide PEC lines

3.1 Methodology and modeling

The objective of this chapter is to study the impact of geometry on the photonic properties of periodic arrays of nanometer-wide metal lines. In particular, the reflectance and transmittance spectra of the structures are studied as a function of the periodicity of the array as well as the width and height of the lines, while maintaining the wavelength of incoming light fixed.

To do so, some simple analytical equations featured in the band structures for the PEC parallel plate waveguide and diffraction gratings are used to qualitatively describe the light interaction. The qualitative description is then compared to quantitative simulations performed by the finite element method software COMSOL Multiphysics®.

The study presented here is relevant for metrology application in the semi-conductor field. Therefore, a sample which is close to what is measured in practice is modeled: an array of metal lines, embedded into a cladding of dielectric material, on top of a substrate of semiconducting material. Fig. 26 depicts the structure of interest, which is composed of a periodic array of perfectly conducting metallic lines of width w and height h separated by a pitch Λ . The cladding material is silicon dioxide (SiO_2) while the substrate is silicon (Si).

The structure is idealized by considering that it is infinite in the horizontal direction and in the direction perpendicular to the plane. Moreover, the lines are considered perfectly parallel to each other (no tapering), equidistant and all with the same height. Besides, the oxide cladding and silicon substrate refractive indices are approximated as purely real, i.e., there is no absorption in those materials.

As discussed at the end of section 2.2.3.2, a single incident wavelength is studied and is fixed at $\lambda_0 = 532\text{ nm}$, which is one of the wavelength typically used in lasers and in metrology tools. The diffraction regime as well as the subwavelength regime are considered, with a pitch varying from around $\lambda_0/5$ to $2\lambda_0$. Typically, the fin height is of the order of 100 nm while the fin width is of the order of tens of nm, although since this is a theoretical work, the effect of greater heights and widths are also explored.

To study the interaction of light with periodic arrays of metal lines, a plane wave of a fixed wavelength incoming on the periodic structure is considered. Upon encountering the first interface, the plane wave is reflected. Since it encounters a periodic structure, it does so according to the modes allowed by the corresponding diffraction grating. Moreover, the array of parallel lines essentially act as an array of PEC parallel plate waveguides, with a separation distance of $d = \Lambda - w$. Therefore, light can only propagate into the grating according to the modes described by the TE or TM band structures, depending on the polarization of the incoming light. It is important to emphasize that the modes are the same

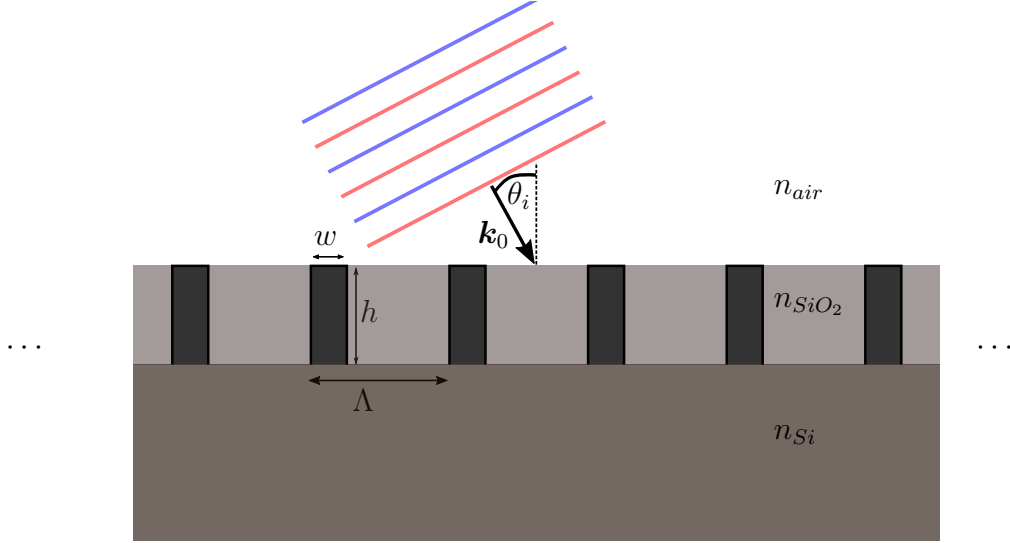


Figure 26: Model of the idealized periodic array of PEC lines upon which a plane wave is incident.

for the periodic as for the single waveguide. Indeed, the field inside a unit cell of the grating does not influence that of the neighboring ones since the lines are made of PEC. Finally, light propagating through a periodic structure also diffracts at the exit, once again according to the modes described by the band structure for diffraction in transmission.

The light interaction is therefore described by three phenomena: diffraction in reflection, PEC parallel plate waveguide and diffraction in transmission. Each of those phenomena is characterized by its own band structure as described in section 2.6. The model upon which this study is based is a superposition of those three band structures, essentially describing how light interacts with the array.

In accordance with the physical parameters associated with the structure described above, the dispersion relation for the waveguide modes (or grating modes), diffraction in reflection modes and diffraction in transmission modes respectively become:

$$\tilde{n}_{eff,m} = \frac{\tilde{k}_{z,g,m}}{k_0} = \sqrt{n_{SiO_2}^2 - \left(\frac{m\lambda_0}{2(\Lambda - w)} \right)^2}, \quad m \in \mathbb{N}, \quad (99)$$

$$\frac{\tilde{k}_{z,r,p}}{k_0} = \sqrt{n_{air}^2 - \left(n_{air} \sin(\theta_i) + \frac{p\lambda_0}{\Lambda} \right)^2}, \quad p \in \mathbb{Z}, \quad (100)$$

$$\frac{\tilde{k}_{z,t,q}}{k_0} = \sqrt{n_{Si}^2 - \left(n_{air} \sin(\theta_i) + \frac{q\lambda_0}{\Lambda} \right)^2}, \quad q \in \mathbb{Z}, \quad (101)$$

where g stands for *grating* and refer to the waveguide modes, r stands for reflection and t stands for transmission. In the case of TE polarization, m cannot be 0. The complete band structure for TE and TM are very cumbersome and are therefore presented in the appendix (Figs. 112 and 113) for the most general case, with all modes featured below a pitch

$\Lambda = 1000 \text{ nm}$ and non-normal incidence.

In this master thesis however, only the normal incidence is explored. In that case, the dispersion relations become:

$$\tilde{n}_{eff,m} = \frac{\tilde{k}_{z,g,m}}{k_0} = \sqrt{n_{SiO_2}^2 - \left(\frac{m\lambda_0}{2(\Lambda - w)} \right)^2}, \quad m \in \mathbb{N}, \quad (102)$$

$$\frac{\tilde{k}_{z,r,p}}{k_0} = \sqrt{n_{air}^2 - \left(\frac{p\lambda_0}{\Lambda} \right)^2}, \quad p \in \mathbb{Z}, \quad (103)$$

$$\frac{\tilde{k}_{z,t,q}}{k_0} = \sqrt{n_{Si}^2 - \left(\frac{q\lambda_0}{\Lambda} \right)^2}, \quad q \in \mathbb{Z}. \quad (104)$$

Here, a simplified version of the band structures is presented in Figs. 27 and 28 for readability. It considers normal incidence, so that the diffraction modes are degenerate, and it features only the symmetric waveguide modes, which, as shall be seen later, are the only one that are excited. In addition, only the four first diffraction modes in transmission are plotted, since the higher order ones are barely excited, as shall also be seen later.

In this work, we propose to make an extensive use of the band structures to qualitatively describe how light interacts with the array. For a given set of parameters Λ, w, h and θ , a band structure associates, a wave number along z to each mode. In the case of PEC lines, for each set of parameters, the associated wave number is either purely real or purely imaginary, meaning that the mode either propagates without absorption or is evanescent.

3.1.1 COMSOL Multiphysics[®]

The band structure is a powerful tool to understand qualitatively how light interacts with the array. However, it is not quantitative and it does not tell how the power is distributed into each propagating mode. For this calculation, a more elaborate numerical [40] or analytical [41] approach has to be applied. The more similar the field distributions of the exciting wave and the excited mode are at the matching plane, the higher the excitation efficiency of these modes by the incident field is. This similarity is expressed by an overlap integral [41]. Furthermore, the similarity between the propagation constant of the incoming wave, $k_{0,z} = k_0 \cos(\theta_i)$, and the propagating constant inside the grating, $\tilde{k}_{z,m}$, also determine how much energy of the incident wave is coupled into a specific mode [42]. In this study, the analytical part is limited to the qualitative band structure while the quantitative part is performed by FEM simulations.

COMSOL Multiphysics[®] is a cross-platform finite element analysis, solver and multi-physics simulation software. It allows conventional physics-based user interfaces and coupled systems of partial differential equations and it provides an IDE and unified workflow for electrical, mechanical, fluid, acoustics, and chemical applications. COMSOL encompasses all of the steps in the modeling workflow: from defining geometries, material properties, and the physics that describe specific phenomena to solving and postprocessing models for producing

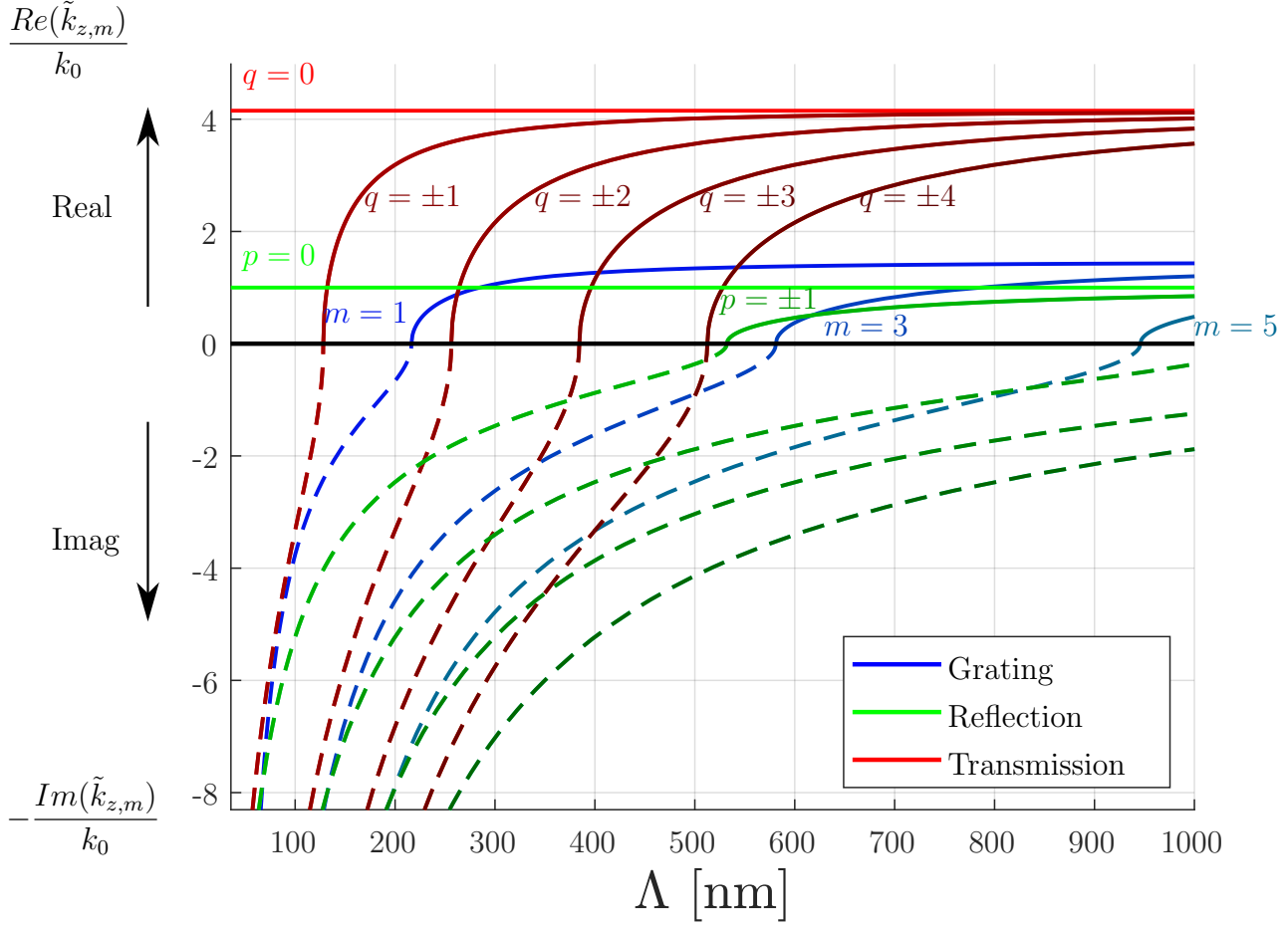


Figure 27: Band structure for the array of PEC lines under TE illumination, which features only the modes that are excited below a pitch $\Lambda = 1000\text{nm}$, for a free-space wavelength $\lambda_0 = 532\text{nm}$, width $w = 34\text{nm}$, refractive indices $n_{air} = 1$, $n_{Si} = 4.15$, $n_{SiO_2} = 1.45$ and $\theta_i = 0^\circ$. The solid lines represent the real part of the wave number, while the dashed lines represent the opposite of its imaginary part. Blue curves correspond to waveguide modes, green curves correspond to diffraction in reflection modes and red curves correspond to diffraction in transmission modes. To make the plot more readable, only the first few diffraction modes are plotted since the higher order ones are barely excited. Similarly, only the symmetric TE waveguide modes are plotted, as the asymmetric modes are not excited by a symmetrical plane wave.

accurate and trustworthy results [43].

In this master thesis, COMSOL Multiphysics[®] is used to simulate the situation represented in Fig. 26 and compute the fields distribution resulting from the interaction of light with the structure, which is then used to calculate the reflectance and transmittance spectra in a quantitative way. The analytical model, i.e., the band structure framework, is used to explain how those spectra vary as a function of the geometrical parameters.

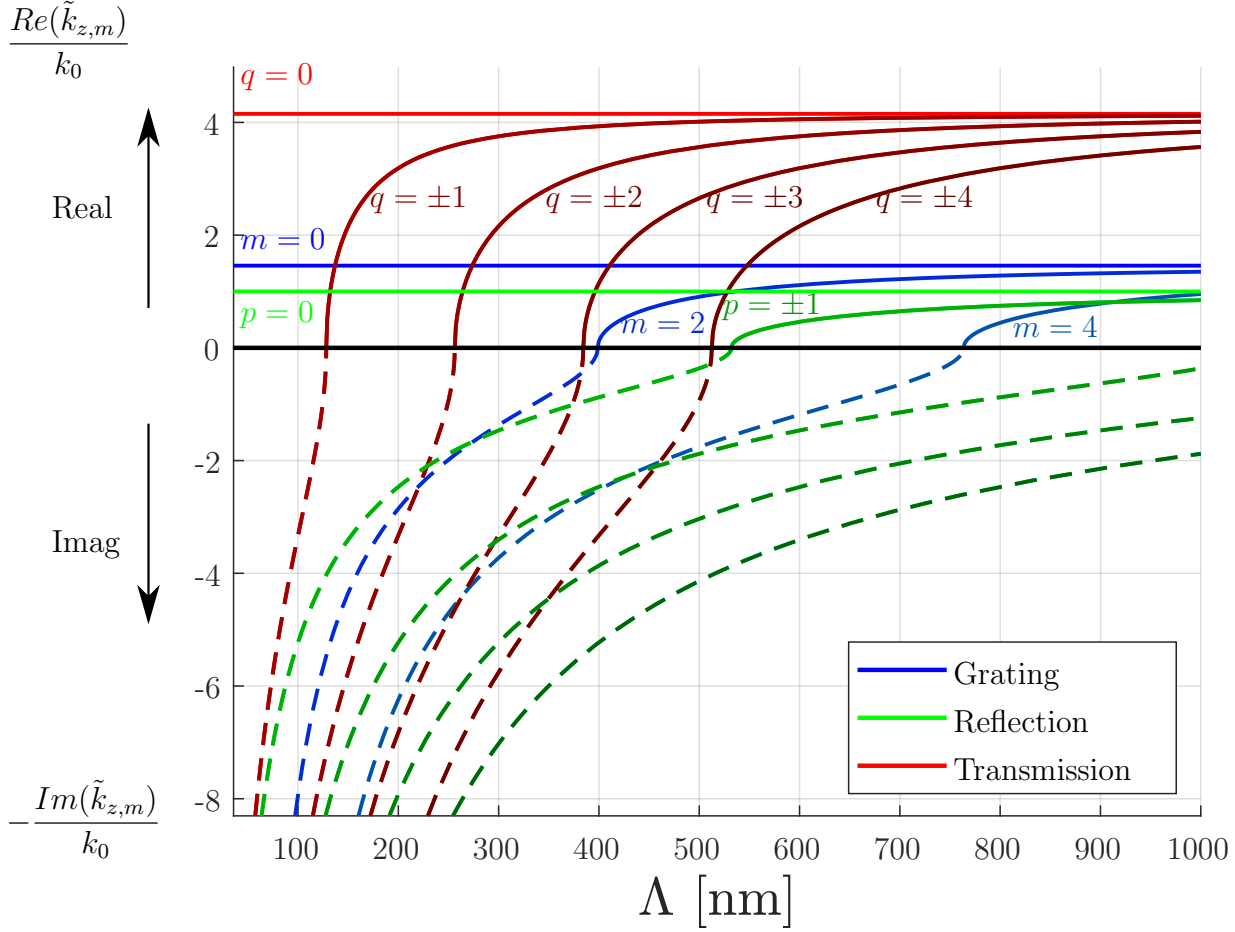


Figure 28: Band structure for the array of PEC lines under TM illumination, which features only the modes that are excited below a pitch $\Lambda = 1000\text{nm}$, for a free-space wavelength $\lambda_0 = 532\text{nm}$, width $w = 34\text{nm}$, refractive indices $n_{air} = 1$, $n_{Si} = 4.15$, $n_{SiO_2} = 1.45$ and $\theta_i = 0^\circ$. The solid lines represent the real part of the wave number, while the dashed lines represent the opposite of its imaginary part. Blue curves correspond to waveguide modes, green curves correspond to diffraction in reflection modes and red curves correspond to diffraction in transmission modes. To make the plot more readable, only the first few diffraction modes are plotted since the higher order ones are barely excited. Similarly, only the symmetric TM waveguide modes are plotted, as the asymmetric modes are not excited by a symmetrical plane wave.

To model our structure, a 2D unit cell is defined in COMSOL with the geometrical parameters of the array, and periodic boundary conditions are applied on each side to simulate the infinite nature of the idealized structure. Fig. 29 depicts the geometry implemented in the software. Periodic boundary conditions are applied on the left and right vertical edges. An input port from which the incident is excited is defined on the top horizontal edge. This is also where the reflectance is calculated. Similarly, an output port is defined on the bottom horizontal edge, where the wave exits and where the transmittance is calculated. The refractive index of each medium is applied to the corresponding area. The schemes of this

implementation are pictured in the appendix from Figs. 114 to 116. For metals, the n and κ values are interpolated from a set of experimental data found in literature [44]. To simulate a perfect electrical conductor, the corresponding PEC boundary condition (total reflection) is applied on the edges of the metal line. The triangular mesh is generated automatically while making sure that the elements are able to capture the smallest geometrical feature and therefore have a maximum length of the order of $w/5$. The software then solves the wave equation over the computational domain according to the boundary and initial conditions that were specified. Any physical field or scalar value (reflectance, transmittance, absorptance, electric field distribution, ...) can then be retrieved from the study. It is also possible to sweep any geometrical or material parameter to conduct a study on the effect of that parameter on the reflectance and transmittance spectra.

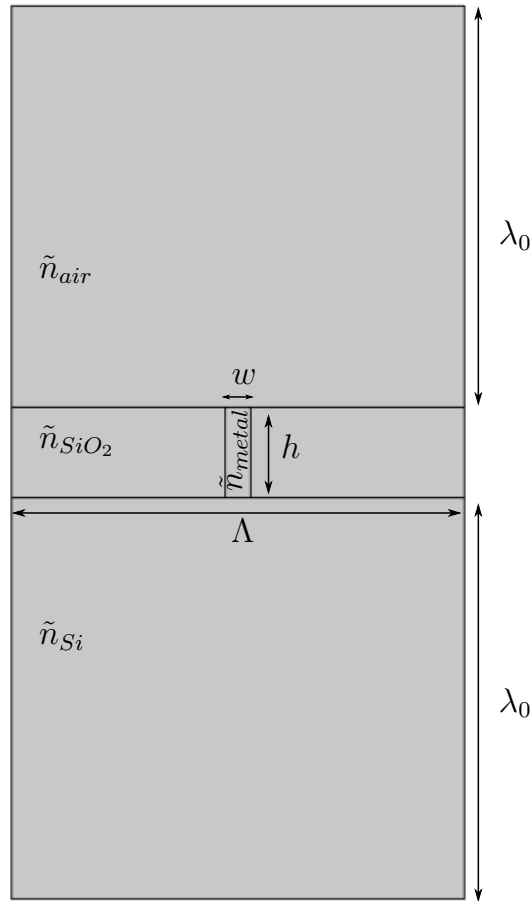


Figure 29: Geometry defined in the COMSOL software.

3.2 Effect of the geometry

In order to study how varying the geometrical parameters of the array modify the reflectance and transmittance spectra, let us consider again a normally incident plane wave on the PEC grating. Since the pitch has been at the center of our analysis thus far, it is be the

first parameter to be analyzed. The reflectance and transmittance spectra are presented as a function of the pitch. Then the variations of the electric field distribution in the unit cell are also presented to support the observations and to highlight the key features of the pitch influence. Like the pitch, the width has an effect on the availability of modes and therefore is the next parameter to be studied. Finally, it is the effect of height that is studied. Especially, a comparison is made between the spectra and 2D maps of an array of 500 nm tall lines with an array of 100 nm lines, as a function of the pitch. Then the reflectance spectrum is also studied as a function of the height. For each of these geometrical parameters, the TE and TM polarizations are compared.

3.2.1 Effect of pitch

The simulation consists in a normally incident plane wave on an array of PEC lines of width $w = 34$ nm and height $h = 100$ nm. The pitch is responsible for the number of modes that are available for both grating and diffraction modes: the larger the pitch, the more modes are propagating. The associated cutoff pitches Λ_c for each mode (grating or diffraction in reflection/transmission) and each order that is featured in the band structures of Figs. 27 and 28 are gathered in Table 1. The grating modes are labeled with the associated polarization (TE or TM) for which the mode is symmetric. This notation is used because the anti-symmetric modes are not excitable. For each polarization, the first mode is symmetric. However the index for the symmetric modes are different in each case due to the existence of order 0 in the case of TM polarization, which brings a shift in the indices.

Mode\Order	0	1	2	3	4	5
Grating	0 (TM ₀)	217,44 (TE ₁)	398,75 (TM ₂)	581,13 (TE ₃)	763,51 (TM ₄)	945,9 (TE ₅)
Reflection	0	532	/	/	/	/
Transmission	0	128	256	384	512	/

Table 1: Cutoff pitches (nm) for each mode featured on the band structure associated to a normally incident plane wave on an array of PEC lines of width $w = 34$ nm. The polarization label for the grating modes indicate for which polarization the associated mode is symmetric. The dashes correspond to modes which have a cutoff pitch larger than 1000 nm and are therefore not featured here or which are barely excited and not relevant to the study.

Figs. 30 and 31 (resp. 32 and 33) feature the reflectance and transmittance spectra of an array of PEC lines as a function of the pitch in the case of TE (resp. TM) polarized light. These will be explained using the band structures of Figs. 27 and 28.

For TE polarized light at low pitch, the cutoff pitch for TE₁ mode at $\Lambda = 217$ nm is not yet reached and light cannot propagate into the array but is reflected instead, yielding a maximum in reflectance. When approaching the cutoff pitch, light starts to penetrate more deeply. As the penetration depth increases, a fraction of the light reaches the substrate, reducing the total reflectance until it starts decreasing more sharply due to light being coupled into the now propagating TE₁ mode, which is now propagating. As the pitch further increases, the fill factor decreases and so does the reflectance. This is in line with

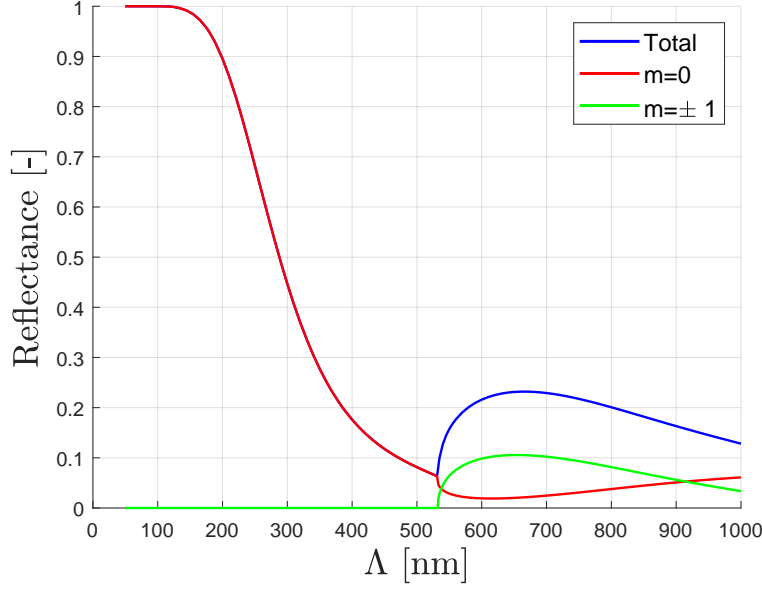


Figure 30: Reflectance spectrum of a normally incident TE polarized plane wave interacting with an array of PEC lines with width $w = 34$ nm and height $h = 100$ nm, as a function of the pitch Λ . The plot features the different diffraction orders. The spectrum is calculated using FEM.

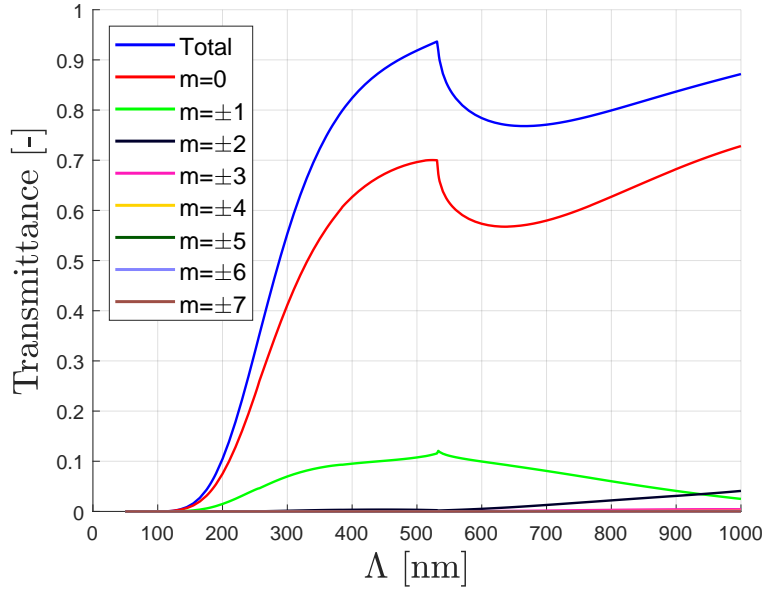


Figure 31: Transmittance spectrum of a normally incident TE polarized plane wave interacting with an array of PEC lines with width $w = 34$ nm and height $h = 100$ nm, as a function of the pitch Λ . The plot features the different diffraction orders. The spectrum is calculated using FEM.

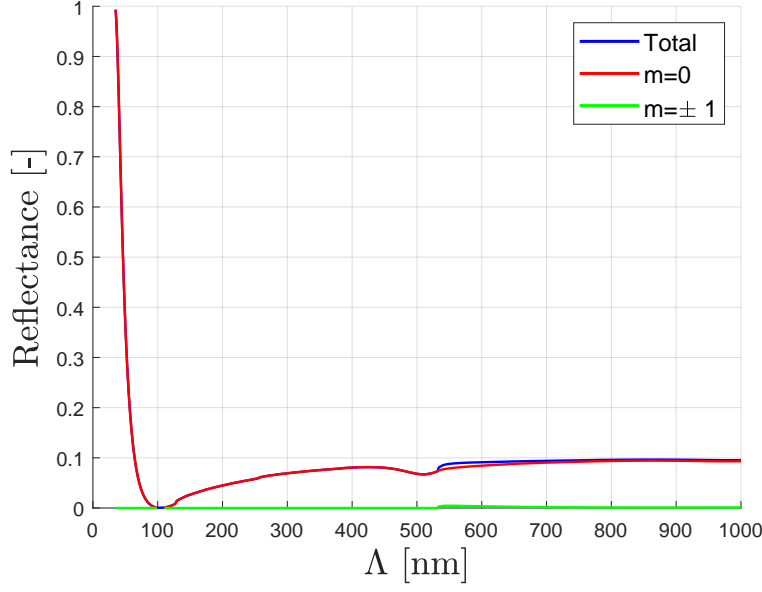


Figure 32: Reflectance spectrum of a normally incident TM polarized plane wave interacting with an array of PEC lines with width $w = 34$ nm and height $h = 100$ nm, as a function of the pitch Λ . The plot features the different diffraction orders. The spectrum is calculated using FEM.

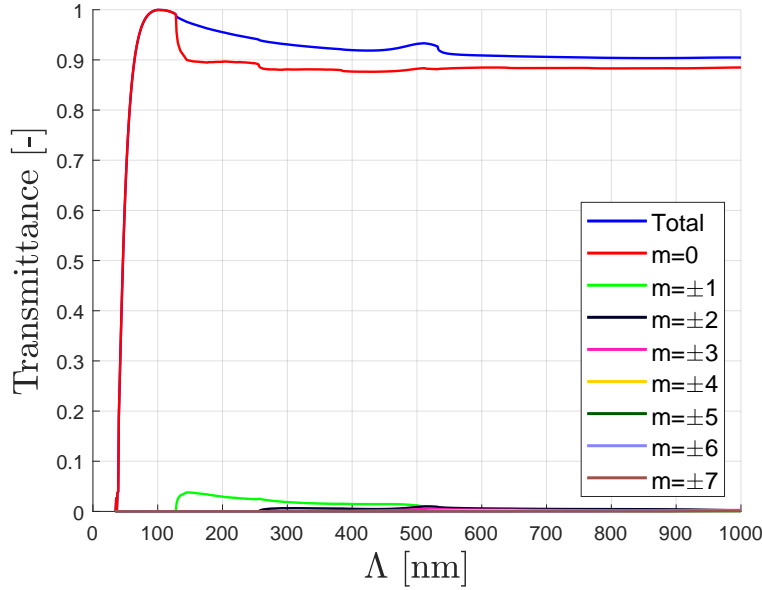


Figure 33: Transmittance spectrum of a normally incident TM polarized plane wave interacting with an array of PEC lines with width $w = 34$ nm and height $h = 100$ nm, as a function of the pitch Λ . The plot features the different diffraction orders. The spectrum is calculated using FEM.

intuition, as the proportion of reflecting PEC with respect to transmitting oxide is reduced. At $\Lambda = 532 \text{ nm}$, there is a sharp transition in the spectrum as the cutoff pitch for the first diffraction order for reflection at $\Lambda = 532 \text{ nm}$ is reached and light is also coupled into the first diffraction mode in reflection.

For TM polarized light, the reflectance in Fig. 32 starts at 1 when $w = \Lambda$, and quickly drops to very small values. According to our band structure model featured in Fig. 28, this result is unexpected. Indeed, the dispersion relations of the TM modes depicted there show that the wave number associated to the TM_0 mode is a constant which has no imaginary part, i.e. the mode is propagating with the same wavelength regardless of the pitch and is not attenuated. As a consequence, the reflectance is expected to be smaller than 1 and constant, irrespective of the pitch. In the asymptotic case where the pitch is equal to the width, the unit cell is completely filled with perfectly conducting metal, which fully reflect the incoming light. It is therefore easy to see that the current model fails to capture how light couples into the TM_0 mode as the fill factor w/Λ gets close to 1: according to this model, light should propagate in the same way in an array of PEC lines, irrespective of pitch, as it does in an homogeneous oxide, which does not follow the intuition and which is not what is observed in the simulations. While the TM_0 mode does propagate like in the oxide for increasing pitch, it is expected that light gets entirely reflected when the array converges to a slab of PEC, as seen in the spectra obtained in Figs. 33 and 32.

There is a problem with the current model: it considers that the fundamental mode of the TM polarization is non-dispersive as a function of the pitch, while the simulations clearly show that this is not the case. It is however possible to explain the spectrum by replacing the TEM mode with a mode calculated using an effective medium approximation (EMA), so that the pitch dependence is incorporated into the model. The structure can be considered as an homogeneous medium with an associated effective permittivity $\tilde{\epsilon}_{eff}$ that is a function of the geometrical parameters.

There exist several effective medium theories that were developed by different authors to homogenize a medium (Maxwell-Garnett, Bruggeman, and others...) [45] [46] [47] [48]. The EMA replaces the periodic array by an homogeneous but anisotropic material, i.e. which exhibits birefringence, and is well suited for this study. The effective permittivity for the TM polarization is then given by:

$$\frac{1}{\epsilon_{eff, TM}} = \frac{1}{\frac{f_{SiO_2}}{\epsilon_{SiO_2}} + \frac{f_{PEC}}{\epsilon_{PEC}}}, \quad (105)$$

where $f_{PEC} = f$ is the fill factor w/Λ and $f_{SiO_2} = 1 - f$, and the permittivity writes:

$$\frac{1}{\epsilon_{eff, TM}} = \frac{1}{\frac{1-f}{\epsilon_{SiO_2}} + \frac{f}{\epsilon_{PEC}}}. \quad (106)$$

In the case of TM polarization, a finite permittivity which is a function of the fill factor $f = w/\Lambda$ is obtained and is given by:

$$\epsilon_{eff, TM} = \frac{\epsilon_{SiO_2}}{1 - f}, \quad (107)$$

from which an effective refractive index is derived:

$$n_{eff,TM} = \frac{n_{SiO_2}}{\sqrt{1-f}}. \quad (108)$$

From this equation, one can see that the effective refractive index tends to that of an homogeneous oxide slab when the fill factor is small but goes to infinity when the fill factor approaches 1, corresponding to a PEC slab for which the reflectance goes to 1. This behavior is in qualitative agreement with what is expected from the structure and therefore this effective refractive index is included in the model instead of the TEM mode, to which it converges for increasing pitch. Moreover, this new TM_0 mode will be referred to as the EMA mode. The band structure is modified in accordance to this result in Fig. 34.

Moving back to Fig. 33, the reflectance starts at 1, as expected by our modified model, then decreases to a very small value, which is in the case unexpected as the effective refractive index of the EMA mode decreases monotonically. This unexpected phenomenon of very high transmittance is known as extraordinary optical transmission (EOT): in the case of TM polarization, it is possible to achieve very high transmission even for tiny transmitting apertures in a reflecting medium, through the coupling of light into the EMA fundamental mode, which undergoes thin-film interferences in the grating [49]. Indeed, in the low-pitch region, the effective refractive index of the EMA mode varies very quickly. As a result, the conditions for thin-film interferences are scanned over very quickly, as per Eq. (72), and the reflectance varies a lot. At around $\Lambda = 100$ nm, the effective refractive index is such that there is a minimum in reflectance due to this phenomenon. As the pitch increases, the effective refractive index converges to a constant and so does the reflectance. When the cutoff for diffraction in reflection is reached, there is no resonance in reflectance as it was the case for the TE polarization. This is due to the fact that the 0^{th} order light in air and silicon are plane waves which perfectly match the EMA mode of the grating, which is also a plane wave. As a consequence, light mostly couples into these very similar modes and a lot less into the higher diffraction orders, which propagate at an angle and therefore do not match very well with an normally incident plane wave.

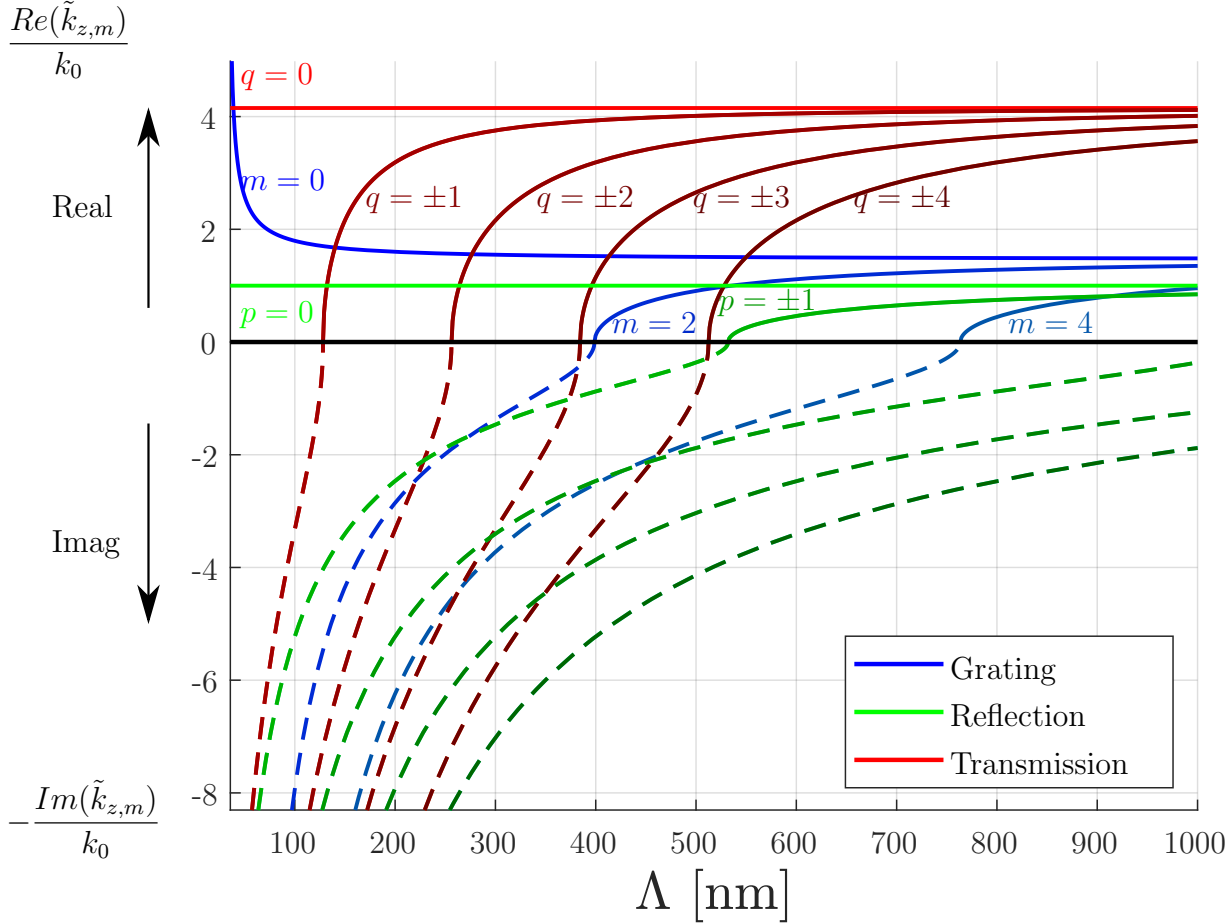


Figure 34: Band structure for the array of PEC lines under TM illumination, which features only the modes that are excited below a pitch $\Lambda = 1000\text{nm}$, for a free-space wavelength $\lambda_0 = 532\text{nm}$, width $w = 34\text{nm}$, refractive indices $n_{air} = 1$, $n_{Si} = 4.15$, $n_{SiO_2} = 1.45$ and $\theta_i = 0^\circ$. The solid lines represent the real part of the wave number, while the dashed lines represent the opposite of its imaginary part. Blue curves correspond to waveguide modes, green curves correspond to diffraction in reflection modes and red curves correspond to diffraction in transmission modes. To make the plot more readable, only the first few diffraction modes are plotted since the higher order ones are barely excited. Similarly, only the symmetric TM waveguide modes are plotted, as the asymmetric modes are not excited by a symmetrical plane wave. The TEM mode is replaced by the EMA mode obtained by effective medium approximation.

Based on the cutoff values of Table 1, it is possible to identify several spectral regions depending on the pitch and to visualize the electric field distribution in each of these regions, highlighting how light propagates in the air, grating and silicon substrate. Each region features a cutoff pitch, and covers the pitch range up to the next cutoff. For each region, the electric field distribution around the cutoff pitch and its evolution up to the next cutoff pitch is analyzed. The different pitch regions are labeled on the superposition of the TE and TM band structure in Fig. 35.

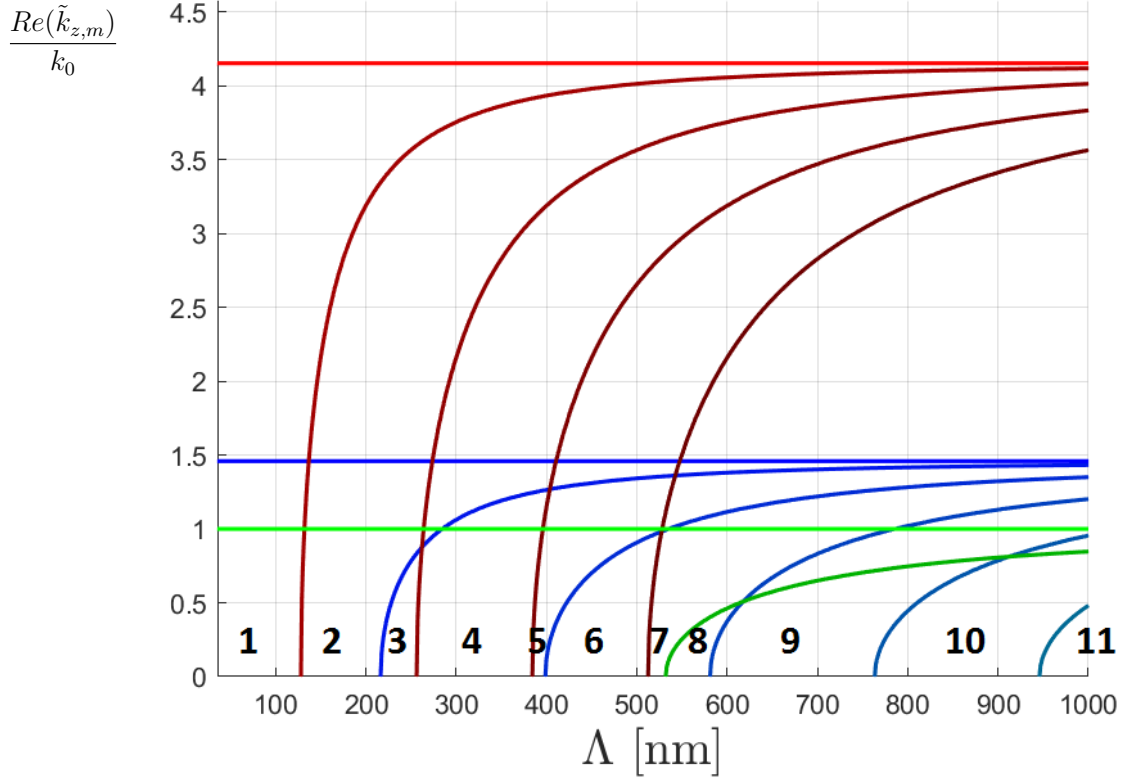


Figure 35: Label of the different spectral regions extracted from the band structure and defined by the cutoff pitch of each mode, for a PEC grating with width $w = 34$ nm and height $h = 100$ nm.

3.2.1.1 Region 1: $\Lambda \in [0, 127]$ nm

Figs. 36 (resp. 37) depict the TE (resp. TM) electric field distribution of spectral region 1, characterized by a pitch smaller than 127 nm. They highlight how TE is cutoff while TM propagates at low pitch. In this case, only the 0^{th} orders are available and so light only propagate as a plane wave as the array supports only the TM propagating mode, and the TE_1 mode is cutoff.

The cutoff is visible in Fig. 36 for TE polarization: the incident plane wave is reflected from the array and creates a standing wave above the structure by interfering with the incident wave. The standing wave is characterized by nodes (blue) and peaks (red) in the 2D map. The wave is evanescent in the array and so the norm of the electric field quickly vanishes below the first interface. In the case of the TM polarization, Fig. 37 shows that the electric field does not vanish as the wave penetrates the array by coupling into the EMA mode, which has no cutoff, and so the norm is finite in the substrate and the wave propagates. At first sight, it might be surprising that the electric field intensity is smaller in the substrate than in the air, while at the same time observing a phenomenon of extremely high transmittance, meaning a very low reflectance. This is because the transmittance is not only proportional to the ratio of electric fields (i.e. the transmission coefficient t) but it must also be scaled up by the ratio of the refractive indices of the two media (i.e. by $n_{Si}/n_{air} = 4.15$ in this case) as per Eq.(66). There is also a standing wave due to reflection but its intensity decreases as the minimum reflectance value around $\Lambda = 100$ nm is approached. It is possible to visualize the jump in electric field between the metal line and the oxide in the case of TM polarization, as there exist a component of the electric field that is normal to the interface and hence discontinuous.

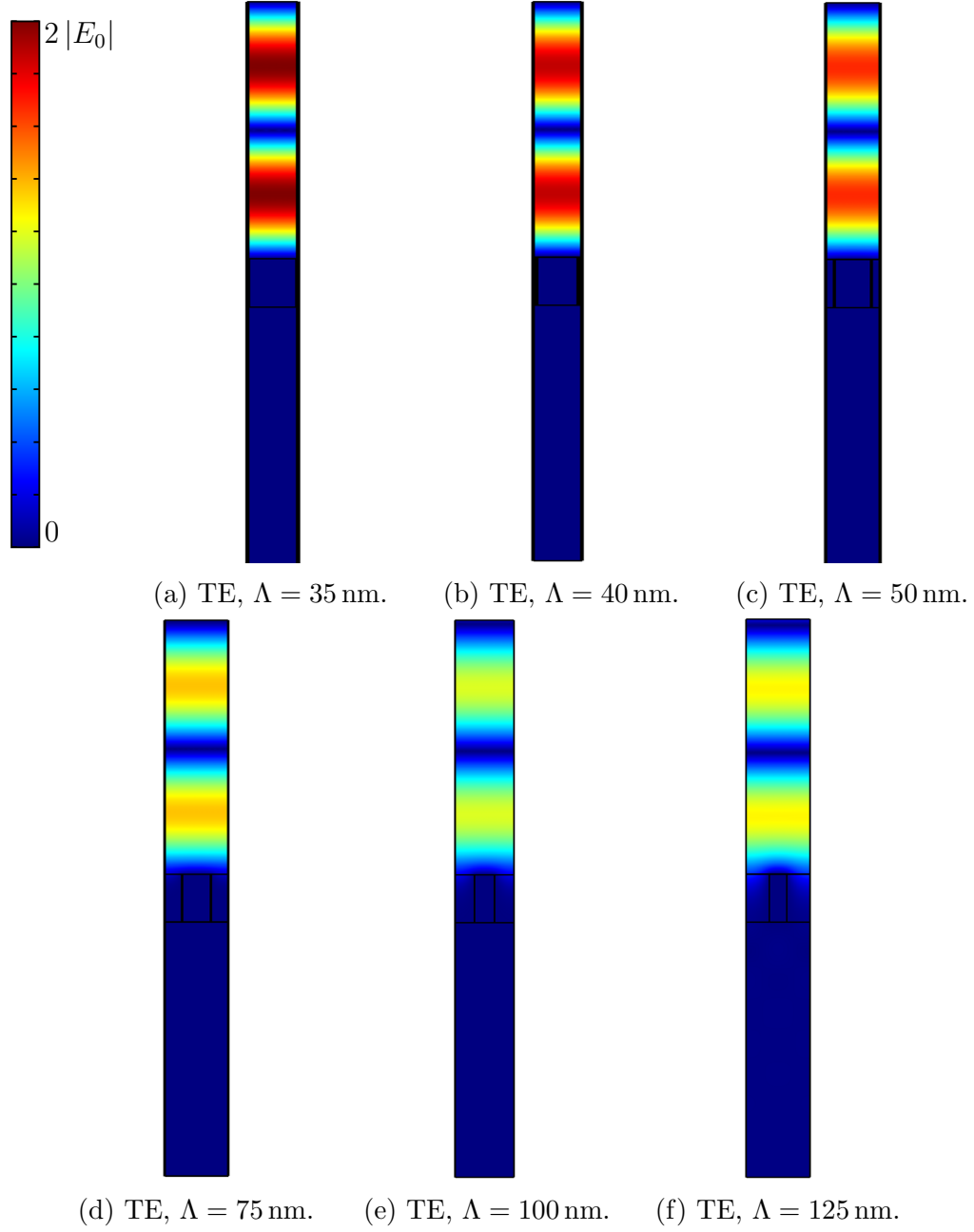


Figure 36: Distribution of the phasor norm of the TE electric field in the unit cell, for an array of PEC lines with width $w = 34$ nm, height $h = 100$ nm in pitch region 1 (Λ between 0 nm and 127 nm).

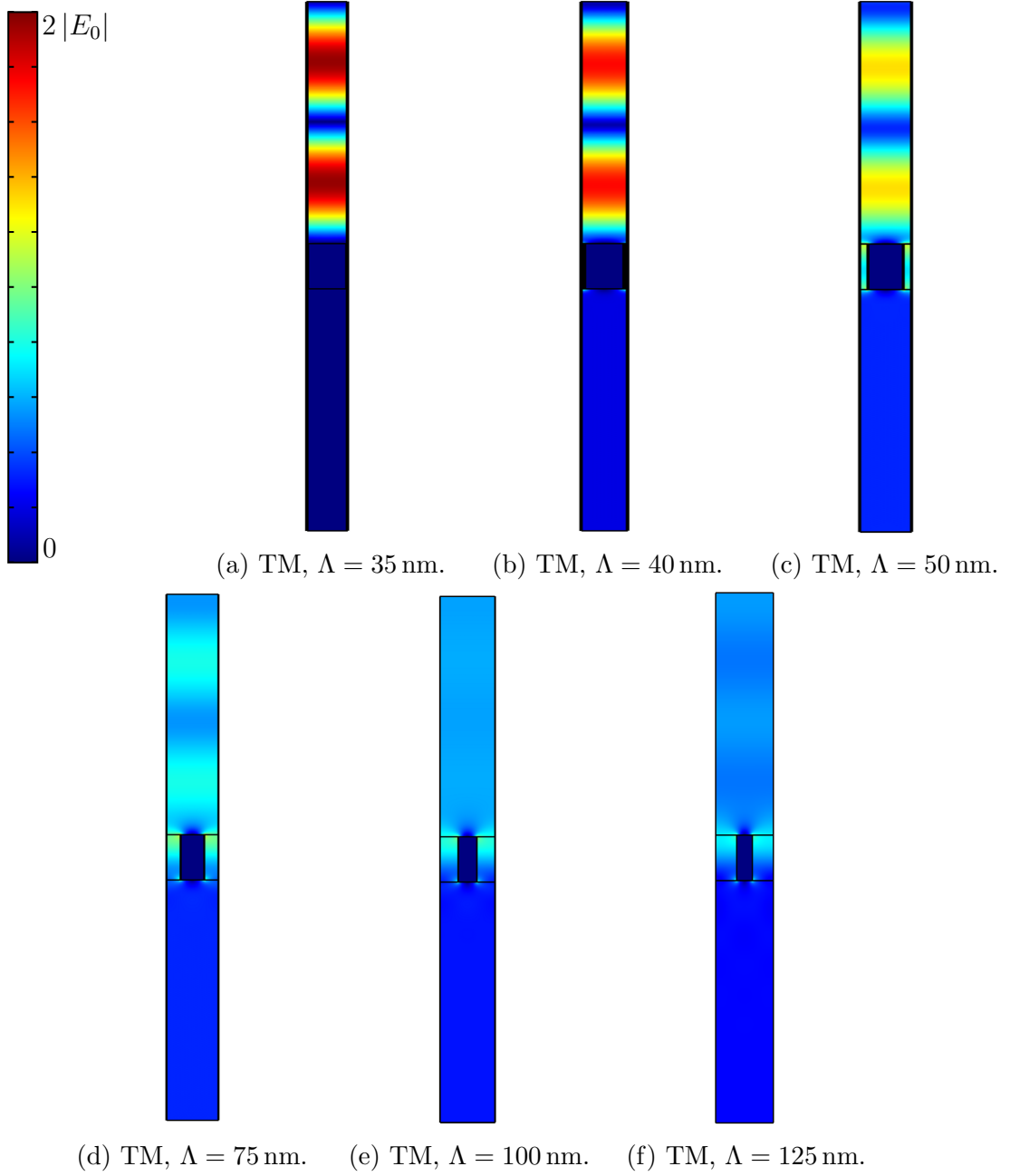


Figure 37: Distribution of the phasor norm of the TM electric field in the unit cell, for an array of PEC lines with width $w = 34$ nm, height $h = 100$ nm in pitch region 1 (Λ between 0 nm and 127 nm).

3.2.1.2 Region 2: $\Lambda \in [127, 217]$ nm

Fig. 38 (resp. 39) depict the TE (resp. TM) electric field distribution of spectral region 2, characterized by a pitch lying between 127 nm and 217 nm. They highlight the activation of the first diffraction mode in transmission for TM.

There, the TE_1 mode is still cutoff, but the first diffraction mode in transmission becomes propagating. Figs. 39a to 39d show the activation of the first diffraction order in transmission in the case of TM polarized light. The cutoff pitch is $\Lambda = 128$ nm. Right below that value, the penetration depth of the mode is larger than it was for $\Lambda = 125$ nm in Fig. 37f, and when reaching $\Lambda = 128$ nm, the mode becomes excitable and extends all the way down the substrate without any attenuation, creating interference patterns in the electric field distribution by superposition the 0^{th} order transmitted plane wave and the order ± 1 diffracted waves.

In the case of TE polarized light, this transition is not visible since barely any light is transmitted through the array due to the TE_1 mode being cutoff. However, as the pitch gets closer to 217 nm, the penetration depth of the evanescent TE_1 mode gets larger and more light reaches the substrate and is able to couple into the propagating diffraction mode, and interference patterns become slightly visible. In addition, the continuity of the electric field is observed for the TE polarization, as it must go to 0 close to the metal line to respect the continuity of the tangential electric field.

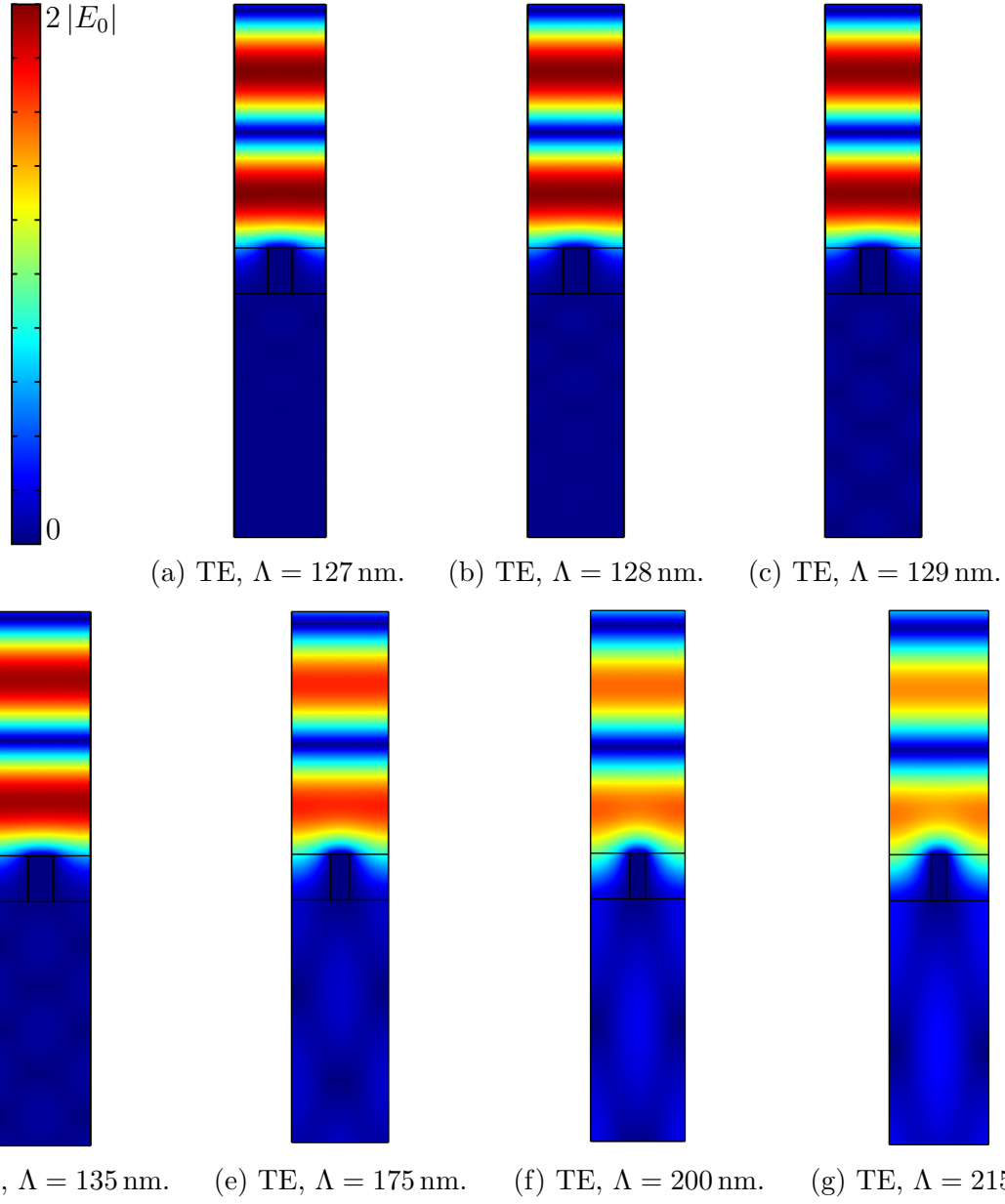


Figure 38: Distribution of the phasor norm of the TE electric field in the unit cell, for an array of PEC lines with width $w = 34$ nm, height $h = 100$ nm in pitch region 2 (Λ between 127 nm and 217 nm).

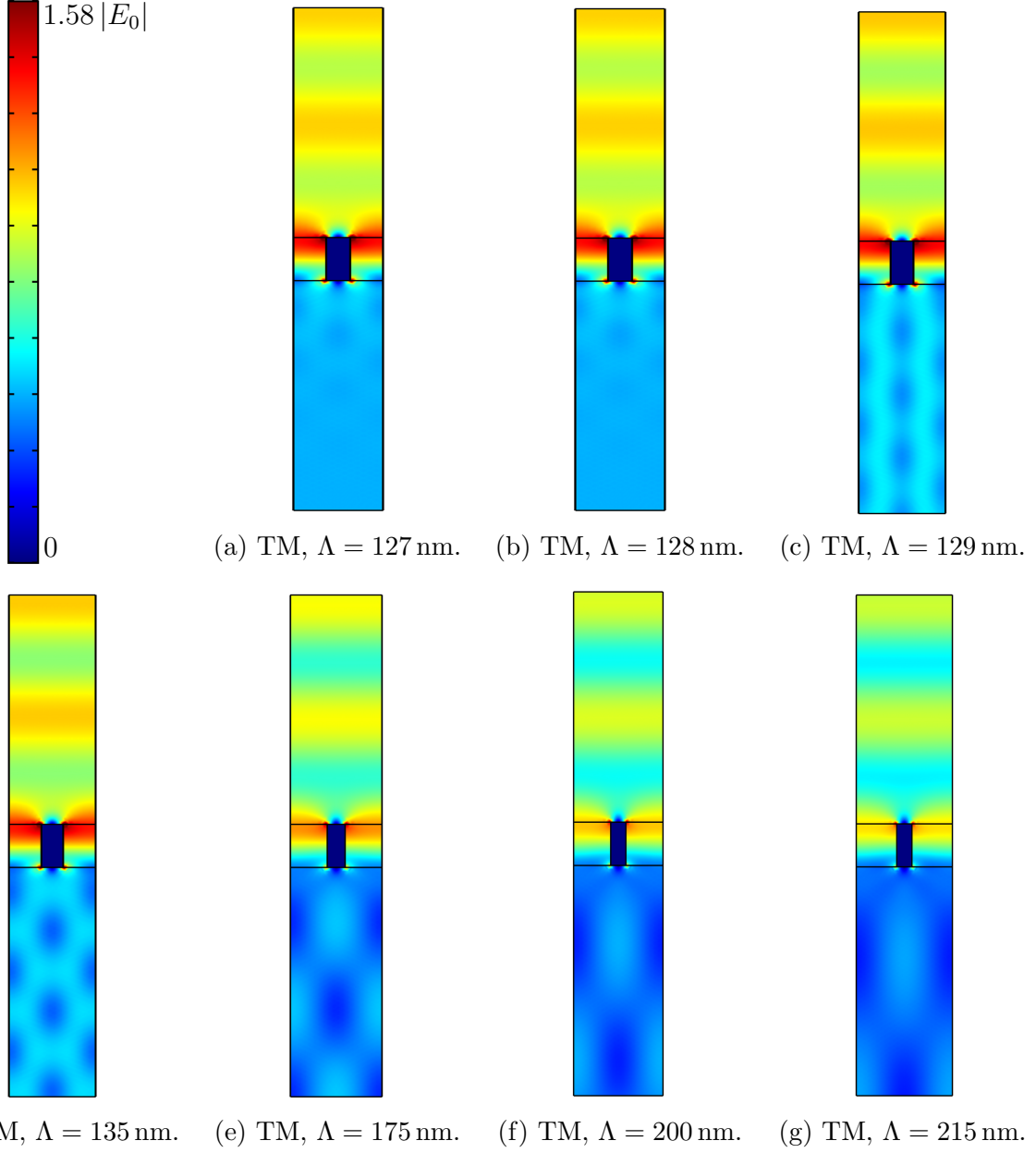


Figure 39: Distribution of the phasor norm of the TM electric field in the unit cell, for an array of PEC lines with width $w = 34$ nm, height $h = 100$ nm in pitch region 2 (Λ between 127 nm and 217 nm).

3.2.1.3 Region 3: $\Lambda \in [217, 256]$ nm

Fig. 40 (resp. 41) depict the TE (resp. TM) electric field distribution of spectral region 3, characterized by a pitch between 217 and 256 nm.

They highlight the activation of the TE_1 mode. The cutoff pitch for the TE_1 mode is $\Lambda = 217.44$ nm. For the TE polarization, a sharp transition between cutoff and propagation could be expected at that pitch. However, since the height of the PEC line is small (100 nm), the penetration depth of that mode was already larger than 100 nm while below the cutoff ($d_p = 107$ nm at $\Lambda = 210$ nm). A smooth transition is therefore observed in the reflectance spectrum and in the electric field distribution. Moreover, the wavelength of the associated mode is larger than the height and it is therefore impossible to visualize a full period over that small distance, although it is possible to visualize a very sharp transition and a full wavelength by moving to taller lines. In that case the penetration depth is always smaller than the line, so that light can only reach the substrate once the cutoff is reached, and the periodicity related to the propagation of the wave can be visualized. This shall be presented in a later section.

In the case of TM polarization, the mode is not activated at all since it is asymmetric and therefore there is no transition to be seen.

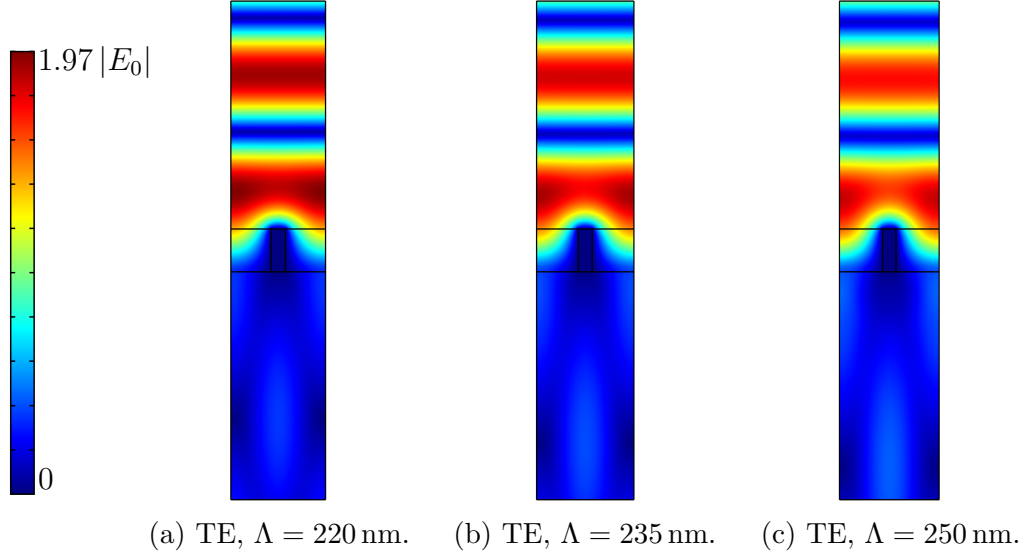


Figure 40: Distribution of the phasor norm of the TE electric field in the unit cell, for an array of PEC lines with width $w = 34$ nm, height $h = 100$ nm in pitch region 3 (Λ between 217 nm and 256 nm).

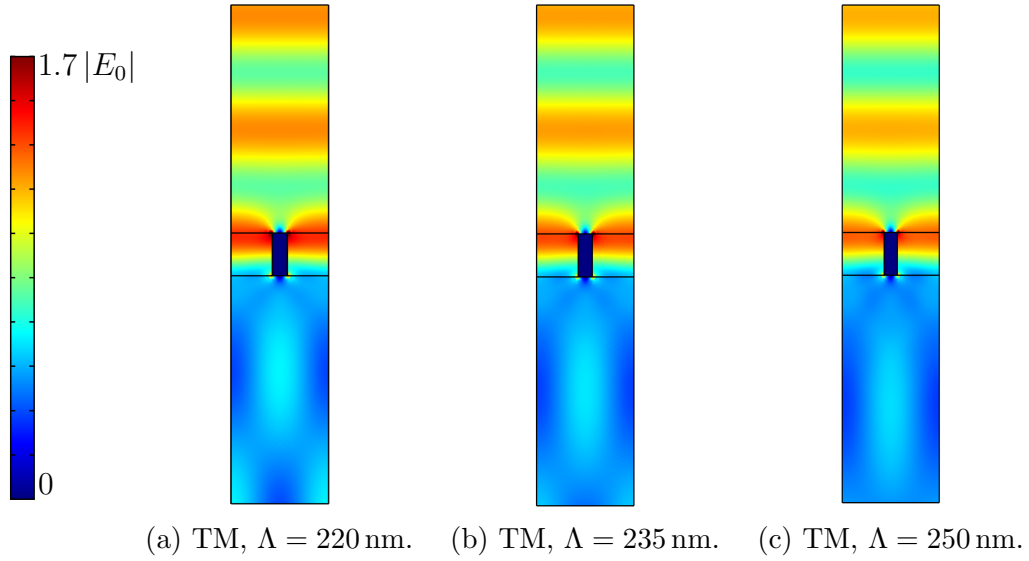


Figure 41: Distribution of the phasor norm of the TM electric field in the unit cell, for an array of PEC lines with width $w = 34$ nm, height $h = 100$ nm in pitch region 3 (Λ between 217 nm and 256 nm).

3.2.1.4 Region 4: $\Lambda \in [256, 384]$ nm

Fig. 42 (resp. 43) depict the TE (resp. TM) electric field distribution of spectral region 4, characterized by a pitch between 256 nm and 384 nm. They highlight the activation of the second order in transmission.

In this range, the second diffraction mode in transmission is activated at 256 nm. According to Fig. 30, the reflectance of the TE polarization is not affected by this mode activation. However, the reflectance in Fig. 32 exhibits a little bump at that pitch and the transition should be more visible. Let us see in Figs. 43a to 43c how the electric field distribution varies around that pitch. In the TM case, some more interference patterns appear when the transition occur, meaning that some light couples into the second order diffraction mode in transmission.

In the case of TE polarization, the electric field distribution also changes a bit although there is no effect on the transmittance. Increasing the pitch up to 380 nm leads to a decrease (resp. increase) in reflectance for TE (TM) polarization. In both cases, the electric field distribution evolves as a result of the geometry variation and not due to the activation of further modes.

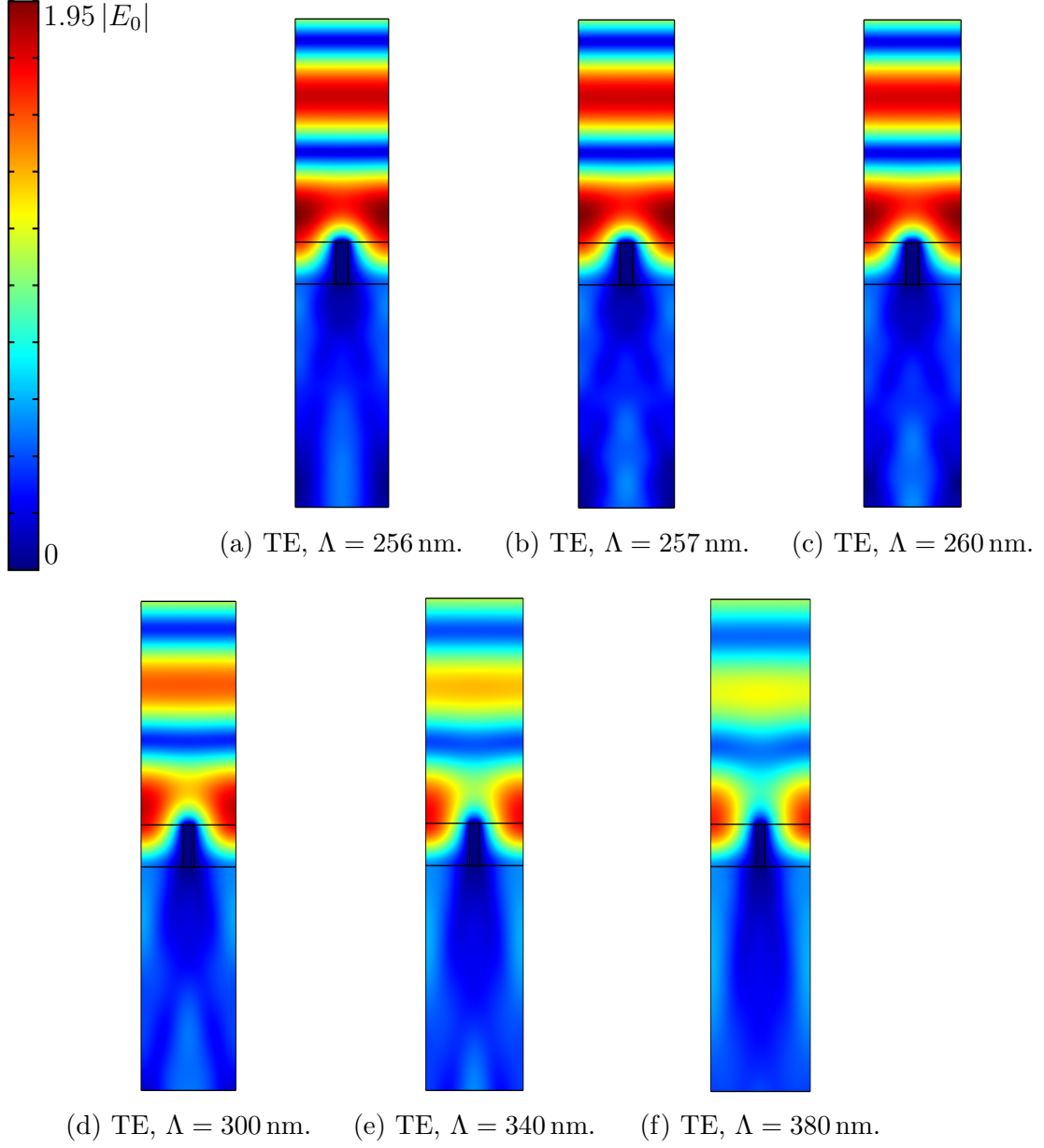


Figure 42: Distribution of the phasor norm of the TE electric field in the unit cell, for an array of PEC lines with width $w = 34$ nm, height $h = 100$ nm in pitch region 4 (Λ between 256 nm and 384 nm).

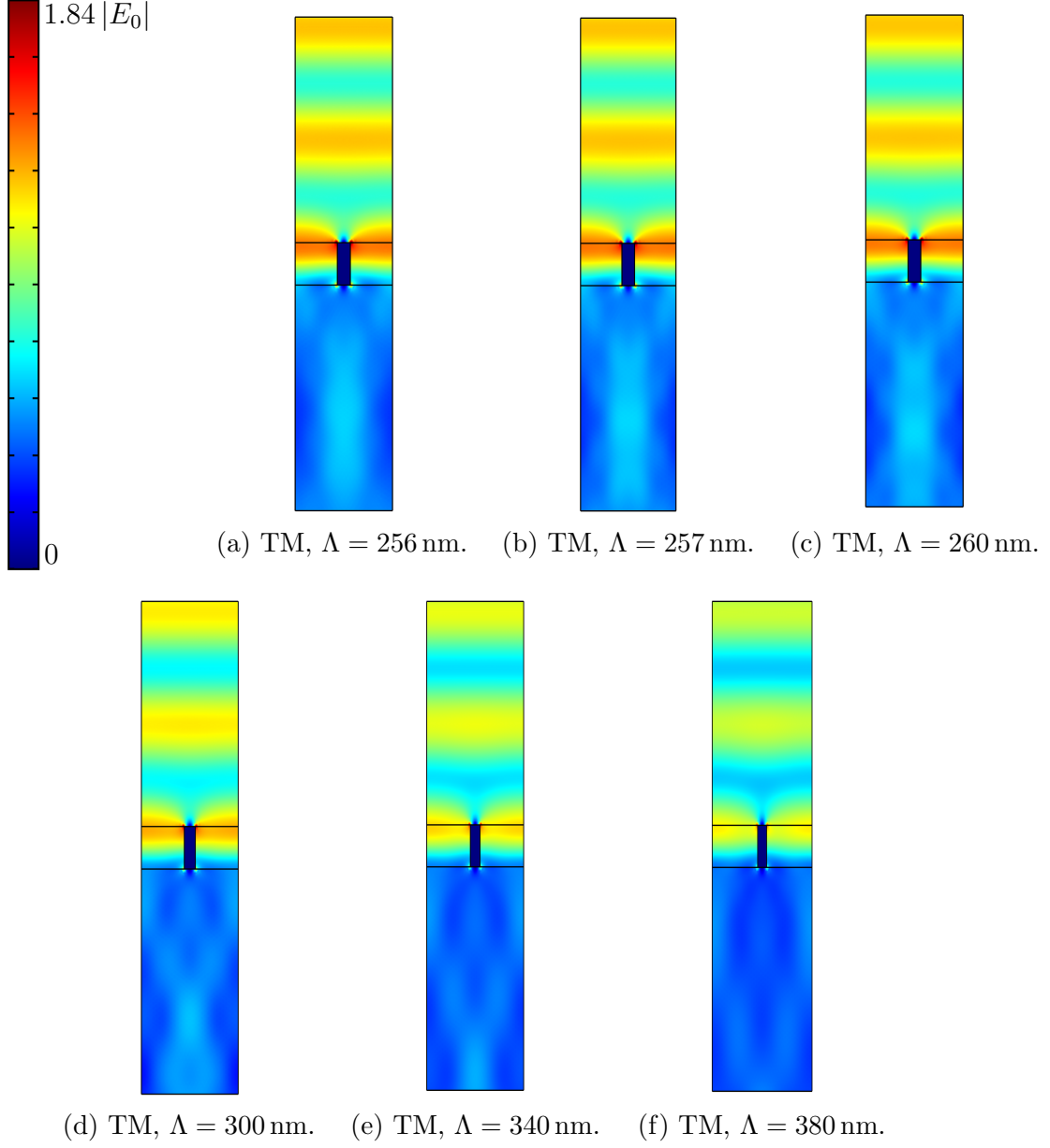


Figure 43: Distribution of the phasor norm of the TM electric field in the unit cell, for an array of PEC lines with width $w = 34$ nm, height $h = 100$ nm in pitch region 4 (Λ between 256 nm and 384 nm).

3.2.1.5 Region 5: $\Lambda \in [384, 398]$ nm

Fig. 44 (resp. 45) depict the TE (resp. TM) electric field distribution of spectral region 5, characterized by a pitch between $\Lambda = 384$ nm to $\Lambda = 398$ nm. They highlight the lack of sharp transition for the third diffraction order in transmission.

This range features the cutoff pitch of the third diffraction order in transmission at 384 nm. Due to the high order nature of this diffraction mode and the availability of the previous orders, this mode is hardly visible in the 2D maps.

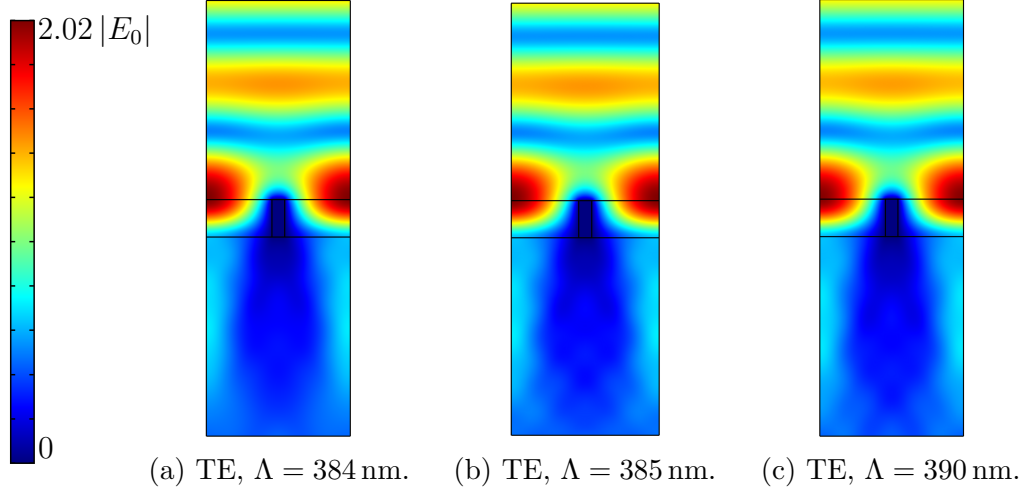


Figure 44: Distribution of the phasor norm of the TE electric field in the unit cell, for an array of PEC lines with width $w = 34$ nm, height $h = 100$ nm in pitch region 5 (Λ between 384 nm and 398 nm).

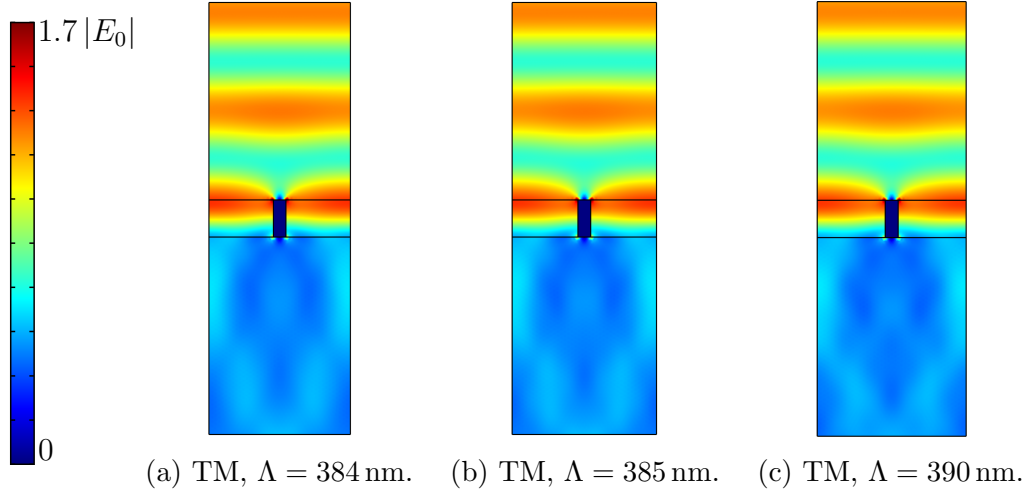


Figure 45: Distribution of the phasor norm of the TM electric field in the unit cell, for an array of PEC lines with width $w = 34$ nm, height $h = 100$ nm in pitch region 5 (Λ between 384 nm and 398 nm).

3.2.1.6 Region 6: $\Lambda \in [398, 512]$ nm

Fig. 46 (resp. 47) depict the TE (resp. TM) electric field distribution of spectral region 6, characterized by a pitch between $\Lambda = 398$ nm and $\Lambda = 512$ nm. they highlight the activation of TM_2 mode and increasing decaying length of the first diffraction order in reflection.

Let us try to visualize the activation of the TM_2 mode, for which the cutoff is $\Lambda = 398$ nm. As can be seen in Fig. 47, this transition is very subtle and is not localized at the cutoff pitch. As the pitch increases, the electric field slowly moves from an homogeneous spatial distribution to a distribution that is slightly more intense midway between the two metal lines and less intense close to the line, in accordance with the TM_2 symmetric cosine featured in Fig. 19 for $m = 2$. The reason why this transition is not sharp is because most of the light prefers to couple into the EMA mode, which has a better matching with the incoming plane wave. However, as the pitch increases and as the cutoff pitch for the first diffraction order in reflection is approached, the penetration depth of that mode increases. As a result, the electric field distribution in the air is modified and better matches the TM_2 grating mode and more light couples into that mode, so that the distribution inside the grating is modified accordingly.

This is visible in particular in the case of TE polarization, where the TE_1 mode has already a varying spatial distribution which allows a better coupling between that mode and the evanescent first diffraction order in reflection, resulting in an electric field distribution in air which is a lot more affected than in the case of TM polarized light. The next region covers the activation of the first diffraction order in reflection.

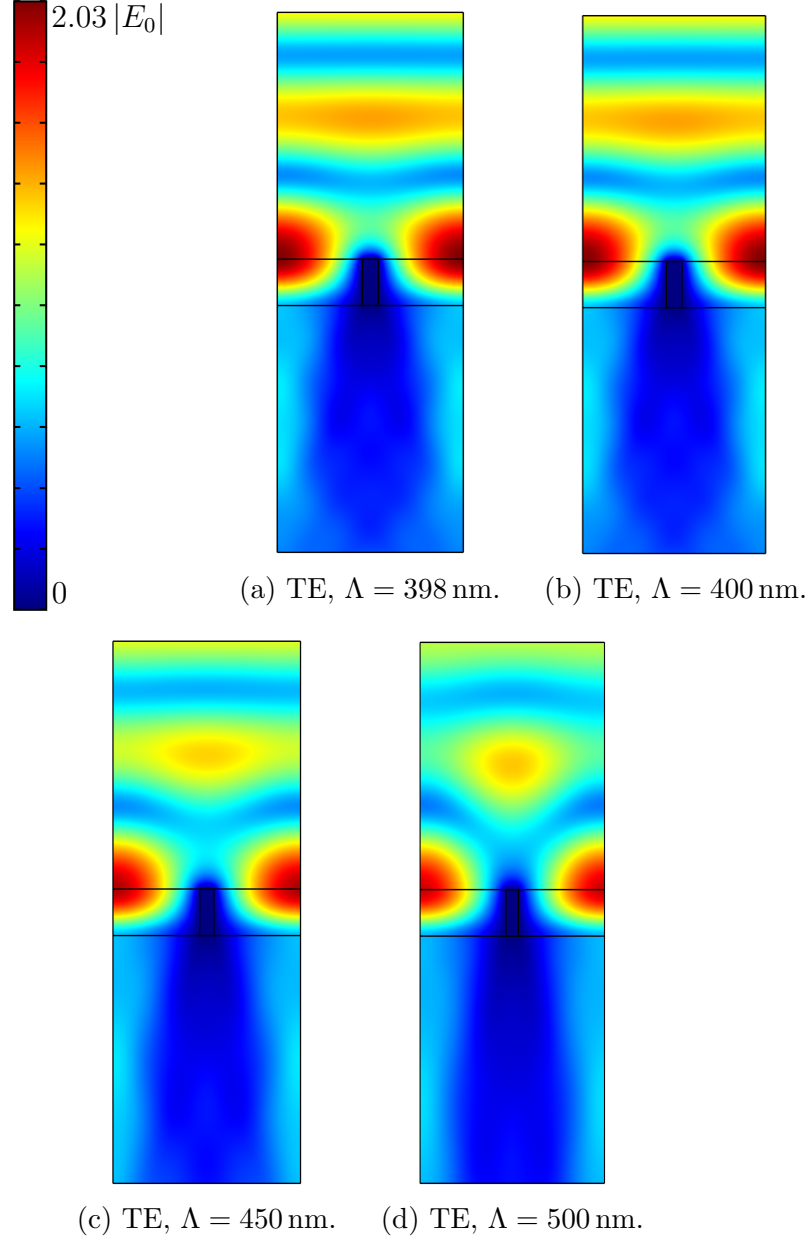


Figure 46: Distribution of the phasor norm of the TE electric field in the unit cell, for an array of PEC lines with width $w = 34$ nm, height $h = 100$ nm in pitch region 6 (Λ between 398 nm and 512 nm).

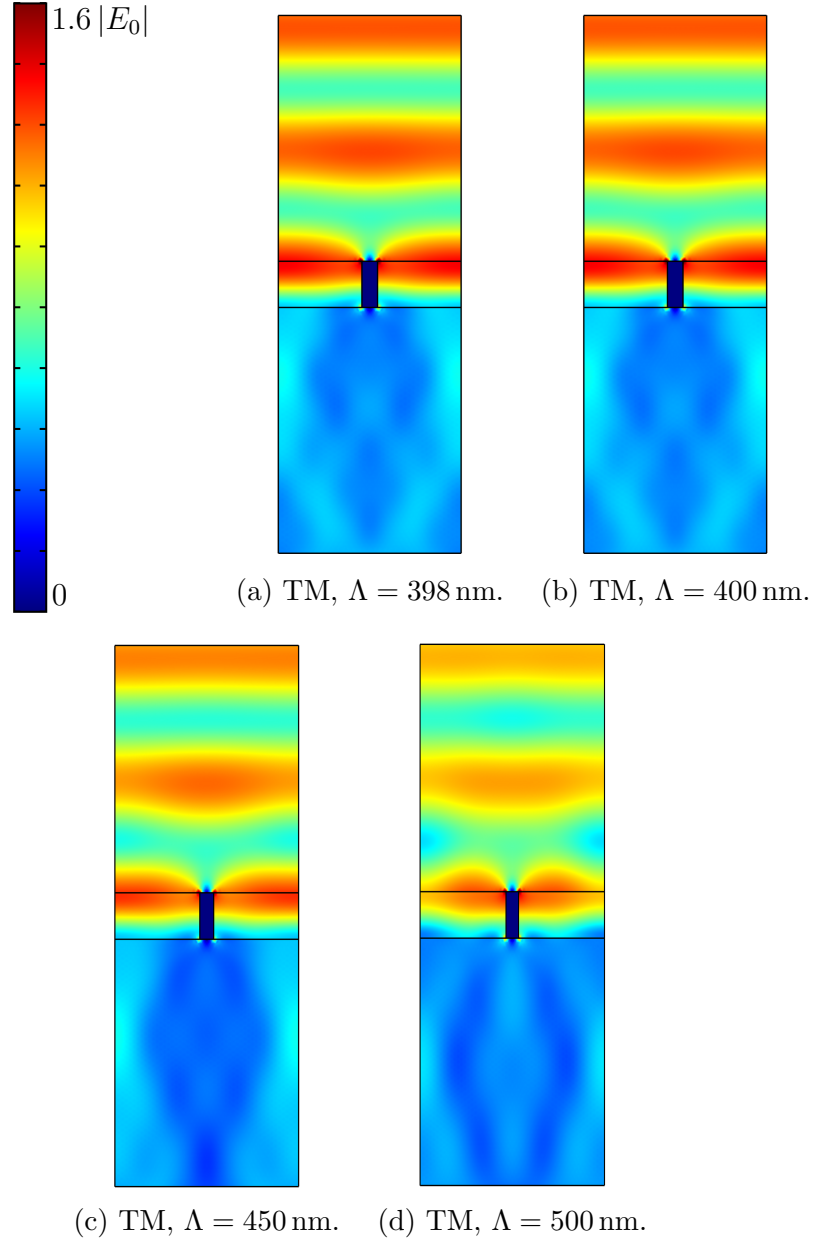


Figure 47: Distribution of the phasor norm of the TM electric field in the unit cell, for an array of PEC lines with width $w = 34$ nm, height $h = 100$ nm in pitch region 6 (Λ between 398 nm and 512 nm).

3.2.1.7 Region 7: $\Lambda \in [512, 532]$ nm

Fig. 48 (resp. 49) depict the TE (resp. TM) electric field distribution of spectral region 7, characterized by a pitch between $\Lambda = 512$ nm and $\Lambda = 532$ nm. They highlight how the fourth diffraction order in transmission is not visible and how the first diffraction order in reflection is close to being propagating.

This range features the cutoff pitches of the fourth diffraction order in transmission. Now, a sharp transition in either reflectance or electric field distribution as a result of the activation of a diffraction mode in transmission is no longer expected. Indeed, the previous order was barely excited and the higher orders will be so even less. The variation in the distribution actually comes from the first diffraction mode in reflection as its cutoff pitch is approached and the field above the grating starts to be modified by the increased decay length of the evanescent mode. The next region covers the activation of that mode.

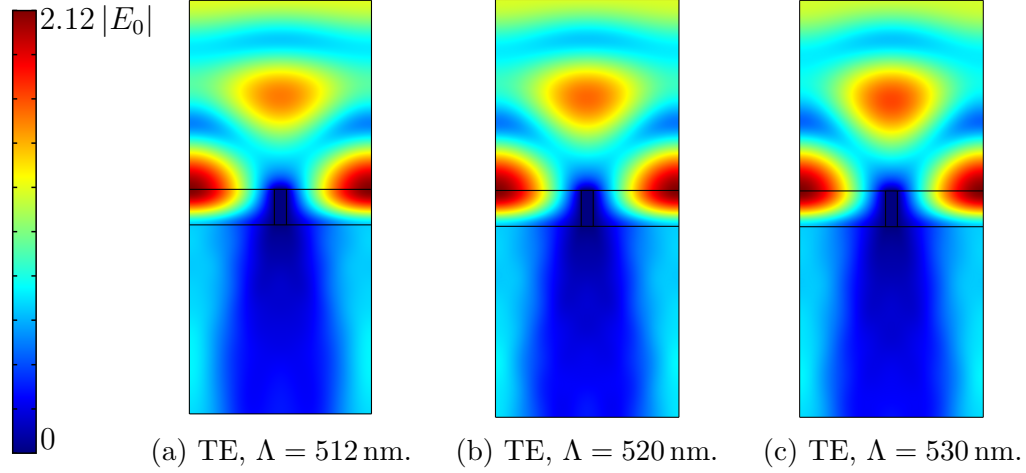


Figure 48: Distribution of the phasor norm of the TE electric field in the unit cell, for an array of PEC lines with width $w = 34$ nm, height $h = 100$ nm in pitch region 7 (Λ between 512 nm and 532 nm).

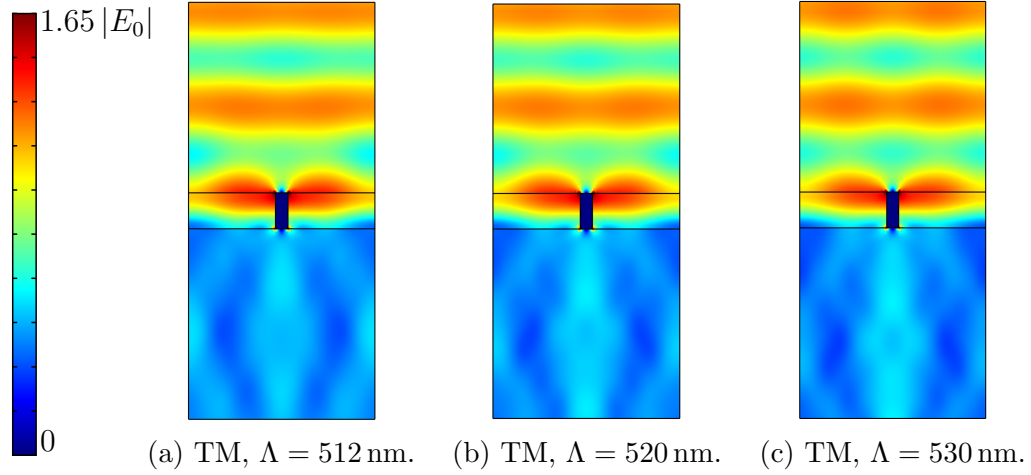


Figure 49: Distribution of the phasor norm of the TM electric field in the unit cell, for an array of PEC lines with width $w = 34$ nm, height $h = 100$ nm in pitch region 7 (Λ between 512 nm and 532 nm).

3.2.1.8 Region 8: $\Lambda \in [532, 581]$ nm

Fig. 50 (resp. 51) depict the TE (resp. TM) electric field distribution of spectral region 8, characterized by a pitch between $\Lambda = 532$ nm and $\Lambda = 581$ nm. They highlight how the first diffraction order in reflection becomes propagating.

As discussed above, close to 532 nm, the decay length of the first diffraction mode in reflection increases with the pitch. As a consequence, the electric field distribution is modified both in the air and in the grating as a result of the coupling between the associated modes. The electric field distribution in the air changes from a uniform plane wave to a non-uniform distribution as a result of interferences. However, below 532 nm, the first diffraction mode is still evanescent and only the electric field close to the array is modified. When the cutoff is reached, the mode is no longer attenuated when moving away from the grating, and the interference patterns affect the whole medium above the array. Again, this is especially visible in the case of the TE mode, as the diffraction modes in the case of TM polarization are excited a lot less efficiently due to light mostly coupling into the plane wave-like EMA mode. In accordance with those observations, the reflectance varies a lot more around a pitch of 532 nm for TE than for TM polarization.

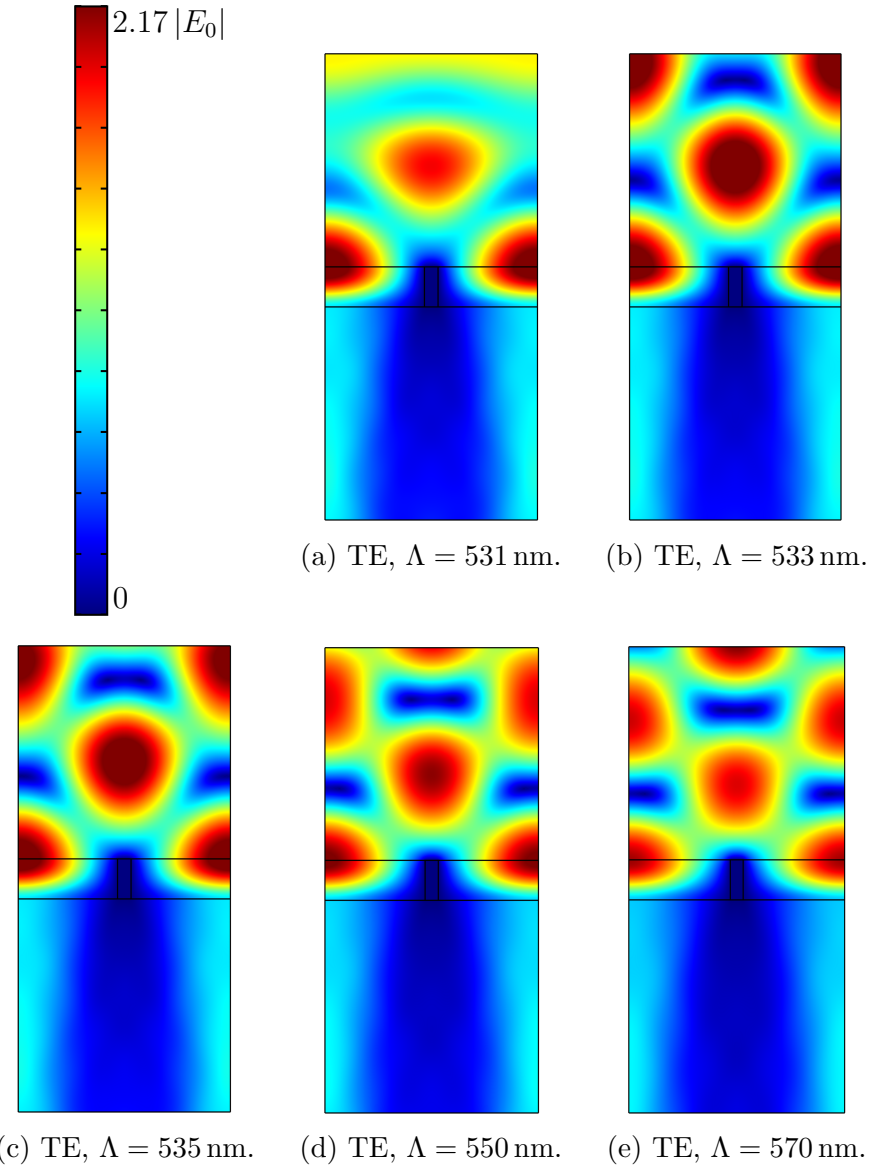
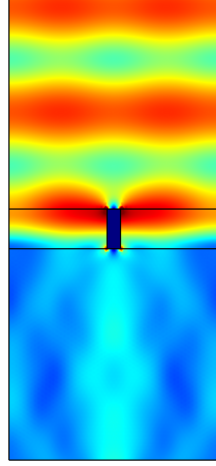
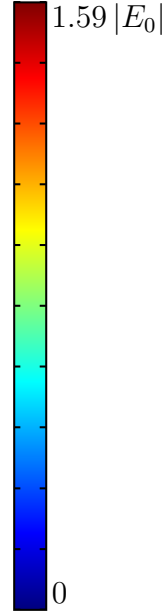
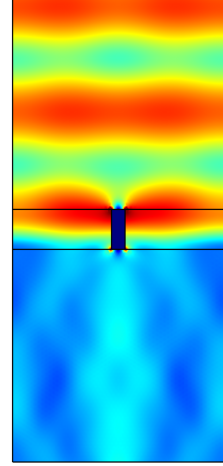


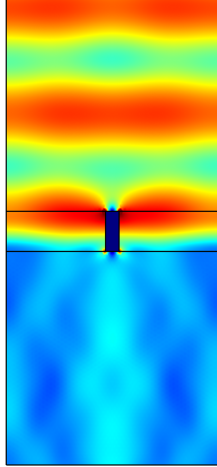
Figure 50: Distribution of the phasor norm of the TE electric field in the unit cell, for an array of PEC lines with width $w = 34$ nm, height $h = 100$ nm in pitch region 8 (Λ between 532 nm and 581 nm).



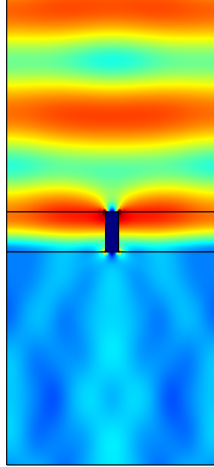
(a) TM, $\Lambda = 531$ nm.



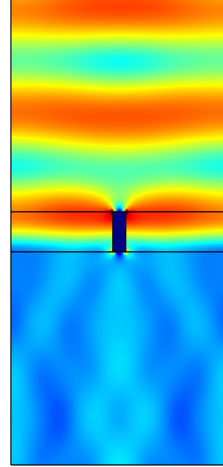
(b) TM, $\Lambda = 533$ nm.



(c) TM, $\Lambda = 535$ nm.



(d) TM, $\Lambda = 550$ nm.



(e) TM, $\Lambda = 570$ nm.

Figure 51: Distribution of the phasor norm of the TM electric field in the unit cell, for an array of PEC lines with width $w = 34$ nm, height $h = 100$ nm in pitch region 8 (Λ between 532 nm and 581 nm).

3.2.1.9 Region 9: $\Lambda \in [581, 763]$ nm

Fig. 52 (resp. 53) depict the TE (resp. TM) electric field distribution of spectral region 9, characterized by a pitch between $\Lambda = 581$ nm and $\Lambda = 763$ nm. They highlight how the TE_3 is hard to visualize.

This region features the activation of the TE_3 mode at 581 nm. It is again hard to visualize a sharp transition as the penetration depth of the mode is already a larger than the height of the array while below 581 nm ($d_p = 141$ nm at $\Lambda = 570$ nm) and the wavelength of the associated mode is larger than the height of the grating. Furthermore, this mode may not be efficiently excited due to it being higher order. Its appearance shall be better visualized when considering a larger height in the next section.

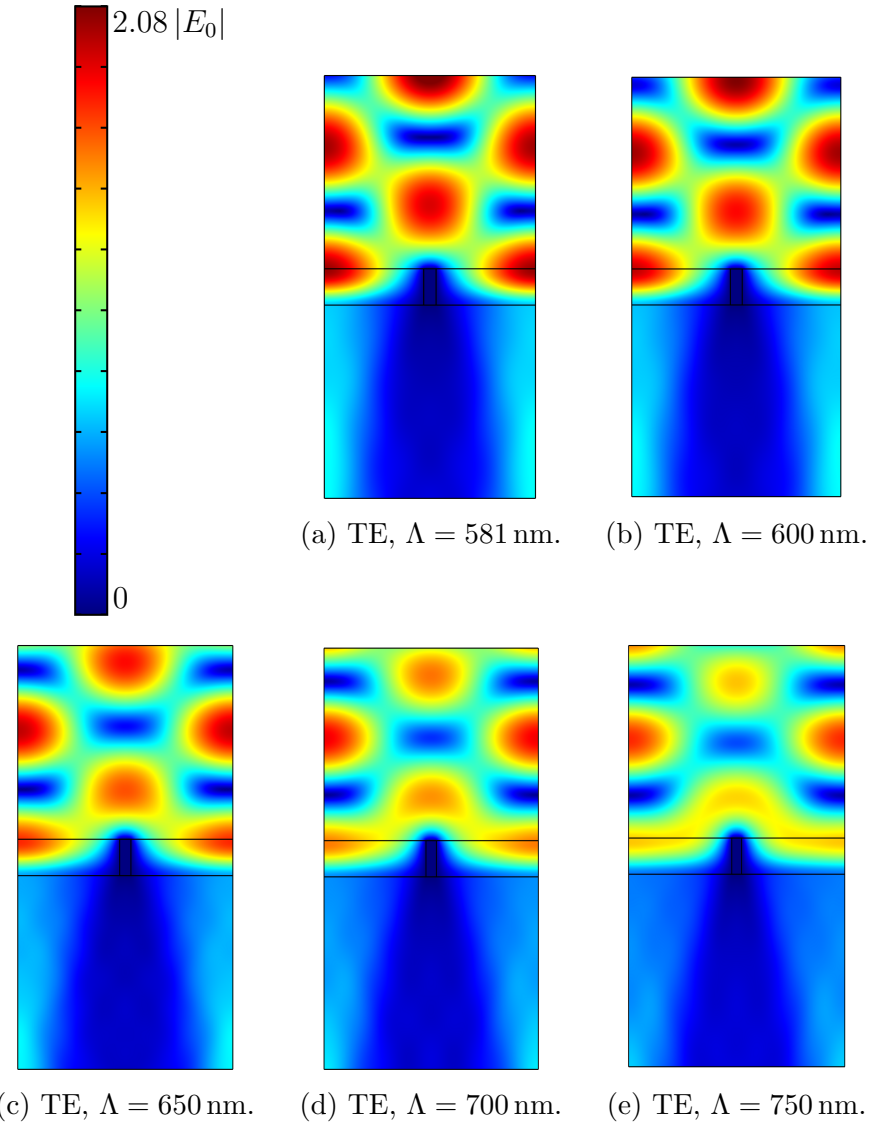


Figure 52: Distribution of the phasor norm of the TE electric field in the unit cell, for an array of PEC lines with width $w = 34$ nm, height $h = 100$ nm in pitch region 9 (Λ between 581 nm and 763 nm).

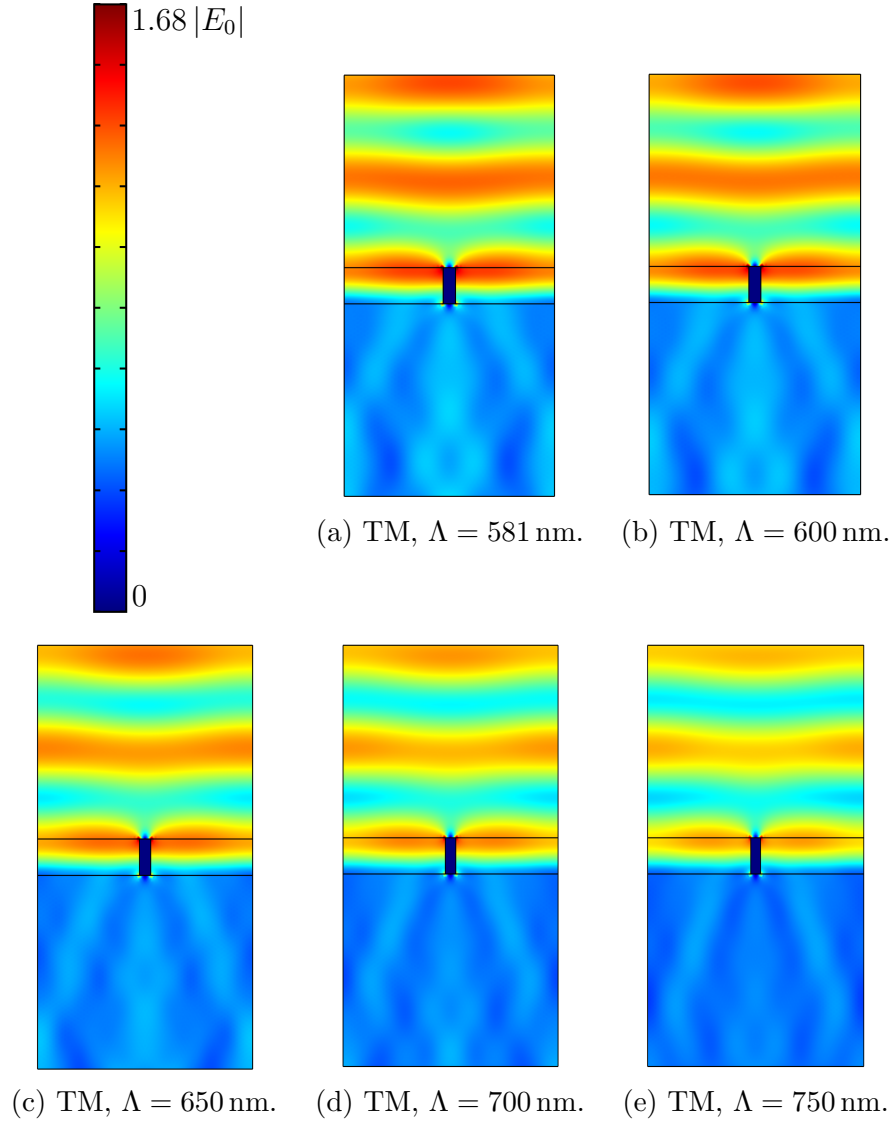


Figure 53: Distribution of the phasor norm of the TM electric field in the unit cell, for an array of PEC lines with width $w = 34$ nm, height $h = 100$ nm in pitch region 9 (Λ between 581 nm and 763 nm).

3.2.1.10 Region 10 and 11: $\Lambda \in [763, 1000]$ nm

Fig. 54 (resp. 55) depict the TE (resp. TM) electric field distribution of spectral region 10, characterized by a pitch between $\Lambda = 763$ nm and $\Lambda = 946$ nm while Fig. 56 (resp. 57/) depict the TE (resp. TM) electric field distribution of spectral region 11, characterized by a pitch between $\Lambda = 946$ nm and $\Lambda = 1000$ nm. They highlight how the TM_4 and TE_5 modes are hard to visualize.

These ranges feature the TM_4 and TE_5 cutoffs at 763 nm and 946 nm. Yet again, in both cases, the activation of the mode is hard to visualize with such a small height. Moreover, those are higher order modes and might not be efficiently excited. It might also become hard to distinguish if the electric field distribution is modified through a change in geometry or solely due to the activation of an additional mode. Here, the geometry might play a greater role since most of the light is already coupled into the lower order modes.

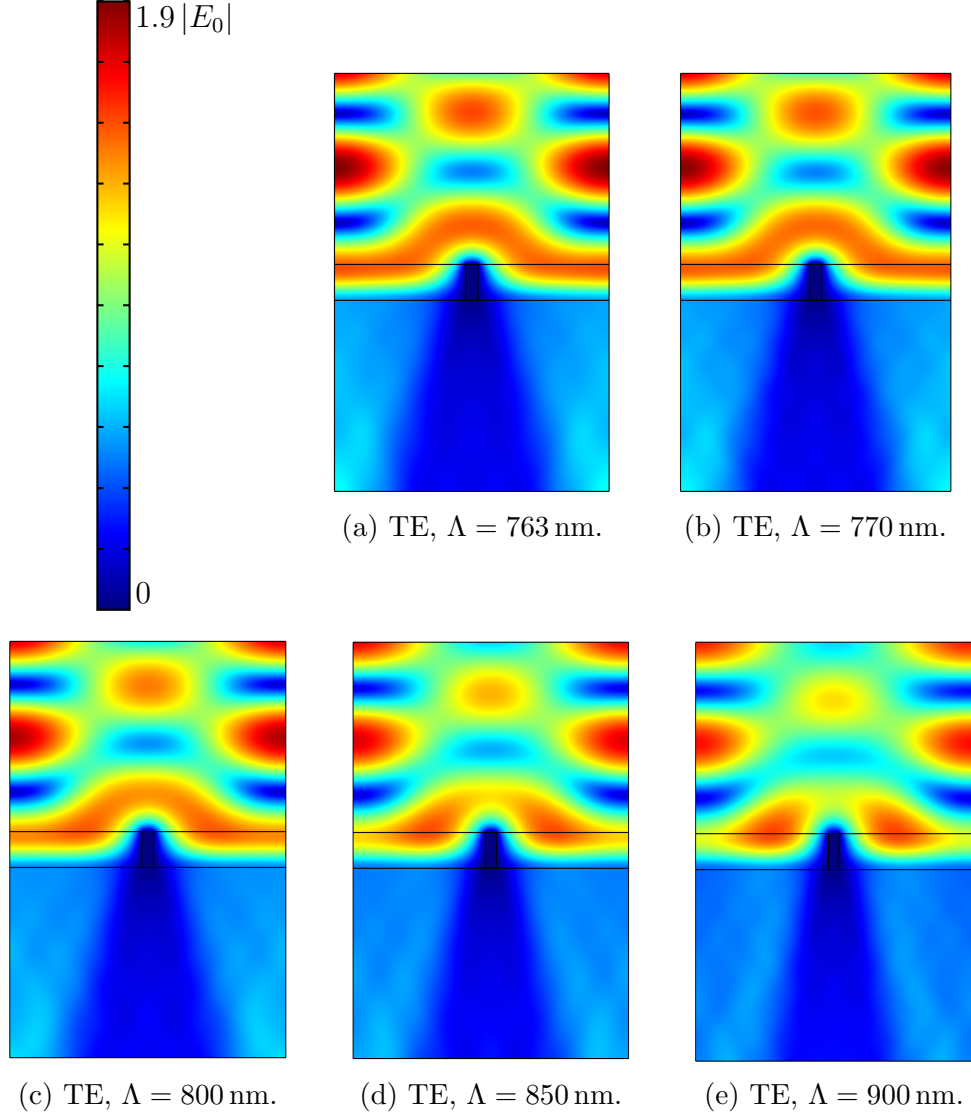


Figure 54: Distribution of the phasor norm of the TE electric field in the unit cell, for an array of PEC lines with width $w = 34$ nm, height $h = 100$ nm in pitch region 10 (Λ between 763 nm and 946 nm).

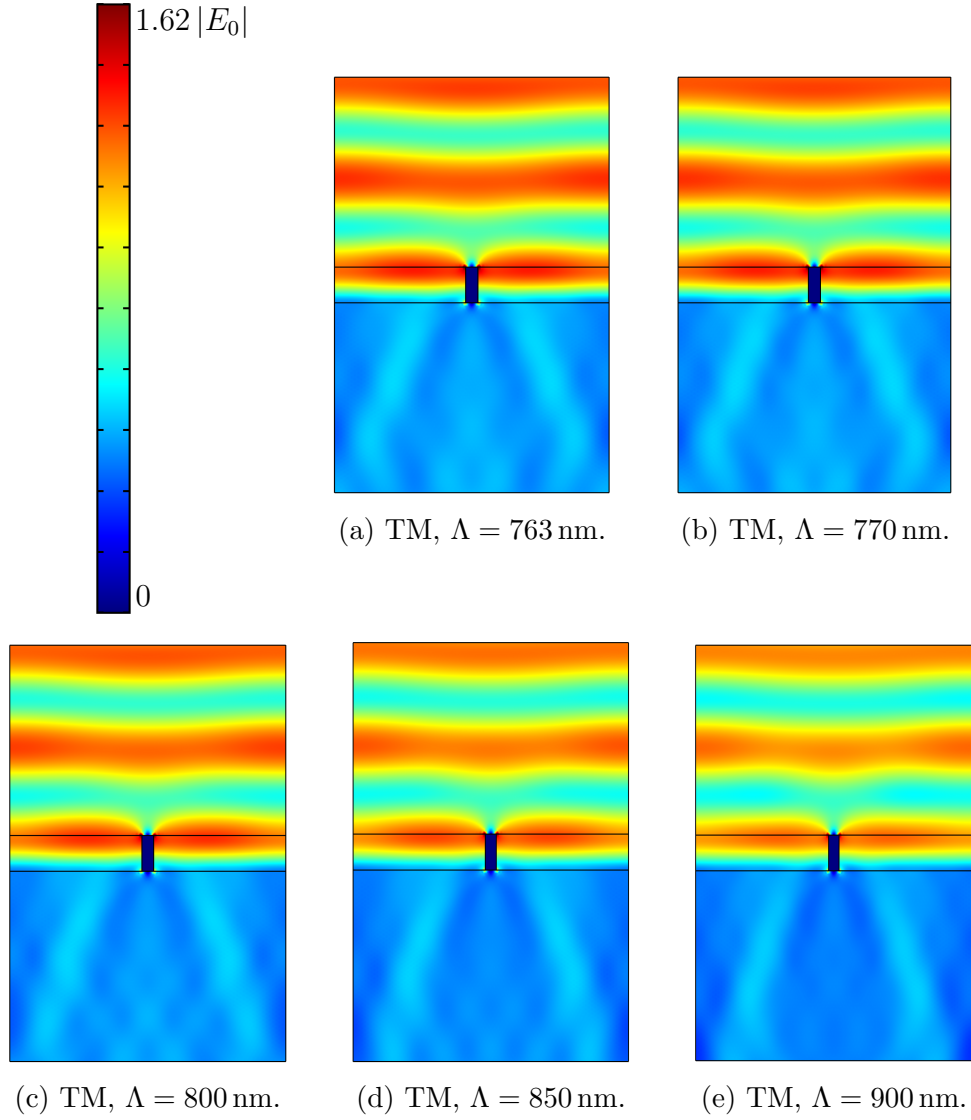


Figure 55: Distribution of the phasor norm of the TM electric field in the unit cell, for an array of PEC lines with width $w = 34$ nm, height $h = 100$ nm in pitch region 10 (Λ between 763 nm and 946 nm).

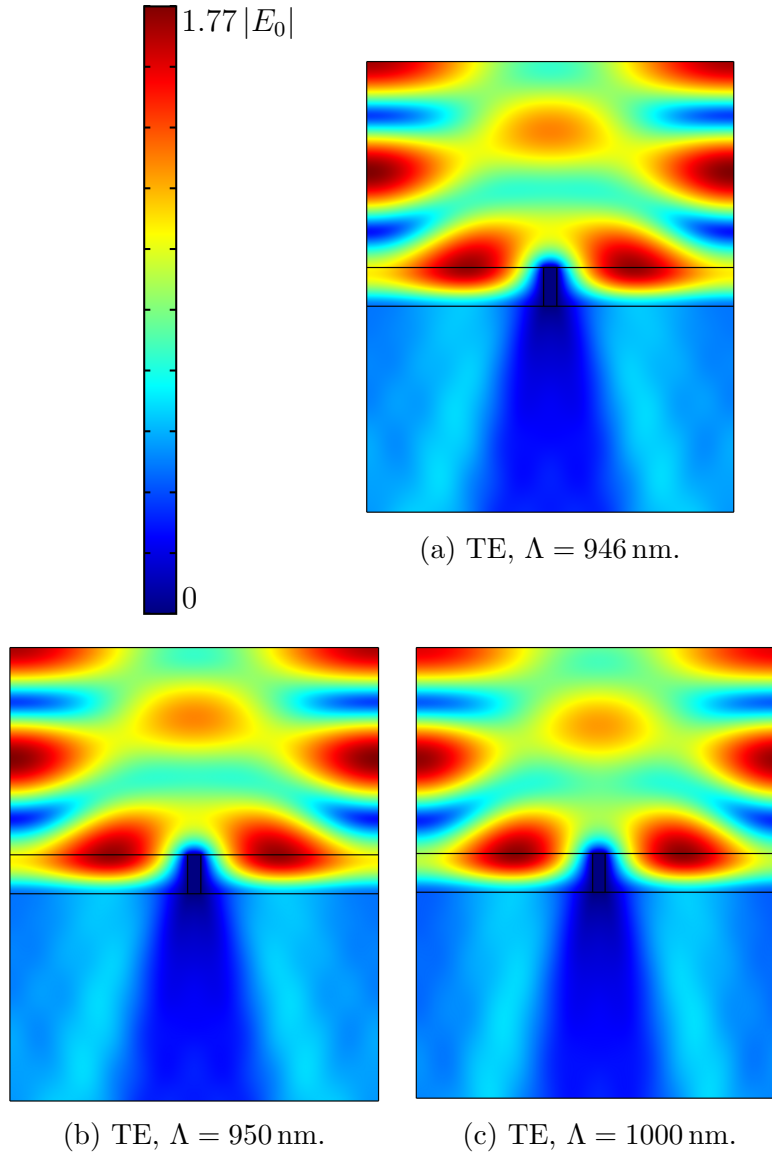


Figure 56: Distribution of the phasor norm of the TE electric field in the unit cell, for an array of PEC lines with width $w = 34$ nm, height $h = 100$ nm in pitch region 11 (Λ between 946 nm and 1000 nm).

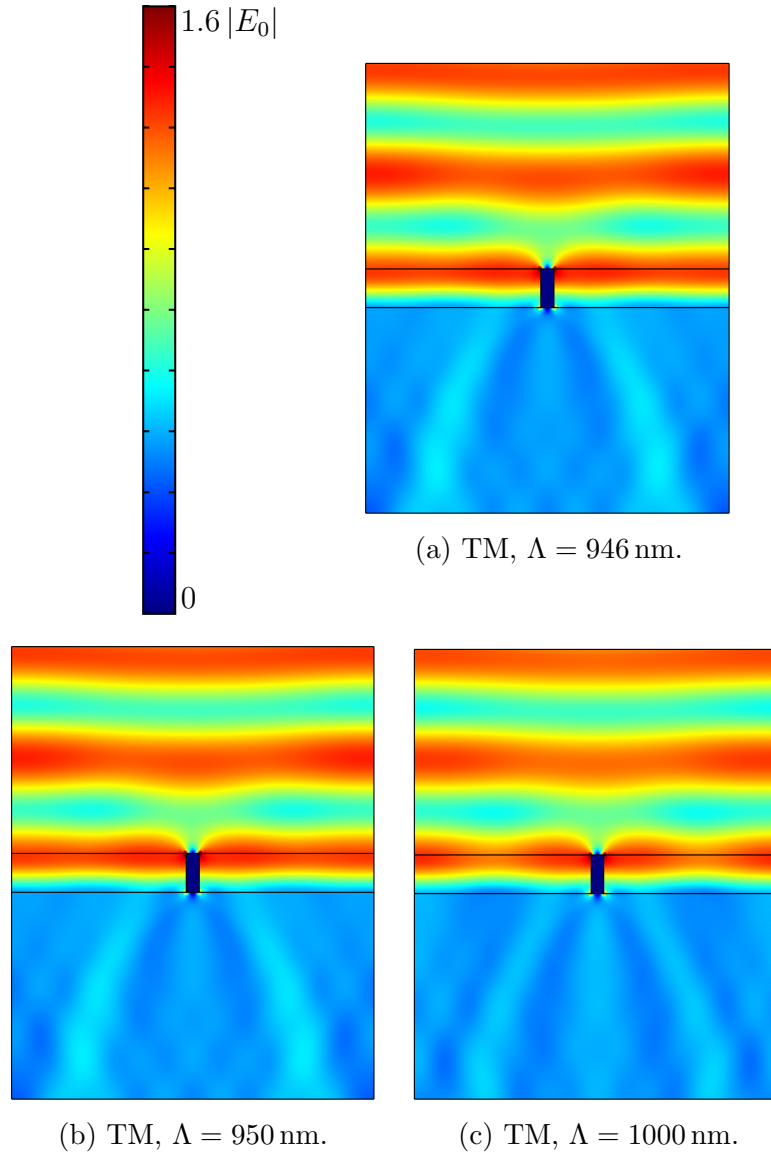


Figure 57: Distribution of the phasor norm of the TM electric field in the unit cell, for an array of PEC lines with width $w = 34$ nm, height $h = 100$ nm in pitch region 11 (Λ between 946 nm and 1000 nm).

The main features that were observed for each spectral region are summarized succinctly in Table 2.

Region	Highlight
1	Cutoff for TE, transmission for TM
2	Activation of first diffraction order in transmission
3	Activation of TE_1
4	Activation of second diffraction order in transmission
5	Third diffraction order mode in transmission hard to visualize
6	Activation of TM_2 , increasing decaying length for first diffraction mode in reflection
7	Fourth diffraction order mode in transmission hard to visualize, first diffraction mode in reflection close to propagation
8	First diffraction mode in reflection becomes propagating
9	TE_3 hard to visualize
10	TM_4 hard to visualize
11	TE_5 hard to visualize

Table 2: Key features presented in each spectral region for Figs. 36 to 57.

The 2D maps allowed the visualization of light propagation through the array by analyzing the electric field distribution in the unit cell. It was possible to visualize the activation of the different modes according to which light is reflected and transmitted. The activation of these modes is a direct consequence of the variation of geometry, i.e., changing the periodicity of the array. Another parameter of interest is the width of the array, which is discussed in the next section.

3.2.2 Effect of width

The relevant scale for the width (or critical dimension cd) of a line in the semiconductor industry is typically of the order of tens of nanometers. Since this is a theoretical study, a larger range can be covered. Fig. 58 (resp. 59) represents the reflectance spectrum of the array for several pitches between 100 nm and 1000 nm, for a height $h = 100$ nm, as a function of the fill factor, for TE (resp. TM) polarized light.

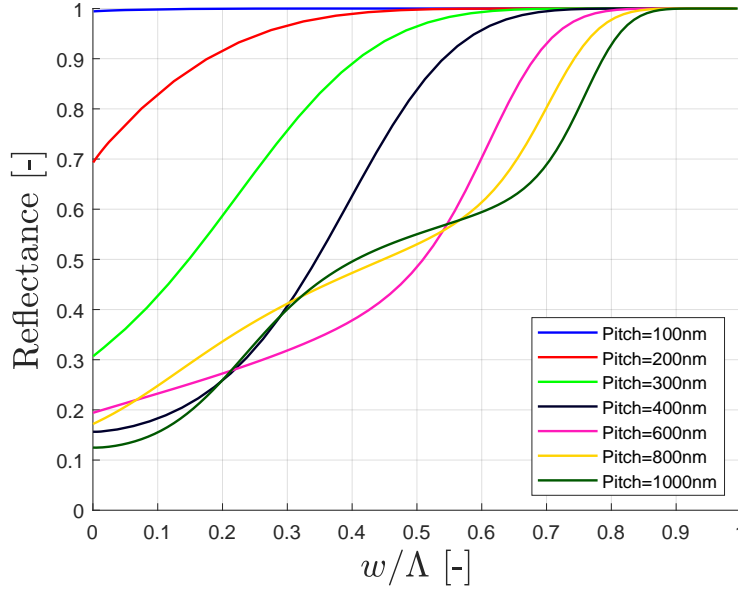


Figure 58: Reflectance spectrum of a normally incident TE polarized plane wave interacting with an array of PEC lines for several pitches for a height $h = 100$ nm, as a function of the fill factor w/Λ . The spectrum is calculated using FEM.

As expected, for the TE polarization the reflectance is at a minimum when the width is at a minimum too. Here, the minimum value for the width is 0.1, such that there is always a metallic line and the waveguide and diffraction modes always exist. The reflectance for an oxide slab (i.e. when the width is 0 and there is no reflective PEC line at all) is $R = 0.112$. As the width increases, the reflectance increases up to 1 as the PEC starts filling up most of the unit cell. The reflectance reaches 1 before the PEC completely fills the unit cell as the separation distance between two PEC interface becomes smaller than the cutoff distance for the TE_1 mode, i.e. $\Lambda - w < 217$ nm. A shift of this cutoff is observed in Fig. (58) as the pitch is modified. In addition, for lower pitch values, the increase in reflectance is very smooth, while for increasing values of the pitch, some oscillations become visible in the reflectance spectrum. Both the diffraction modes and the thin-film interferences may contribute to these. The former become available as the pitch increases, while the latter is induced by the effect of width on the effective refractive index through Eq. 102. These modes are available for a given pitch, and remain propagating as the width is modified. As the electric field distribution is modified at the interfaces between different media, the matching between the modes is modified too and the diffraction modes can be more or less excited as result, causing

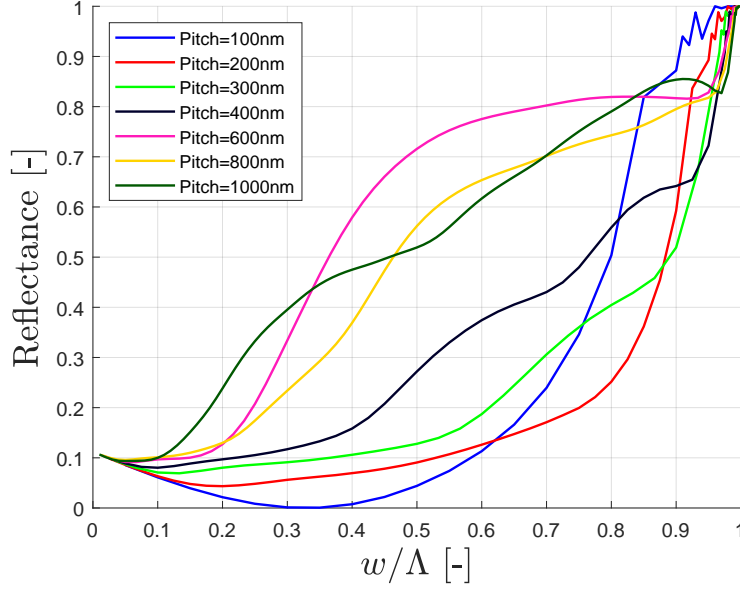


Figure 59: Reflectance spectrum of a normally incident TM polarized plane wave interacting with an array of PEC lines for several pitches for a height $h = 100$ nm, as a function of the fill factor w/Λ .

the oscillations that are observed in the spectrum.

For the TM polarization, all curves converge to the same reflectance $R = 0.112$ when $w = 0$. In addition, they all converge together above $w/\Lambda = 0.9$ and meet at $R = 1$ when $w = \Lambda$. The reflectance seems to be swapped vertically from the TE spectrum: indeed, it is now at the lowest pitch that the reflectance is minimum, which then decreases with increasing pitch. The curve for 100 nm is non-monotonic as a result of thin-film interferences and features the minimum observed in the previous section and which was linked to extraordinary optical transmission (EOT). It is interesting to notice that to achieve the lowest possible reflectance, one should rather consider small pitches than large ones.

For both TE or TM polarization, varying the width has an effect on the reflectance opposite to varying the pitch, since the dispersion relation featured in Eq.102 depends on the difference between Λ and w . Just as the pitch, the width dictates which modes are propagating or evanescent. The big difference lies in the fact that the width only impacts the grating modes and not the diffraction modes, which only depend on the periodicity of the array, i.e. the pitch.

This is illustrated in Figs. 60 and 61. There the first diffraction order is always available regardless of the width. For the TM reflectance, the diffraction is finite as soon as the width is different than 0 nm or 1000 nm. Indeed, at $w = 0$, there is no line at all and therefore no periodicity in the structure, and so no diffraction can occur. At $w = 1000$ width, the PEC takes the whole unit cell and so the medium is homogeneous, which means no diffraction can take place either. In both cases, several diffraction orders in transmission are available.

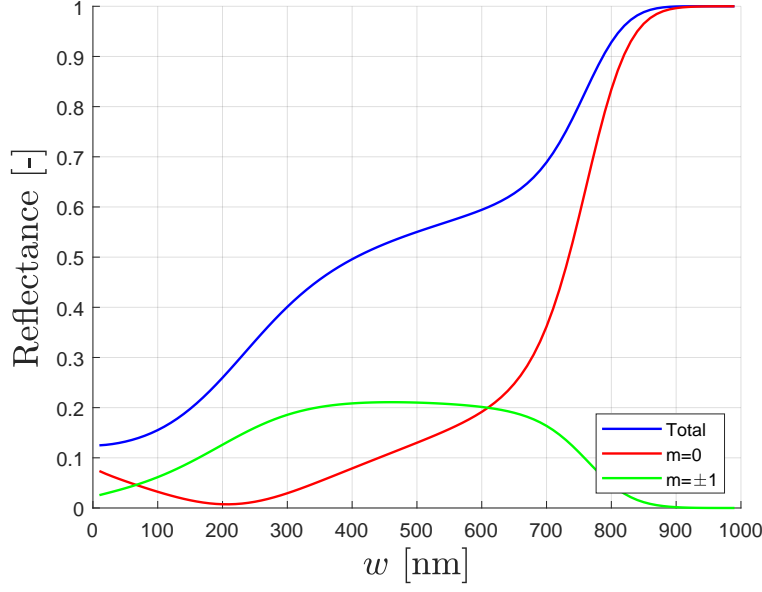


Figure 60: Reflectance spectrum of a normally incident TE polarized plane wave interacting with an array of PEC lines for a pitch $\Lambda = 1000$ nm, for a height $h = 100$ nm, as a function of the width w . The plot features the different diffraction orders. The spectrum is calculated using FEM.

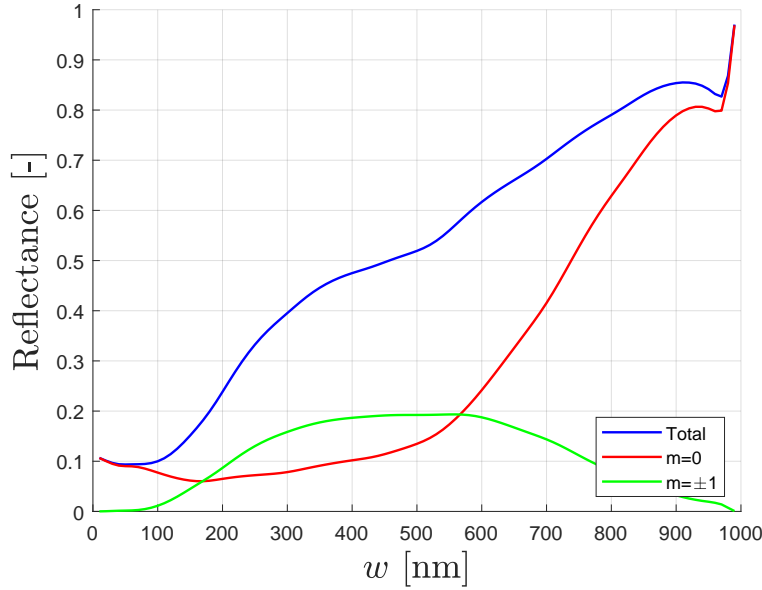


Figure 61: Reflectance spectrum of a normally incident TM polarized plane wave interacting with an array of PEC lines for a pitch $\Lambda = 1000$ nm, for a height $h = 100$ nm, as a function of the width w . The plot features the different diffraction orders. The spectrum is calculated using FEM.

For both reflection and transmission modes, the efficiency of the excitation is modulated by the matching of the electric field at the interfaces, which varies as a function of the width. However, the availability of the diffraction modes is not a function of the width. The lack of effect of width on the diffraction orders activation can be further highlighted by considering an array with a pitch of 400 nm, for which the diffraction in reflection is evanescent, although the three first modes in transmission are still available. These spectra are depicted in Figs. 62 (resp. 63) for TE (resp. TM) polarization.

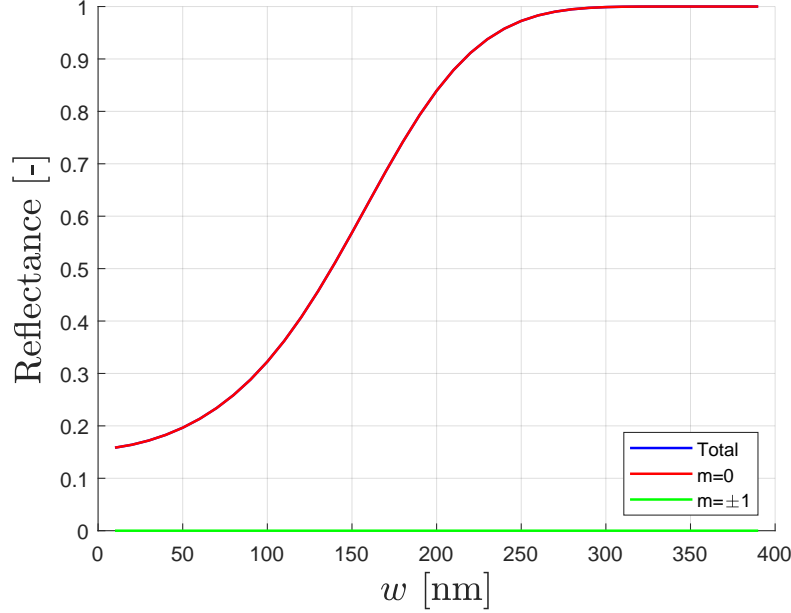


Figure 62: Reflectance spectrum of a normally incident TE polarized plane wave interacting with an array of PEC lines with pitch $\Lambda = 400$ nm and height $h = 100$ nm, as a function of the width w . The plot features the different diffraction orders. The spectrum is calculated using FEM.

At 400 nm pitch, the reflectance spectra show that the power is entirely located into the 0^{th} order mode. For the TE polarization, the spectrum is a lot more simple, as the reflectance simply decreases smoothly with the width. The TM spectrum features some oscillations as the diffraction orders in transmission are more excited than in the case of TE polarization.

In conclusion, globally the width has an effect similar and opposite to that of the pitch, minus the impact on the diffraction orders dispersion relation: as the width increases, so does the reflectance, and the width also dictates which grating modes are available through the separation distance $\Lambda - w$ present in their dispersion relation. However, for a same value of this separation distance, different values of the fill factor w/Λ are possible, which can also yield different reflectance values. Finally, the electric field distribution is also different and therefore, the diffraction modes are excited differently than as a function of the pitch.

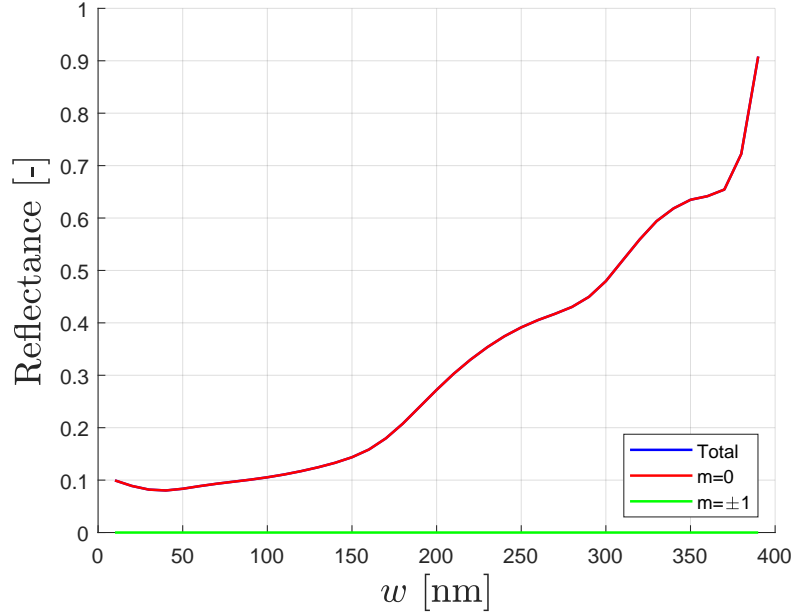


Figure 63: Reflectance spectrum of a normally incident TM polarized plane wave interacting with an array of PEC lines with pitch $\Lambda = 400$ nm and height $h = 100$ nm, as a function of the width w . The plot features the different diffraction orders. The spectrum is calculated using FEM.

3.2.3 Effect of height

In this section, an array similar to the one simulated previously is considered, but this time featuring fins of height $h = 500$ nm instead of 100 nm. The reflectance and transmittance spectra of both TE and TM polarized light are analyzed and compared to the 100 nm case.

Fig. 64 and 65 (resp. 66 and 67) shows the reflectance and transmittance spectrum of an array of PEC 500 nm tall lines under TE (resp. TM) illumination.

By comparing with Fig. 30, one can see the drastic change of spectrum that occur when moving from small fins to taller ones. The first observation is that the light is entirely reflected while below the cutoff pitch for the TE₁ mode. The wave inside the grating is therefore perfectly attenuated. At 217 nm however, the mode suddenly becomes propagating and the reflectance drops very sharply. This was expected, however, one can also notice some very sharp oscillations too when reaching the cutoff. The oscillations are characteristics of thin-film interferences, but here instead of varying the height, it is the effective refractive index that increases from 0 as the pitch increases above the cutoff, while maintaining the height fixed. There are two reason why such sharp peaks are observed: first the effective refractive ratio evolves very quickly when it becomes real, i.e. right after the cutoff pitch, and second, it starts off very small since it is 0 at cutoff and it appears at the denominator of Eq.(72). As a consequence, the conditions for maxima or minima resulting from thin-film interferences are scanned over extremely quickly as the pitch increases, yielding peaks in the

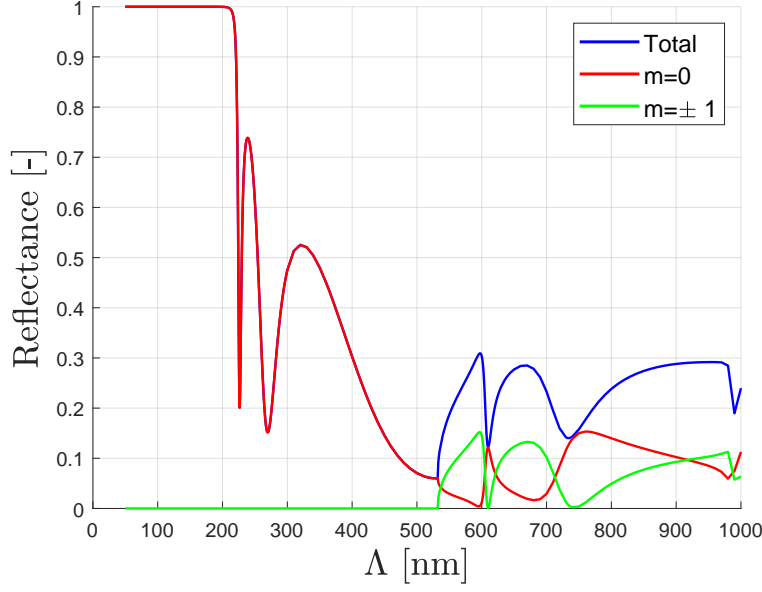


Figure 64: Reflectance spectrum of a normally incident TE polarized plane wave interacting with an array of PEC lines with width $w = 34$ nm and height $h = 500$ nm, as a function of the pitch Λ . The plot features the different diffraction orders. The spectrum is calculated using FEM.

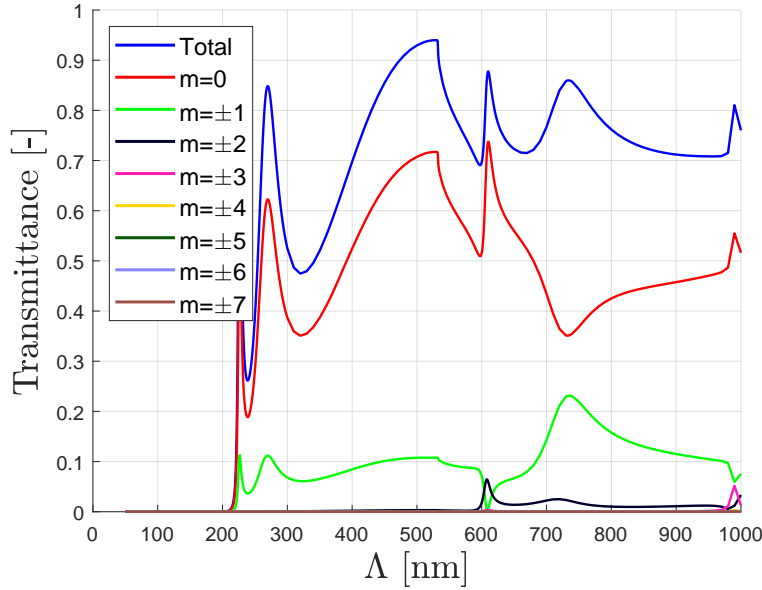


Figure 65: Transmittance spectrum of a normally incident TE polarized plane wave interacting with an array of PEC lines with width $w = 34$ nm and height $h = 500$ nm, as a function of the pitch Λ . The plot features the different diffraction orders. The spectrum is calculated using FEM.

spectrum that are very close together. Such oscillations are therefore visible as a mode gets activated. In Fig. 64, one can clearly see that it happens for the TE_1 and first diffraction mode in reflection at 217 nm and 532 nm respectively. It is less obvious for the TE_3 mode at 581 nm as its oscillations may be superposed to that of the diffraction mode. A different phenomenon occurs for the transmittance, as can be seen in Fig. 65: the oscillations of the first, second and third diffraction modes follow those of the grating modes and do not occur when their own cutoff pitch is each (resp. 128 nm, 256 nm and 384 nm), most likely due to a better matching of the electric fields of the respective modes at the interface for those pitch and height values.

It should be noted however that the conditions for oscillations discussed previously are no longer entirely exact. While Eq.(72) allows us to understand qualitatively why the peaks in the spectrum appear in such a way, it does not predict very accurately their position. First, Eq.(69) for the total reflection coefficient of a thin film is obtained for an homogeneous thin film and might no longer be valid for a patterned structure. Second, and most importantly, Eq.(72) is obtained for a varying height and a fixed refractive index, and the height values corresponding to a peak are the solutions of the following equation:

$$\frac{\partial R}{\partial h} = 0. \quad (109)$$

In our case however, the height is fixed and the pitch values corresponding to a peak are the solutions of the following equation:

$$\frac{\partial R}{\partial \Lambda} = 0 \quad (110)$$

Through the dispersion relation of Eq.(102), the pitch Λ appears in both reflection coefficients of Eq.(69) and also in the wave number of the exponential. From there arises an extremely complicated expression which exact solution is out of the scope of this thesis, but which could explain the nature and position of the peaks that are observed in the spectrum.

The TM case is a lot less spectacular. Fig. 66 shows the reflectance spectrum for the array with 500 nm tall lines in the case of TM illumination.

Since the EMA mode is always propagating, there is no cutoff to be highlighted due to taller lines. Regarding the thin-film interferences, there is also no big oscillation to be seen, but rather very little bumps when the TM_2 and first diffraction mode in reflection get activated at respectively 399 nm and 532 nm. The reason is yet again that most of the power is located into the EMA mode which is a lot more easily excited. Moreover, it has a flat band structure at large pitch (above 200 nm) and its associated effective refractive index is constant. In accordance to the above discussion on the conditions for thin-film interferences, this means that this mode cannot be responsible for such oscillations since both the height and the effective refractive index are fixed. The other modes however (TM_2 , first diffraction mode) do have a varying effective refractive index which can be responsible for oscillations, but since very little power is distributed into these modes, the peaks are not very intense, although it is possible to distinguish them. The extraordinary optical transmission observed for 100 nm is not as intense for 500 nm. There is still a resonance due to thin-film interference, as demonstrated by the non-monotonic spectrum and minimum in reflectance, but it is less intense at this height. In addition, like it was the case for the 100 nm lines, the

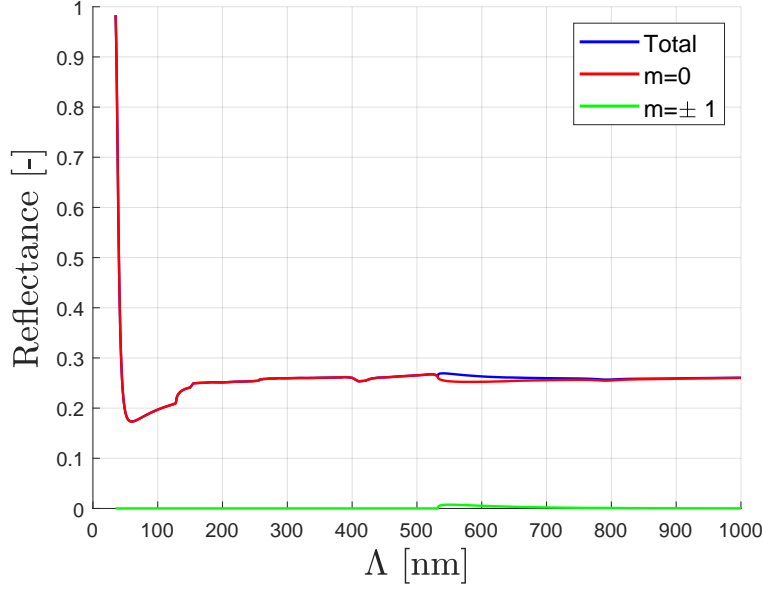


Figure 66: Reflectance spectrum of a normally incident TM polarized plane wave interacting with an array of PEC lines with width $w = 34$ nm and height $h = 500$ nm, as a function of the pitch Λ . The plot features the different diffraction orders. The spectrum is calculated using FEM.

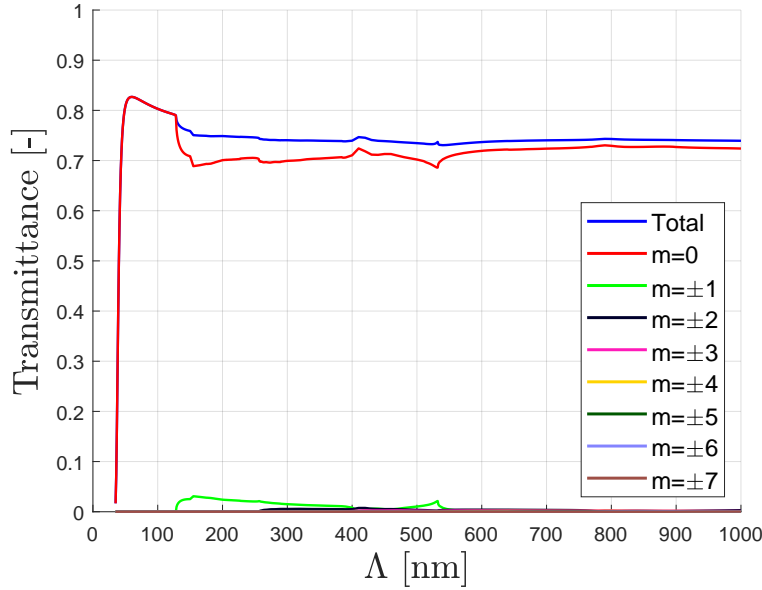


Figure 67: Transmittance spectrum of a normally incident TM polarized plane wave interacting with an array of PEC lines with width $w = 34$ nm and height $h = 500$ nm, as a function of the pitch Λ . The plot features the different diffraction orders. The spectrum is calculated using FEM.

diffraction modes are in general a lot less efficiently excited for the TM polarization than for the TE polarization, as can be observed in Fig. 67. For the TE polarization, thanks to the taller lines and as shall be seen later in this section, the waveguide modes have room to establish themselves and drastically change the electric field distribution inside the grating, therefore allowing a better matching at the interface between the grating and the substrate, whereas for 100 nm lines the spatial distribution was not changed as much, yielding weaker diffraction. Now for the TM polarization, even though several wavelengths of the EMA mode are now visible, the spatial distribution is still that of the initial plane wave, which explains why the matching at the interface is similar to the 100 nm case and the why diffraction is also weak.

A taller fin height should allow a better visualization of the modes propagating through the grating as the fin height is no longer smaller than the wavelength of the mode propagating inside the fins. To visualize them, let us again divide the band structure into different regions, each featuring the activation of a grating mode and this time ignoring the diffraction modes. The different regions are labeled according to the cutoff of the grating modes only and are represented similarly as it was done for the 100 nm case in Fig. 68.

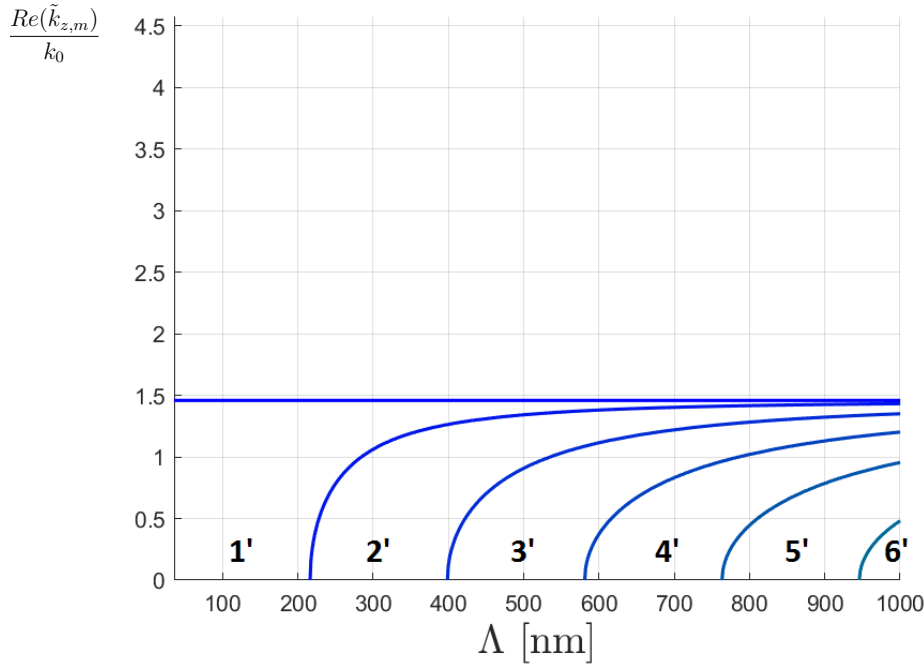


Figure 68: Label of the different spectral regions extracted from the band structure and defined by the cutoff pitch of each grating mode, for a PEC grating with width $w = 34$ nm and height $h = 500$ nm.

3.2.3.1 Region 1': $\Lambda \in [0, 215]$ nm

Fig. 69 (resp. 70) depict the TE (resp. TM) electric field distribution of spectral region 1', characterized by a pitch between $\Lambda = 0$ nm and $\Lambda = 215$ nm. They highlight how TE is cutoff while TM propagates. Several wavelengths are visible.

In this range, only the EMA mode of the TM polarization is propagating since the cutoff pitch for the TE_1 mode is at 217 nm. For the TE illumination, Fig. 69 shows how the TE_1 mode is evanescent below the cutoff located at $\Lambda = 217$ nm and does not propagate at all in the grating. Fig. 69d shows how the penetration depth increases when getting closer to the cutoff: the intensity is a lot less attenuated but the mode still does not propagate and there is no periodicity of the field. In the case of TM illumination, Fig. 70 shows how the EMA mode is present from the start. Its wavelengths are manifest now that there is room for several wavelengths with a 500 nm tall grating.

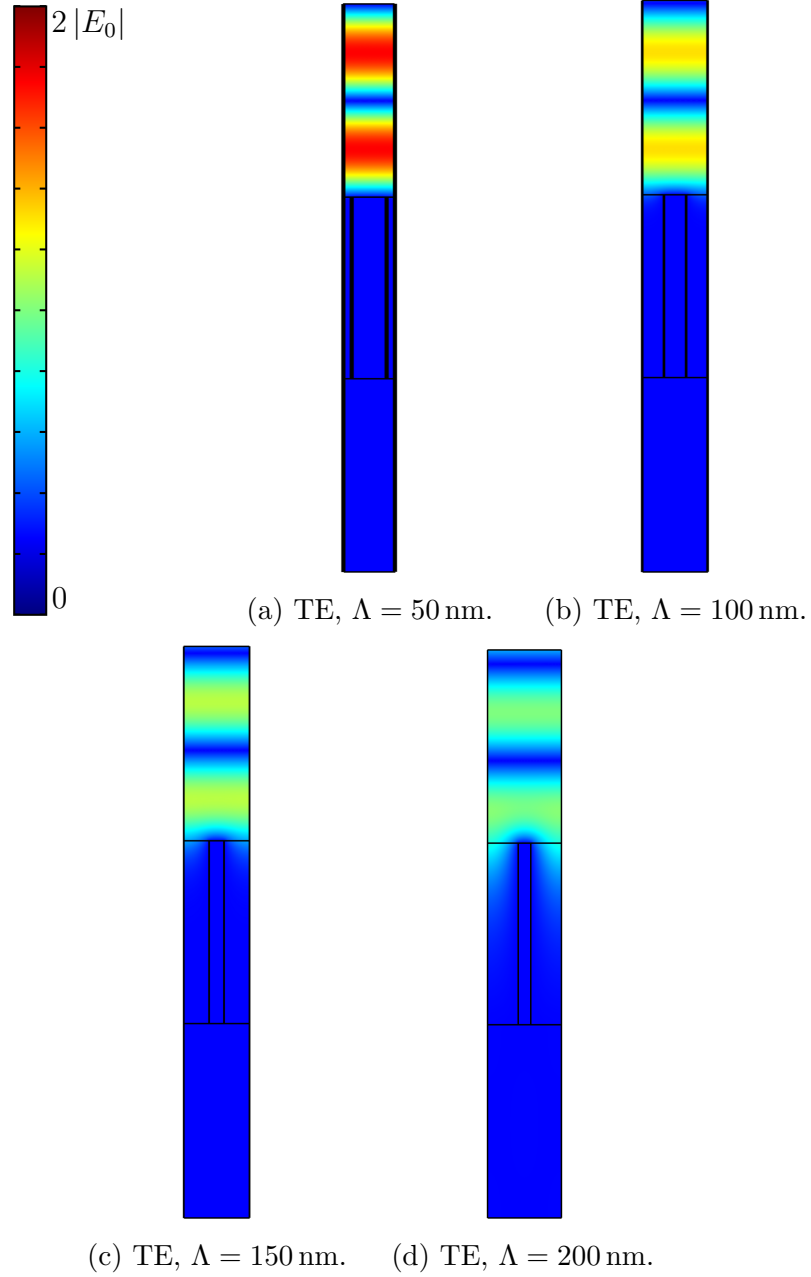


Figure 69: Distribution of the phasor norm of the TE electric field in the unit cell, for an array of PEC lines with width $w = 34$ nm, height $h = 500$ nm in pitch region 1' (Λ between 0 nm and 215 nm).

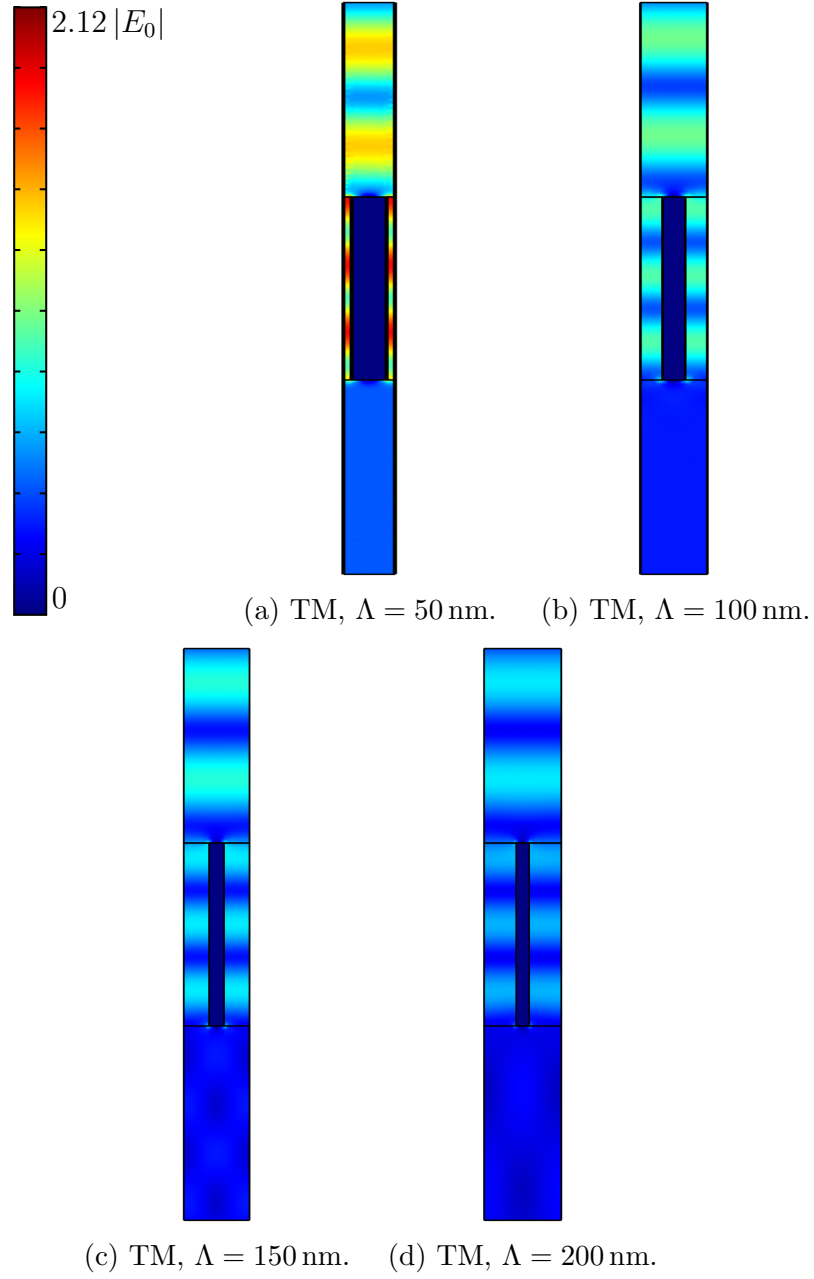
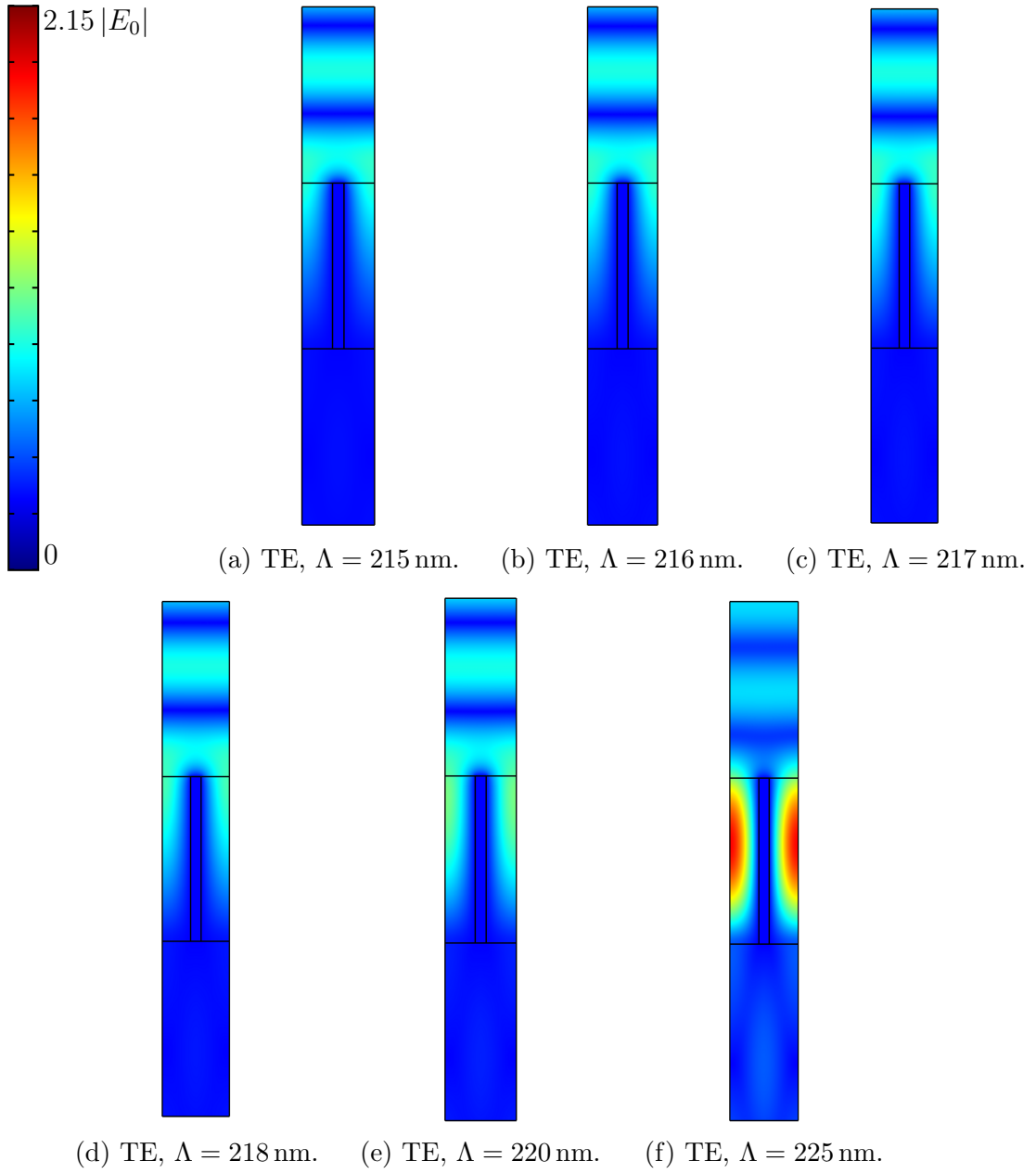


Figure 70: Distribution of the phasor norm of the TM electric field in the unit cell, for an array of PEC lines with width $w = 34$ nm, height $h = 500$ nm in pitch region 1' (Λ between 0 nm and 215 nm).

3.2.3.2 Region 2': $\Lambda \in [215, 400]$ nm

Fig. 71 (resp. 72) depict the TE (resp. TM) electric field distribution of spectral region 2', characterized by a pitch between $\Lambda = 215$ nm and $\Lambda = 400$ nm. They highlight how TE_1 becomes propagating and how more wavelengths are visible as the pitch increases.

Here, the transition of the TE_1 mode is now clearly visible in. At 220 nm, the mode is propagating but its associated wavelength is larger than the height of the array. However, this wavelength changes with the pitch and decreases as the pitch increases, and the wavelengths of the mode becomes visible as well. As before, in the case of TM polarization, the electric field distribution inside the grating is unaffected in this pitch range.



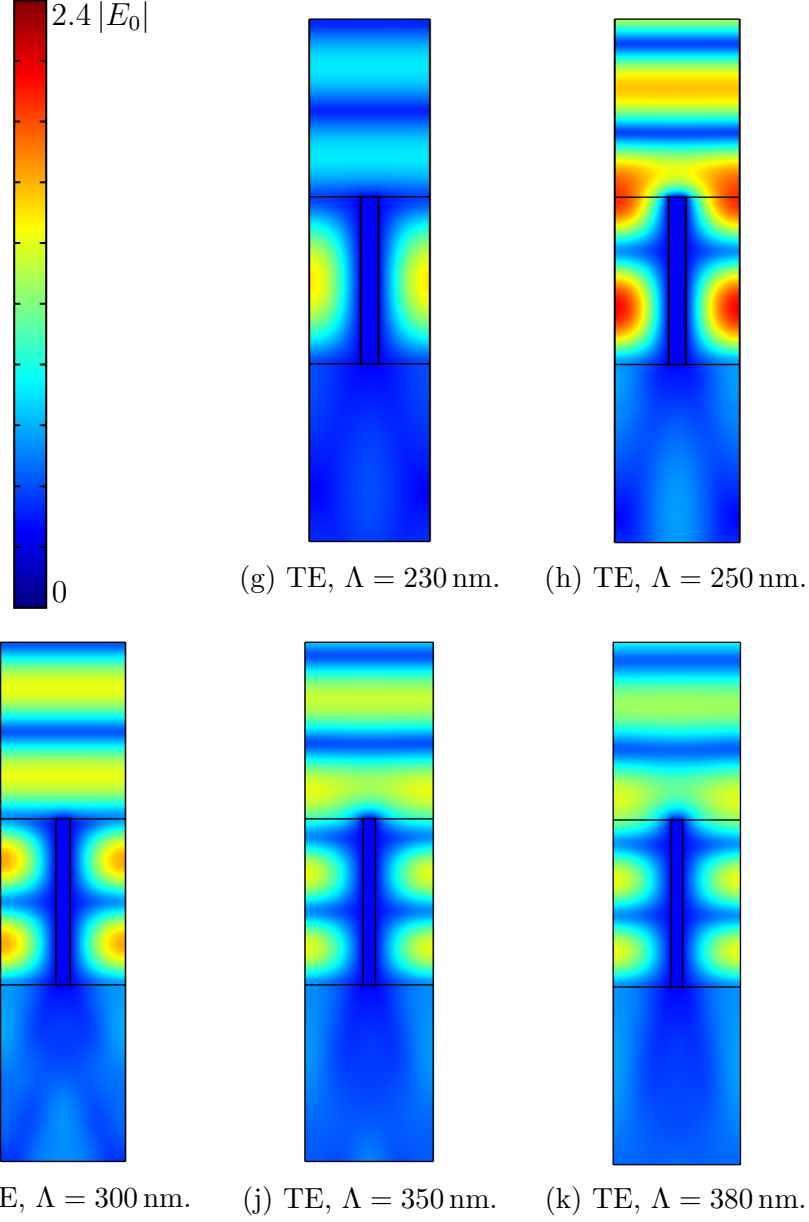
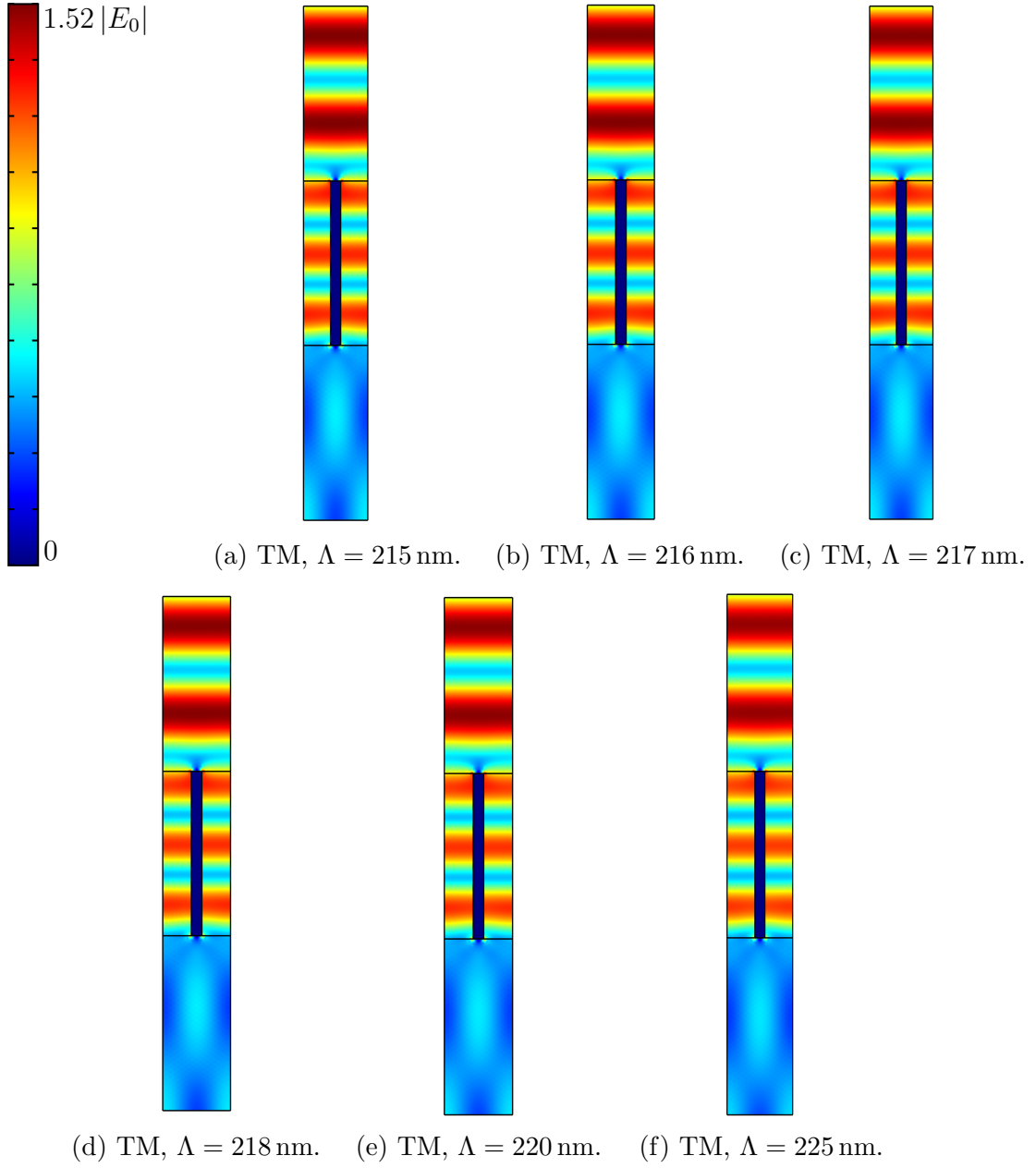


Figure 71: Distribution of the phasor norm of the TE electric field in the unit cell, for an array of PEC lines with width $w = 34$ nm, height $h = 500$ nm in pitch region $2'$ (Λ between 215 nm and 400 nm).



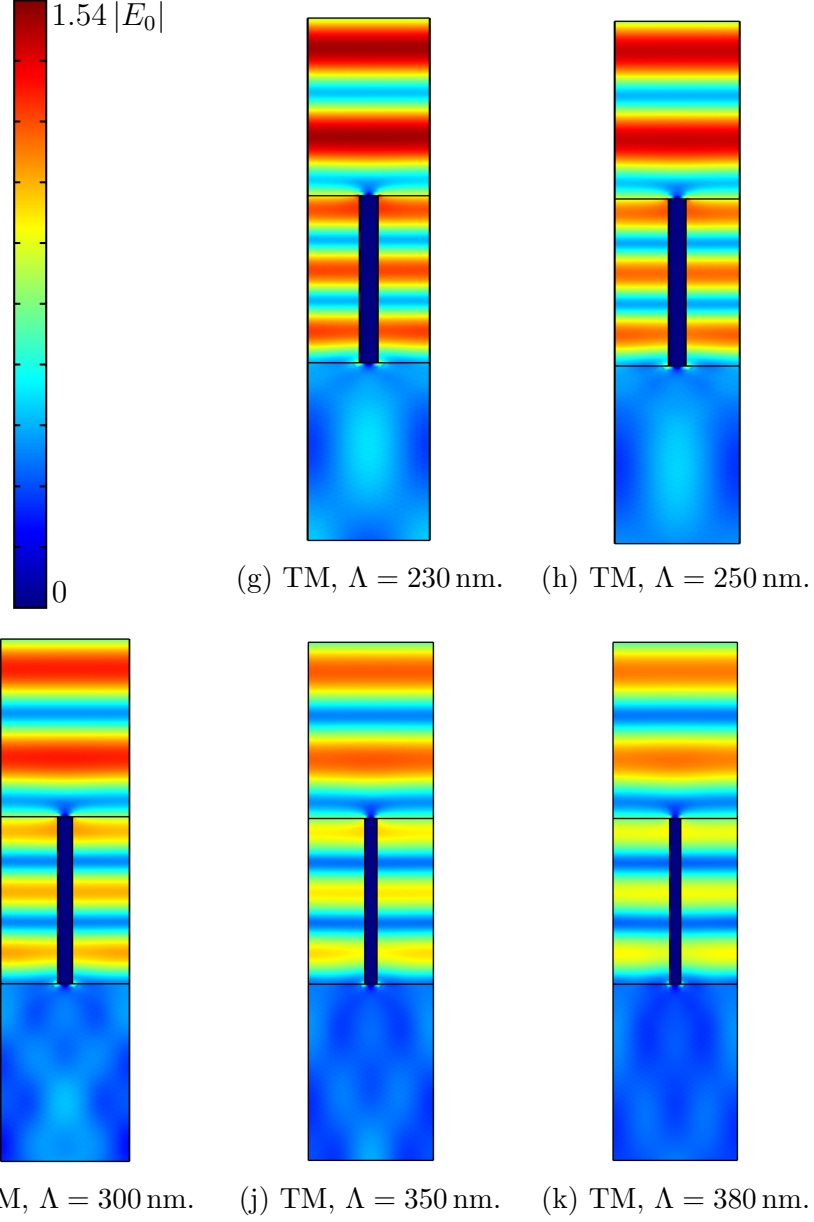


Figure 72: Distribution of the phasor norm of the TM electric field in the unit cell, for an array of PEC lines with width $w = 34$ nm, height $h = 500$ nm in pitch region $2'$ (Λ between 215 nm and 400 nm).

3.2.3.3 Region 3': $\Lambda \in [400, 580]$ nm

Fig. 73 (resp. 74) depict the TE (resp. TM) electric field distribution of spectral region 3', characterized by a pitch between $\Lambda = 400$ nm and $\Lambda = 580$ nm. They highlight the activation of TM_2 .

This range features the activation of the TM_2 mode at 398 nm. The observations here are the same as for the 100 nm tall lines: the transition is not sharp at the cutoff in Fig. 74a because most of the power is in the EMA mode but it becomes increasingly more visible in Figs. 74c to 76a as the first diffraction mode in reflection appears at 532 nm and couples into the now available TM_2 mode. The electric field distribution inside the grating in the case of the TE illumination does not change in this pitch range. It varies slightly when approaching the cutoff for the next grating TE_3 mode at 598 nm.

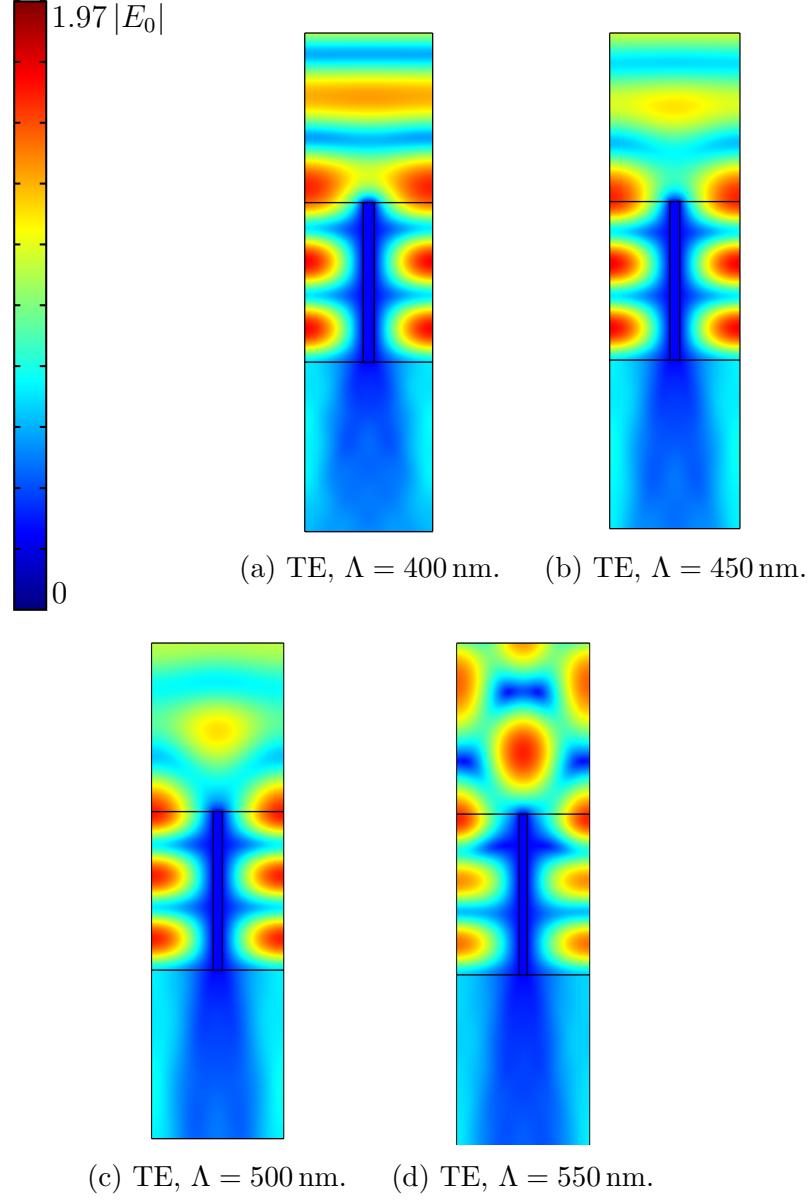


Figure 73: Distribution of the phasor norm of the TE electric field in the unit cell, for an array of PEC lines with width $w = 34$ nm, height $h = 500$ nm in pitch region $3'$ (Λ between 400 nm and 580 nm).

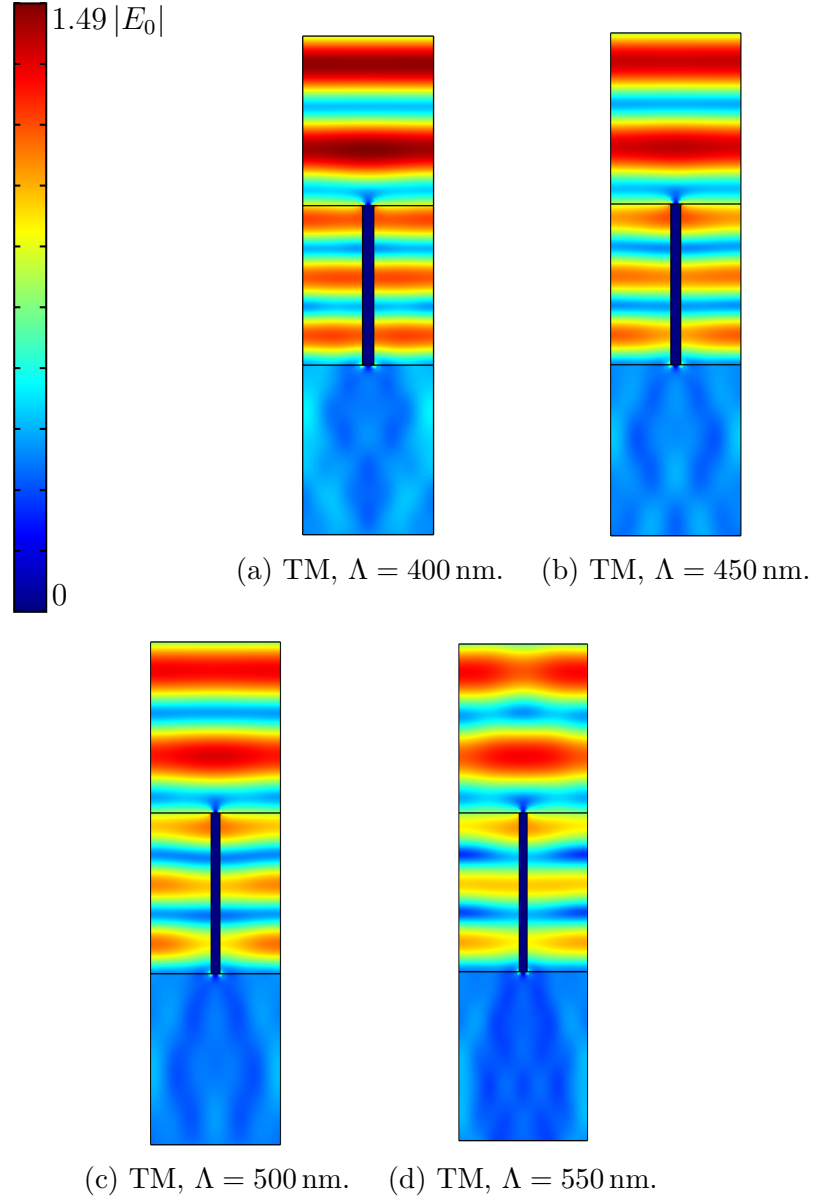
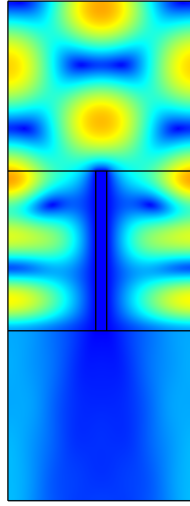
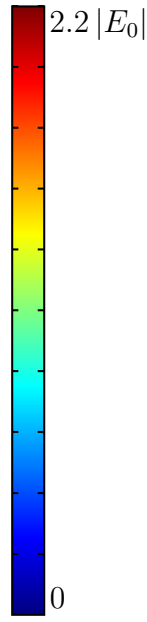


Figure 74: Distribution of the phasor norm of the TM electric field in the unit cell, for an array of PEC lines with width $w = 34$ nm, height $h = 500$ nm in pitch region $3'$ (Λ between 400 nm and 580 nm).

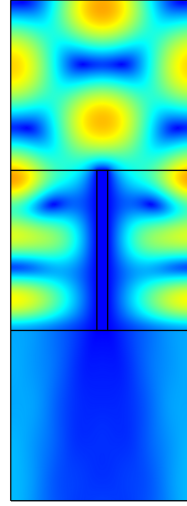
3.2.3.4 Region 4': $\Lambda \in [580, 763]$ nm

Fig. 75 (resp. 76) depict the TE (resp. TM) electric field distribution of spectral region 4', characterized by a pitch between $\Lambda = 580$ nm and $\Lambda = 763$ nm. They highlight the activation of TE_3 .

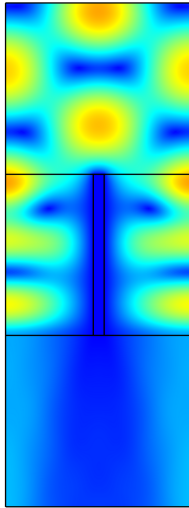
This region features the activation of the TE_3 mode at 581 nm. For TE polarization, the electric field distribution was already starting to change in the previous region when the pitch approached 580 nm. As can be seen in Fig. 75, after the cutoff, the field distribution is strongly modified not only due to the TE_3 mode being activated but also due to the big oscillations induced by thin-film interferences that were mentioned previously. The total field becomes quite complex as the different modes superpose each other, but once the oscillations have settled down above 700 nm, a pattern can be distinguished resulting from the superposition of the sine spatial distributions of the $m = 1$ and $m = 3$ modes represented in Fig. 16. Since the wavelengths associated to these two modes are different, the electric field distribution no longer seems periodic along the length of the lines. However, since both modes are propagating and therefore periodic, the periodicity exists but even longer lines are required to visualize it. Fig. 76 shows how the electric field distribution of the TM illumination is not affected in this pitch range.



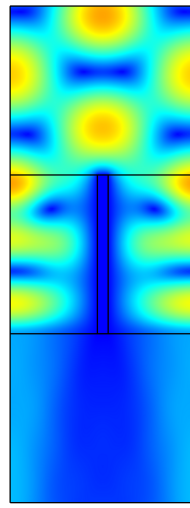
(a) TE, $\Lambda = 580$ nm.



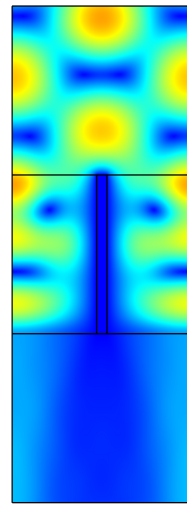
(b) TE, $\Lambda = 581$ nm.



(c) TE, $\Lambda = 581$ nm.



(d) TE, $\Lambda = 585$ nm.



(e) TE, $\Lambda = 590$ nm.

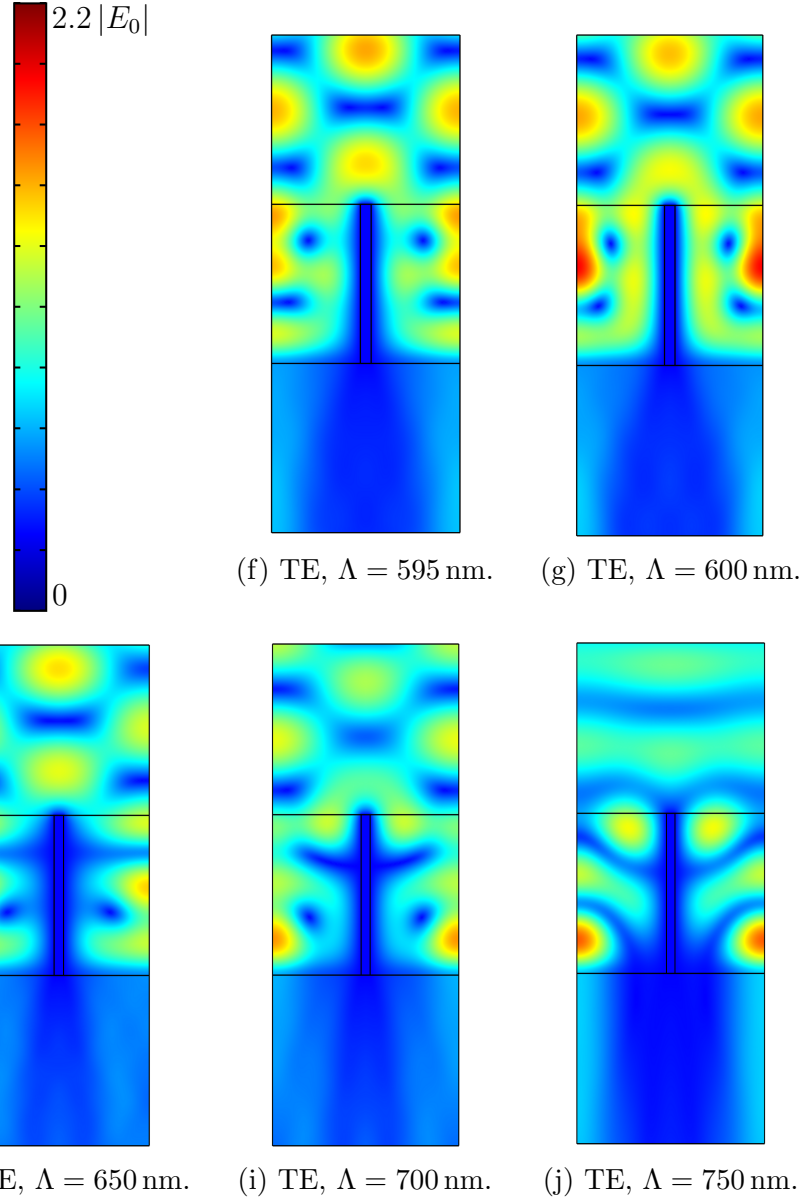
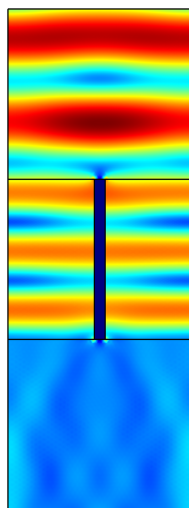
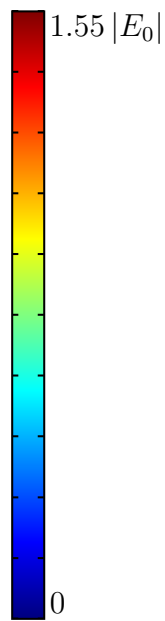
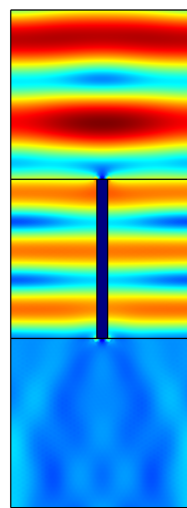


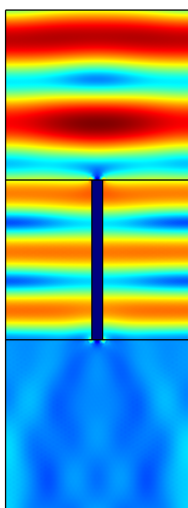
Figure 75: Distribution of the phasor norm of the TE electric field in the unit cell, for an array of PEC lines with width $w = 34$ nm, height $h = 500$ nm in pitch region 4' (Λ between 580 nm and 763 nm).



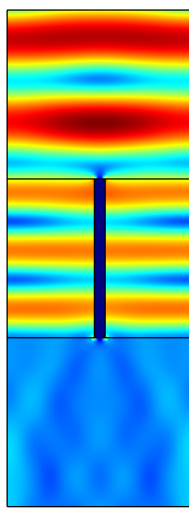
(a) TM, $\Lambda = 580$ nm.



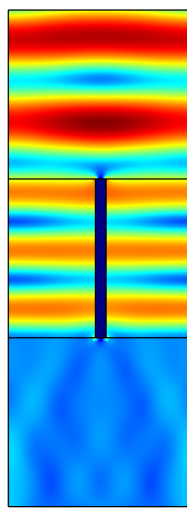
(b) TM, $\Lambda = 581$ nm.



(c) TM, $\Lambda = 582$ nm.



(d) TM, $\Lambda = 585$ nm.



(e) TM, $\Lambda = 590$ nm.

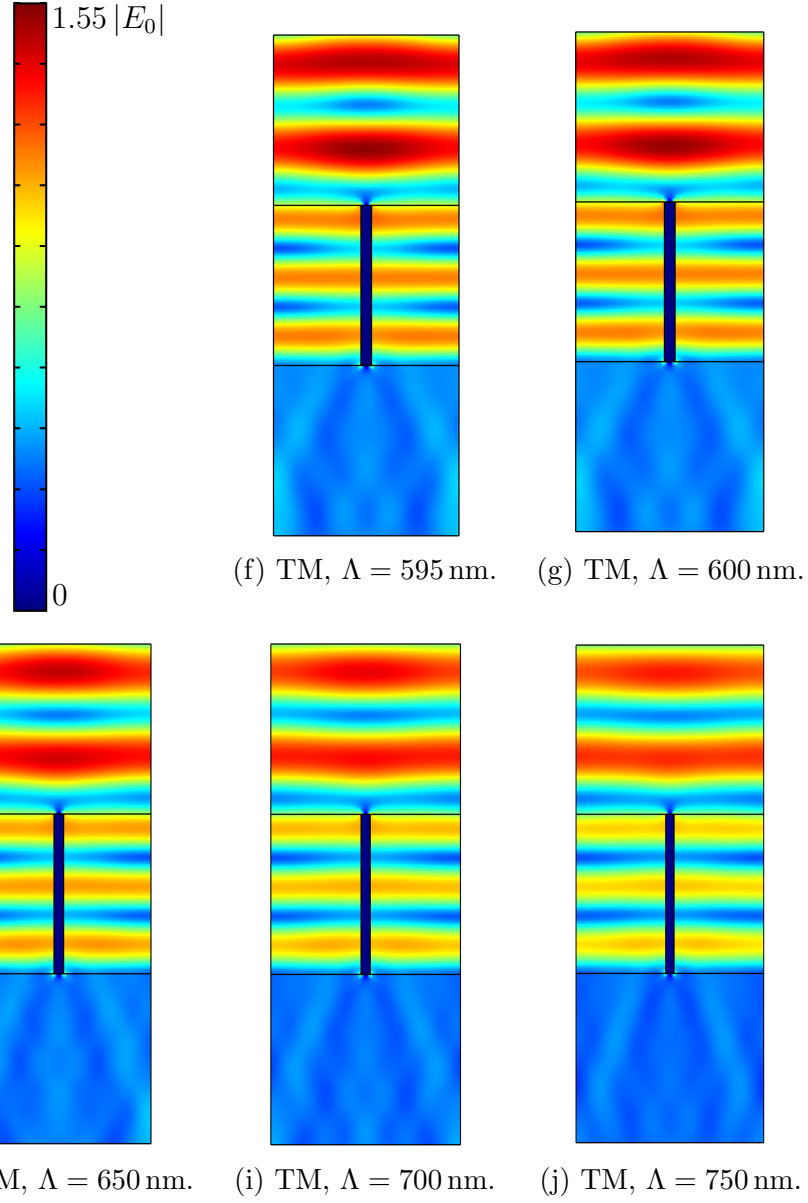


Figure 76: Distribution of the phasor norm of the TM electric field in the unit cell, for an array of PEC lines with width $w = 34$ nm, height $h = 500$ nm in pitch region 4' (Λ between 580 nm and 763 nm).

3.2.3.5 Region 5': $\Lambda \in [763, 945]$ nm

Fig. 77 (resp 78) depict the TE (resp. TM) electric field distribution of spectral region 5', characterized by a pitch between $\Lambda = 763$ nm and $\Lambda = 945$ nm. They highlight how TM_4 is hard to visualize.

This region features the cutoff pitch of the TM_4 at 763 nm. However, this mode is of high order: it is harder to excite and it is harder to distinguish between the presence of the different modes and the influence of geometry.

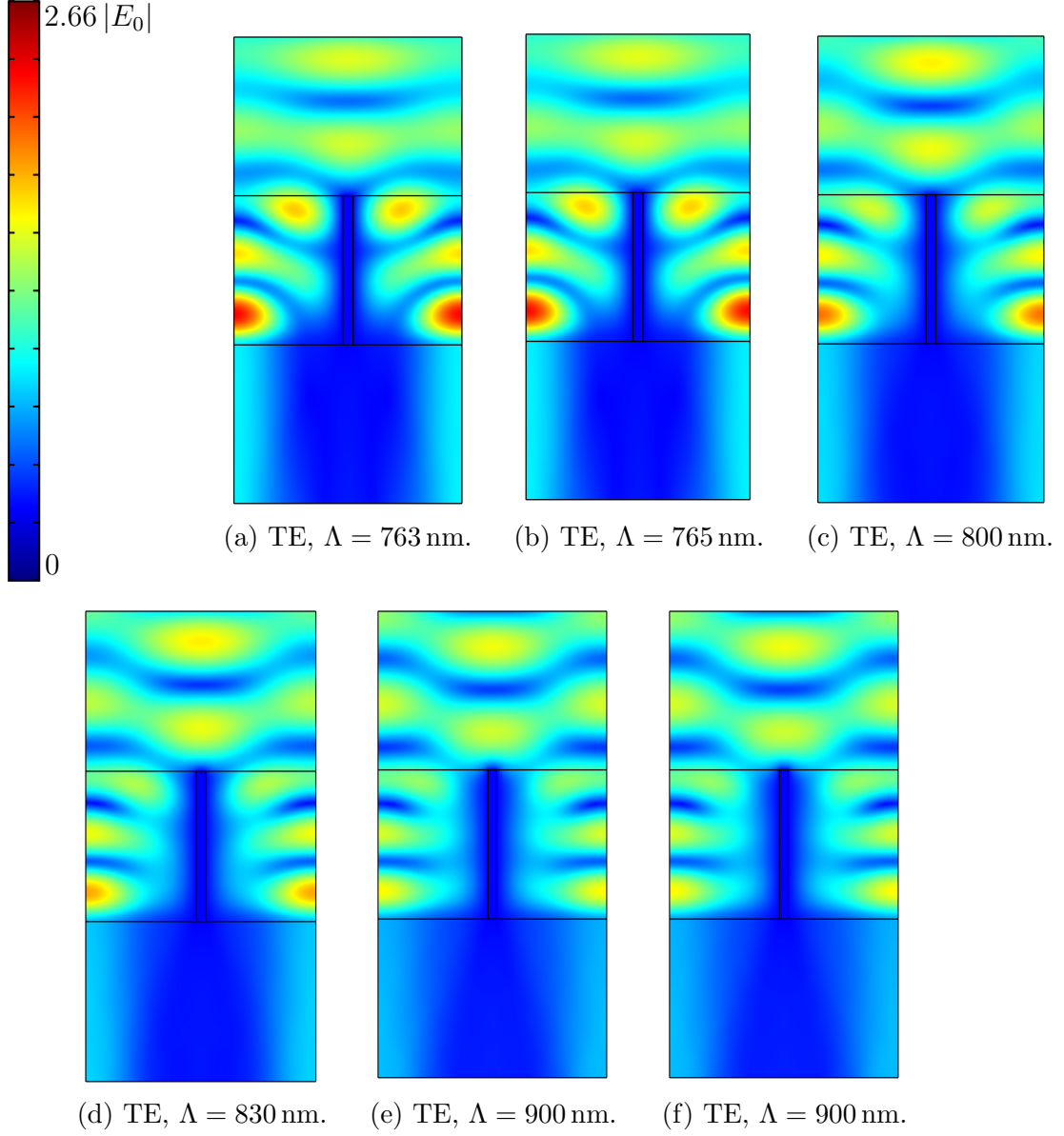


Figure 77: Distribution of the phasor norm of the TE electric field in the unit cell, for an array of PEC lines with width $w = 34$ nm, height $h = 500$ nm in pitch region 5' (Λ between 763 nm and 945 nm).

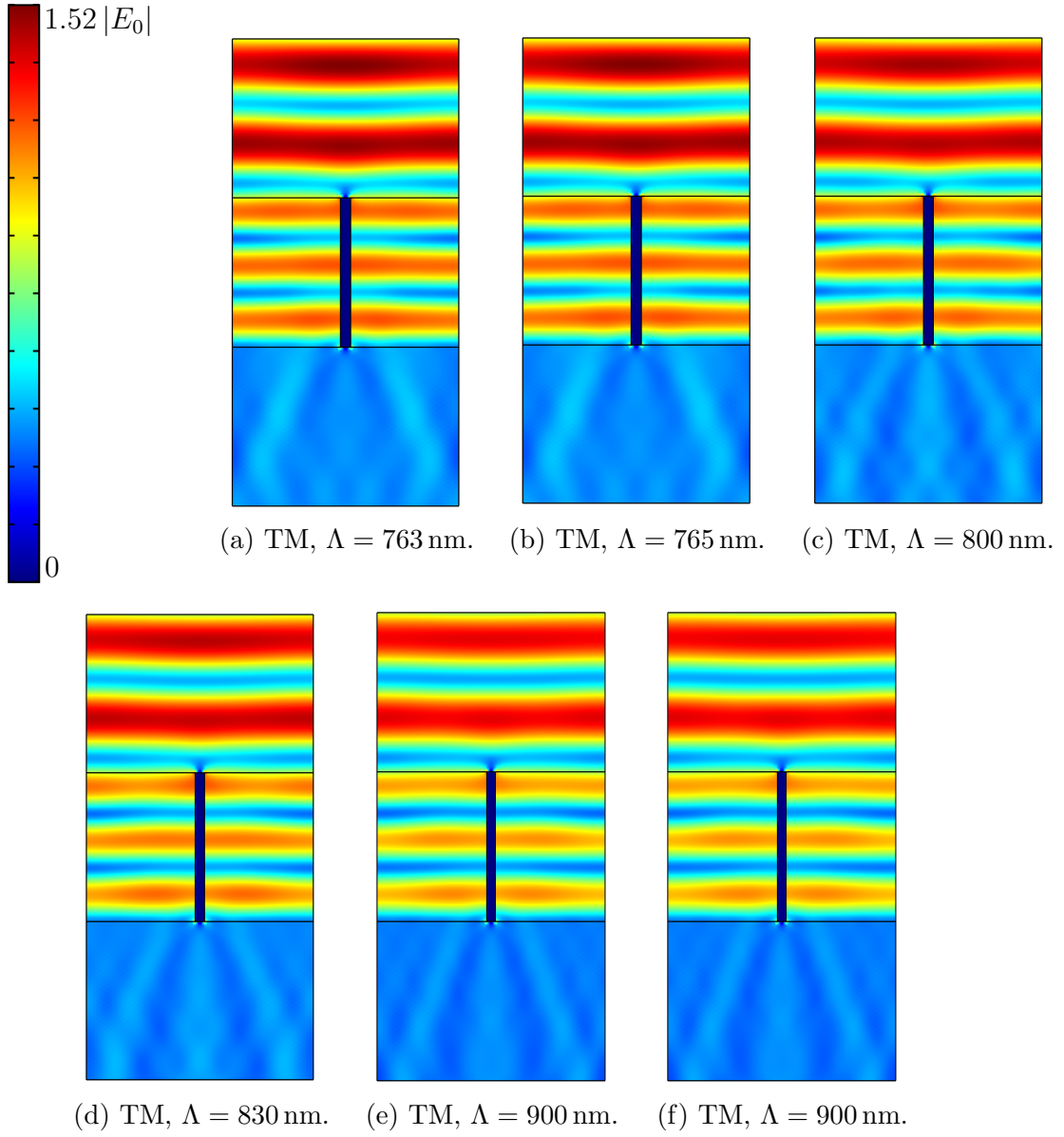


Figure 78: Distribution of the phasor norm of the TM electric field in the unit cell, for an array of PEC lines with width $w = 34$ nm, height $h = 500$ nm in pitch region 5' (Λ between 763 nm and 945 nm).

3.2.3.6 Region 6': $\Lambda \in [945, 1000]$ nm

Fig. 79 (resp. 80) depict the TE (resp. TM) electric field distribution of spectral region 6', characterized by a pitch between $\Lambda = 945$ nm and $\Lambda = 1000$ nm. They highlight how it is difficult to distinguish the TE₅ from the other modes.

This region features the cutoff pitch of the TE₅ mode at 946 nm. Similarly to the TM₄ mode of the previous region, it is a high order mode is harder harder to excite. It is also difficult to distinguish between the presence of the different modes and the influence of geometry.

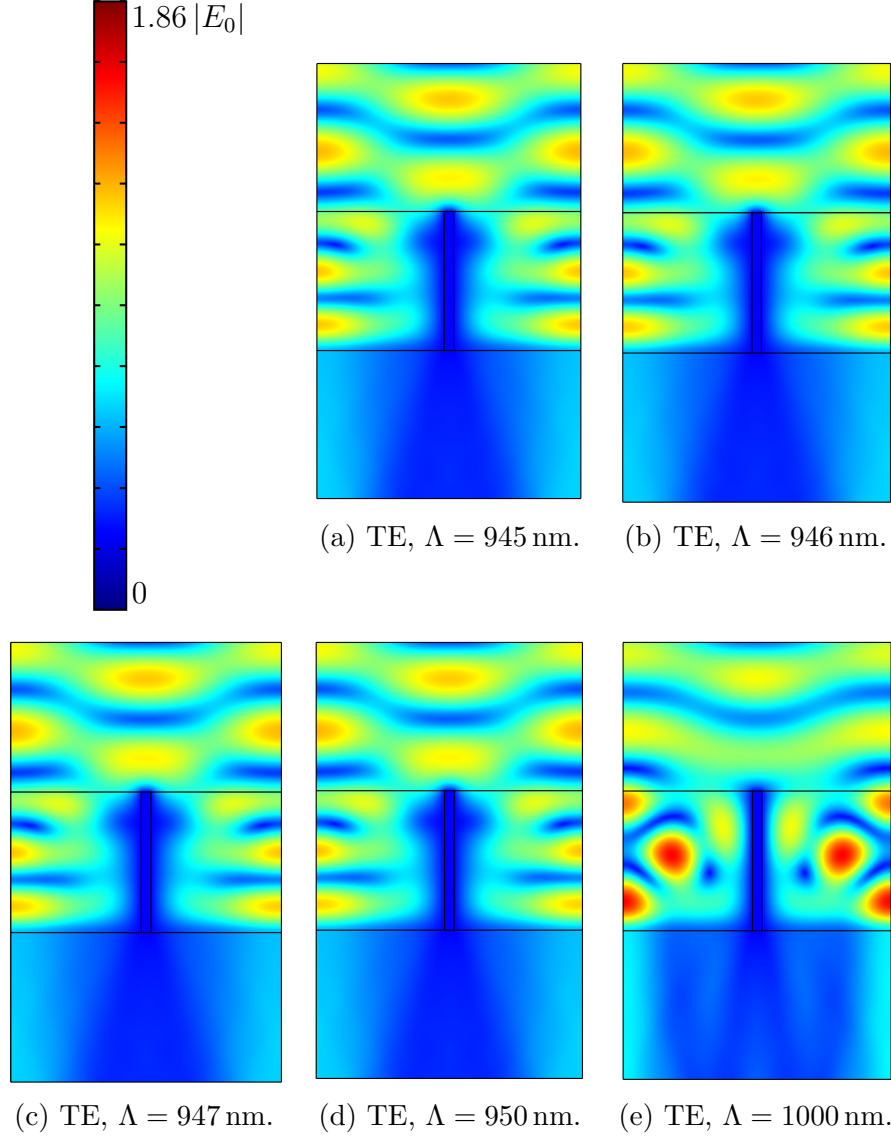


Figure 79: Distribution of the phasor norm of the TE electric field in the unit cell, for an array of PEC lines with width $w = 34$ nm, height $h = 500$ nm in pitch region $6'$ (Λ between 945 nm and 1000 nm).

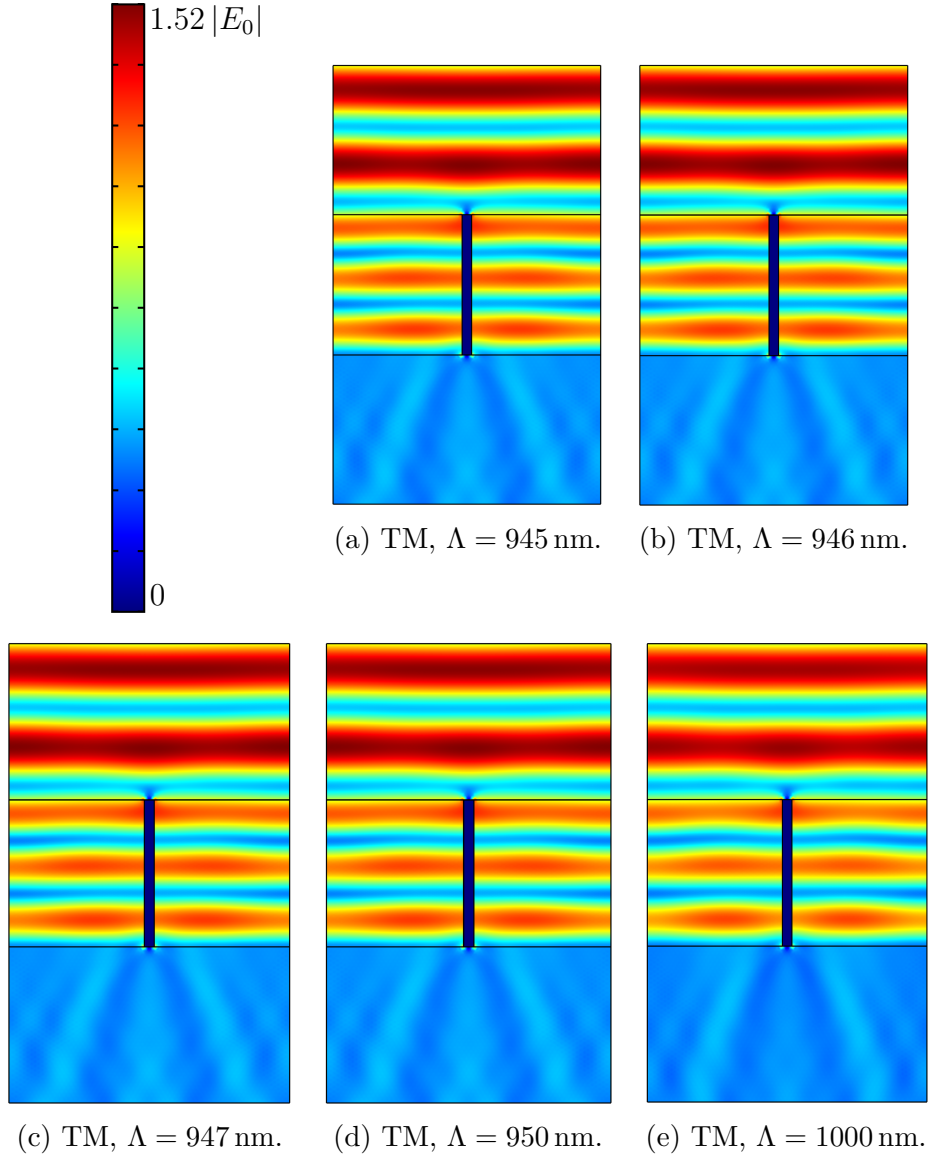


Figure 80: Distribution of the phasor norm of the TM electric field in the unit cell, for an array of PEC lines with width $w = 34$ nm, height $h = 500$ nm in pitch region 6' (Λ between 945 nm and 1000 nm).

The main features that were observed for each spectral region are summarized succinctly in Table 3.

Region	Highlight
1'	Cutoff for TE, transmission for TM, several wavelengths are
2'	Activation of TE_1 , several wavelengths become visible
3'	Activation of TM_2
4'	Activation of TE_3
5'	TM_4 hard to visualize
6'	TE_5 hard to distinguish from other modes

Table 3: Key features presented in each spectral region for Figs. 69 to 80.

It was seen how modifying the height of the array can strongly modify how the pitch affects the reflectance spectrum due to thin-film interferences and wave attenuation. It is also relevant to analyze the reflectance spectrum of the array as a function of the height. Fig. 81 (resp. 82) shows this spectrum in the case of TE (resp. TM) illumination and illustrates the thin-film interferences occurring when the refractive index (related to pitch here) is fixed and the height is varied.

For the TE polarization, the first observation is that at low pitch, i.e. below the TE_1 cutoff of 217 nm, the reflectance quickly goes to 1 as the height increases. This is in accordance with the observations of the previous sections: when the mode is cutoff, at small height, a portion of the light which was not fully attenuated is still able to reach the substrate and propagate. When the height of the array increases however, the lines are tall enough so that no light reaches the substrate and the reflectance therefore goes to 1. One can also see how at a 200 nm pitch, being closer to the cutoff, the penetration depth is larger and more light reaches the substrate for small height than in the case of 100 nm pitch.

The next observation is that there are indeed oscillations induced by height when the TE_1 mode is able to propagate, i.e. for pitch 300 nm and above. It appears that each curve is different: for each pitch, the peaks occur for different height values. This can be explained from the dispersion relation presented in the band structure of Fig. 27, where it can be seen that the effective refractive index, which intervenes in the condition for thin-film interferences, evolves with the pitch. Therefore, each curve has a different condition on the height multiples for peaks to happen.

In addition, the oscillations are not as regular as in the case of an homogeneous material. A reason for this is that the medium is no longer homogeneous but is a patterned structure to which an effective refractive index can be associated, which is however still an approximation and the structure might behave differently with respect to thin-film interferences.

Two surprising phenomena can be seen in Fig. 81. First, the maxima and minima seem to change as the height increases. This is unexpected since the material is not absorbing and the height should only induce the peaks but not have an effect on the value of the peaks themselves. However, as it was seen just before, even though the material is not absorbing, the light propagates through the structure by coupling into the TE_1 , TE_3 and TE_5 modes, which have a cutoff. It is therefore possible that some of the light tries to couple into higher

order modes but gets more efficiently attenuated as the height increases, which explains the increase in reflectance. Second, some unexpected additional oscillations are present at higher pitch. Indeed, for 800 nm and 1000 nm pitch, there is a bump around 150 nm and 350 nm height, respectively. This kind of oscillation is not present in the case of an homogeneous medium, in which the light propagates according to a single mode. Here, several modes are available, and in the case of 800 nm and 1000 nm pitch, both the TE_1 and TE_3 modes are propagating, and even the TE_5 mode for 1000 nm pitch. Since there is a different effective refractive index associated to each of those modes, the condition for thin-film interference might differ from one another, and a phenomenon similar to a superposition of periodic functions with different frequencies appear, resulting in that additional elbow.

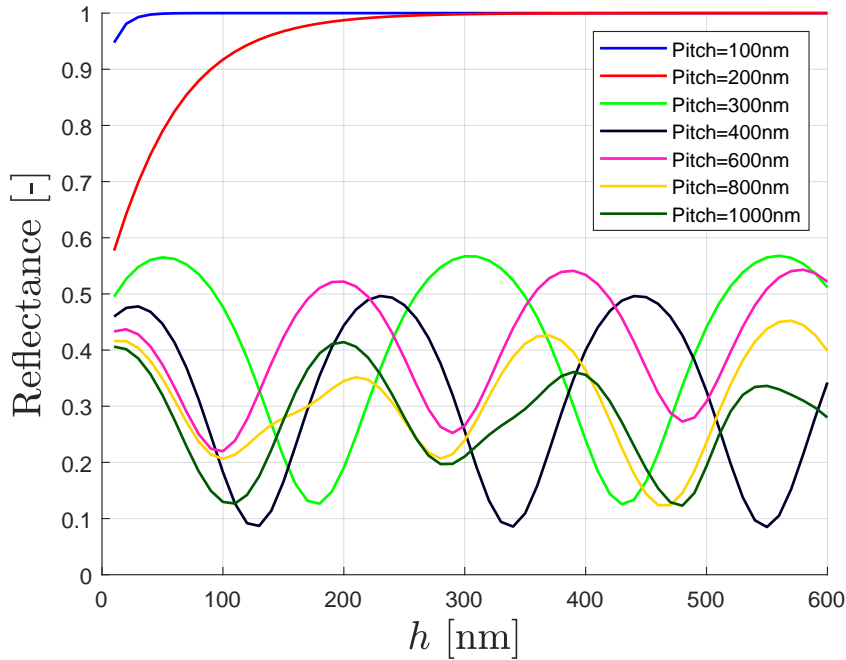


Figure 81: Reflectance spectrum of a normally incident TE polarized plane wave interacting with an array of PEC lines with width $w = 34$ nm as a function of the height h . The plot features several values for the pitch of the grating. The spectrum is calculated using FEM.

In the case of TM polarization, there is very little discrepancy between the different pitches. This can again be explained by the fact that most of the power is located in the EMA mode, which effective refractive index tends to a constant value (that of silicon oxide n_{SiO_2}) for pitches above 100 nm, as can be seen in the band structure of Fig. 34. At 100 nm pitch, the ratio is slightly higher than for the other curves, which explains the slightly higher reflectance and the slightly shifted positions of the peaks. If the pitch was to decrease further, it was seen that the reflectance would go to 1, regardless of the height, as the array approaches a slab of PEC. In addition, Fig. 82 confirms that the EOT observed previously is indeed a consequence of thin-film interferences, as the reflectance is minimum at around 100 nm height, while for 500 nm height, it is indeed smaller at low pitch, as it was observed

at the beginning of this section.

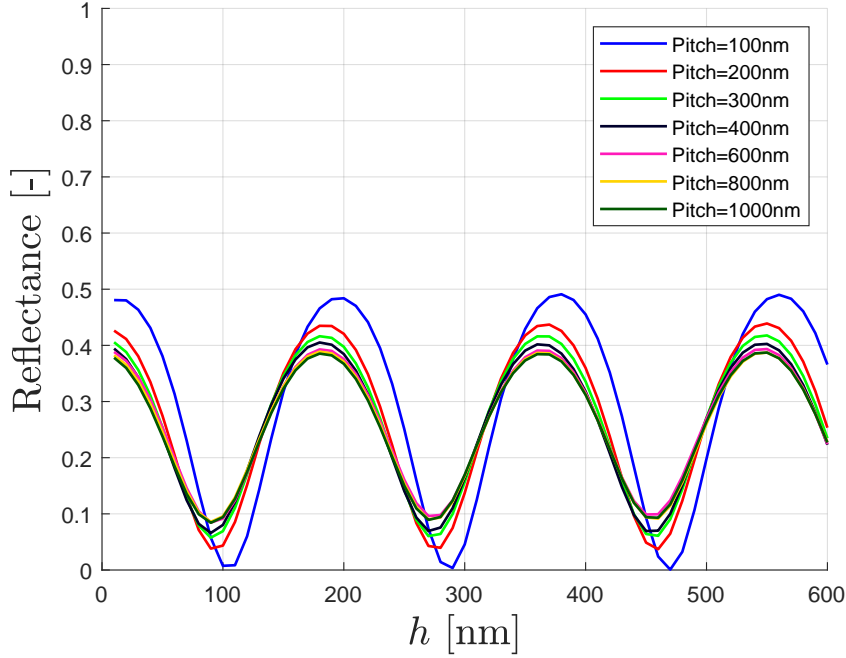


Figure 82: Reflectance spectrum of a normally incident TM polarized plane wave interacting with an array of PEC lines with width $w = 34$ nm as a function of the height h . The plot features several values for the pitch of the grating. The spectrum is calculated using FEM.

In conclusion, as the height does not appear in the mathematical expressions of the dispersion relations (102) to (104), it does not modify how light propagates through the structure. The modes and their cutoff are the same as when the height h is 100 nm. However, the height can have an effect in two ways. First, by having a larger height, while at a pitch below the cutoff for a given mode, the corresponding evanescent modes are fully attenuated by the time light reaches the substrate interface. Indeed, as it was seen previously, the evanescent mode can have a penetration depth which is larger than 100 nm, so that light with finite intensity could reach the substrate in the case of 100 nm lines. This is longer be the case when considering taller fins, where the evanescent modes are completely attenuated before reaching the substrate and it is possible to observe sharp transitions when the modes are activated. Second, a height which is of the order of the incoming wavelength may give rise to thin-film interferences due to the reflection on the substrate interface. Moreover, this effect can be coupled with the variation of the pitch, which modifies the effective refractive index, which in turns affects the position of the maxima and minima resulting from thin-film interferences.

3.3 Summary

The effect of the geometrical parameters on the reflectance and transmittance spectra was discussed based on the band structures of Figs. 27 and 28.

It was seen how the pitch is responsible for the activation of both the grating and the diffraction modes. For TE polarization, the cutoff as well as the first diffraction orders were visualized in Figs. 30 and 31. The cutoff was highlighted thanks to some 2D maps in Fig. 38. For TM polarization, there was no such cutoff, but a phenomenon of extraordinary optical transmission (EOT), as seen in Fig. 32, while the diffraction orders were less efficiently excited. The band structure failed to capture the geometric dependence of the TEM mode and the effective medium approximation (EMA) was invoked to adapt it into the band structure of Fig. 34 as the EMA mode.

The width was also responsible for the activation of the grating modes but had no effect on the diffraction modes. Increasing the width had an effect similar to decreasing the pitch.

The height was responsible for thin-film interferences, featured in Figs. 81 and 82, and allowed a better visualization of the attenuation of the evanescent modes and the sharpness of their transition at a cutoff, such as in the 2D maps of Fig. 69. For the TE polarization, the strong dependence of the effective refractive index on the pitch lead to very different characteristics of the thin-film interferences. In addition, this strong dependence lead to intense oscillations of the reflectance around cutoffs, as seen in Fig. 64. For TM polarization, the almost constant effective refractive index of the EMA mode at large pitch lead to very similar curves instead. However at low pitch, its quick variation was responsible for the EOT.

4 Light interaction with periodic arrays of nanometer-wide metal lines

4.1 Methodology and modeling

Let us now analyze how light interacts with the same periodic array composed of real absorbing metal lines instead of perfect electrical conductor. The situation is basically the same as it was for the PEC lines and is described in section 3.1, but the PEC is replaced by a real metal.

In particular, copper is studied, which n and κ values are taken from [44]. At a free-space wavelength of $\lambda_0 = 532\text{ nm}$, they take the following values: $n = 1.11$ and $\kappa = 2.6$. The main difference is of course that the extinction coefficient κ is now finite, in opposition to the PEC where it was infinite. Now, the interface conditions of Eq.(7) to (10) state that the displacement and magnetic fields must be continuous at an interface with copper, since there is no surface charge or current density for a real metal. Besides, the electric field inside a real metal can be finite, therefore, the waveguide theory developed in section 2.6.1 is no longer valid, as the electric field cannot be imposed to be 0 at the metal interface. As a result, an analytical expression for the dispersion relation of the grating modes for copper lines is not easily derived. However, it is possible to derive a band structure numerically by solving an eigenvalue wave equation in a weak formulation using COMSOL [20]: the results for both TE and TM polarizations are plotted in Figs. 83 and 84 respectively. Since the

diffraction phenomenon is a direct consequence of the periodicity only and not of the nature of the periodic element, the dispersion relation of the diffraction modes is not expected to be modified from a PEC to a real metal.

There are some noticeable differences between this band structure and the one for PEC

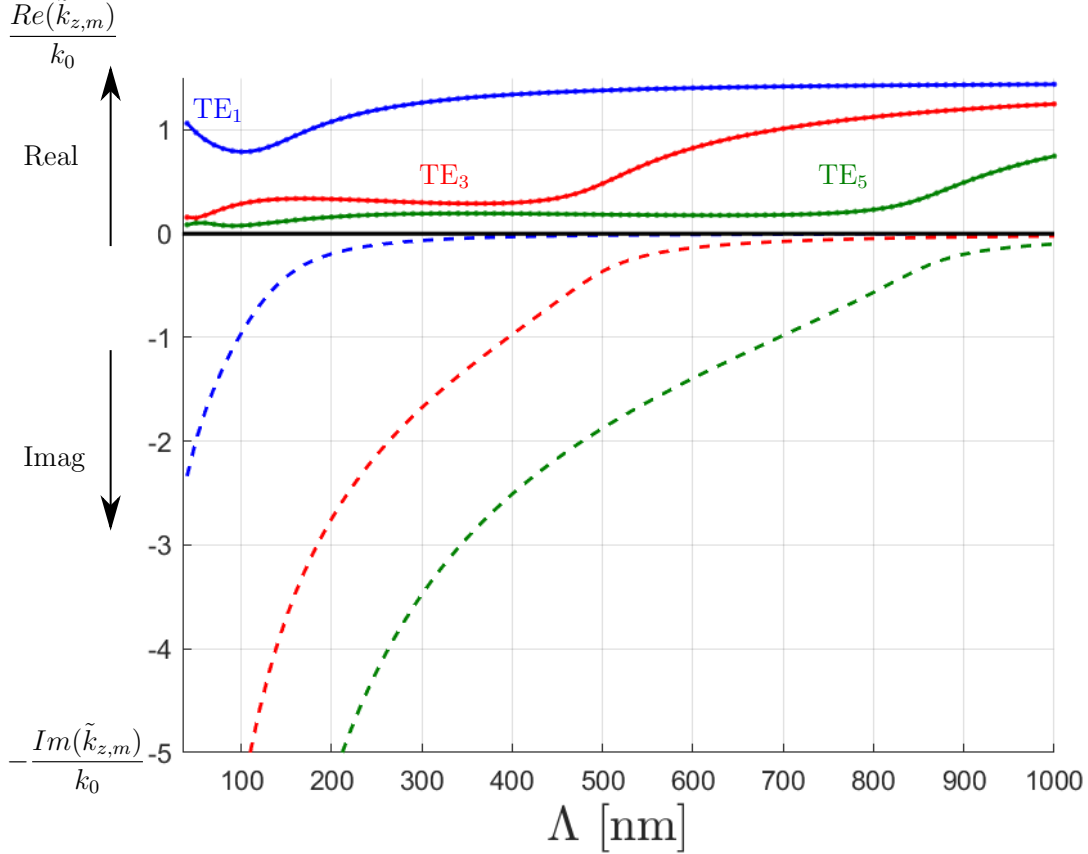


Figure 83: Band structure for the symmetric grating modes of the array of copper lines under TE illumination below $\Lambda = 1000$ nm, for a free-space wavelength $\lambda_0 = 532$ nm, width $w = 34$ nm, refractive indices $n_{air} = 1$, $n_{Si} = 4.15$, $n_{SiO_2} = 1.45$ and $\theta_i = 0^\circ$. The solid lines represent the real part of the wave number, while the dashed lines represent the opposite of its imaginary part.

featured in Fig. 17. First, the wave number has now both a real and imaginary part, whereas in the case of PEC lines, it was entirely real or imaginary, respectively above or below the cutoff pitch for the corresponding mode. This means that in the case of copper, a mode can have an oscillatory propagating component, which is simultaneously attenuated as it propagates, as can be seen by plugging a complex refractive index $\tilde{n} = n - j\kappa$ into the wave equation, as it was done in Eq. 39. Second, there is no sharp cutoff of the modes, where the imaginary part of the wave number goes to 0 and its real part quickly grows. Instead, the transitions are a lot smoother, and although the real (resp. imaginary) part of the wave number tends to 0 when a mode is cutoff (resp. propagating), it is still finite. However it is still possible to associate a cutoff pitch to each mode, by defining it as the pitch at which the real part becomes larger than the imaginary part. One can see that those cutoff pitches are similar to those of PEC modes (see Table 1). For the TE polarization, since the TE_1 mode

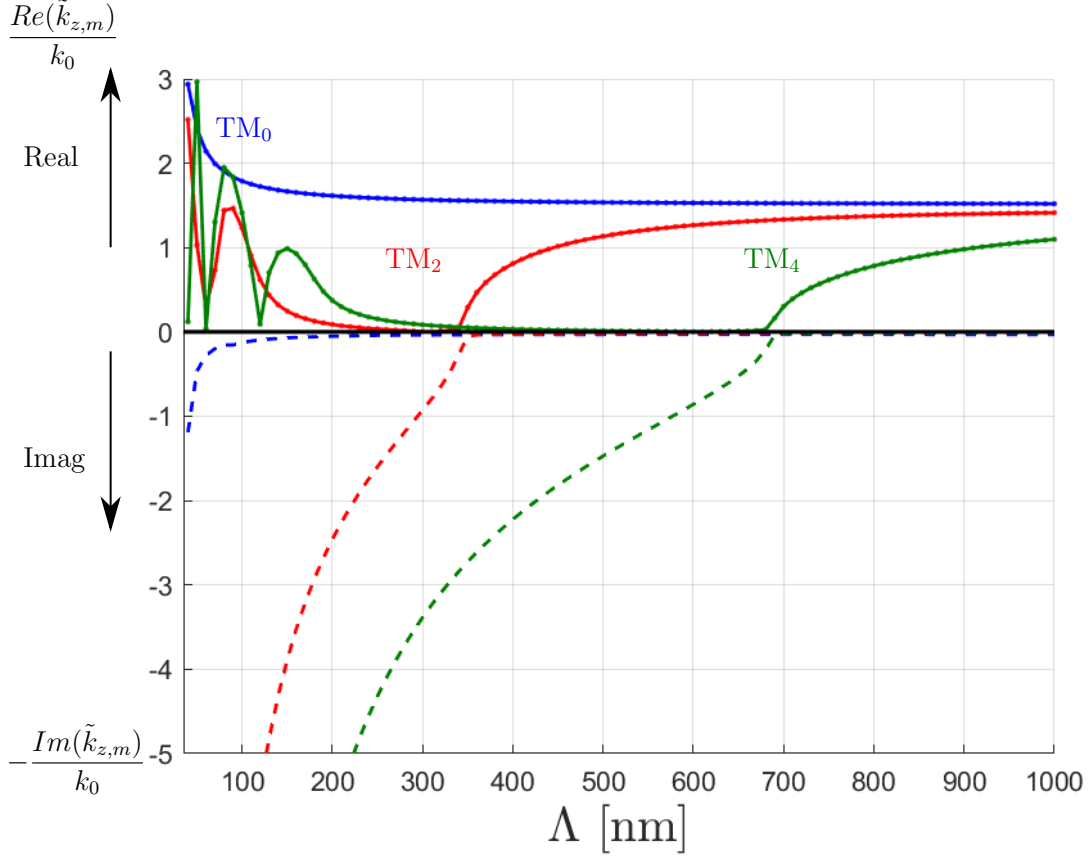


Figure 84: Band structure for the symmetric grating modes of the array of copper lines under TM illumination below $\Lambda = 1000$ nm, for a free-space wavelength $\lambda_0 = 532$ nm, width $w = 34$ nm, refractive indices $n_{air} = 1$, $n_{Si} = 4.15$, $n_{SiO_2} = 1.45$ and $\theta_i = 0^\circ$. The solid lines represent the real part of the wave number, while the dashed lines represent the opposite of its imaginary part.

is not as efficiently cutoff at low pitch as it was in the case of PEC lines, light is expected to be coupled into that mode and be transmitted even at low pitch.

The TM band structure of Fig. 84 bears more similarities with its PEC counterpart: although there always is a finite real part for the higher order modes, their imaginary part is always a lot larger than the real one, and than that the TM_0 mode, until their respective cutoff. In addition, the TM_0 is never cutoff, as it was the case for the PEC band structure.

4.2 Effect of the geometry

Similarly to what was done in section 3.2, the effect of the pitch, width and height of the copper array on the reflectance and transmittance spectra are studied on the basis of the band structures of Figs. 83 and 84. In addition, some key 2D maps are provided to highlight the main observations. The results are compared to those obtained for the PEC grating.

4.2.1 Effect of pitch

Figs. 85 and 86 (resp. Figs. 88 and 89) depict the reflectance and transmittance spectra for the TE (resp. TM) polarization, for the structure composed of copper lines with width $w = 34 \text{ nm}$ and height $h = 100 \text{ nm}$.

First, for the TE polarization, it appears that the reflectance does not go to 1 as the fill factor w/Λ approaches 1, i.e. at low pitch. The reflectance does go to a maximum value but the light is not entirely reflected. This does not mean however that it is transmitted instead for a slab of copper: the finite optical constants of copper mean that part of the light is reflected and part of it penetrates into the material, where it is absorbed. The part of light that was not yet absorbed when reaching the substrate can be transmitted (but also reflected) at the substrate interface, into which it propagates. Therefore, for a slab of copper, i.e. when $w = \Lambda$, the reflectance takes the finite value of a copper thin film, including interferences. However, as can be seen in Fig. 86, no light is transmitted and everything is in fact absorbed by the copper film. Fig. 87 represents the absorptance of the copper grating as a function of the pitch. By conservation of energy, the absorptance is simply the difference $A = 1 - R - T$. One can see that it is greater at low pitch, when the fill factor is close to 1 where most of the grating is composed of absorbing material. As the pitch increases however, the transmittance directly increases as some light is able to propagate through the oxide, whereas for the PEC line the TE_1 cutoff had to be reached before any transmission occurred. Surprisingly, at low pitch, the absorptance also increases with the pitch, until it reaches a maximum. This can be explained by noticing that once light starts propagating into the grating, the active surface of the copper lines is larger and there is therefore more room for absorption through the sides of the lines, whereas light only penetrated the material from the topmost interface when $w = \Lambda$.

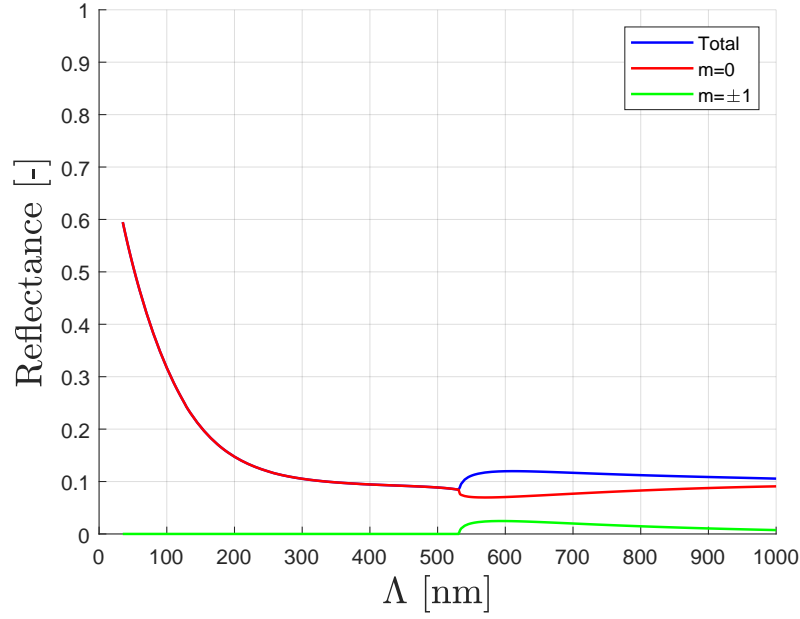


Figure 85: Reflectance spectrum of a normally incident TE polarized plane wave interacting with an array of copper lines with width $w = 34$ nm and height $h = 100$ nm, as a function of the pitch Λ . The plot features the different diffraction orders. The spectrum is calculated using FEM.

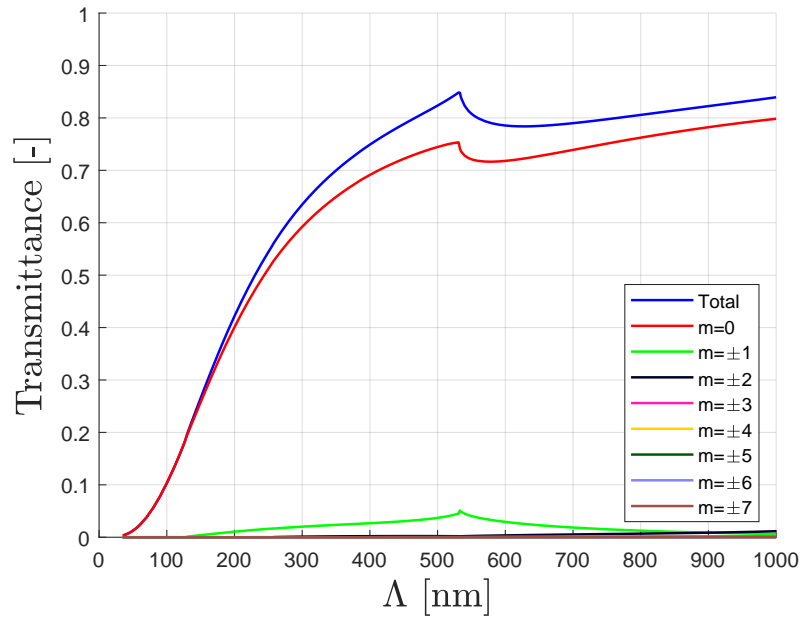


Figure 86: Transmittance spectrum of a normally incident TE polarized plane wave interacting with an array of copper lines with width $w = 34$ nm and height $h = 100$ nm, as a function of the pitch Λ . The plot features the different diffraction orders. The spectrum is calculated using FEM.

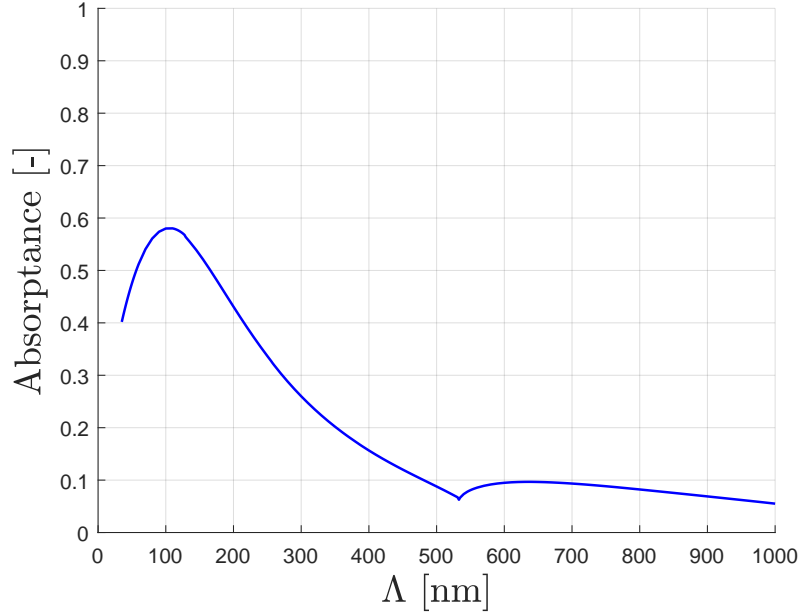


Figure 87: Absorptance spectrum of a normally incident TE polarized plane wave interacting with an array of copper lines with width $w = 34$ nm and height $h = 100$ nm, as a function of the pitch Λ . The spectrum is calculated using FEM.

The evolution of the TM spectra in Fig. 88 is a lot sharper at low pitch, as light quickly couples into the fundamental TM mode once the oxide starts filling the grating. Both polarizations seem to converge to the same R,T,A values of a silicon oxide slab as the pitch gets larger.

A second observation is that the diffraction occurs for the same pitch as it did for the PEC lines, comforting us in the idea that the diffraction dispersion relation is not impacted by the nature of the lines. The spectra for the diffraction modes have a similar shape to those observed for the PEC lines but they seem to be less efficiently excited in the case of copper lines.

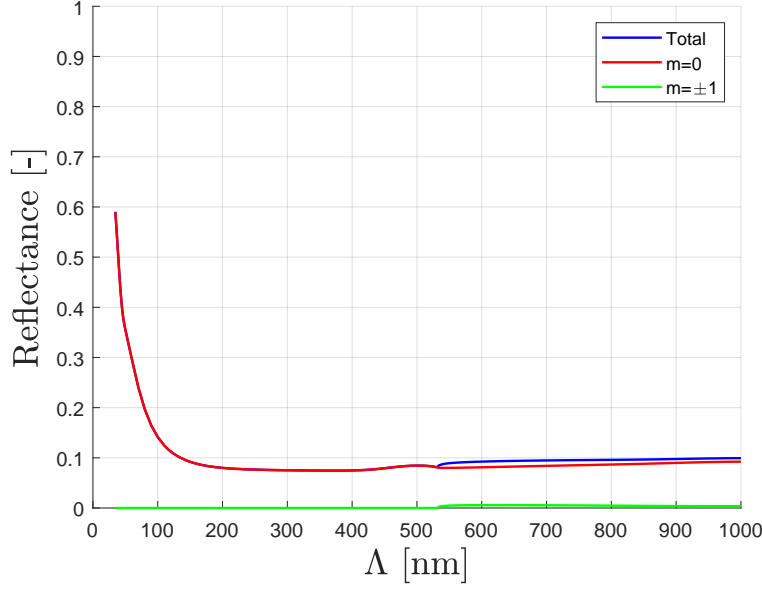


Figure 88: Reflectance spectrum of a normally incident TM polarized plane wave interacting with an array of copper lines with width $w = 34$ nm and height $h = 100$ nm, as a function of the pitch Λ . The plot features the different diffraction orders. The spectrum is calculated using FEM.

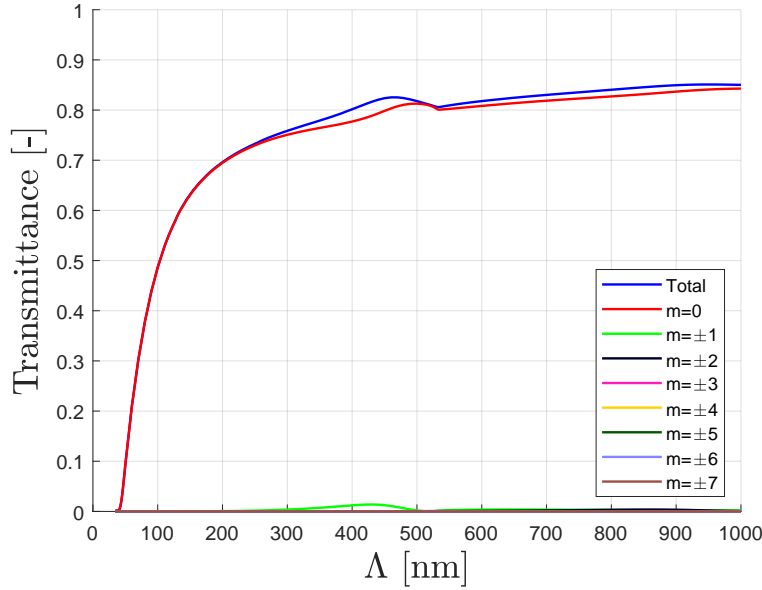


Figure 89: Transmittance spectrum of a normally incident TM polarized plane wave interacting with an array of copper lines with width $w = 34$ nm and height $h = 100$ nm, as a function of the pitch Λ . The plot features the different diffraction orders. The spectrum is calculated using FEM.

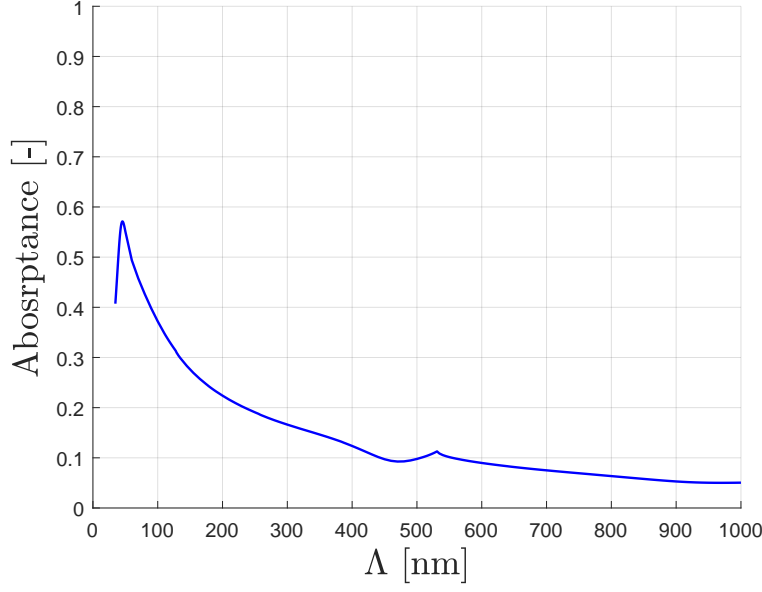
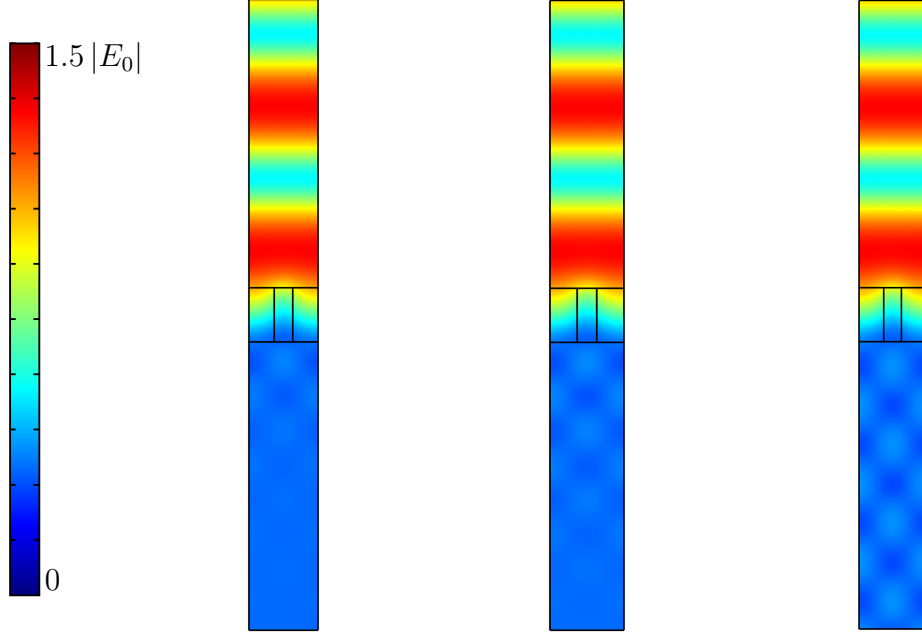


Figure 90: Absorptance spectrum of a normally incident TM polarized plane wave interacting with an array of copper lines with width $w = 34$ nm and height $h = 100$ nm, as a function of the pitch Λ . The spectrum is calculated using FEM.

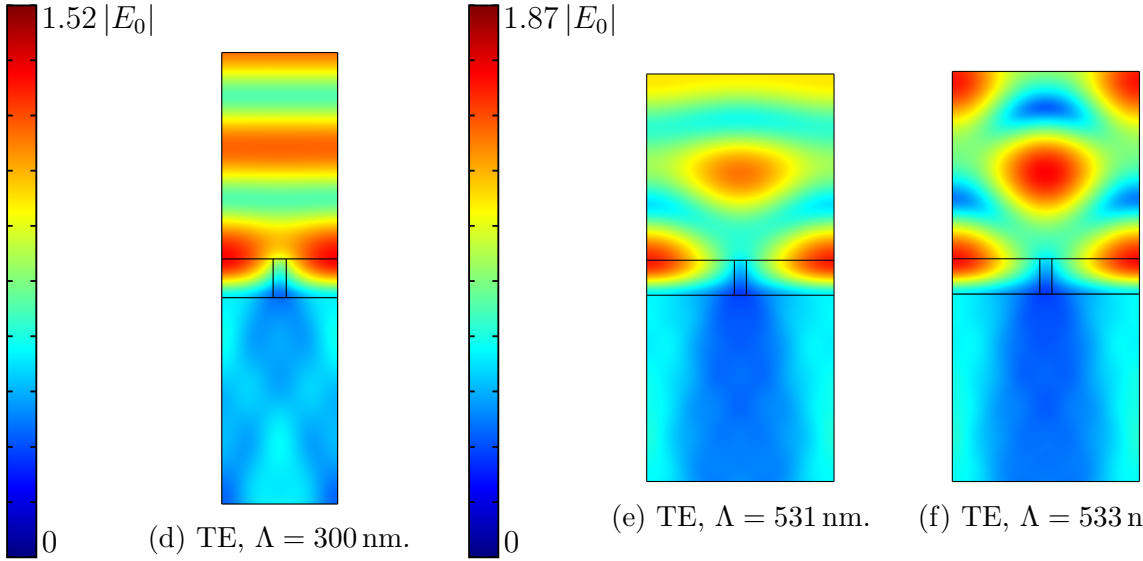
Let us have a look at some 2D maps of the electric field distribution to highlight the differences between the copper lines and PEC lines. Fig. 91 and 92 contain the electric field 2D maps for several key values of the pitch between 0 and 1000 nm.

Let us start with the TE polarization. The 2D maps of Fig. 91 indeed confirm that there is some transmission even at low pitch, as the norm of the electric field in the substrate is finite, and that there is no transition between fully evanescent and fully propagating but instead a smooth one. As a consequence of the finite transmittance, the first diffraction mode in transmission is now visible in the case of TE polarization, where it was not the case for the PEC lines. The transition from evanescent to propagating mode is clearly visible in Figs. 91a to 91c. In addition, the 2D maps show that the electric field is not 0 inside the metallic lines, like it was for PEC. Instead, the field is finite but is quickly attenuated when moving away from the edges. The field is also attenuated in the oxide, as the modes are not either propagating or evanescent but always a combination of the two, so there is also some attenuation there. Around 128 nm for example, the band structure of Fig. 83 indicates that the extinction coefficient of the TE_1 mode is close to 1, which is two times lower than the extinction coefficient of copper at for a wavelength of 532 nm. From the same band structure, it can be inferred that the extinction coefficient of the TE_1 mode will decrease as the pitch increases and more light will reach the substrate, leading to more transmission. In both the PEC and copper cases, the continuity of the tangential components of the electric field is satisfied.

The 2D maps also show that the maximum intensity of the electric field is lower than it was for PEC lines. This is both due to absorption and transmission: some of the intensity is lost



(a) TE, $\Lambda = 127$ nm. (b) TE, $\Lambda = 128$ nm. (c) TE, $\Lambda = 129$ nm.



(d) TE, $\Lambda = 300$ nm.

(e) TE, $\Lambda = 531$ nm. (f) TE, $\Lambda = 533$ nm.

directly through absorption through the lines, while a portion of the light is transmitted, spreading the power more evenly. As a consequence, the standing wave observed on top of the grating for low pitch does not have peaks at $2|E_0|$ but at $1.5|E_0|$ and does not have nodes at 0 but at some finite value. Moreover, the diffraction modes are excited a lot less intensely than with the PEC lines, and the diffracted wave in reflection is weaker for the copper lines, resulting in less intense interference patterns. At pitches between 532 nm and 1000 nm, the field looks more like the incident plane wave than the pattern resulting from intense interferences.

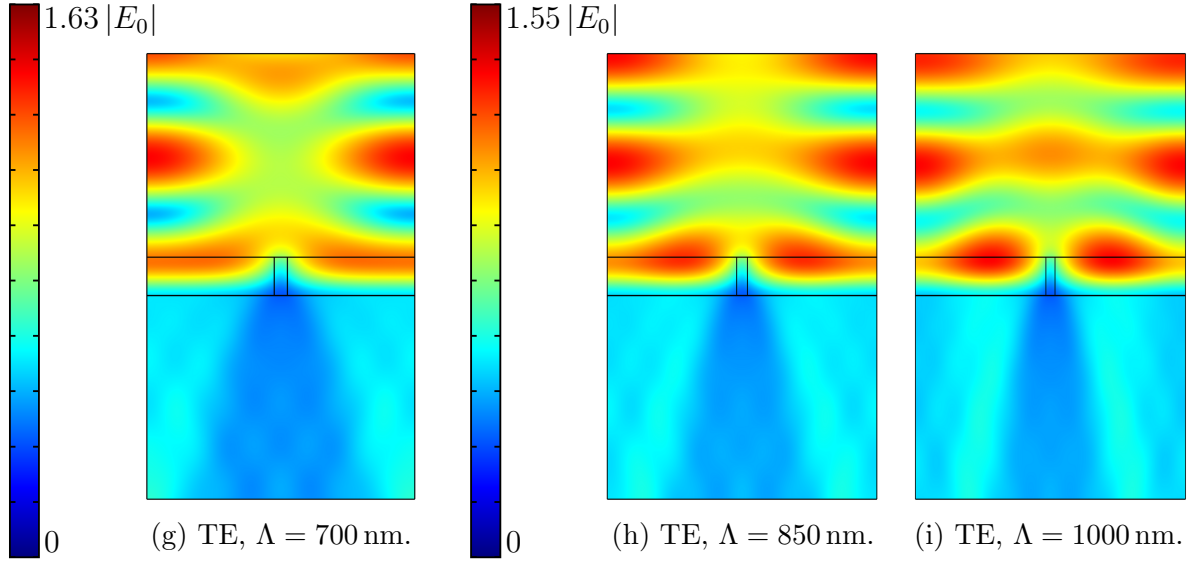
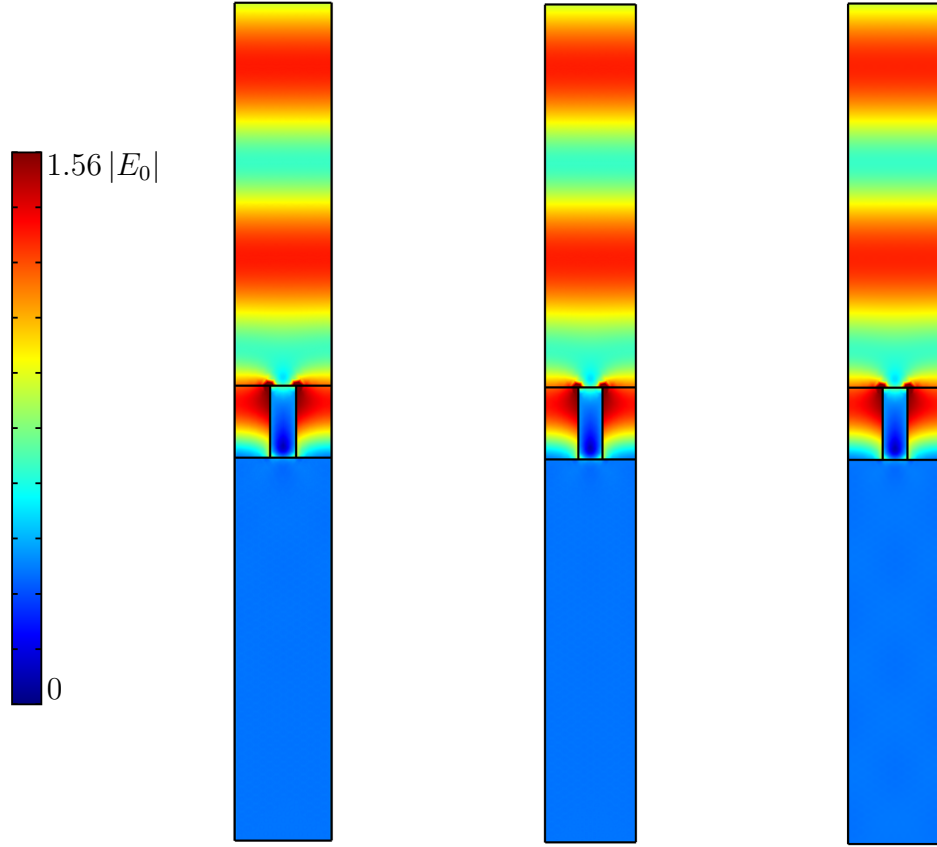
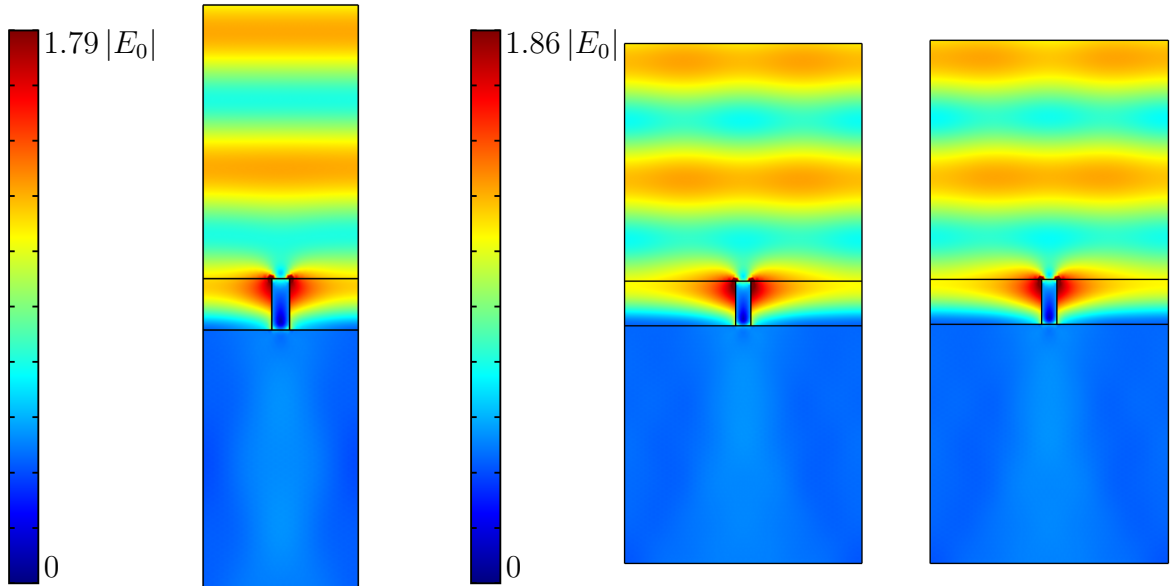


Figure 91: Distribution of the phasor norm of the TE electric field in the unit cell, for an array of copper lines with width $w = 34$ nm, height $h = 100$ nm, and for several pitches between 0 nm and 1000 nm.

Let us now move to TM polarization. Surprisingly, the diffraction order in transmission at 128 nm is no longer visible in the 2D maps of Fig. 92. However some interference patterns are visible for higher pitches. The diffraction in reflection is even weaker than for the TE polarization and little change is observed in the electric field distribution when sweeping the pitch values: the field above the grating does not shift much from its initial plane wave geometry as the diffracted reflected wave does not cause much interferences. The electric field inside the copper is a lot less intense than the one in the oxide, as permitted by the discontinuity of the normal component of the electric field. Due to the low amount of diffraction, the reflectance and transmittance spectra both vary very smoothly from their minimum (resp. maximum) to maximum (resp. minimum) value, with little interferences.



(a) TM, $\Lambda = 127$ nm. (b) TM, $\Lambda = 128$ nm. (c) TM, $\Lambda = 129$ nm.



(d) TM, $\Lambda = 300$ nm.

(e) TM, $\Lambda = 531$ nm. (f) TM, $\Lambda = 533$ nm.

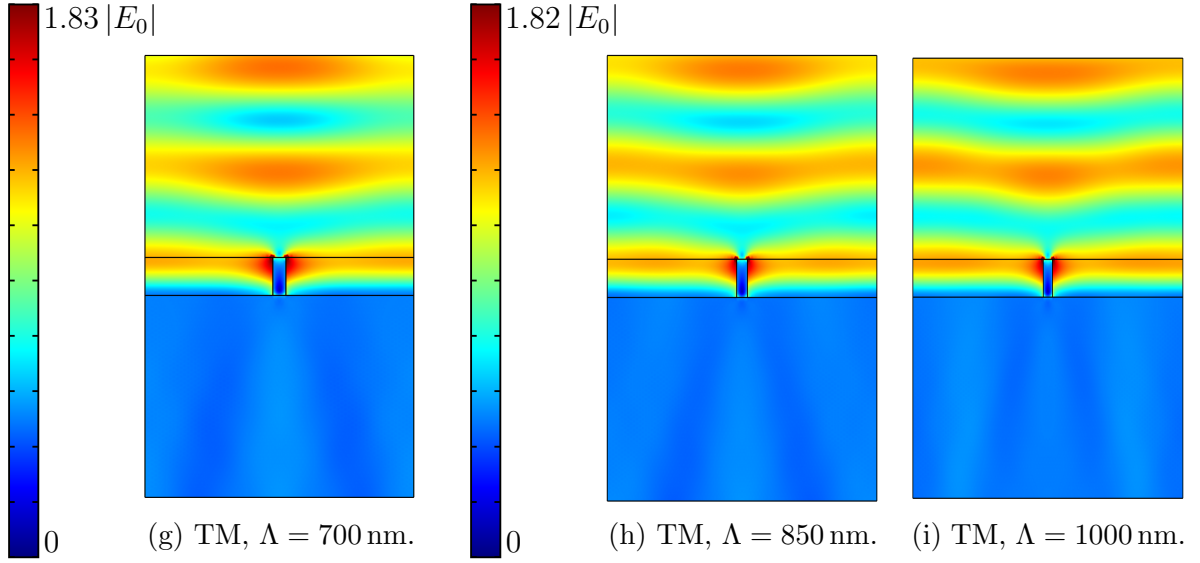


Figure 92: Distribution of the phasor norm of the TM electric field in the unit cell, for an array of copper lines with width $w = 34$ nm, height $h = 100$ nm, and for several pitches between 0 nm and 1000 nm.

4.2.2 Effect of width

The effect of the width on the array of copper lines is now compared with respect to its effect on the array of PEC lines. Figs. 93 and 94 (resp. 95 and 96) depict the reflectance and transmittance spectra for TE (resp. TM) polarization as a function of the width, for a fin height of 100 nm and several pitches between 0 nm and 1000 nm.

The reflectance for the TE polarization in Fig. 93 does not feature the cutoff of the PEC lines, where the reflectance would go to 1 as soon as $\Lambda - w = 217$ nm. Here instead, the reflectance start from its value for an oxide slab and smoothly increases to its value for a copper thin film. At low pitch, this increase is smoother as there is no diffraction mode to induce any oscillation. Some small oscillations are however visible for higher pitches. In fact, the results are very similar to the PEC lines in terms of shape of the spectra. Indeed, the effect of the cutoff put aside, the reflectance spectrum of the TE polarization looks like a scaled down version of the PEC case: the reflectance is minimum when the width is minimum and increases with it. The main difference lies in the maximum value of the reflectance: it goes up to 1 for a PEC slab but only up to around 0.6 for the copper slab, as is expected from the finite optical constants and absorptance.

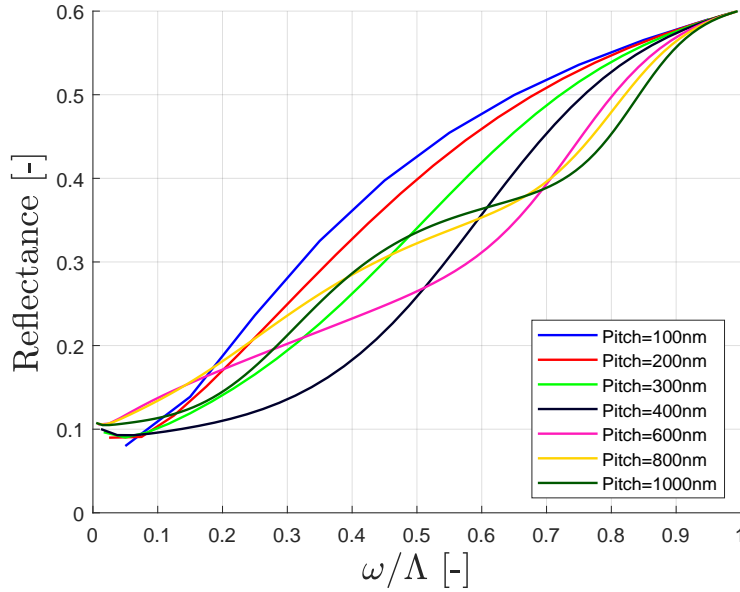


Figure 93: Reflectance spectrum of a normally incident TE polarized plane wave interacting with an array of copper lines for several pitches for a height $h = 100$ nm, as a function of the fill factor w/Λ . The spectrum is calculated using FEM.

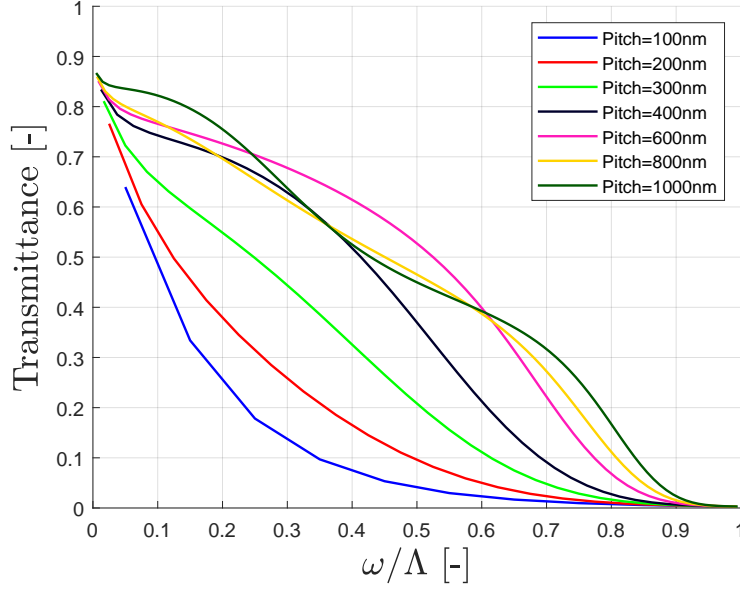


Figure 94: Transmittance spectrum of a normally incident TE polarized plane wave interacting with an array of copper lines for several pitches for a height $h = 100$ nm, as a function of the fill factor w/Λ . The spectrum is calculated using FEM.

For the TM polarization, the different curves in Fig. 95 are a lot more similar than for the PEC ones. However, the same comments can somewhat be made for the TM polarization regarding the graph being a scaled down version of the PEC one, although due to absorption, the minimum in reflectance observed in Fig. 95 no longer corresponds to a maximum in transmittance, as can be seen in Fig. 96. In addition, there is more no obvious minimum in reflectance (or EOT) to be seen. The reason is that the thin-film interferences observed for the PEC lines do not occur at the same pitch for the copper lines and that there is absorption. In addition, the reflectance increases almost linearly for all pitches when the fill factor approaches 1. Whereas some light was still transmitted at low pitch for the PEC lines, there is almost no transmission when the fill factor is larger than 0.6 as the light coupled into the fundamental TM mode is also absorbed. Finally, less oscillations are visible in general due to the more weakly excited diffraction orders.

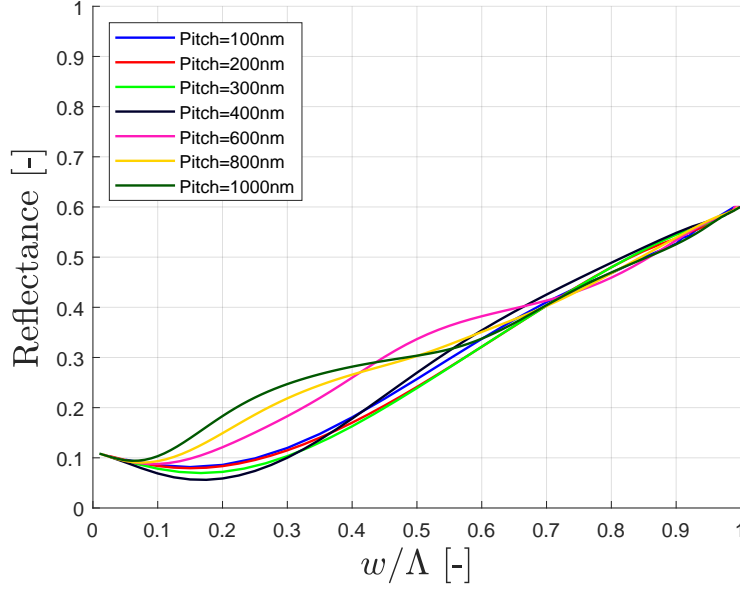


Figure 95: Reflectance spectrum of a normally incident TM polarized plane wave interacting with an array of copper lines for several pitches for a height $h = 100$ nm, as a function of the fill factor w/Λ . The spectrum is calculated using FEM.

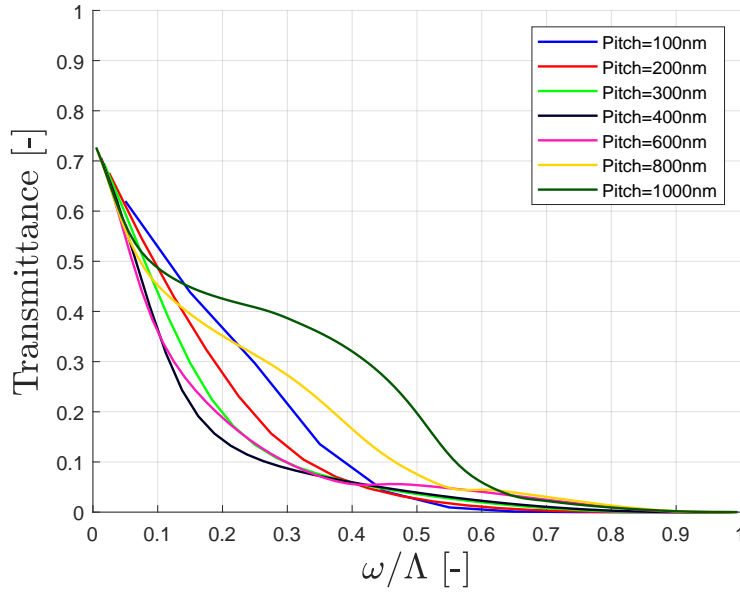


Figure 96: Transmittance spectrum of a normally incident TM polarized plane wave interacting with an array of copper lines for several pitches for a height $h = 100$ nm, as a function of the fill factor w/Λ . The spectrum is calculated using FEM.

The comments about diffraction are highlighted by considering a pitch $\Lambda = 1000$ nm. They can be further highlighted by removing some of the diffraction induced by the high

pitch value and considering a array with 400 nm pitch, as it was done for the PEC grating. The results are pictured in Figs. 97 and 98 (resp. 99 and 100) for the TE and TM spectra for a pitch $\Lambda = 1000$ nm (resp. $\Lambda = 400$ nm). For a pitch of 1000 nm, the first diffraction mode is again excited as soon as the fill factor is different than 0 or 1, as it was the case for the PEC lines. The curves are very similar to the PEC ones as the same diffraction orders are excited in the same proportions and the main difference lies in the maximum reflectance value. At $\Lambda = 400$ nm, the power is again entirely located in the fundamental mode for the reflectance and the graph is mostly a scaled down version of the PEC reflectance, to which the same comment on the maximum reflectance value applies.

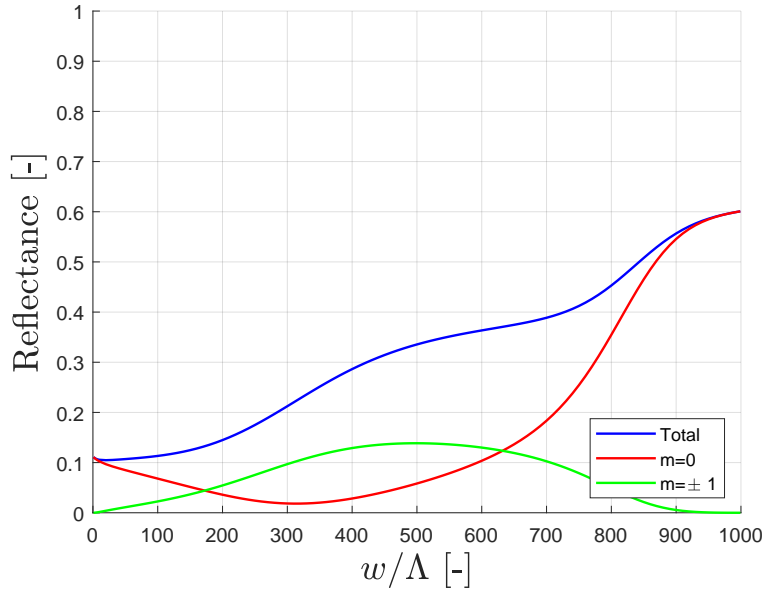


Figure 97: Reflectance spectrum of a normally incident TE polarized plane wave interacting with an array of copper lines with pitch $\Lambda = 1000$ nm and height $h = 100$ nm, as a function of the width w . The plot features the different diffraction orders. The spectrum is calculated using FEM.

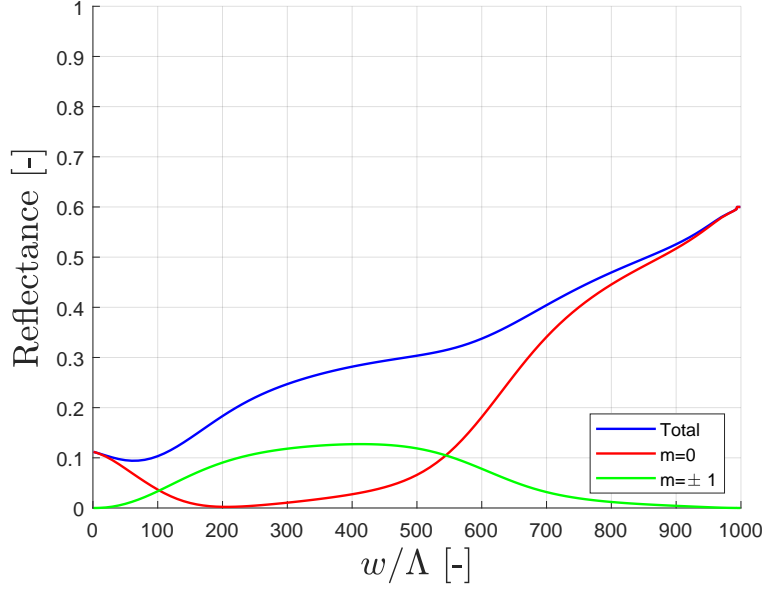


Figure 98: Reflectance spectrum of a normally incident TM polarized plane wave interacting with an array of copper lines with pitch $\Lambda = 1000$ nm and height $h = 100$ nm, as a function of the width w . The plot features the different diffraction orders. The spectrum is calculated using FEM.

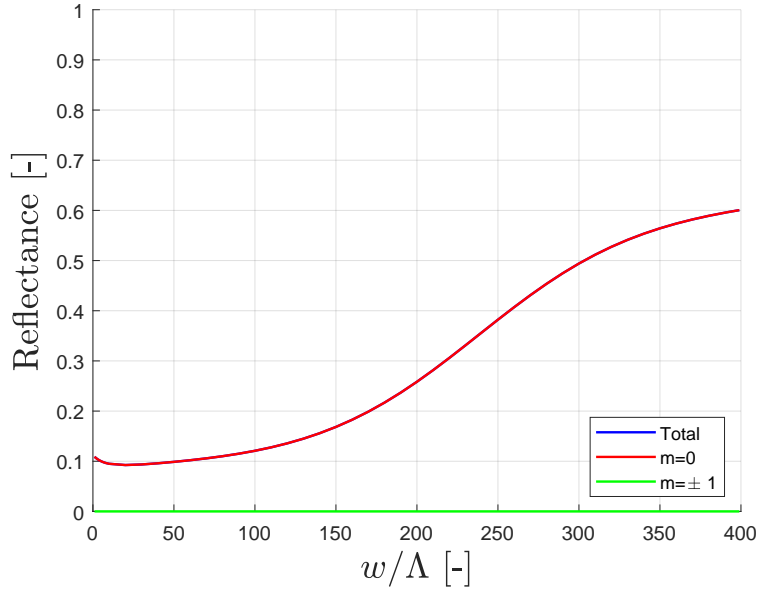


Figure 99: Reflectance spectrum of a normally incident TE polarized plane wave interacting with an array of copper lines with pitch $\Lambda = 400$ nm and height $h = 100$ nm, as a function of the width w . The plot features the different diffraction orders. The spectrum is calculated using FEM.

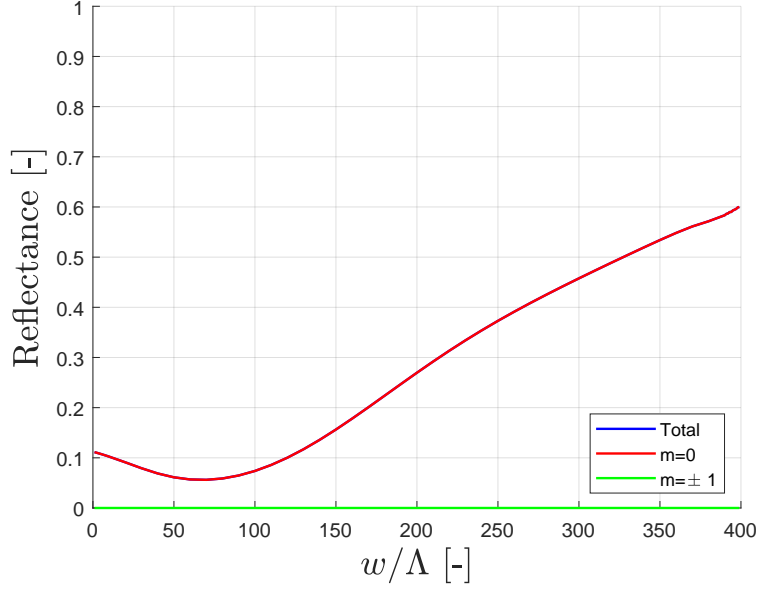


Figure 100: Reflectance spectrum of a normally incident TM polarized plane wave interacting with an array of copper lines with pitch $\Lambda = 400$ nm and height $h = 100$ nm, as a function of the width w . The plot features the different diffraction orders. The spectrum is calculated using FEM.

Now that a real metal is considered, it might be possible to observe surface plasmon polaritons (SPPs). As explained in section 2.6.3, those field enhancement confined to the metal and propagating along its surface can be excited if there is a longitudinal component of the electric field. At normal incidence, this component is maximum at the passing of a diffraction order, when the angle associated to the diffracted mode is 90° . Fig. 101 shows the comparison between the distribution of $|E_y|^2$ for a copper thin film and PEC thin film.

As can be seen, there is a concentration of the electric field localized on the metal surface for the copper, which is absent in the case of the PEC. Indeed, Fig. 101a can be seen as a superposition of Figs. 25a and 25c. This indicates that an electromagnetic wave travels laterally at the metal-air interface. As the width is varied, a resonance effect can be observed where the SPPs reflected as the edge of the thin film interfere together and they become more intense when $w \approx \lambda_0/2$. The presence of SPPs is a manifestation of the absorbing nature of the metal, however their direct effect on the reflectance and transmittance spectra presented in this section are unclear, as their impact is shadowed by that of diffraction, and a mode decomposition method is required to separate their various consequences, which is out of the scope of this master thesis. Besides, it is the effect of the geometrical parameters on the general reflectance and transmittance spectra that this study is concerned with, which is why the SPPs are not studied in more details. It should also be noted that SPPs were not observed in transmission in these simulations.

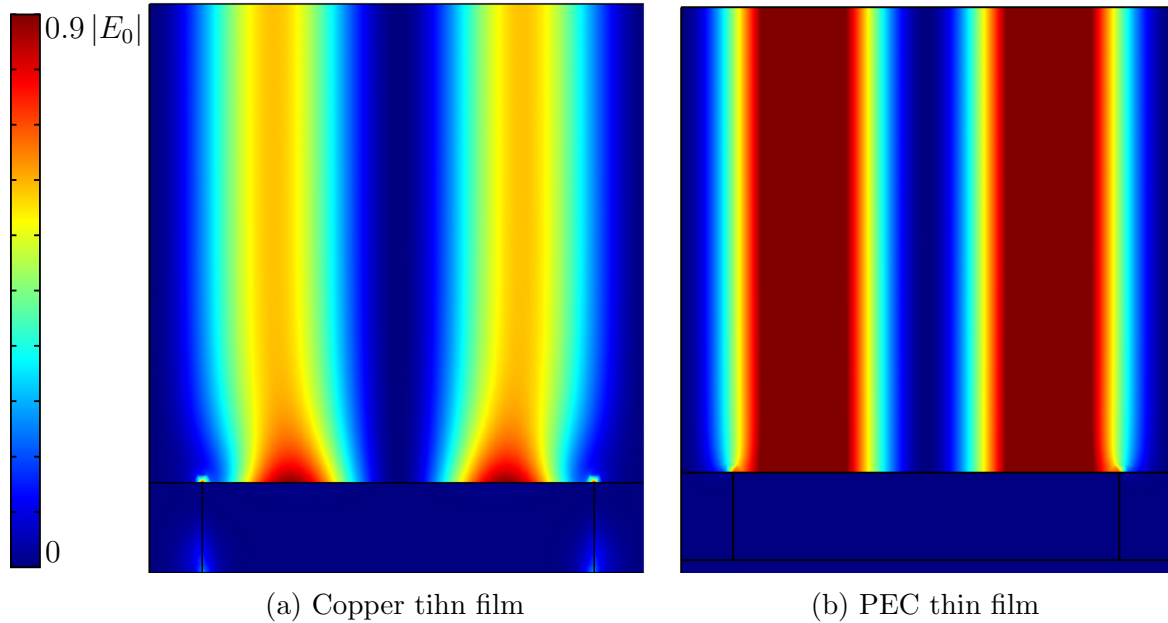


Figure 101: Distribution of the squared norm of the y electric field component $|E_y|^2$ at a pitch $\Lambda = 533$ nm, i.e. at the passing of the first diffraction order in reflection, for a 100 nm thin film with width $w = 420$ nm under TM illumination at $\lambda_0 = 532$ nm.

4.2.3 Effect of height

In the same fashion as for the PEC lines, the height of the lines is increased to $h = 500$ nm to highlight the effect of taller lines while varying the pitch. Figs. 102 to 104 feature the R, T and A spectra of the TE polarization while Figs. 105 to 107 feature those of the TM polarization.

For the TE polarization, one can quickly see that the absorptance is larger for 500 nm than it is for 100 nm. The reason is obvious: the copper lines being taller, there is a higher quantity of absorbing material. Looking at the reflectance spectrum, one can distinguish some slight oscillations around 200 nm and 600 nm. Those pitch regions correspond to the cutoff pitch regions of the TE_1 and TE_3 modes. The origin of those oscillations is the same that was discussed in the case of the PEC lines, however they are a lot less intense for the copper lines. Let us recall that for the PEC grating, the oscillations had their origin in the rapidly varying refractive index of a mode as a function of the pitch. As a consequence, the conditions for peaks due to thin-film interference were quickly scanned over, leading to fast oscillations. In the case of copper lines, one can see from the band structure of Fig. 83 that the refractive index vary a lot more slowly around the cutoffs than the PEC did, leading to less intense oscillations. With taller lines, the diffraction modes are also now more efficiently excited. This could be due to the modification of the electric field distribution inside the grating, which taller line allows for several wavelengths to develop which can lead to a better matching between the grating electric field and that of the diffraction modes.

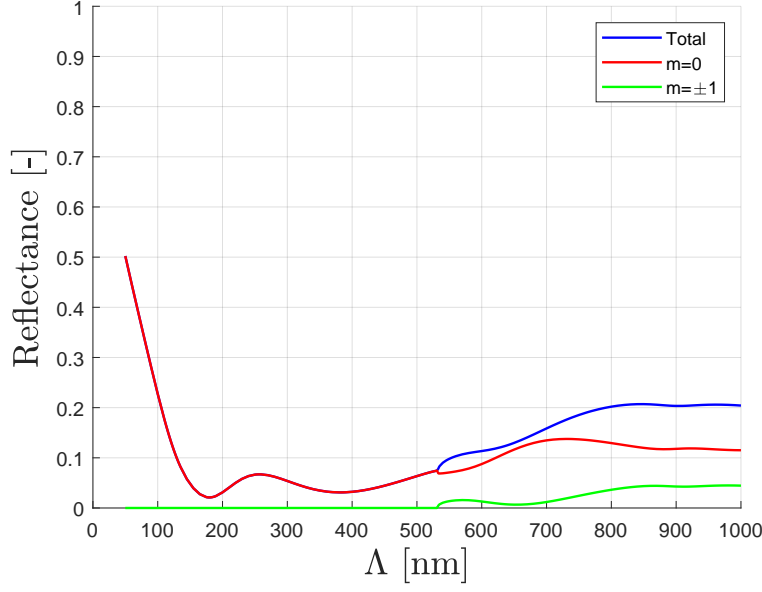


Figure 102: Reflectance spectrum of a normally incident TE polarized plane wave interacting with an array of copper lines with width $w = 34$ nm and height $h = 500$ nm, as a function of the pitch Λ . The plot features the different diffraction orders. The spectrum is calculated using FEM.

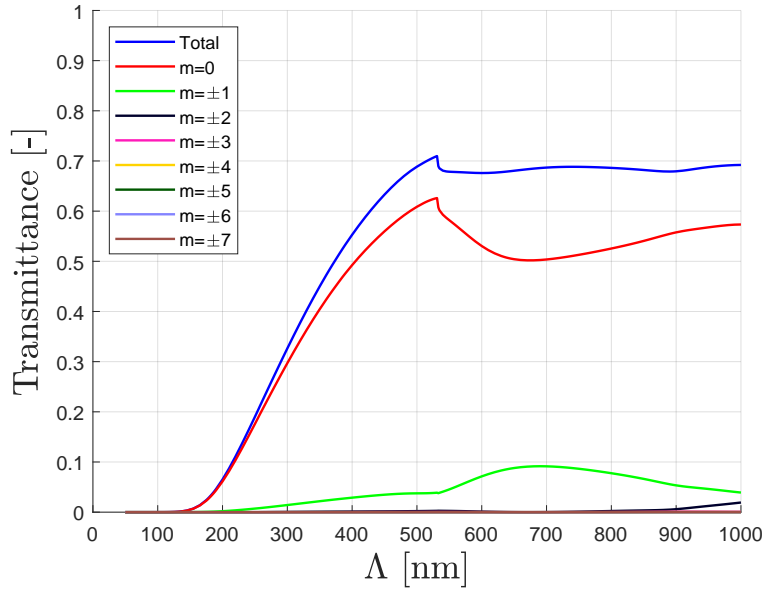


Figure 103: Transmittance spectrum of a normally incident TE polarized plane wave interacting with an array of copper lines with width $w = 34$ nm and height $h = 500$ nm, as a function of the pitch Λ . The plot features the different diffraction orders. The spectrum is calculated using FEM.

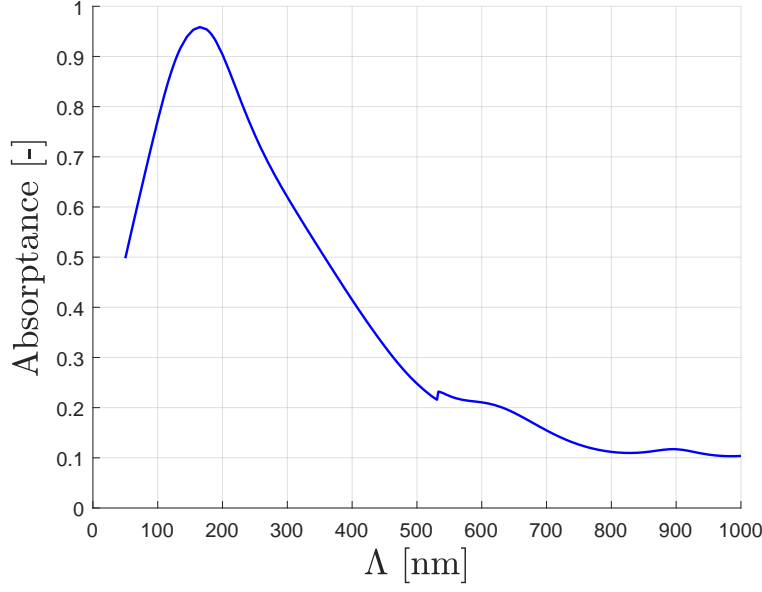


Figure 104: Absorptance spectrum of a normally incident TE polarized plane wave interacting with an array of copper lines with width $w = 34$ nm and height $h = 500$ nm, as a function of the pitch Λ . The spectrum is calculated using FEM.

For the TM polarization, the same observations as for the PEC grating can be made: since most of the light couples into the fundamental TM mode, which refractive index vary slowly if at all, as seen the band structure of Fig. 84, there is little oscillation in the spectra due to the thin-film interference induced by a pitch variation. However, the elbow at around 100 nm pitch is more pronounced now than for the 100 nm tall lines, as a result of thin-film interferences, which resonant effect is manifestly more intense for 500 nm. This result is opposite to that of the PEC grating but since the effective refractive indices of each mode differ it is natural that the conditions for peaks are affected and differ from copper to PEC. Again, the diffraction orders are more efficiently excited.

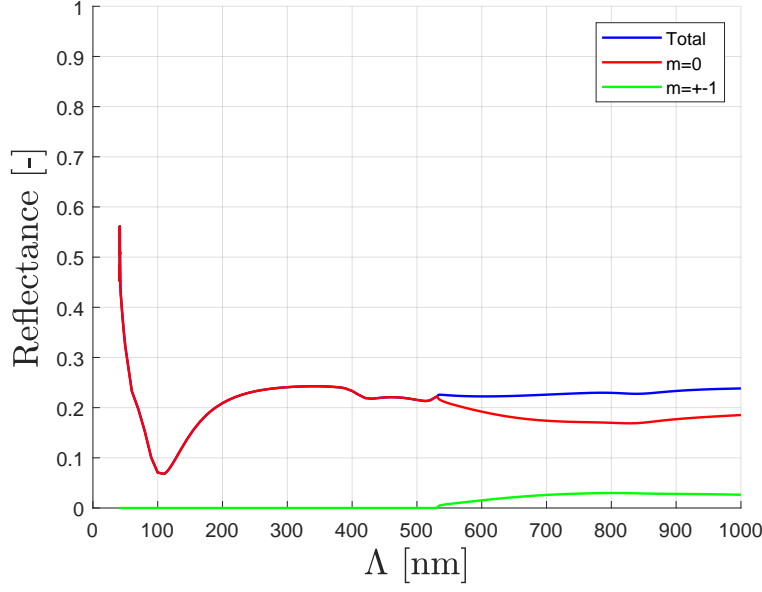


Figure 105: Reflectance spectrum of a normally incident TM polarized plane wave interacting with an array of copper lines with width $w = 34$ nm and height $h = 500$ nm, as a function of the pitch Λ . The plot features the different diffraction orders. The spectrum is calculated using FEM.

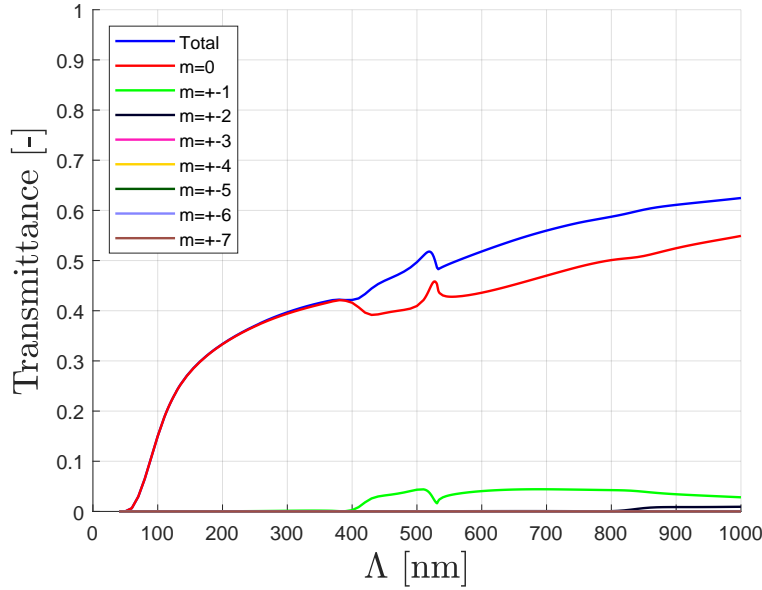


Figure 106: Transmittance spectrum of a normally incident TM polarized plane wave interacting with an array of copper lines with width $w = 34$ nm and height $h = 500$ nm, as a function of the pitch Λ . The plot features the different diffraction orders. The spectrum is calculated using FEM.

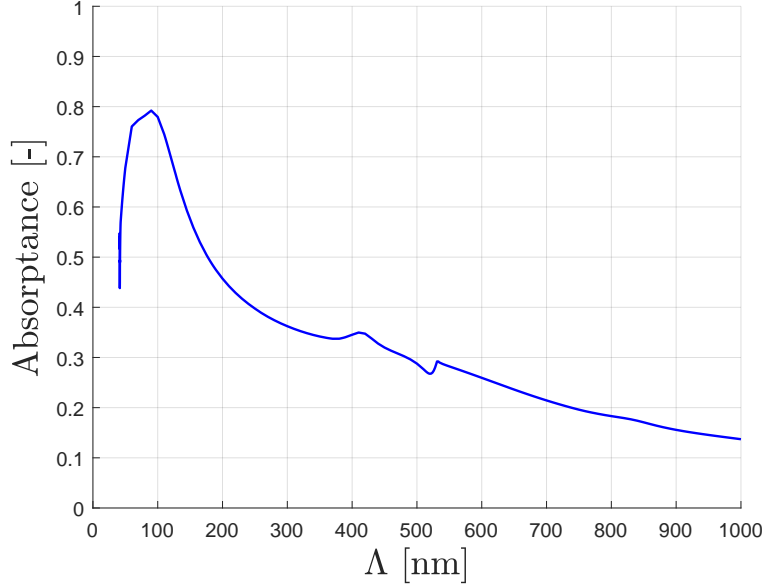
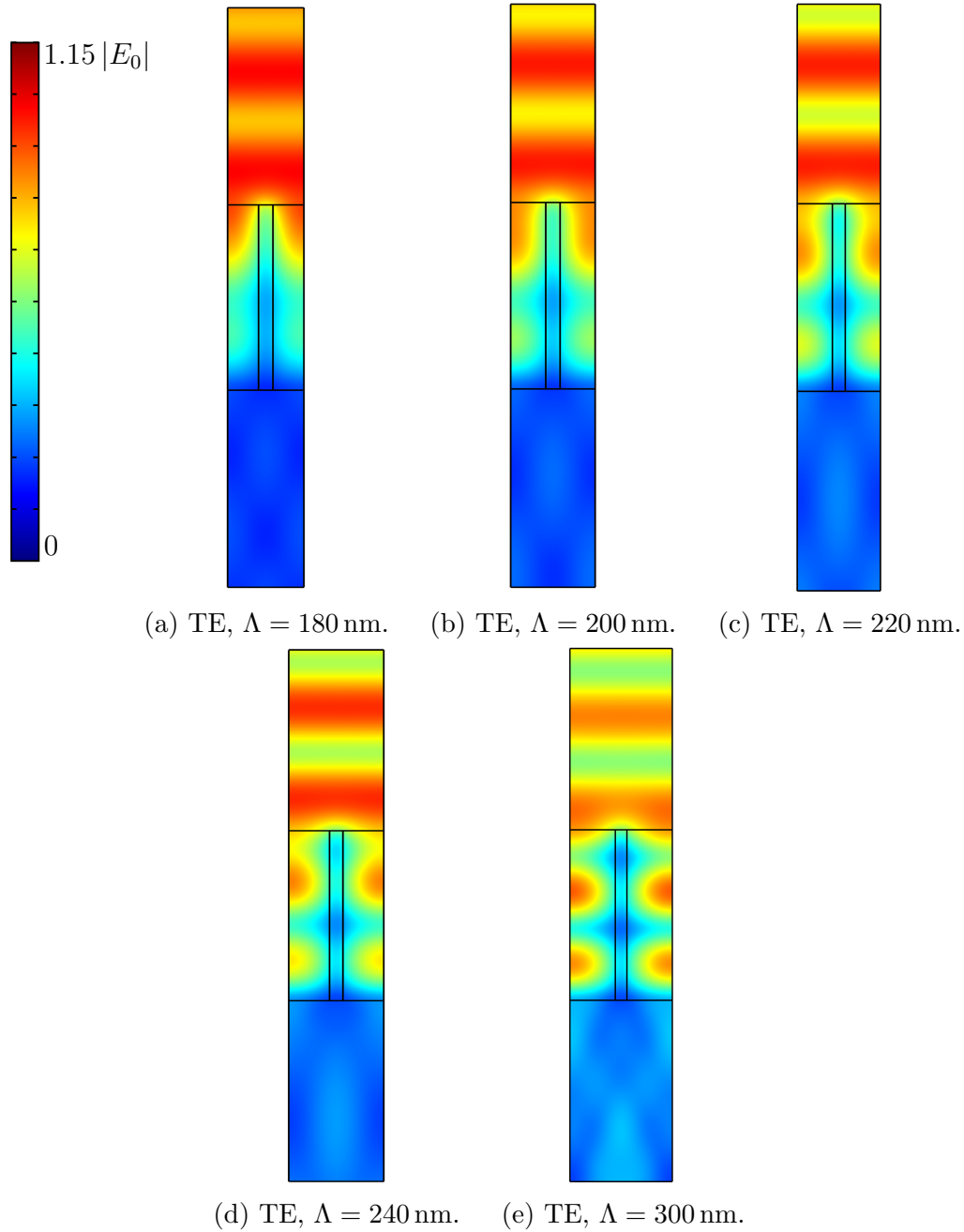


Figure 107: Absorptance spectrum of a normally incident TM polarized plane wave interacting with an array of copper lines with width $w = 34$ nm and height $h = 500$ nm, as a function of the pitch Λ . The spectrum is calculated using FEM.

The previous observations can be highlighted by looking at some 2D maps of the electric field distribution for a grating of 500 nm tall copper lines. Figs. 108 and 109 respectively the 2D maps for TE and TM polarizations.

For TE, it is interesting to look at the transition of the TE_1 mode. As it was discussed previously, with copper lines, the transition is not very sharp but rather smooth. Figs. 108a to 108e show how light is increasingly transmitted as the TE_1 mode becomes less and less attenuating. Thanks to the taller lines, it is possible to visualize several wavelengths of the mode, which has a similar distribution in the oxide than the PEC TE_1 mode, but in this case there is a non-zero electric field inside the line. In addition, it is possible to visualize how the intensity of the electric field is decreased as the wave propagate in the grating, and less so as the pitch increases and the extinction coefficient of the mode decreases accordingly. On top of the grating, the standing wave has peaks (resp. nodes) with even lower (resp. higher) electric field intensity than with the 100 nm tall lines. Indeed, with taller lines, even less light can make a round trip and interference with the incoming plane wave to create a standing wave, but these interferences increase as the pitch increases and light is less attenuated as it travels inside the grating. Around 500 nm, Figs. 108f to 108h show how the electric field distribution in the grating is modified, both due to the diffracted mode in reflection but also due to the TE_3 mode being less and less evanescent in this pitch range. A similar behavior was observed for the PEC lines although the transition occurred for a higher pitch and was sharper. Also, the field does not change that much as a result of oscillations, which are weaker in the case of copper lines. Moving to higher pitch ranges, Figs. 108i to 108k allow us to see that the field inside the grating is quite similar to that of the PEC grating, although

less intense. Indeed, the field inside the grating is mostly a superposition of the TE_1 and TE_3 modes. At those high pitches, they are weakly attenuated as they propagate. Finally, the interference patterns on top of the grating are more visible in the case of 500 nm tall line due to the more efficiently excited diffraction modes.



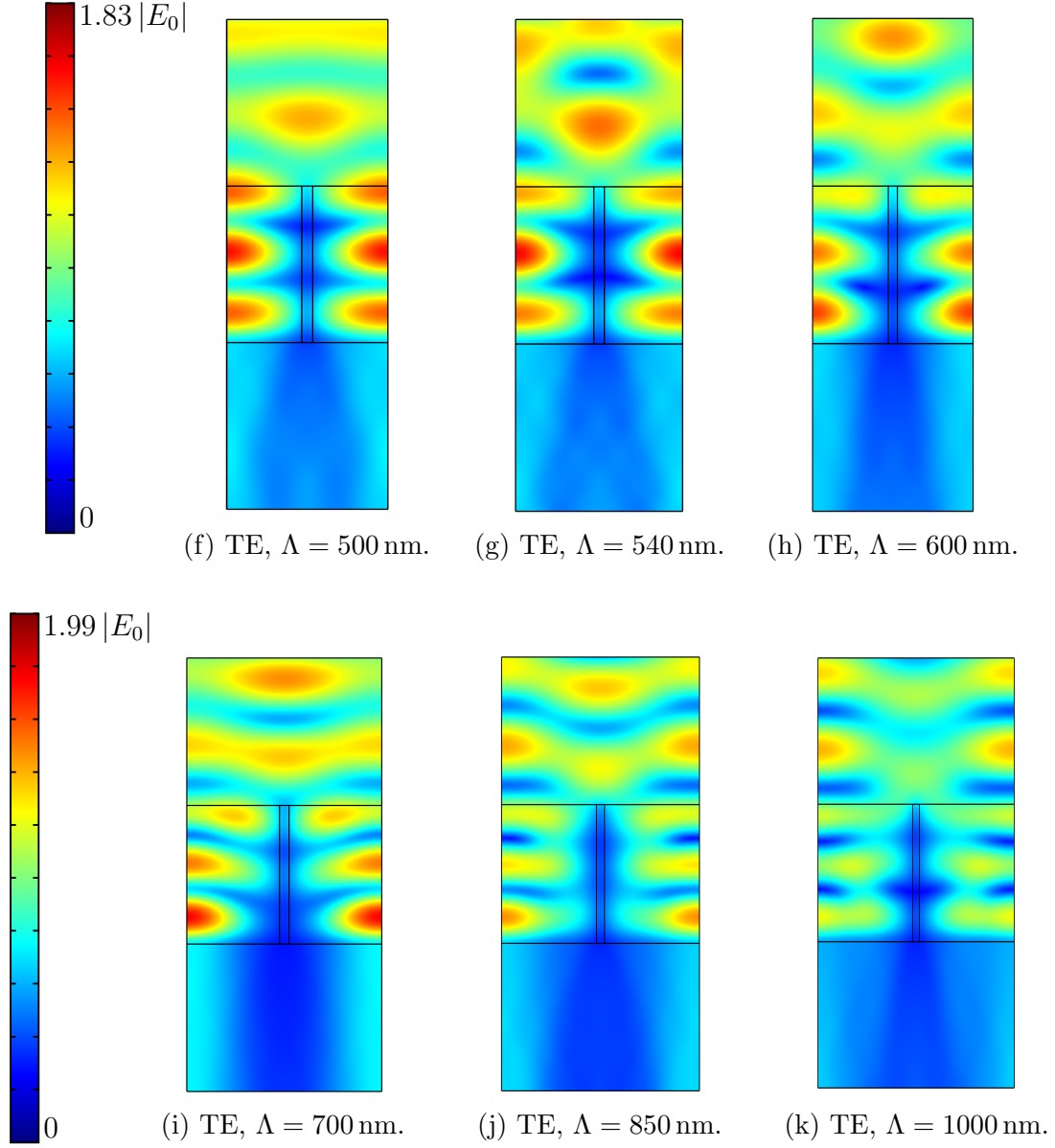
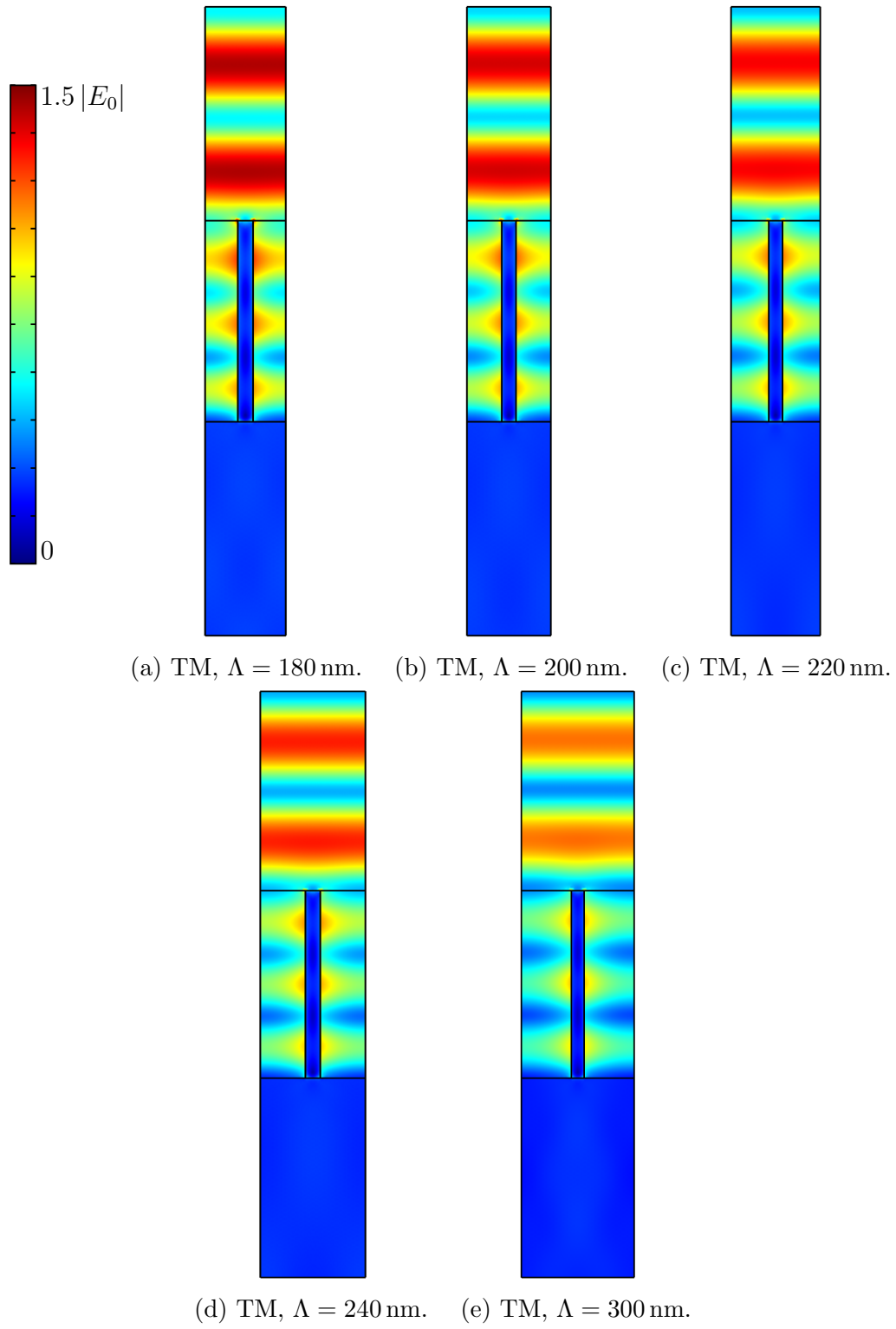


Figure 108: Distribution of the phasor norm of the TE electric field in the unit cell, for an array of copper lines with width $w = 34$ nm, height $h = 500$ nm, and for several pitches between 0 nm and 1000 nm.

For the TM polarization, Fig. 109 shows that the wavelengths are already visible from the start, according to the presence of the TM_0 mode. The mode is also less attenuated than for the TE polarization. Those observations are in accordance with the low extinction coefficient of the TM_0 mode observed in the band structure of Fig. 84. Here, the field is more intense close to the copper line, whereas it was uniform for the PEC lines: in the case of a real absorbing metal, the fundamental TM_0 mode is no longer an homogeneous plane wave as it was for the PEC waveguide. Due to the finite conductivity of the metal, the spatial distribution of the electric field is affected close to the line and its intensity decreases further into the oxide. It is also interesting to notice the presence of another mode than the TM_0 one as the pitch increases: the electric field spatial distribution no longer is uniform but the field in the center of the oxide becomes more intense. This feature was only weakly observed in the case of the PEC lines. Finally, the interference patterns on top of the grating are also more visible than they were for the 100 nm tall lines.



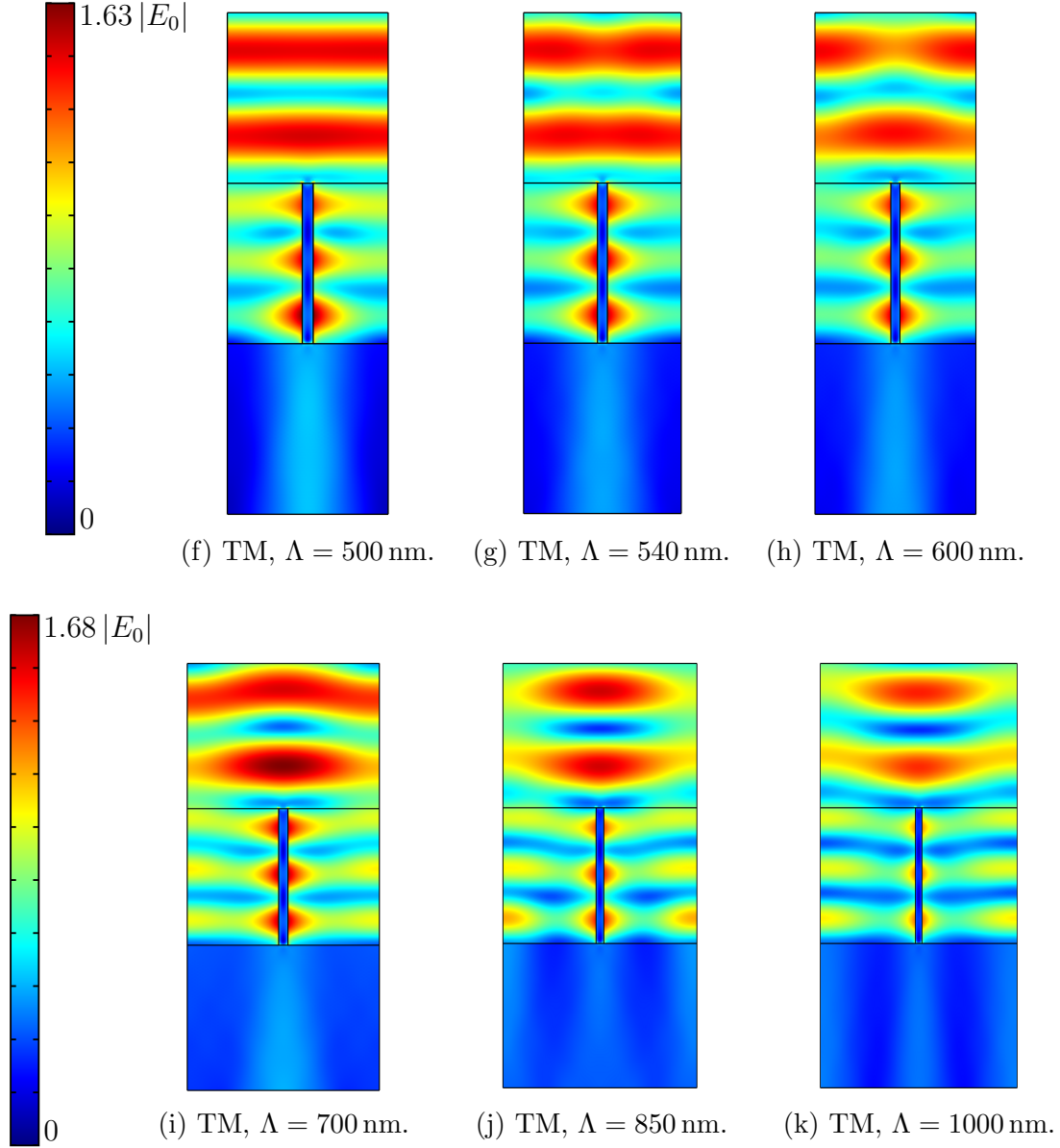


Figure 109: Distribution of the phasor norm of the TM electric field in the unit cell, for an array of copper lines with width $w = 34$ nm, height $h = 500$ nm, and for several pitches between 0 nm and 1000 nm.

It was just seen how the reflectance, transmittance and absorptance spectra of the grating evolved when the height of lines was increased from 100 nm to 500 nm. It is now time to see how the spectra vary as a function of the height, for different values of the pitch. Figs. 110 and 111 respectively feature the TE and TM reflectance spectra of the copper array as a function of the height.

To begin with, in the case of TE polarization for a 100 nm pitch, the reflectance quickly goes to a constant finite value, which is not 1 like it was for the PEC lines . This is due to two factors: first, the growing line which absorbs more and more light and second, the high extinction coefficient of the grating modes at low pitch. As a consequence, as the height increases less and less light reaches the substrate until no light is able to make a round trip in the grating and the value taken by the reflectance is therefore only that of the air/substrate interface, which is now independent of the height of the grating. The reflectance for 200 nm is lower since light can transmit into the grating more efficiently as the TE_1 mode becomes available. Some slight oscillations are visible due to thin-film interferences but the reflectance also converges to a constant as more and more copper is there to absorb light when the height is increased. For larger values of the pitch, the extinction coefficient of the fundamental TE_1 mode is negligible and the attenuation is now only due to the copper absorption. As a result, thin-film interferences can now fully take place as it is seen for the higher pitches. Those oscillations are however damped by the copper absorption and the reflectance always eventually converges to a constant as the height becomes large enough to absorb everything. In opposition to the PEC lines, the different curves are not too different from each other and slowly seem to converge to a common one that would be that of a silicon oxide slab, whereas each curve was very different for the PEC case, again due to the quickly varying refractive index of the PEC modes compared to the copper modes. Indeed, the refractive index of the TE_1 mode featured in Fig. 83 is almost constant and very slowly increases with the pitch, leading to very similar curves for each pitch for thin-film interferences.

Looking at the TM polarization, the behavior is similar to that of the PEC lines although here there is more variation as the refractive index of the TM_0 mode is less constant as a function of pitch than the one for PEC, and therefore there is more variations in the different curves, as it is seen here. Again, the curve for 100 nm is the most shifted as in that case the refractive index changes a lot when the array is further filled with reflecting and absorbing copper, i.e., at low pitch. The same difference between PEC and copper is present here too as the oscillations are damped as a function of the height by the growing absorbing lines.

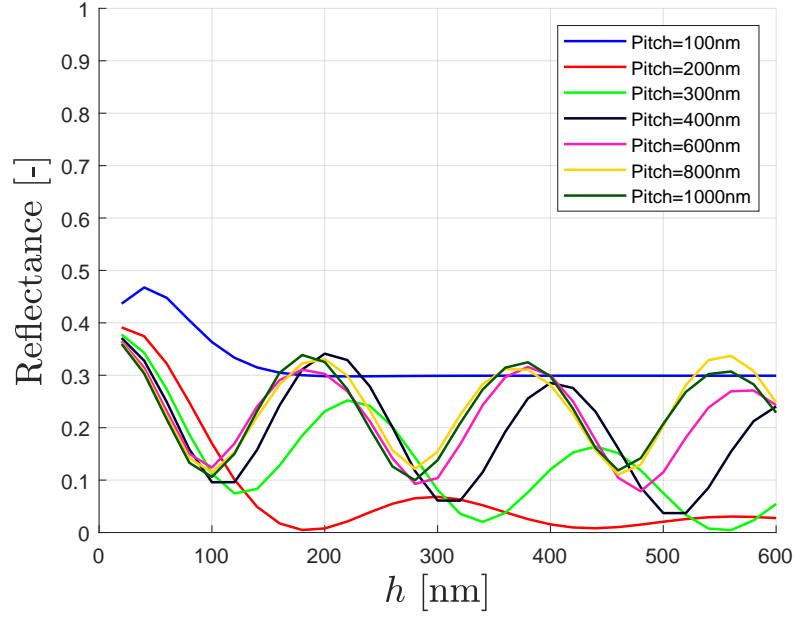


Figure 110: Reflectance spectrum of a normally incident TE polarized plane wave interacting with an array of copper lines with width $w = 34$ nm as a function of the height h . The plot features several values for the pitch of the grating. The spectrum is calculated using FEM.

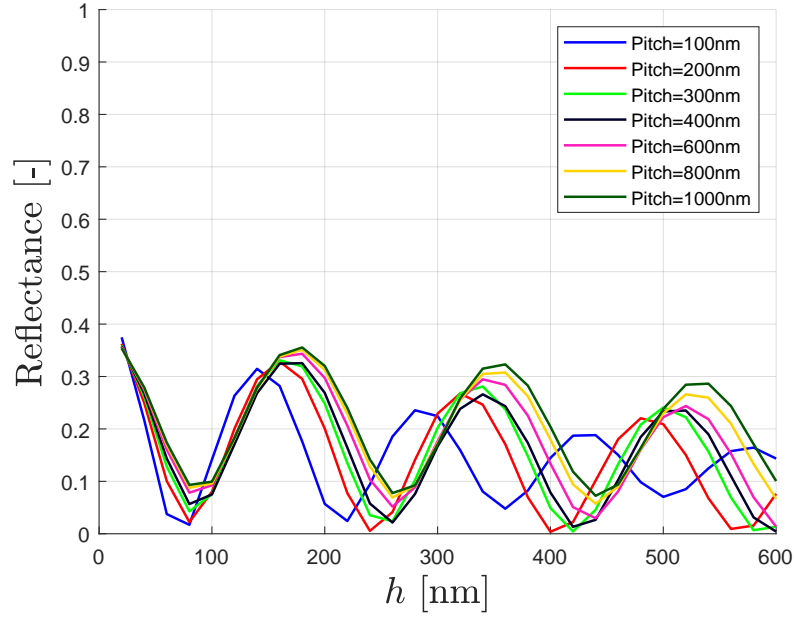


Figure 111: Reflectance spectrum of a normally incident TM polarized plane wave interacting with an array of copper lines with width $w = 34$ nm as a function of the height h . The plot features several values for the pitch of the grating. The spectrum is calculated using FEM.

4.3 Summary

The same methodology as the one of section 3 was used. The effect of the geometry on the reflectance and transmittance spectra of an array made of copper lines was discussed based on the band structures of Figs. 83 and 84. According to these band structures, the effective refractive index of the grating modes can now simultaneously have a real and an imaginary part and it varies a lot less sharply than its PEC counterpart. This translates into attenuation and less sharp cutoff. Moreover, the absorption of the copper lead to reduced values for the reflectance and transmittance.

The pitch was also responsible for the activation of both the grating and diffraction modes. Figs. 85 and 88 show that the spectra globally have the same shape as the PEC ones and that the diffraction modes were excited for the same pitch as for the PEC lines, although less efficiently. The TE spectrum confirmed that there were no sharp cutoff for the grating modes, as it can for example be highlighted in Fig. 91a. TM polarization was very similar to the PEC, although no EOT was seen for 100 nm, due to a different effective refractive index. The effect of width on the activation of the grating modes was a lot less obvious than with the PEC array since there is no more sharp cutoff. Instead, increasing the width mostly increased the reflectance from a minimum to a maximum, as seen in Figs. 58 and 59.

The height was again responsible for thin-film interferences, as showed by Figs. 110 and 111. The absorption of copper can be visualized, as more light is absorbed with increased line height. For copper, the TE effective refractive index varies a lot more slowly than the PEC one as a function of pitch and as a consequence, the different pitches of Fig. 110 were quite similar. However, the TM curves are more disparate as the copper TM_0 is different than the EMA mode. For the same reason, the EOT is now seen for $h = 500$ nm instead of 100 nm. A taller line height also allowed a better visualization of the modes for both TE and TM, as seen in Figs. 108 and 109. The copper TE_1 mode looks similar to the PEC one while the copper TM_0 mode is a bit different than the EMA one, featuring a higher field density in the vicinity of the metal line due to the continuity of the magnetic field across the line interface.

5 Conclusion and outlooks

In this master thesis, the interaction of light with periodic arrays of nanometer-wide metal lines was studied. To do so, extensive use of wave optics, waveguide and diffraction grating theories was made to better understand the interaction of light with a structure made of perfect electrical conductor (PEC) lines, both for TE and TM polarizations. In particular, we proposed to gather the results of those theories in an original band structure to understand how light can couple into the array as a function of the geometrical parameters. The structure was viewed as periodic metallic waveguides simultaneously constituting a diffraction grating. The model was used to analyze quantitative numerical finite element calculations of reflectance and transmittance spectra and was able to explain the different variations of the spectra, although it could not predict their amplitudes for a given set of geometrical parameters, nor could it predict the proportion of power that was located in each propagating mode of the band structure.

First, an array of PEC lines was studied. The effect of the geometrical parameters are summarized in section 3.3. The pitch was responsible for the activation of both the waveguide and diffraction modes. The cutoff was visible for TE while extraordinary optical transmission (EOT) was observed for TM. The width only affected the waveguide modes, and had an effect opposite to the pitch. The height was responsible for thin-film interferences and highlighted the attenuation of evanescent modes. In general, the TE band structure was able to predict the behavior of the reflectance and transmittance spectra, while the TM band structure had to be modified with the effective medium approximation (EMA), as the TEM was unable to describe the geometric dependence of the spectra at low pitch due to its non-dispersive aspect.

Then, an array of copper line was studied and compared to the array of PEC lines. The results are summarized in section 4.3. The TE and TM band structures used for copper predicted some attenuation for the modes as well as less sharp transitions. The pitch was also responsible for the activation of waveguide and grating modes. No clear cutoff pitch was visible for the former, while the cutoff pitches were the same as PEC for the latter. EOT was observed for TM at a height different than for the PEC lines. The effect of width on the waveguide modes was less visible due to their smoother effective refractive index. However, it was possible to observe surface plasmon polaritons (SPPs) at large width, but their effect on the spectra was unclear. The height was again responsible for thin-film interferences and allowed a better visualization of the modes propagating in the grating. The spatial distribution of copper TE_1 mode appeared to be very similar to the PEC one, while the TM_0 mode featured some less expected field concentration near the metal lines. The absorbing nature of copper lead the reflectance and transmittance to be scaled down with respect to those of PEC.

In conclusion, the insight developed by studying an array of PEC lines was crucial to understand the interaction of light with the an array of real metal lines. While the TE behavior could be predicted by the corresponding band structure, some particular attention

was required by the TM description, which in some cases failed to describe the spectra.

To go further, some additional geometrical parameters could be considered, namely the incidence angle and the tapering (sidewall angle of the metallic lines). The incidence angle is expected to modify the dispersion relation of the diffraction modes while leaving those of the waveguide modes unchanged. A non-normal incidence angle should nonetheless modify how light couples into those waveguide modes as it might yield a better or worse matching at the interface for specific modes. The sidewall angle is expected to induce a height dependence of the effective refractive index associated to a waveguide mode, as the separation distance between two metallic plates now depends on the height. Moreover, it is the value of this distance at the bottom of the line, where the width is the largest, that would fix the cutoff of a waveguide mode, and some higher cutoff pitches should result from this geometrical feature.

Additionally, it would be interesting to put more work into the understanding of the light coupling mechanism, i.e., the matching at an interface and the integral overlap methods. This would allow a better physical understanding of the light interaction with the array that is not limited to a qualitative description of the different available modes, and might give some understanding as to why one waveguide or diffraction mode is more excited in one case than in another, which was not always explainable in the frame of this master thesis.

Ideally, a quantitative link more elaborate than the Fresnel equations could be made between the dispersion relations featured in the band structures and the reflectance and transmittance of the array, as the model used in this text was not able to produce such quantitative results. The SPPs were not covered in details in this text but it might be interesting to measure their impact on the reflectance and transmittance spectra. Since SPPs are features of real metals that can result from a coupling mechanism such as a diffraction grating, they could have a place of interest in an improvement of this thesis.

Finally, some other metals could be considered as well and then compared to both the PEC lines and copper lines to further increase the understanding of the effect of the finite optical constants and material properties on the reflectance and transmittance spectra.

6 Acknowledgments

Writing this master thesis certainly proved to be a huge challenge, especially so in the context of the 2019-2020 pandemic where many stress factors were piling up and making it hard to find the motivation to work on a master thesis. However I had the chance to have a very comprehensive team to work with, which inspired me to always put more effort into my work.

I would first like to thank Janusz, who first proposed the thesis subject. He demonstrated a passionate involvement for my work, constantly motivating and reassuring me, bringing good mood to the meetings and making sure I make some progress, while I know that too often some master thesis supervisors are just missing in action, leaving their student on their own.

Then, I would like to thank Andrzej, who spent a lot of time gathering literature, theories and videos to help me start this thesis, and then spent even more time teaching me how run simulations, giving in depth explanations on any questions I had and also spending time introducing me to imec's premises, where sadly I did not have the chance to spend much time in the end.

Finally, I would like to thank Mr. Vanderheyden, who provided me with the subject proposition and introduced me to Janusz. Mr. Vanderheyden was always available for discussion and prompt to respond to emails, always gave some very appreciated feedback when needed, and was very comprehensive when I was crumbling under the workload of other courses and could not put much work into the thesis.

Finally, I would like to thank my mother for his constant support and for not giving me too much chores to do while I was working on the thesis.

I would like to thank those persons again for their understanding when times were hard, especially when the decision was taken to report the thesis to august.

7 Appendix

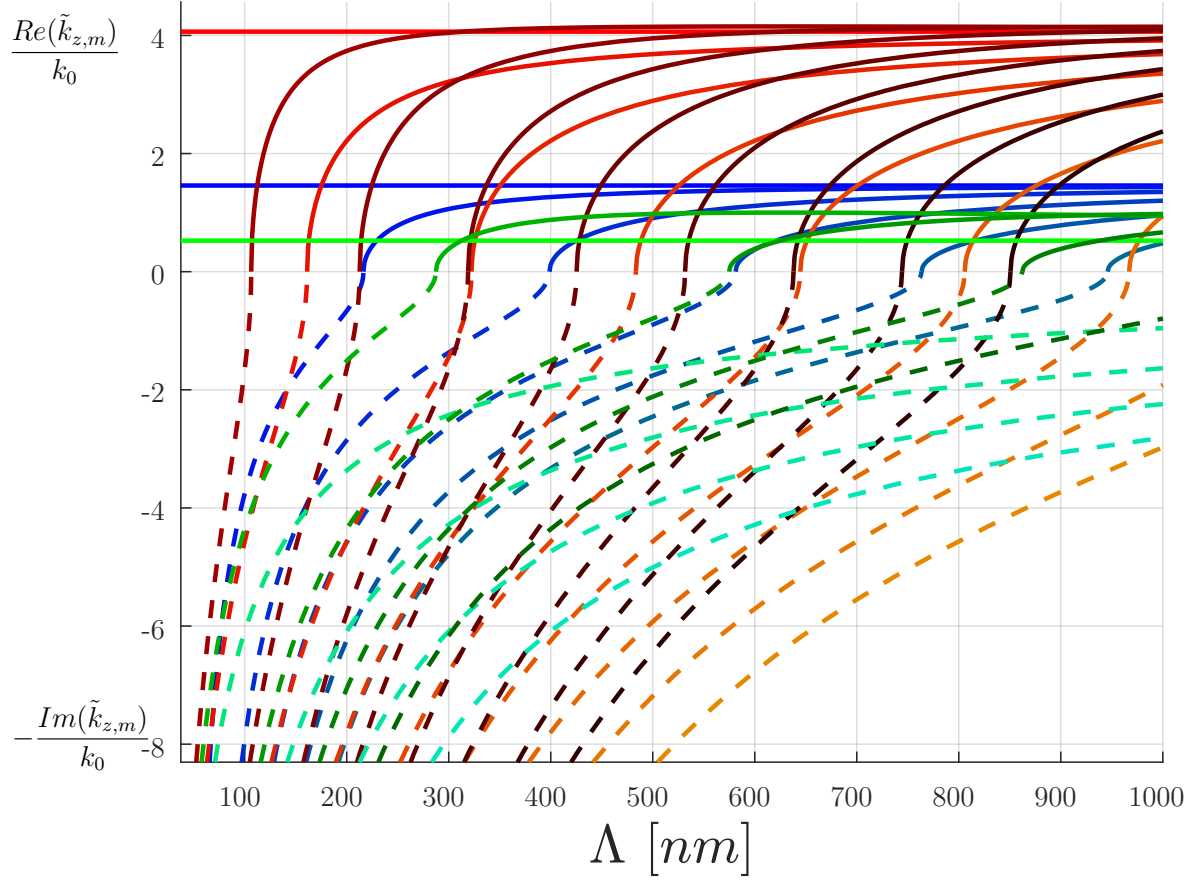


Figure 112: Band structure for the array of PEC lines under TM illumination, which features all the modes contained below a pitch $\Lambda = 1000\text{nm}$, for a free-space wavelength $\lambda_0 = 532\text{ nm}$, width $w = 34\text{nm}$, refractive indices $\tilde{n}_{air} = 1$, $\tilde{n}_{Si} = 4.15$, $\tilde{n}_{SiO_2} = 1.45$ and $\theta_i = 45^\circ$. The solid lines represent the real part of the wave number, while the dashed lines represent the opposite of its imaginary part. Blue curves correspond to waveguide modes, green curves correspond to diffraction in reflection modes and red curves correspond to diffraction in transmission modes.

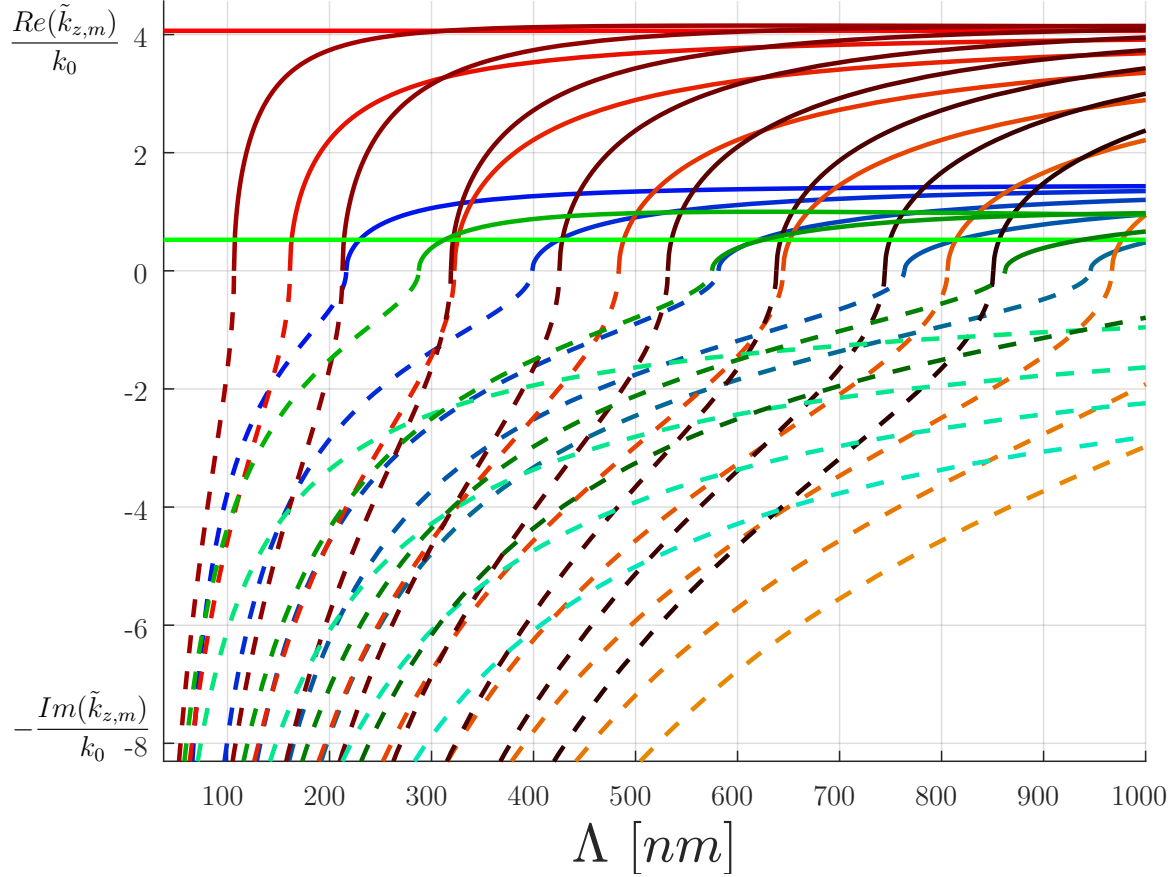


Figure 113: Band structure for the array of PEC lines under TE illumination, which features all the modes contained below a pitch $\Lambda = 1000\text{nm}$, for a free-space wavelength $\lambda_0 = 532\text{nm}$, width $w = 34\text{nm}$, refractive indices $\tilde{n}_{air} = 1$, $\tilde{n}_{Si} = 4.15$, $\tilde{n}_{SiO_2} = 1.45$ and $\theta_i = 45^\circ$. The solid lines represent the real part of the wave number, while the dashed lines represent the opposite of its imaginary part. Blue curves correspond to waveguide modes, green curves correspond to diffraction in reflection modes and red curves correspond to diffraction in transmission modes.

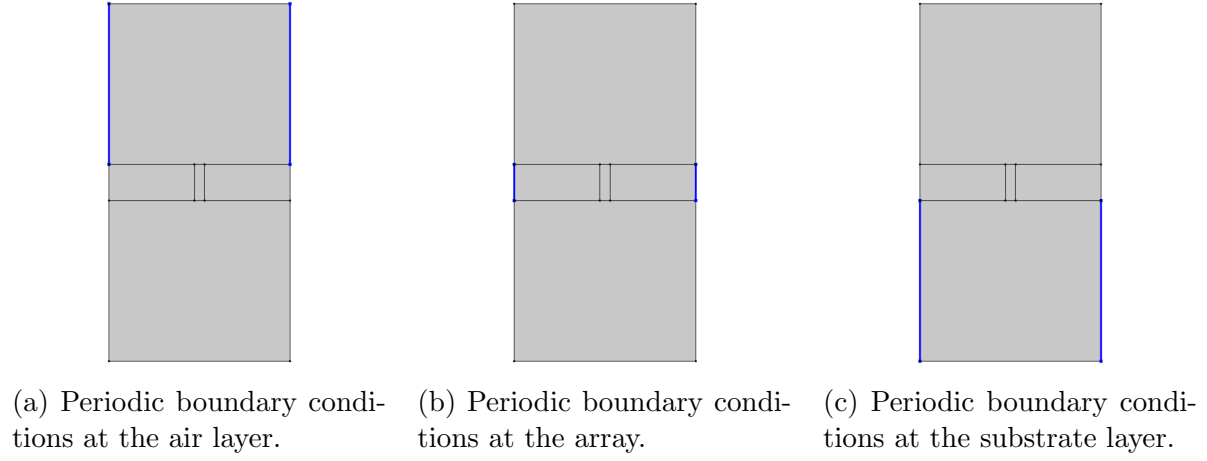


Figure 114: Periodic Periodicity boundary conditions.

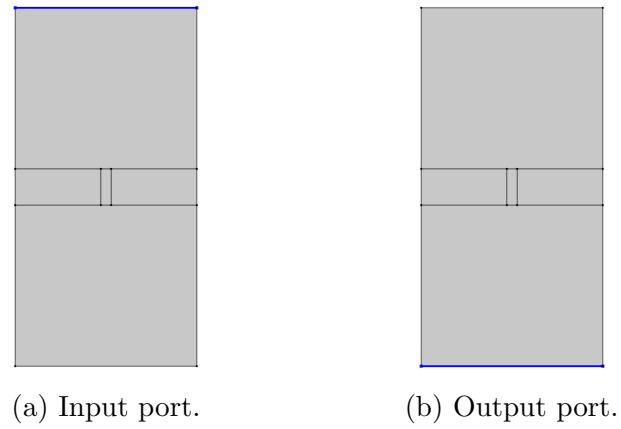
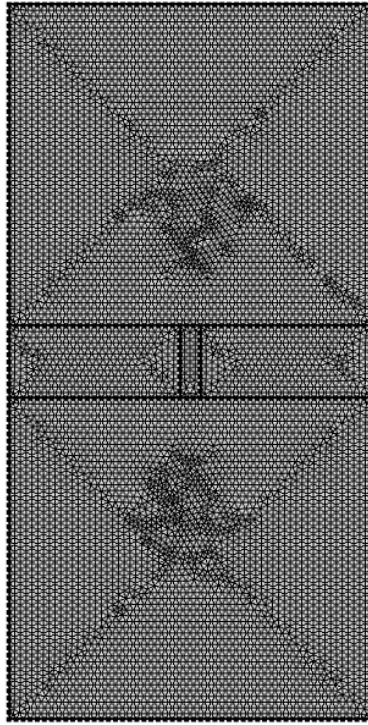
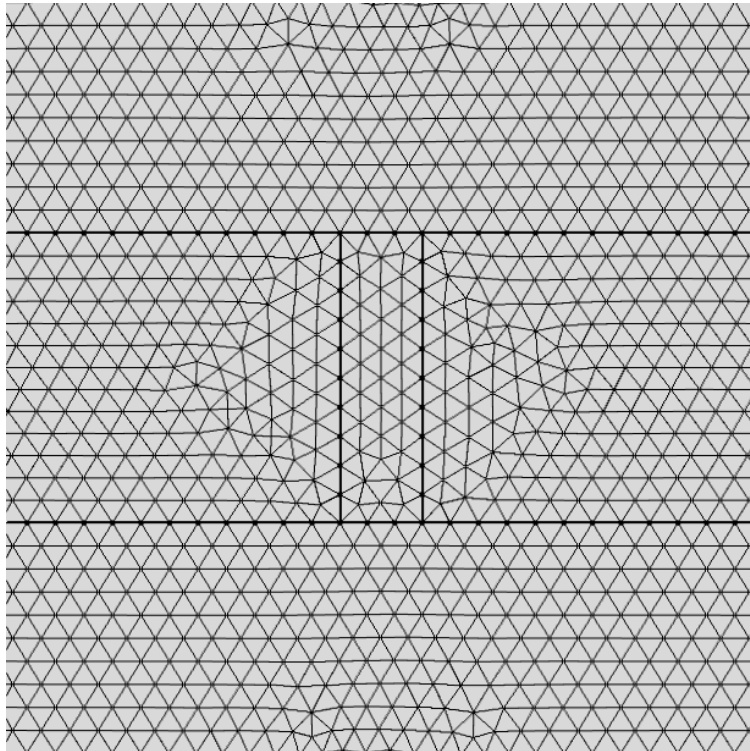


Figure 115: Input and output ports.



(a) Automatic triangular mesh.



(b) Automatic triangular mesh - zoom.

Figure 116: Automatic triangular mesh.

References

- [1] Mun Seok Jeong et al. “Optical Characterization of Nanomaterials”. In: Journal of Nanomaterials 2014 (2014), pp. 1–2. ISSN: 1687-4110. DOI: 10.1155/2014/739212.
- [2] Benoît Vanderheyden. “ELEN069 - Nanoelectronics / Optoelectronics”. University of Liège, 2019.
- [3] Lukas Novotny and Bert Hecht. Principles of nano-optics. Cambridge university press, 2012.
- [4] Challa SSR Kumar. UV-VIS and photoluminescence spectroscopy for nanomaterials characterization. Springer, 2013.
- [5] Karen Reinhardt and Werner Kern. Handbook of silicon wafer cleaning technology. William Andrew, 2018.
- [6] Kenneth E Bean and WR Runyan. Semiconductor integrated circuit processing technology. Addison-Wesley, 1990.
- [7] Gordon E Moore. “Cramming more components onto integrated circuits”. In: Proceedings of the IEEE 86.1 (1998), pp. 82–85.
- [8] Metrology. https://semiengineering.com/knowledge_centers/manufacturing/process/metrology/. Accessed: 19/05/2020.
- [9] Metrology and Inspection. <https://www.hitachi-hightech.com/global/products/device/semiconductor/metrology-inspection.html>. Accessed: 19/05/2020.
- [10] David J Whitehouse. Handbook of surface metrology. CRC Press, 1994.
- [11] Alain C Diebold. Handbook of silicon semiconductor metrology. CRC Press, 2001.
- [12] D Keith Bowen and Brian K Tanner. X-ray metrology in semiconductor manufacturing. CRC Press, 2018.
- [13] Linda Towidjaja et al. “Back end of line metrology control applications using scatterometry”. In: Metrology, Inspection, and Process Control for Microlithography XX. Ed. by Chas N. Archie. Vol. 6152. International Society for Optics and Photonics. SPIE, 2006, pp. 688–699. DOI: 10.1117/12.656515. URL: <https://doi.org/10.1117/12.656515>.
- [14] M. G. Faruk et al. “Enabling Scatterometry as an In-Line Measurement Technique for 32 nm BEOL Application”. In: IEEE Transactions on Semiconductor Manufacturing 24.4 (2011), pp. 499–512.
- [15] Christopher J Raymond. “Scatterometry for semiconductor metrology”. In: Handbook of silicon semiconductor metrology. CRC Press, 2001, pp. 477–514.
- [16] H Jobin Yvon. Strain measurements of a Si cap layer deposited on a SiGe substrate determination of the SiGe composition. Springer, 2013.
- [17] Andrzej Gawlik et al. “Critical dimension metrology using Raman spectroscopy”. In: Applied Physics Letters 117.4 (2020), p. 043102.

- [18] Janusz Bogdanowicz et al. “Nanofocusing of light into semiconducting fin photonic crystals”. In: Applied Physics Letters 108.8 (2016), p. 083106.
- [19] Andrzej Gawlik et al. “Enhanced light coupling into periodic arrays of nanoscale semiconducting fins”. In: Applied Physics Letters 113.6 (2018), p. 063103.
- [20] Andrzej Gawlik et al. “Size-dependent optical properties of periodic arrays of semiconducting nanolines”. In: Optics Express 28.5 (2020), p. 6781. DOI: 10.1364/oe.386964.
- [21] Cyriaque Genet and Thomas W Ebbesen. “Light in tiny holes”. In: Nanoscience And Technology: A C World Scientific, 2010, pp. 205–212.
- [22] Hyungsoon Im et al. “Vertically oriented sub-10-nm plasmonic nanogap arrays”. In: Nano letters 10.6 (2010), pp. 2231–2236.
- [23] I. Chernykh et al. “Optical properties of 1D metal nanogratings”. In: Journal of Surface Investigation 5 (Oct. 2011), pp. 941–944. DOI: 10.1134/S1027451011100065.
- [24] Alfredo Bermúdez, Dolores Gómez, and Pilar Salgado. “Maxwell’s equations in free space”. In: Mathematical Models and Numerical Simulation in Electromagnetism. Cham: Springer International Publishing, 2014, pp. 53–65. ISBN: 978-3-319-02949-8. DOI: 10.1007/978-3-319-02949-8_4. URL: https://doi.org/10.1007/978-3-319-02949-8_4.
- [25] David J Griffiths. Introduction to electrodynamics. 2005.
- [26] L.C. Shen and Jin Au Kong. Applied electromagnetism. PWS Engineering, 1995. ISBN: 9780534076207. URL: <https://books.google.be/books?id=X2p7Pt9lP0IC>.
- [27] Julius Adams Stratton. Electromagnetic theory. Vol. 33. John Wiley & Sons, 2007.
- [28] Neil W Ashcroft, N David Mermin, et al. Solid state physics [by] Neil W. Ashcroft [and] N. David Mermin. 1976.
- [29] Richard Fitzpatrick. “Introduction to plasma physics”. In: The University of Texas at Austin: sn (2008), p. 242.
- [30] Frederick Wooten. Optical properties of solids. Academic press, 2013.
- [31] Mark Fox. Optical properties of solids. 2002.
- [32] P. B. Johnson and R. W. Christy. “Optical Constants of the Noble Metals”. In: Phys. Rev. B 6 (12 Dec. 1972), pp. 4370–4379. DOI: 10.1103/PhysRevB.6.4370. URL: <https://link.aps.org/doi/10.1103/PhysRevB.6.4370>.
- [33] MAX BORN and EMIL WOLF. “CHAPTER XIII - OPTICS OF METALS”. In: Principles of Optics (Sixth Edition). Ed. by MAX BORN and EMIL WOLF. Sixth Edition. Pergamon, 1980, pp. 611–664. ISBN: 978-0-08-026482-0. DOI: <https://doi.org/10.1016/B978-0-08-026482-0.50020-7>. URL: <http://www.sciencedirect.com/science/article/pii/B9780080264820500207>.
- [34] James M Palmer. “The measurement of transmission, absorption, emission, and reflection”. In: Handbook of optics 2 (1995), pp. 25–1.
- [35] Pochi Yeh et al. Optical waves in layered media. Vol. 95. Wiley Online Library, 1988.

- [36] Dr. Raymond C. Rumpf. “EE533-Computational Electromagnetics”. University of Texas at El Paso, College of Engineering, Department of Electrical and Computer Engineering, 2020.
- [37] Junxi Zhang, Lide Zhang, and Wei Xu. “Surface plasmon polaritons: physics and applications”. In: Journal of Physics D: Applied Physics 45.11 (2012), p. 113001.
- [38] J. M. Steele et al. “Metallodielectric gratings with subwavelength slots: Optical properties”. In: Physical Review B 68.20 (2003), p. 205103. ISSN: 1098-0121. DOI: 10.1103/physrevb.68.205103.
- [39] J. M. Steele et al. “Metallodielectric gratings with subwavelength slots: Optical properties”. In: Phys. Rev. B 68 (20 Nov. 2003), p. 205103. DOI: 10.1103/PhysRevB.68.205103. URL: <https://link.aps.org/doi/10.1103/PhysRevB.68.205103>.
- [40] Wangtao Lu, Ya Yan Lu, and Dawei Song. “A Numerical Mode Matching Method for Wave Scattering in a Layered Medium with a Stratified Inhomogeneity”. In: SIAM J. Sci. Comput. 41 (2019), B274–B294.
- [41] Weijian Yang. “High Contrast Gratings for Integrated Optoelectronics”. PhD thesis. EECS Department, University of California, Berkeley, Dec. 2014. URL: <http://www2.eecs.berkeley.edu/Pubs/TechRpts/2014/EECS-2014-197.html>.
- [42] Tina Clausnitzer et al. “An intelligible explanation of highly-efficient diffraction in deep dielectric rectangular transmission gratings”. In: Optics express 13.26 (2005), pp. 10448–10456.
- [43] COMSOL Multiphysics website. <https://www.comsol.com/comsol-multiphysics>. Accessed: 13/05/2020.
- [44] P. B. Johnson and R. W. Christy. “Optical Constants of the Noble Metals”. In: Phys. Rev. B 6 (12 Dec. 1972), pp. 4370–4379. DOI: 10.1103/PhysRevB.6.4370. URL: <https://link.aps.org/doi/10.1103/PhysRevB.6.4370>.
- [45] Vadim A. Markel. “Introduction to the Maxwell Garnett approximation: tutorial”. In: JOSA A 33.7 (2016), pp. 1244–1256. ISSN: 1520-8532. DOI: 10.1364/josaa.33.001244.
- [46] Philippe Lalanne and Jean-Paul Hugonin. “High-order effective-medium theory of subwavelength gratings in classical mounting: application to volume holograms”. In: JOSA A 15.7 (1998), pp. 1843–1851.
- [47] FJ Garcia-Vidal, L Martin-Moreno, and JB Pendry. “Surfaces with holes in them: new plasmonic metamaterials”. In: Journal of optics A: Pure and applied optics 7.2 (2005), S97.
- [48] Shiwei Tang et al. “Effective-medium theory for one-dimensional gratings”. In: Physical Review B 91.17 (2015), p. 174201.
- [49] Thomas W Ebbesen et al. “Extraordinary optical transmission through sub-wavelength hole arrays”. In: Nature 391.6668 (1998), pp. 667–669.